POLITECNICO DI TORINO

Corso di Laurea Magistrale
in Ingegneria Matematica

Tesi di Laurea magistrale

Circular Shallow Water Profiles

Relatori
Prof. Lamberto Rondoni
Prof. Luca Ridolfi

Candidato
Diego Urbani

Anno Accademico 2022/2023

A nonna Angela, a me,
al ricordo delle nostre
passeggiate insieme,
lungo il fiume,
controcorrente.

Abstract

Inspired by pertinent literature in the context of Analogue Gravity, this work analyzes the stream profiles of a fluid film flowing along a radially symmetric, inclined bed with different bottom topographies, in the framework of a 2-D Shallow-water model in radial symmetry. First, steady state profiles are obtained without including turbulent friction, with different slopes and three kinds of bottom topography: flat, stepped and sinusoidal. The flat bottom produces new kinds of orbits with a two Critical Froude Horizons behaviour, because of the interplay between Discharge Conservation and Momentum Balance, which is affected by the presence of slope. The stream profiles obtained for the stepped bottom exhibit instead an energy jump, which allows to interpret discontinuities as orbit jumps. The sinusoidal profile instead can be seen as a sinusoidal perturbation of the flat one: the response of the stream to the amplitude of such perturbation is found to be dependent on an inequality involving Radiant Specific Kinetic Height, and can be amplifying, stabilizing or damping. When turbulent friction (modeled with Chézy parametrization) is included, the stream profiles obtained for the same bottom topographies result to be governed by gravity in case of subcritical regime and by friction in case of supercritical one. In addition, also novel bottom topographies ensuring energy conservation, critical depth and uniform height are obtained. The solutions with Hydraulic jump, represented as a shock discontinuity of zero order, are then obtained and the limits of such representation are analyzed. Finally, a Perturbation Equation of the Shallow-water model is obtained to serve as a future work on Linear Stability analysis.

Acknowledgements

Sembrerebbe un gesto di educazione, gentilezza e quasi dovere morale quello di ringraziare tutte le persone che, a loro modo, ti accompagnano in un viaggio così lungo: lunghe liste di familiari, amici, parenti e colleghi che popolano almeno una pagina di questo capitolo che, in effetti, rappresenta l'unico vero momento di riflessione nel percorso universitario che ci concediamo per raccontare di noi stessi.
Pensiamo a chi ci ha permesso di portare avanti questo percorso, lo citiamo e lo ringraziamo.
Pensiamo a chi ci è venuto incontro in un momento di aiuto, lo citiamo e lo ringraziamo.
Pensiamo a chi rideva con noi in quelle belle serate infinite tra i locali del centro, lo citiamo e lo ringraziamo.
E' così che nascono queste pagine: citazioni e ringraziamenti di persone che solo adesso ci sono sembrate indispensabili al raggiungimento di questo traguardo, lunghi elenchi di predicati verbali e complementi senza i quali la sintassi di questa esperienza sembra sbriciolarsi in un elenco sparpagliato di nomi, soggetti fluttuanti, opachi riflessi di un «Io» costretto ad usare uno specchio per non sentirsi solo.
Quell' «Io» senza il quale, però, tutte queste pagine non potrebbero nemmeno scriversi.
E' per questo che questo capitolo sarà dedicato a sette persone indispensabili alla sua stesura: il Prof. Rondoni ed il Prof. Ridolfi relatori di questa Tesi, il mio compagno Gabriele, mio fratello Michelangelo e tre di quegli «Io» che, per una volta, vorrebbero sentirsi importanti per i loro predicati verbali, non solo per i complementi.
Ringrazio il Prof. Rondoni e il Prof. Ridolfi per avermi permesso di riprendere questo lavoro dopo un lungo momento di pausa, per avermi dato le linee guida giuste per esprimere al meglio il mio bagaglio di conoscenze, per aver insistito anche sugli aspetti di perfezionamento e avermi aiutato a dare una direzione a questo lavoro: per me è stata un'occasione di crescita culturale, professionale e personale.
Ringrazio il mio amore Gabriele: sei stato il mio supporto e la mia spalla sin dai primi giorni in cui ci siamo conosciuti, hai riacceso le luci del mio percorso e hai fatto in modo che non si spegnessero più. Mi hai sempre detto quando non andava, a costo di litigare e quando hai capito che ero pronto, mi hai spronato a riprendere questo lavoro e a metterci una quadra.
Ringrazio mio fratello Michelangelo, custode dei miei segreti e delle mie emozioni: sei stato il primo a sapere di tanti avvenimenti della mia vita e ad accoglierli con il candore della tua età, nonstante sia così differente dalla mia. Grazie per aver tenuto per te, per un bel pò, il fatto che avevo ripreso a scrivere.

Ringrazio il Diego del 2014: la sua intraprendenza, la sua curiosità, la voglia di andare fino in fondo e gli impegni che amava prendersi lo hanno portato ad iniziare questo viaggio con tutte le difficoltà e gli imprevisti di un'orizzonte temporale così vasto.
Ringrazio il Diego del 2015: il suo primo dolore, le sue fragilità, le sue preoccupazioni e la sua confusione hanno insegnato all'altro Diego che la bellezza della vita risiede anche nel riuscire ad affrontare, a viso aperto, ciò che ci fa del male e a continuare ciò che si è iniziato.
Ringrazio il Diego del 2019: mettere un punto sui tanti anni passati a nascondersi dalla sua vera identità ha insegnato agli altri Diego che ciò che noi reputiamo un problema corre sempre più veloce di noi, quando ci diamo alla fuga.
Ringrazio il Diego di oggi: è riuscito ad affermarsi, ad essere indipendente, a fare ciò che gli piace e a portare a termine con un pò di sacrificio ciò che aveva iniziato. Un sacrificio ripagato dalla soddisfazione e dall'amore che ha sempre avuto per le Scienze, prime su tutti le Scienze Matematiche.
Già, ringrazio anche la Matematica e la passione che, come nient'altro, riesce a darmi e sempre mi darà.
Ringrazio la mia famgilia, tutti i miei amici e cugini folignati, i miei amici di Porto Sant'Elpidio, i miei amici di Bovolone e i miei colleghi del Team Workflow di Fiege Logistics Verona.
Infine, un ringraziamento speciale anche a chi, fermandosi alla mia apparenza un pò sorniona, ha pensato che non fosse abbastanza per farcela. A quella manciata di persone incontrate nel corso di questa esperienza dedico una canzone del mitico Alberto Sordi: "E va'... E va'...", in tutto lo splendore del suo ritornello.
Ah già, dimenticavo: grazie Loredana, per avermi spinto per lungo tempo a guardare dentro me stesso, a non scoraggiarmi e a non dimenticare mai il mio valore.

Contents

O insensata cura de' mortali,
quanto son difettivi silogismi
quei che ti fanno in basso batter l'ali!

Chi dietro a iura, e chi ad amforismi
sen giva, e chi seguendo sacerdozio,
e chi regnar per forza o per sofismi,

e chi rubare, e chi civil negozio,
chi nel diletto de la carne involto
s'affaticava e chi si dava a l'ozio,

quando, da tutte queste cose sciolto,
con Beatrice m'era suso in cielo
cotanto gloriosamente accolto. [...]

Intra Tupino e l'acqua che discende
del colle eletto dal beato Ubaldo,
fertile costa d'alto monte pende,

onde Perugia sente freddo e caldo
da Porta Sole; e di rietro le piange
per grave giogo Nocera con Gualdo.

Di questa costa, là dov'ella frange
più sua rattezza, nacque al mondo un sole,
come fa questo tal volta di Gange.

Però chi d'esso loco fa parole,
non dica Ascesi, ché direbbe corto,
ma Oriente, se proprio dir vuole.

[Dante Alighieri, Divina Commedia,
Paradiso, Canto XI, Versi 1-12, 42-54]

Introduction

Circular Shallow Water profiles have found progressively greater interest in the field of Hydrodynamics, although the related literature remains currently narrower and less systematic with respect to that on Open Channel flows, for which notable textbooks, including Ref. [36], organize the main theoretical aspects and applications.
The most common situation to observe Circular Shallow Water profiles comes from the daily experience: a water jet impinging on the kitchen sink, forming an inner circular, thin film (where water flows rapidly) followed by an outer region with increased height (where water flows more slowly). By introducing the Froude Number $Fr = U/\sqrt{gh}$, where U is the mean velocity of the flow, h is the water depth and g is the gravitational constant, the inner region is characterized to have $Fr > 1$ while, on the contrary, the outer region is characterized to have $Fr < 1$ and they are respectively denoted as *supercritical* and *subcritical* regimes. The transition from the inner supercritical region, where the gravity waves can only propagate upstream, to the outer subcritical region, where gravity waves can propagate both downstream and upstream, takes place through a marked shock discontinuity of the flow features (including depth) usually referred to as "Circular Hydraulic Jump", which is well shown in Fig. 1. This common phenomenon was described also by Leonardo da Vinci in the 16th century (Ref. [6]), but the first notable experimental study is dated 1820 and has been carried out by the Italian mathematician and hydraulic engineer Giorgio Bidone, in Ref. [7]. One of the first attempts to provide instead a mathematical description of Hydraulic Jump in Open Channel flows by means of Continuity and Momentum equations was made by Lord Rayleigh in Ref. [35], which included also a description of the Circular Hydraulic Jump as a bore on a small scale.
A notable work in modelling Circular Hydraulic Jump is that in Ref. [8], which makes use of both a 2D Shallow-water model in radial symmetry and Boundary Layer equations to obtain a qualitative description of the dynamics and a scaling law for the radial position. Other related works include [22, 23].
Practical applications of stream profiles in radial symmetry can be found in the field of River Engineering for the design of stilling basins (Ref. [1, 28]), where the related studies are mostly focused on finding and estimating practical measures to control the formation of circular hydraulic jumps (such as jump position and sequent depth ratio).
However, a fascinating point of view, which highlights one more time the interdisciplinarity of Hydrodynamics, is provided by the analogies between the behaviour of Shallow-water streams and several cosmological phenomena, in the wider context of Analogue Gravity

(Ref. [5]). The aim of the research related to Analogue Gravity is to find analogs of relativistic gravitational fields within other physical systems ([5]), usually well understood. An early work (1981) in this sense is provided in Ref. [40], where it is shown that there exist well known acoustic phenomena having the same properties of the black holes, as far as the quantum thermal radiation is concerned.
The advantage of finding well described physical analogs of more complex phenomena is not only to provide a more accurate theoretical description by means of well understood properties, but also to reproduce them in a proper laboratory setting, with simpler instrumentation. This is the case of the Shallow-water experiments carried out in Ref. [18], which aimed to reproduce the *Standing Accretion Schock Instability* happening into the stellar core during the collapse that originates a neutron star, completed by a 2D Shallow-water model where the aforementioned shock-instability is represented by that of the circular hydraulic jump, in a convergent radial flow.
In Ref. [20] the Circular Hydraulic Jump, in divergent radial flow, is instead taken as a hydrodynamic analogue of a White Hole (i.e., a time-reversed Black Hole), described from a Dynamical Systems point of view as a Saddle-Node Bifurcation.
Despite all of these applications, few works aim to provide an organic classification of steady Shallow Water Profiles in radial symmetry: these include Ref. [42], where the supercritical and subcritical solutions are obtained for a stream flowing in both convergent and divergent direction over a horizontal bed, finding analytical form by means of a perturbative expansion and modeling hydraulic jump as a shock discontinuity of 0 length. Finally, another work which provides a classification of steady Circular Shallow-water profiles is that in Ref. [29], where flows along a horizontal bed in both convergent and divergent direction are taken into account, including also turbulent friction, in order to find analogies with the aforementioned cosmological phenomena, including black holes, white holes and neutron stars.
Despite the fascinating connections highlighted between different physical phenomena observed at distant scales and the refined theoretical and experimental methods used, all of the previous works are focused on specific aspects of model adopted. This results in the lack of a unified mathematical point of view which, starting from the governing equation, would make able to reproduce the main physical aspects and explicit the energetic contributes that drive the behaviour of the stream properties. In this context, this work aims to enrich the classification of steady Circular Shallow water profiles started in Ref. [29], by including in the set of de Saint-Venant equations in radial symmetry the slope of a bed of general inclination angle $\phi \in [0, \pi[$ with respect to the ground level and the presence of a non-flat bottom topography, for instance sinusoidal and negative stepped. The general appearance, due to the radial, axially-symmetric geometry, will be that of a Horizontal, a Cone or a Funnel bed depending on whether $\phi = 0$, $\phi \in]0, \pi/2[$ or $\phi \in]\pi/2, \pi[$, as shown in Figures 2, 3, while the bottom topography is represented as a departure from the flat bottom. Beyond the analytical and computational effort that requires the introduction of the aforementioned features in the model and the deduction of general properties from it, the complexity they add opens to a wider variety of novel solutions with respect to what already discussed in [29, 42]. This is particularly visible by the introduction of the sole bed slope, which in case of a funnel-shaped bed gives rise to stream profiles reaching critical conditions at exactly two points, exhibiting a so called *two Froude Horizons* behaviour.

Profiles connecting two critical horizons were already documented in [29] for a horizontal bed and flat bottom when turbulent friction is included, along with the corresponding astrophysical analog (Ref. [40, 46]), but our results show that the same can be obtained by simply changing the bed inclination, showing a beautiful connection between apparently different dynamics and proving that the same phenomenon can be also reproduced by means of a different laboratory setting.
Inspired by similar observations, especial attention is dedicated throughout the whole work to the monotony properties of the stream profiles obtained, which are strongly related to the interplay between the bed slope, the presence of turbulent friction and the bottom topography considered, the latter being evident in the geometric shape of the profiles. In particular, by introducing *Radiant Specific Kinetic Height* (which arises by the first derivative of the Stream Head) and *Radiant Specific Discharge* (this one already introuced in [29]), respectively describing the distribution of Kinetic Height and Volumetric Flowrate along the radial coordinate, it is possible not only to find the exact monotony intervals, but also a physical explanation of the monotony properties and the flow amplitude response to the sinusoidal bottom topography.
The development of Circular Hydraulic Jump in the solution is investigated by means of a detailed analysis of the dynamical systems describing the height profiles, valid for general bottom topographies satisfying certain regularity requirements and highlighting an important difference between the flat bottom and the sinusoidal bottom: while in the first case the possibility of hydraulic jump is connected to the presence of a focus in the physical region of the phase space, multiple focus followed by as many saddle points can arise, depending on the Stream Energy balance. The hydraulic jump is then treated as a shock discontinuity of zero length, its position being determined as the intersection between the specific supercritical and subcritical forces, which include the sole contributes due to hydrostatic and dynamic pressure. This is an important simplification, since coherently with Ref. [29, 42] lateral hydrostatic components and bed friction are neglected.
Intrinsic in the depth-averaging process giving rise to the Shallow-water equations is the hypothesis of *gradually varied flow* (Ref. [36]), which drives the choice of the parameter values for the simulations and provides an additional element to interpret the solutions. In this sense, the case of sinusoidal bottom topography can be considered as non violating the hypothesis of gradually varied flow for sufficiently small amplitudes and wavenumbers and can serve as a starting point for future studies on Roll-waves Instability in radial symmetry, similarly to what done in Ref. [4] in a Cartesian geometry for open channel flows. The same is not true instead for stepped bottom topography, for which the high steepness around the step make the Shallow-water approximation useless and not suitable for the study of the consequent hydraulic jump, which is complicated by separation phenomena and air-water interactions (Ref. [41, 43]). However, it remains as a valid academic example helping to understand the variations of stream energy from an orbit of the phase space to another and to explore the validity limits of the Shallow-water model adopted.
The work is organized as follows:

- Chapter 1 is devoted to the formulation and the mathematical analysis of a non-dimensional, 2D Shallow-water model in radial, axially symmetric geometry, taking into account a basal slope due to the inclination with respect to gravity direction, a

general bottom topography and the presence of turbulent friction;

- in Chapter 2, the general model is particularized to the case in which turbulent friction is neglected and stream profiles and features are obtained for flat, sinusoidal and stepped bottom topographies;
- in Chapter 3, friction is included into the model, employed in its general form, in order to first obtain three notable topographies which show that, thanks to friction, it is possible to obtain stream profiles preserving energy, maintaining same depth and maintaining critical depth; for second, the general model including friction is applied to obtain again stream profiles for flat, sinusoidal bottom topography and negative stepped;
- in Chapter 4, steady state solutions for depth and velocity are perturbed and a system of partial differential equations (time-space depending) is obtained for the perturbations; the problem is then particularized to the steady solution of uniform depth, in order to obtain the sole governing equations of the perturbations.

Although the main goal is to provide steady solutions with a potentially wide range of applications, some brief reminds to the cosmological analogs previously described are possible, in order to give physical significance to certain solutions.

(a) (b) (c)

Figure 1: **Circular Hydraulic Jump and Wave propagation.** The three figures depict the Circular Hydraulic Jump generated by a jet impinging on a steel plate. The yellow natural dye is oil-based, in order to avoid mixing with water, and is injected by a syringe. Fig. 1(a) - Circular Hydraulic Jump. Fig. 1(b) - The yellow die is injected into the supercritical region. It is evident a Mach Cone, indicating a sole upstream propagation of gravity waves. Fig. 1(b) - The yellow die is injected into the subcritical region. It is evident in the yellow dye drop a blurred boundary surrounding a more concentrated drop, indicating that gravity waves can propagate both downstream and upstream.

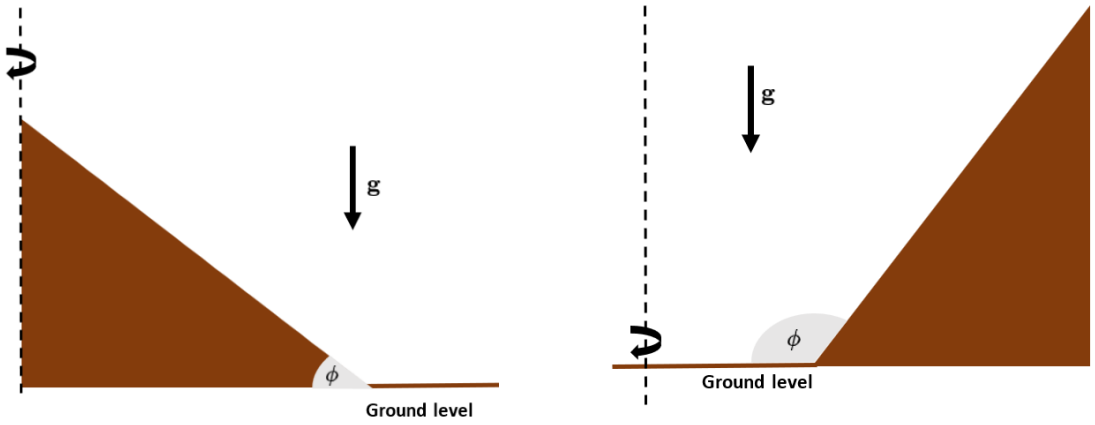

(a) (b)

Figure 2: **Section of a Cone and a Funnel bed with Flat Bottom.** Fig. 2(a) - Section of a Cone-shaped bed ($\phi \in]0, \pi/2[$). Fig. 2(b) - Section of a Funnel bed ($\phi \in]\pi/2, \pi[$). The black dashed line represents represents the rotation axis that allows to obtain the Cone and Funnel beds by a rotation of 360° around it. The other notations are clear from the picture.

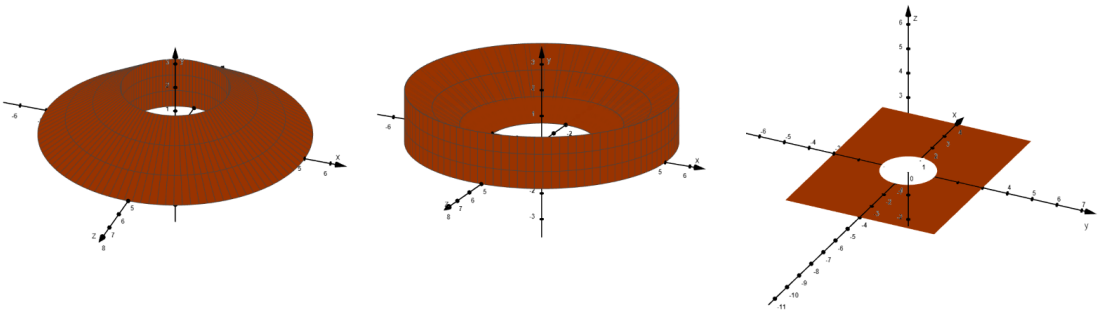

(a) (b) (c)

Figure 3: **Appearance of Cone, Funnel and Horizontal bed with Flat Bottom.** Fig. 3(a) - Cone-shaped bed in three dimensions. Fig. 3(b) - Funnel-shaped bed in three dimensions. Fig. 3(c) - Horizontal bed in three dimensions. The presence of the central holes for which the fluid is drained will be clear within the next chapters. Figures are realized with GeoGebra.

Chapter 1

General Model and Profile Equation

This chapter is devoted to the formulation of a two-dimensional Shallow water model to describe the flow features of a fluid film flowing along an inclined bed, along with a bottom topography simulating possible irregularities with respect to the flat bottom. Radial symmetry will be taken into account, as done in [29] for the case of Horizontal Bed with flat bottom. Additionally, also turbulent friction will be included in the model. The general formulation that will be introduced in this Chapter is similar to that in [4] except for the geometry, which due to the radial symmetry allows to write the two dimensional equations in polar coordinates and to neglect the dependence on the angular coordinate [1]. The chapter organizes as follows:

- dimensional model formulation in polar coordinates, assuming radial symmetry and steady state;
- choice of reference units and formulation of the non-dimensional, stationary model;
- analytic discussion of the stationary model.

The aim is to obtain a general, non-dimensional equation describing fluid depth for the steady state profiles, that will be useful to perform Linear Stability Analysis, as a future work.

1.1 Dimensional Equations

The first step to formulate the model is to define the geometry. As was early mentioned in the Introduction, the problem will be considered in radial, axially-symmetric geometry, thus the bed will appear as Horizontal, Cone-shaped or Funnel-shaped depending on the

[1] In [4] the geometric setting is Cartesian and one-dimensional.

angle ϕ formed with the ground level, as shown in Figures 2, 3. Therefore, it is useful to start by describing a single section of the bed. Let consider an inclined plane forming an angle $\phi \in [0, \frac{\pi}{2}[\cup]\frac{\pi}{2}, \pi[$ with respect to the ground level (orthogonal to the gravity direction), assumed to be clockwise oriented. Moreover, let consider a cartesian reference with origin placed along the inclined plane, x-axis tangent to the incline. Although it appears reasonable to fix the reference system in such a way the x-axis points towards the flow direction, that is, along the favourable slope, its direction is determined as follows:

- towards the direction of the favourable slope for Cone-shaped beds, i.e., $\phi \in]0, \pi/2[$;
- towards the direction of the opposite slope for Funnel-shaped beds, i.e., $\phi \in]\pi/2, \pi[$.

The reason of this choice has the only purpose to use the same concept of *convergent* and *divergent* streams, which are defined as streams respectively flowing along increasing and decreasing ξ. This will be clearer in Sec. 1.4.1, where the transformation of the general equation under spatial flow inversion will be discussed.
Finally, assume instead the y-axis orthogonal to the x-axis, pointing in the direction opposite to gravity. A sketch of the geometrical setting is reported in Fig. 1.1, after changing to polar coordinates that will be soon introduced.
Let consider the generic height $z = z(x)$ of the fluid with respect to the incline. Then the gravitational force (per unit of fluid weight) can be evaluated as:

$$P = -g \cos\phi \nabla z$$

where:

$$z(x) = h(x) + z_b(x) - x \sin\phi$$

In the proposed setting:

- $z_b(x)$ is a function, assumed for simiplicity at least $C^2(\mathbb{R})$, which maps the height profile of a physical irregularity of the bottom at coordinate x: if $z_b(x) > 0$, the irregularity lies over the plane and vice versa, while if $z_b(x) \equiv 0$ the bottom is flat;
- $h(x)$ is the fluid depth with respect to the bottom; $x \sin\phi$ is instead related to the basal slope and represents a positive contribute to the gravitational potential, as expected since the x-axis points towards the direction favourable to the slope.

For simplicity:

- ϕ will be called *basal angle*, and the related slope will be called *basal slope*;
- $z_b(x)$ will be called *bottom topography*, given the role of such function

Finally, bottom friction is included into the model by means of the following term:

$$j = C_f f(u, h) \tag{1.1}$$

whose specific expression depends on the model adopted for the closure of drag term. Therefore, de Saint-Venant's Equations are formulated as:

$$\begin{cases} \frac{\partial u}{\partial t} + u\frac{\partial u}{\partial x} = g\cos\phi\left(\tan\phi - \frac{\partial h}{\partial x} - \frac{\partial z_b}{\partial x}\right) - C_f f(u,h) \\ \frac{\partial h}{\partial t} + \frac{\partial (hu)}{\partial x} = 0 \end{cases} \tag{1.2}$$

Several kinds of friction parametrization can be considered, included Manning-Strickler ([37]). Here, as in [29], the following family of drag parametrizations will be taken into account:

$$j = \frac{|u|^\alpha}{C^2 h^\beta} u = \frac{1}{C^2}\frac{\mathrm{sgn}(u)u^{\alpha+1}}{h^\beta} \tag{1.3}$$

where $C_f = 1/C^2$, being C the *Chézy Coefficient*, and $f(u,h) = u|u|^\alpha/h^\beta$. In particular, fully developed turbulent flow will be assumed, in such a way $\alpha = \beta = 1$ and one has the so called *Chézy Parametrization*:

$$j = \frac{u|u|}{C^2 h} = \frac{1}{C^2}\frac{\mathrm{sgn}(u)u^2}{h} \tag{1.4}$$

Consider now radial symmetry [2]. In order to write the equation according to such geometry, which is reported in Fig. 1.1, let consider the change to polar coordinates:

$$\begin{cases} x = r\cos\theta \\ z = r\sin\theta \end{cases} \tag{1.5}$$

where $r > 0$ and $\theta \in [0,\, 2\pi]$.
For the transformation of the differential operators it is taken into account that the partial derivative $\frac{\partial}{\partial x}(\cdot)$ involved in the right member of the momentum equation and the one involved in the continuity equation derive respectively from gradient and divergence operators. Therefore, the system turns into the following:

$$\begin{cases} \frac{\partial u}{\partial t} + u\frac{\partial u}{\partial r} = g\cos\phi\left(\tan\phi - \frac{\partial h}{\partial r} - \frac{\partial z_b}{\partial r}\right) - \frac{1}{C^2}\frac{\mathrm{sgn}(u)u^2}{h} \\ \frac{\partial h}{\partial t} + \frac{1}{r}\frac{\partial}{\partial r}(rhu) = 0 \end{cases} \tag{1.6}$$

Assuming steady state:

$$\begin{cases} u\frac{du}{dr} = g\cos\phi\left(\tan\phi - \frac{dh}{dr} - \frac{dz_b}{dr}\right) - \frac{1}{C^2}\frac{\mathrm{sgn}(u)u^2}{h} \\ \frac{1}{r}\frac{d}{dr}(rhu) = 0 \end{cases} \tag{1.7}$$

[2] Due to radial symmetry, the dependencies on the angular coordinate θ and the derivatives with respect to it are neglected.

Let consider the Continuity Equation reported in (1.7). Multiplication of both members by $2\pi r$ and the application of Fundamental Theorem of Calculus allow to obtain:

$$2\pi r h u = Q \tag{1.8}$$

being Q the total volumetric flowrate [3], which is constant and provides a relation between radial distance, depth and velocity. Considering instead the Momentum Balance equation of (1.7), one can divide both members by $g\cos\phi$ (it is possible because the angle $\phi = \frac{\pi}{2}$ is excluded in the classical model of inclined plane) to obtain:

$$\frac{1}{g\cos\phi} u \frac{du}{dr} = \tan\phi - \frac{dh}{dr} - \frac{dz_b}{dr} - \frac{1}{C^2}\frac{\mathrm{sgn}(u)u^2}{h} \tag{1.9}$$

By using:

$$u\frac{du}{dr} = \frac{d}{dr}\left(\frac{1}{2}u^2\right)$$

and re-arranging the members, the equation assumes the following form:

$$\frac{d}{dr}\left(\frac{u^2}{2g\cos\phi} + h\right) = \tan\phi - \frac{dz_b}{dr} - \frac{1}{C^2}\frac{\mathrm{sgn}(u)u^2}{h} \tag{1.10}$$

One can define the stream head as follows:

$$H = \frac{u^2}{2g\cos\phi} + h \tag{1.11}$$

and rewrite equation (1.11) in the form:

$$\frac{dH}{dr} = \tan\phi - \frac{dz_b}{dr} - \frac{1}{C^2}\frac{\mathrm{sgn}(u)u^2}{h} \tag{1.12}$$

which shows that, in general, stream energy is not conserved, due to the interplay between basal slope, bed topography and bottom friction. The first novelty with respect to [29] is that the stream head can also increase: this happens when the right hand side member of Equation 1.12 is positive, i.e., when the energy contribute of basal slope overbalances those of friction and bottom topography, as the following inequality shows:

$$\tan\phi \geq \frac{dz_b}{dr} + \frac{u|u|}{C^2 h} \tag{1.13}$$

[3] Notice that, in dimensional terms, one has $[Q] = [L]^3[T]^{-1}$. This expression provides an additional, simple motivation for the identification of the integration constant with the volumetric flow rate.

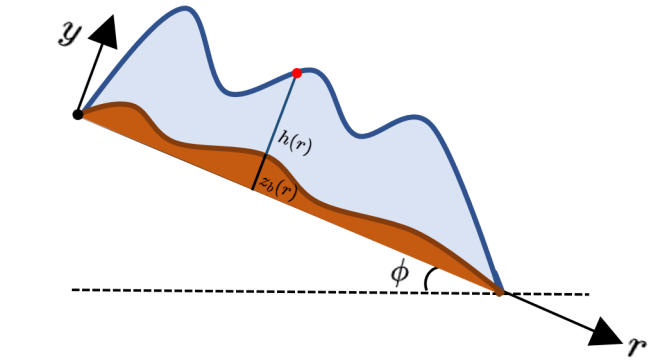

(a)

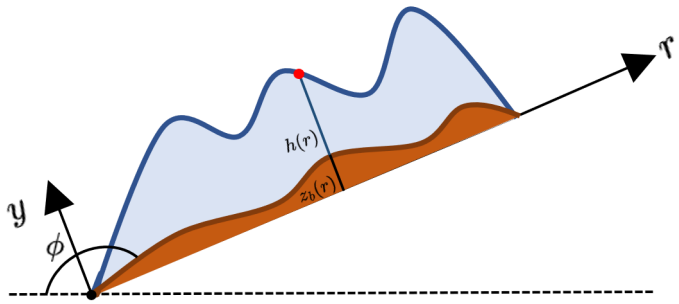

(b)

Figure 1.1: **Geometry for the Inclined Bed with Bottom Topography.** Left and right figure respectively refer to the section along a single radiant for the the cases $0 < \phi < \frac{\pi}{2}$ (Cone-shaped) and $\frac{\pi}{2} < \phi < \pi$ (Funnel-shaped).

1.2 Non-Dimensional Variables and Notable Relations

Since H is non constant, as discussed before, it appears natural to use as vertical reference unit the value of the stream head at the boundary, H_0, in order to define the variables:

$$y := \frac{h}{H_0} \tag{1.14}$$

and:

$$\zeta := \frac{z_b}{H_0} \tag{1.15}$$

A natural reference unit for the velocity of the fluid can be identified in a *modified* Torricellian velocity, which takes into account only the vertical component $g\cos\phi$ of the gravity, that is, $U_0 = \sqrt{2gH_0\cos\phi}$. In this way, the non-dimensional velocity is:

$$\nu := \frac{u}{\sqrt{2gH_0\cos\phi}} \tag{1.16}$$

By plugging (1.14) and (1.16) into (1.8), the following equation is obtained:

$$ry\nu = \frac{Q}{2\pi H_0\sqrt{2gH_0\cos\phi}}$$

The second member of such equation has the dimension of a length and can be chosen as a radial reference unit. Therefore, by defining:

$$R := \frac{Q}{2\pi H_0\sqrt{2gH_0\cos\phi}}$$

the non-dimensional radius is:

$$\xi = \frac{r}{R} \tag{1.17}$$

The previous introduction of the *modified* Torricellian velocity motivates the definition of the Froude Number as follows:

$$Fr = \frac{u}{\sqrt{gh\cos\phi}} \tag{1.18}$$

By plugging (1.14), (1.16), (1.17) into (1.8), one obtains:

$$\nu = \frac{1}{\xi y} \tag{1.19}$$

Moreover, by plugging (1.19) and (1.14) into (1.18), one finally obtains:

$$Fr = Fr(\xi, y) = \frac{1}{\xi}\sqrt{\frac{2}{y^3}} \tag{1.20}$$

It is worth to notice that:

$$Fr(\xi, y) = 1 \iff y = \sqrt[3]{\frac{2}{\xi^2}} \tag{1.21}$$

which provides the locus of the points where the stream is in critical condition. Finally,

the *Radiant Specific Discharge* is introduced:

$$Q_r = \frac{Q}{2\pi r} \tag{1.22}$$

that, in non-dimensional form, is simply defined as:

$$q = q(\xi) = \frac{1}{\xi} \tag{1.23}$$

1.3 Non-Dimensional Equation

By plugging (1.14), (1.16), (1.17) into Equation (1.10), one obtains:

$$\frac{d}{d\xi}\left(\frac{1}{\xi^2 y^2} + y\right) = \gamma_b - \frac{d\zeta}{d\xi} - \frac{R}{H_0} \cdot \frac{2g\cos\phi \ \ \mathrm{sgn}(\nu)}{C^2} \cdot \frac{1}{\xi^2 y^3} \tag{1.24}$$

which, after few calculation, is equivalent to the so called Bresse **Profile Equation** ([15]):

$$\frac{dy}{d\xi}(1 - \frac{2}{\xi^2 y^3}) = \gamma_b - \frac{d\zeta}{d\xi} + \frac{2}{\xi^3 y^2} - \frac{\alpha}{\xi^2 y^3} \tag{1.25}$$

The equation depends on two parameters (apart from those related to bottom topography), which are defined as follows:

$$\alpha := \frac{R}{H_0} \cdot \frac{2g\cos\phi \ \ \mathrm{sgn}(\nu)}{C^2} \tag{1.26}$$

is a parameter related to friction and determines whether the flux is convergent ($\alpha < 0$) or divergent ($\alpha > 0$), while:

$$\gamma_b := \frac{R}{H_0}\tan\phi \tag{1.27}$$

encloses the dependence on the basal slope. Equation 1.25 is general and, depending on the values of the parameters and bottom topography, a large variety of solution can be obtained. Some notable cases are summarized into Table 1.1, obtained for $\zeta(\xi) \equiv 0$ (flat bottom); other bottom topographies, such as sinusoidal and step, will be discussed within the next chapters.

1.4 Mathematical Analysis of Profile Equation

In this section, some mathematical aspects of Profile Equation 1.25 will be discussed.

Table 1.1: Some notable settings obtained from Eq. 1.25, for notable values of the parameters and flat bottom. Here, "Inv." stands for "Inviscid", while "Vis." stands for "Viscous". The dependance on the sign of α will be investigated within the next chapters.

	Plane Inv.	Plane Vis.	Cone Inv.	Cone Vis.	Funnel Inv.	Funnel Vis.
$\zeta(\xi)$	0					
γ_b	0	0	>0	>0	<0	<0
α	0	$\neq 0$	0	$\neq 0$	0	$\neq 0$

1.4.1 Physical Domain and Symmetry

Since ξ is the non-dimensional radius, it is assumed to be positive. Moreover, Since $y = y(\xi)$ is the fluid depth with respect to the bottom, negative depth points would be located under the bottom: thus, it appears natural to consider only positive y, and the domain of interest is finally:

$$\mathcal{D} = \{\xi > 0\} \times \{y > 0\}$$

Notice that, by applying the transformation:

$$\xi \to -\xi \tag{1.28}$$

and plug it into Equation 1.25, one obtains:

$$\frac{dy}{d\xi}(1 - \frac{2}{\xi^2 y^3}) = \gamma_b - \frac{d\zeta}{d\xi} + \frac{2}{\xi^3 y^2} - \frac{\alpha}{\xi^2 y^3} \tag{1.29}$$

which is identical to 1.25, except for the sign of γ_b. This indicates that considering negative values of ξ brings to same stream solutions, but on opposite basal slope, thus indicating that the flow direction can be inverted. This happens because, due to Transformation 1.28, one has:

$$\begin{cases} \nu = 1/\xi y \to -\nu \\ \alpha = \frac{R}{H_0} \cdot \frac{2g\cos\phi}{C^2} \cdot \mathrm{sgn}(\nu) \to -\alpha \end{cases}$$

Finally, notice that if $\alpha = 0$, $\gamma_b = 0$ and $\zeta(\xi) \equiv 0$, Eq. 1.29 modifies as:

$$\frac{dy}{d\xi}(1 - \frac{2}{\xi^2 y^3}) = \frac{2}{\xi^3 y^2} \tag{1.30}$$

and the transformation :

$$\xi \to -\xi$$

brings to an identical equation, guaranteeing perfect symmetry.
What discussed before has an important implication for all of the solutions that will be described throughout the whole work: a single Equation describes a orbit on the Phase Plane (that, as will be shown later, is split into two branches by the Critical Line) which provides two families of solutions along two opposite directions with respect to the reference systems illustrated in Fig. 1.1:

- those on **Convergent** direction, i.e., along decreasing ξ;
- those on **Divergent** direction, i.e., along increasing ξ.

1.4.2 On the sign of α

The two families of solutions along convergent or divergent direction, previously described in Sec. 1.4.1, make the stream flow on two opposite directions. Since bottom friction is always opposite to the motion direction, the sign of α must be chosen subsequently, in particular:

- $\alpha > 0$ for flows along divergent direction (i.e., in the same direction of the ξ-axis as in Fig. 1.1);
- $\alpha < 0$ for flows along convergent direction (i.e., in the opposite direction of the ξ-axis as in Fig. 1.1).

What here discussed will be used in Chapter 3, where stream profiles in presence of friction are simulated and discussed.

1.4.3 The Hypothesis of Gradually Varied Flow

The use of a 2D Shallow-water approximation brings with it a series of hypothesis to be satisfied and that determine the validity of the model itself. Beyond the hypothesis that the characteristic transversal dimensions of the flow can be neglected with respect to the longitudinal ones, which justify the name "Shallow water", an additional one is that of *gradually varied flow*, which can be summarized by the following two points (Ref. [36]):

- the flow is steady under the observation time interval;
- the streamlines along the depth can be considered nearly parallel.

In this way, variations of the flow properties along the normal direction can be neglected. In order to ensure the validity of the hypothesis of gradually varied flows, few assumptions must be taken into account for the values of the model parameters, enclosed into Eq. 1.25:

- the basal slope γ_b must be sufficiently small in order to guarantee that energy gains or losses with respect to the boundary Stream Head are not significant;
- for the same reason, the departures from the flat bottom represented by the bottom topography $\zeta(\xi)$ must be contained both in height and slope $\zeta'(\xi)$;

- the turbulent friction coefficient α must be sufficiently small in order to guarantee that energy losses do not cause rapid variations of the stream properties.

Regarding the choice of a suitable bottom topography, in Ref. [42], by means of a perturbative expansion, the following upper-bound is obtained in order to ensure the validity of the hypothesis of gradually varied flow:

$$\zeta(\xi) \leq \frac{3}{2} - \left(\frac{3\sqrt{3}}{\xi}\right)^{\frac{2}{3}} \tag{1.31}$$

In this work no upper bounds are obtained. However, as will be seen within the next sections, the parameter chosen will automatically satisfy Ineq. 1.31. In particular:

$$\gamma_b \in [-0.1, 0.1] \tag{1.32}$$

The hypothesis of gradually varied flow will be violated in two situations: the first, arising naturally from the dynamics, is nearby the hydraulic jump; the second, instead, is the case of stepped bottom topography around the step region, due to the high steepness. This allows to conclude that the results obtained have only a limited physical meaning, despite their help in understanding the flow dynamics.

1.4.4 Phase Plane

Equation 1.25 can be rearranged considering that $\xi > 0$ and $y > 0$ for the multiplications, in order to obtain the following equation:

$$\frac{dy}{d\xi} = \frac{(\gamma_b - \zeta')\xi^3 y^3 + 2y - \alpha\xi}{\xi^3 y^3 - 2\xi} = \frac{N(\xi, y)}{D(\xi, y)} \tag{1.33}$$

where $\zeta' = \frac{d\zeta}{d\xi}$. The second member is surely finite if both $N(\xi, y)$ and $D(\xi, y)$ are non-zero and is exactly zero when $N(\xi, y) = 0$ and $D(\xi, y) \neq 0$, in this case allowing to recover the constant constant depth solution already seen in Sec. 3.1.2. Particular attention is to be paid to couples (ξ, y) such that both $N(\xi, y)$ and $D(\xi, y)$ equal zero, lying in the so called *nullclines*. Remembering Eq. 1.21, one can find that:

$$y = \sqrt[3]{\frac{2}{\xi^2}} \Leftrightarrow Fr(\xi, y) = 1 \tag{1.34}$$

This allows to conclude that $D(\xi, y) = 0$ for couples (ξ, y) such that $Fr = 1$, therefore the nullcline described by the denominator coincide with the *Critical Line* within the domain $\mathcal{D}$.
Basing instead on the definition of $N(\xi, y)$ itself, the couples $(\xi, y) \in \mathcal{D}$ such that $N(\xi, y) = 0$ satisfy the following equation:

$$\gamma_b \xi^3 y^3 - \zeta' \xi^3 y^3 + 2y - \alpha\xi = 0 \tag{1.35}$$

The lines $N(\xi, y) = 0$ and $D(\xi, y) = 0$, described by Eq. 1.34, 1.35, organize the geometry of the phase space and their intersections govern the behaviour of the trajectories. The radii at which of the the previous lines intersect, if there exist, can be determined by plugging Eq. 1.34 into Eq. 1.35 which, after some algebra, leads to the following equation in the unknown ξ:

$$\zeta' = \gamma_b - \frac{\alpha}{2} + 2^{\frac{1}{3}}\ \xi^{-\frac{5}{3}} \tag{1.36}$$

The nature of Eq. 1.36 (implicit or explicit) depends on the bottom topography $\zeta(\xi)$ chosen (by means of its first derivative) and the only physical solutions ξ_* are the positive ones. However, by simple re-arrangement of the members and restriction to the set $\{\xi > 0\}$, one concludes that Eq. 1.36 does not admit any physical solution if the following condition holds:

$$-\gamma_b + \zeta'_* \leq -\frac{\alpha}{2} \tag{1.37}$$

where $\zeta'_* = \frac{d\zeta}{d\xi}|_{\xi=\xi_*}$. Let define:

$$\gamma(\xi) := \gamma_b - \frac{d\zeta}{d\xi} \tag{1.38}$$

representing the topographical slope "faced by the stream" while flowing, due to both basal slope and bottom topography. Then such condition expresses that physical points at which $\frac{dy}{d\xi} = [\frac{0}{0}]$ can exist only if the energy contribute of the bed slope γ is greater than friction dissipation. Notice that if for all $\xi > 0$ the following inequality holds:

$$-\gamma_b + \zeta'(\xi) \leq -\frac{\alpha}{2} \tag{1.39}$$

then by integration of the two members of such inequality 1.39 within $[\xi_0, \xi]$, assuming $\xi > \xi_0$ for simplicity and using the monotony property of the integrals, one obtains that:

$$\zeta(\xi) \leq \zeta(\xi_0) + (\gamma_b - \frac{\alpha}{2})(\xi - \xi_0) \tag{1.40}$$

where in the second member the asymptotic profile described by Eq. 3.23 can be recognized. Therefore, if the slope of the bed topography function is bounded by $\gamma_b - \frac{\alpha}{2}$, the line represented by the aforementioned profile can be interpreted as the boundary of the region in which values such that $\frac{dy}{d\xi} = [\frac{0}{0}]$ are not possible. Finally, if one plugs Eq. 1.36 (evaluated at $\xi = \xi_*$) into Eq. 1.34, one obtains the heights at which the two organizing lines intersect:

$$y_* = \sqrt[5]{\frac{2}{(-\gamma_b + \zeta'_* + \frac{\alpha}{2})^2}} \tag{1.41}$$

where $\zeta'_* = \frac{d\zeta}{d\xi}_{|\xi=\xi_*}$.
Assume there exist points (ξ_*, y_*) such that $\frac{dy}{d\xi} = [\frac{0}{0}]$. The nature of such points depends on the bed topography considered and the friction coefficient, and can be deduced by Eq. 3.1, transformed to an equivalent set of two ordinary differential equation in the parameter $s \in \mathbb{R}$ (which corresponds to a parametrization of the curves $(\xi(s), y(s))$ in the phase space). This procedure is analogous to what done in [8] and brings to the following system:

$$\frac{d}{ds}\begin{bmatrix}\xi\\ y\end{bmatrix} = \begin{bmatrix}\xi^3 y^3 - 2\xi\\ (\gamma_b - \zeta')\xi^3 y^3 + 2y - \alpha\xi\end{bmatrix} \tag{1.42}$$

where it can be defined the vector function $\mathbf{F} : \mathbb{R}^2 \to \mathbb{R}^2$ as:

$$\mathbf{F}(\xi, y) = \begin{bmatrix}\xi^3 y^3 - 2\xi\\ (\gamma_b - \zeta')\xi^3 y^3 + 2y - \alpha\xi\end{bmatrix} = \begin{bmatrix}F_1(\xi, y)\\ F_2(\xi, y)\end{bmatrix}$$

In this setting, curves described by $N(\xi, y) = 0$ and $D(\xi, y) = 0$ represent the nullclines of 1.4.4, while the solutions of Equations 1.34, 1.36 can be easily thought as the equilibrium points of the previous system, whose nature is determined by the Jacobian Matrix of the system evaluated at the equilibrium points considered. Let start computing the entries of the Jacobian Matrix of $\mathbf{F}$:

$$\mathbf{J_F}(\xi, y) = \begin{bmatrix}3\xi^2 y^3 - 2 & 3\xi^3 y^2\\ y^3(3\gamma_b\xi^2 - 3\zeta'\xi^2 - \xi^3\zeta'') - \alpha & 3\xi^3 y^2(\gamma_b - \zeta') + 2\end{bmatrix} \tag{1.43}$$

In order to evaluate $\mathbf{J_F}$ at the equilibrium point, one can define for the sake of clearness:

$$t_* = -\gamma_b + \frac{\alpha}{2} + \zeta'_* \tag{1.44}$$

and, more in general:

$$t = t(\xi) = -\gamma_b + \frac{\alpha}{2} + \zeta'(\xi) \tag{1.45}$$

which can be interpreted as a *generalized slope* including the contribute of friction (in terms of energy subtraction), the first evaluated at the eventual equilibrium points, the second in a general point $\xi > 0$.
Then, since equations 1.34 and 1.36 hold, one can operate the following substitutions:

$$\begin{cases} y_* = 2^{\frac{1}{3}}\xi_*^{-\frac{2}{3}} \\ \xi_* = 2^{\frac{1}{5}}t_*^{-\frac{3}{5}} \end{cases} \tag{1.46}$$

By using what reported before, one obtains:

$$\begin{cases} \frac{dF_1}{d\xi}|_{(\xi_*,y_*)} = 4 \\ \frac{dF_1}{dy}|_{(\xi_*,y_*)} = 6t_*^{-1} \\ \frac{dF_2}{d\xi}|_{(\xi_*,y_*)} = -6t_* + 2\alpha - 2^{\frac{6}{5}} t_*^{-\frac{3}{5}} \zeta_*'' \\ \frac{dF_2}{dy}|_{(\xi_*,y_*)} = 3\alpha t_*^{-1} - 4 \end{cases} \tag{1.47}$$

which are the components of the Jacobian matrix evaluated at the equilibrium points. By plugging $\gamma_b = 0$ and $\zeta(\xi) = 0$ (identically zero) into 1.47 one can find that the Jacobian matrix for the case of Horizontal Bed with Flat Bottom assumes the following simpler form:

$$\mathbf{J_F}(\xi_*, y_*)_{\text{hor, flat}} = \begin{bmatrix} 4 & \frac{12}{\alpha} \\ -\alpha & 2 \end{bmatrix} \tag{1.48}$$

Notice that, in this specific case, both the Jacobian Determinant and Trace are found to be independent on the friction coefficient α, and so the eigenvalues do: therefore, the nature of the equilibrium point does not depend on friction, coherently with the results found by [29]. Back to the general equation, the Jacobian matrix is:

$$\mathbf{J_F}(\xi_*, y_*) = \begin{bmatrix} 4 & 6t_*^{-1} \\ -6t_* + 2\alpha - 2^{\frac{6}{5}} t_*^{-\frac{3}{5}} \zeta_*'' & 3\alpha t_*^{-1} - 4 \end{bmatrix} \tag{1.49}$$

from which:

$$(\text{tr } \mathbf{J_F})|_{(\xi_*,y_*)} = \frac{dF_1}{d\xi}|_{(\xi_*,y_*)} + \frac{dF_2}{dy}|_{(\xi_*,y_*)} = 3\alpha t_*^{-1} \tag{1.50}$$

and:

$$(\det \mathbf{J_F})|_{(\xi_*,y_*)} = \frac{dF_1}{d\xi}|_{(\xi_*,y_*)} \frac{dF_2}{dy}|_{(\xi_*,y_*)} - \frac{dF_2}{d\xi}|_{(\xi_*,y_*)} \frac{dF_1}{dy}|_{(\xi_*,y_*)} = 4(5 + 6 \cdot 2^{\frac{1}{5}} \zeta_*'' t_*^{-\frac{3}{5}}) \tag{1.51}$$

The signs of expressions 1.50, 1.51 determine those of the eigenvalues of $\mathbf{J_F}$ and, therefore, the nature of the equilibrium point. The study of the sign of $(tr\ \mathbf{J_F})_{|_{(\xi_*,y_*)}}$ and $(det\ \mathbf{J_F})_{|_{(\xi_*,y_*)}}$ leads to the following inequalities:

$$\begin{cases} 3\alpha t_*^{-1} \geq 0 \\ 5 + 6 \cdot 2^{\frac{1}{5}} \zeta_*'' t_*^{-\frac{3}{5}} \geq 0 \\ t_* > 0 \end{cases}$$

Notice that substantial differences arise with respect to the case of Horizontal Bed with Flat Bottom. Indeed, the sign of the trace generally depends on the sole α. In particular, if the equilibrium point lies within the physical region $\mathcal{D}$, that is, $t_* > 0$, the trace assumes the same sign of α, thus allowing to obtain both unstable configurations (saddle point,

when determinant is negative) and stable configurations (stable node or focus, when the determinant is positive). It is important to notice that while the instability of the equilibrium point for the linearized system implies the instability for the nonlinear system, the contrary is generally not true (that is, the stability of the linearized system does not imply the stability of the nonlinear one) . However, notice that if $\alpha < 0$, with α chosen in such a way that the determinant remains positive, if the equilibrium point lies in the physical region, then one has:

$$0 \geq \frac{\alpha}{2} \geq \gamma_b - \zeta'_*$$

from which:

$$\zeta'_* \geq \gamma_b$$

Therefore, in this situation, friction acts as a control on the positive energy contribute given by the slope, guaranteeing the stability of the equilibrium point (in the linearized system). Further details will be provided for the specific kinds of beds that will be examined within the next sections.

1.4.5 Hydraulic Jump as a Shock Discontinuity

The presence of friction in the model opens to the possibility of having a transition from the supercritical to the subcritical stream through a hydraulic jump. As described in [29], it can manifest in the form of turbulent bores or undular jump, depending on the Froude Number in a neighbourhood of the jump. For the purpose of this work, however, it is modelled as a shock discontinuity of zero length, coherently with [29, 42]. This is a significant simplification, since it means to neglect most of the physics, included the eddy formation and the air entrainment (Ref. [14, 27]), which cannot be described by a simple Shallow-water model. However, this assumption has the privilege of making the model capturing basic physical aspects (such as energy dissipation across the jump and its position) with relatively simple mathematics. Moreover, the presence of the Hydraulic Jump can be deduced by simply finding critical points (such as focus) of the dynamical system 1.42, where the gradually varied flow hypothesis ceases to be valid and a discontinuity arises (Ref. [36]).
To do so, let consider a short reach of circular sector of stream, with central angle θ to delimit an infinitesimal volume enclosing the whole hydraulic jump, as in Fig. 1.2. In order to apply the the Global Momentum Equation, let consider a section of height h and arc length $r\theta$ enclosed into the volume, so its area is $\Omega = rh\theta$. Lateral hydrostatic components and bottom friction are neglected, so that the only force components are given by the hydrostatic force and the dynamic force which, in dimensional terms, are expressed by:

$$F_h = p_G\Omega = \gamma_s h_G \Omega = \gamma_s r\theta \frac{h^2}{2} \tag{1.52}$$

where $h_G = h^2/2$ is the baricentric coordinate of the immersed section and γ_s is the fluid specific weight, while:

$$F_d = \beta\rho\frac{Q^2}{\Omega} = \beta\rho\Omega u^2 = \beta r\theta u(hu) = \beta r\theta uq \tag{1.53}$$

where β is the momentum coefficient, u is the velocity and q is the radiant specific discharge, being $q = Q/2\pi r = hu$ in force of the Continuity Equation 1.8. By assuming fully turbulent flow then $\beta = 1$ and the momentum equation across the section becomes, in dimensional terms:

$$F_h + F_d = const \tag{1.54}$$

Introducing non-dimensional variables, one then obtains the following final equation, analogue of that obtained in [29]:

$$F(\xi, y) = y^2 + \frac{4}{\xi^2 y} \equiv const \tag{1.55}$$

where $F(\xi, y)$ is denoted in this work as *Specific Force*.
One can then obtain the jump position by simple intersection of the Specific Forces for the subcritical and supercritical branches. This procedure will be followed from now and throughout the whole work to determine the jump position.

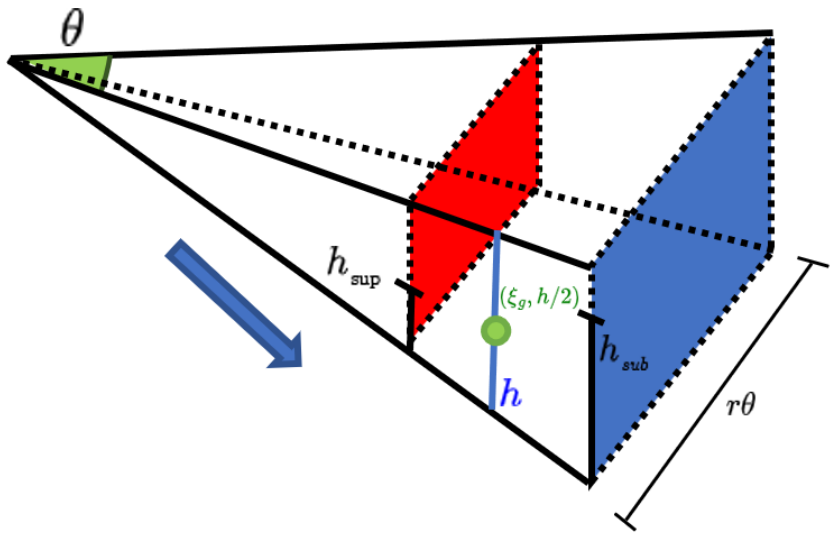

Figure 1.2: **Force Balance to determine Hydraulic Jump Position.** In this figure, θ denotes the central angle, $(\xi_G, h/2)$ the coordinates of the baricentre of the immersed section. The red and blue sections delimit the volume containing the jump, with h_{sup} and h_{sub} being the supercritical and subcritical heights in proximity of the hydraulic jump. The blue arrow indicates the flow direction.

1.4.6 Stiffness and Numerical Methods

The presence of a singularity expressed by the Critical Line $y = \sqrt[3]{2/\xi^2}$ and of possible critical points of the dynamical system 1.42 make concrete the possibility of having regions in which the height profile $y = y(\xi)$ approaches the singularities with nearly vertical tangent (and this will be the case, as will be seen later in the next chapters), thus System 1.42 is stiff ([30]). This is not surprising, as it happens also for the stream profiles in open channel flows (Ref. [36, 25]), but suggests that numerical solutions of 1.42 should be obtained with proper numerical methods. In particular, the majority of the cases will be solved with the *Variable Step Variable Order* (VSVO) method `ode15s` already implemented in MATLAB® (Ref. [34]). Alternatively, another method that is used in specific cases is "StiffnessSwitching" method for NDSolve function available in Wolfram Mathematica 12, which appears to perform better than `ode15s` for the case of stepped bottom topography.

Chapter 2

Stream Profiles for Inviscid de Saint-Venant's Equations

In this chapter, the solutions of Eq. 1.25 will be analyzed in **absence of friction**, for different values of basal slope γ_b and bed topographies $\zeta(\xi)$. Therefore, for the whole chapter, $\alpha = 0$ will be considered, corresponding to the case of a negligible value of the friction coefficient, i.e., $C_f \approx 0$.
In this case, Profile Equation 1.25 assumes the form:

$$\frac{d}{d\xi}\left(\frac{1}{\xi^2 y^2} + y\right) = \gamma_b - \frac{d\zeta}{d\xi} \tag{2.1}$$

where it can be recognized the function

$$\tilde{H} := \frac{1}{\xi^2 y^2} + y \tag{2.2}$$

representing the non-dimensional Stream Head. Let denote the radial coordinate of the boundary by ξ_0. Then, by the scaling chosen reported at the top of Section 1.2, one has the following boundary condition:

$$\tilde{H}(\xi_0) = 1 \tag{2.3}$$

To solve Eq. 2.1, one can simply integrate the two members within the interval $[\xi_0, \xi]$, use the Fundamental Theorem of Calculus and enforce the Boundary Condition 2.3 to obtain:

$$\frac{1}{\xi^2 y^2} + y - 1 = \gamma_b(\xi - \xi_0) - [\zeta(\xi) - \zeta(\xi_0)] \tag{2.4}$$

The so obtained equation is no longer differential and once the topology of the bed (i.e., the slope parameter γ_b and the irregularity profile $\zeta(\xi)$) is known, it can be solved numerically.

For this purpose, the following function is introduced:

$$F(\xi, y) = \frac{1}{\xi^2 y^2} + y - 1 - \gamma_b(\xi - \xi_0) + [\zeta(\xi) - \zeta(\xi_0)] \tag{2.5}$$

which is defined on $\mathbb{R}^2 \setminus \{(0,0)\}$. Then the curve described by Eq. 2.4 can be interpreted as the zero-level curve of $F(\xi, y)$ and describes the behaviour of the solutions y.
The case of inclined bed with flat bottom is recovered by imposing $\zeta(\xi) \equiv const$ into Eq. 2.4 (for simplicity $\zeta(\xi) \equiv 0$):

$$\frac{1}{\xi^2 y^2} + y = 1 + \gamma_b(\xi - \xi_0) \tag{2.6}$$

In this case, the stream head varies linearly with the radial distance, with slope governed by γ_b. In particular:

- if $\gamma_b > 0$ (Cone-shaped), the stream head increases;
- if $\gamma_b < 0$ (Funnel-shaped), the stream head decreases.

If additionally $\gamma_b = 0$ is considered, the case of Horizontal Bed with Flat Bottom can be recovered and Equation 2.4, which now describes the energy conservation, becomes the following:

$$\frac{1}{\xi^2 y^2} + y = 1 \tag{2.7}$$

Latterly, if one considers the case in which only $\gamma_b = 0$, one obtains the equation for a plane bed with a prescribed bottom topography $\zeta = \zeta(\xi)$:

$$\frac{1}{\xi^2 y^2} + y = 1 - [\zeta(\xi) - \zeta(\xi_0)] \tag{2.8}$$

2.1 Case 0 - Horizontal Bed with Flat Bottom

In this Section, solutions of Equation 1.25 will be analyzed in the case of Horizontal Bed with Flat Bottom, i.e., $\gamma_b = 0$ and $\zeta(\xi) \equiv 0$. Therefore, the proper form of the Profile Equation to be used is Eq. 2.7. Such case was deeply discussed in [29] [1] where a series of analytical and numerical results were obtained and classified to find astrophysical analogous of the stream profiles described, in the context of Analogue Gravity (Ref. [5, 20, 46]). Some of the notation of the previous article will be used in this Section and, generally, in the following sections and chapters.

[1] The current case of Horizontal Bed with Flat Bottom is named in [29] as "Isentropic", due to the astrophysical analog which refers to.

2.1.1 Numerical and Analytical Results

Equation 2.7 is here reported for the sake of clearness:

$$\frac{1}{\xi^2 y^2} + y = 1$$

Then it can be re-formulated, by using Def. 2.2 of the Stream Head, as:

$$\tilde{H}(\xi) \equiv 1 \tag{2.9}$$

Therefore, Eq. 2.7 describes constant Stream Head orbits and expresses nothing but the Stream Energy conservation.
In order to analyze the corresponding, Height Profiles $y = y(\xi)$, one can re-arrange Eq. 2.7 (considering $\xi > 0$ and $y > 0$) to obtain:

$$\xi = \xi(y) = \frac{1}{y\sqrt{1-y}} \tag{2.10}$$

which is not injective, therefore suggesting that the inverse relation $y(\xi)$ is a curve described by two branches. Fig. 2.1(a) confirms the observations coming from non-injectivity: the orbit $y = y(\xi)$ is split by the Critical Line (where $Fr(\xi, y) = 1$ into a Supercritical (lower) and Subcritical (upper) branch, as shown by the Froude Number in Fig. 2.1(c) . Each branch, thanks to the symmetry property discussed in Sec. 1.4.1, represents two possible solutions, depending on the flow is on convergent (along decreasing ξ) or divergent (along decreasing ξ).
An interesting feature emerges by observing the orbits: the two branches join solely at a minimum radius ξ_{min}, which lies on the Critical Line $y_{min} = y(\xi_{min})$. Mathematically, it can be determined by looking for the stationary points of function $\xi(y)$ in 2.10, obtaining:

$$(\xi_{min}, y_{min}) = \left(\frac{3\sqrt{3}}{2}, \frac{2}{3}\right)$$

Using the same notation of [29] in the context of Analogue Gravity, often throughout this work the term *Froude Horizon* will be used to denote points at which Critical Conditions are reached, like ξ_{min}.
In view of what just discussed, each of the two branches can be exemplified by the following physical situations:

- a stream starting in supercritical (subcritical) condition from an external annular gate placed at radius $\xi = \xi_0$ and flowing along convergent direction (maintaining constant Stream Head and Discharge), until reaching critical conditions at the edge of a hole, at $\xi = \xi_{min}$, where the flow is drained;
- a stream emerging in critical conditions from an internal source, whose external edge is located at radius $\xi = \xi_{min}$, and flowing in supercritical (subcritical) conditions.

Flow feautures and Stream Profiles are reported respectively in Figures 2.1, 2.2.
The convergent flow previously described helps understanding the physical reason why the minimum radius ξ_{min} arises in this case and for many other solutions throughout this work. Indeed, such behaviour finds an explanation in the governing equations of the current case, which impose constant Discharge (Volumetric Flow Rate) and Stream Head. If the fluid emerges from an annular gate and flows along convergent direction within the bounded region delimited by the annular gate and no hole is present, keeping the same Discharge would make the flow height dramatically increase and the Stream Head would no longer be constant as prescribed: the only way to keep both constant is to drain the fluid with a hole of radius ξ_{min}, i.e., that the flow attains critical conditions at $\xi = \xi_{min}$. Similarly, if the flow is divergent from a critical source, its radius ξ_{min} is that guaranteeing the flow to maintain constant Stream Head and Discharge.
The way used by [29] to illustrate this behaviour, the same used in this work, is by means of *Radiant Specific Discharge* introduced in 1.23: if one pulls its definition into Eq. 2.7 and re-arranges the members to explicit q, one obtains the relation:

$$q(y) = y\sqrt{1-y} \tag{2.11}$$

which is non monotonic. In particular $q(y)$ attains its maximum at $y = y_{min}$, i.e., where the flow necessary reaches critical conditions.

2.1.2 Role of Benchmark Case for Boundary Conditions

Through the next sections, different geometries will be taken into account, described by gradually more complex equations. The present case, however, will be considered as a benchmark when imposing boundary conditions. Indeed, the orbit described by Eq. 2.7 represents the locus of the points (ξ, y) of constant Stream Head, since there the non-dimensional Stream Head $\tilde{H}(\xi, y)$ is 1, but at the same time it is obtained by using $H_0 = H(\xi_{BC})$ (the dimensional Stream Head at the boundary) as reference scale.
In most of the cases that will be discussed later on in this work, unitary Stream Head $\tilde{H}$ will be imposed at a specific point ξ_0, but this has to be made by fixing supercritical and subcritical heights $y_{0,sup}$ and $y_{0,sub}$ for which $\tilde{H}(\xi_0, y_{0,(\cdot)}) = 1$. Therefore, $y_{0,sup}$ and $y_{0,sub}$ will be selected by the supercritical and subcritical branches of the orbit described by 2.10.

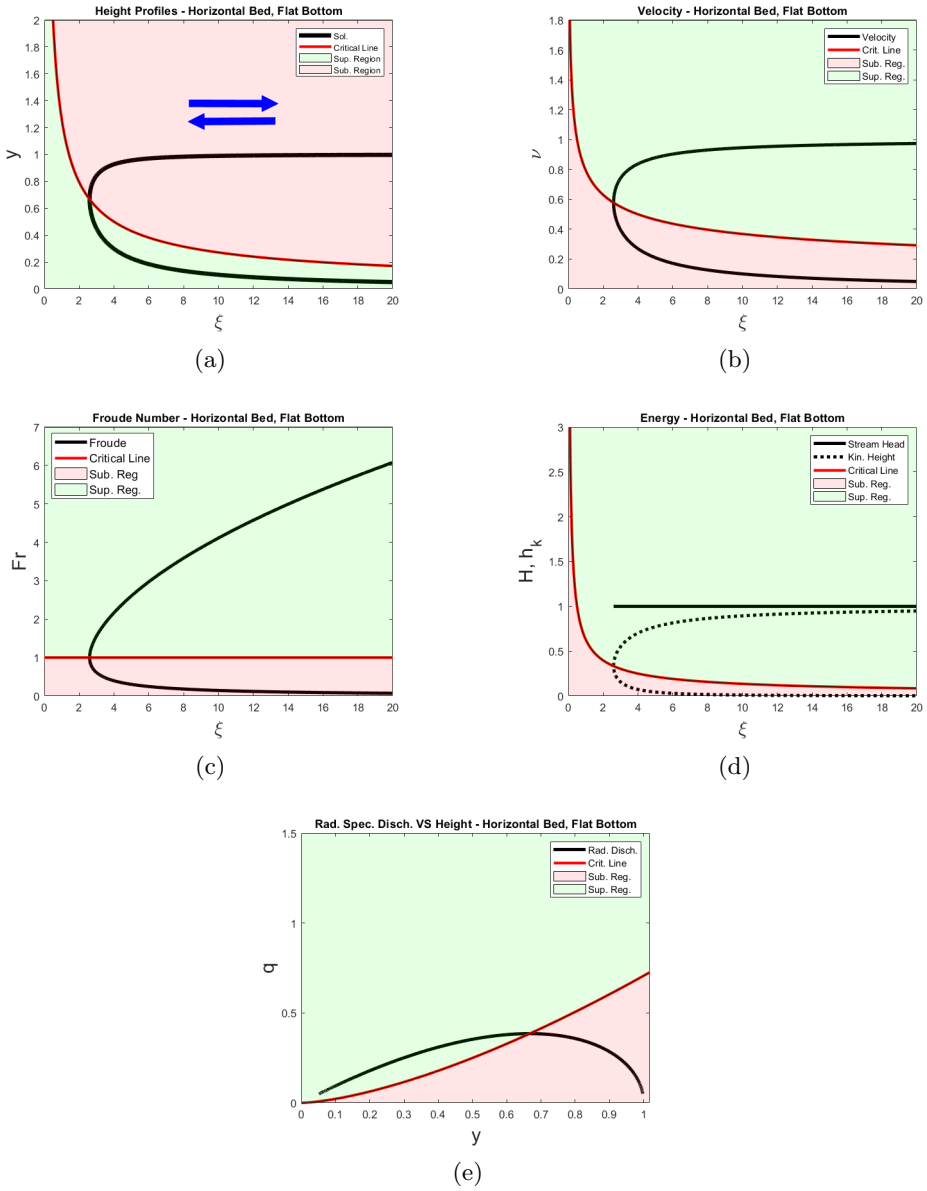

Figure 2.1: **Stream flowing along an Horizontal Bed with Flat Bottom,** $\gamma_b = 0$**,** $\zeta(\xi) \equiv 0$**.** Blue arrows indicate that each branch of the curves represents two solutions, depending on the Convergent (along decreasing ξ) or Divergent (along increasing ξ) direction of the flow. Fig. 2.1(a) - Supercritical and Subcritical Height Profiles. Fig. 2.1(b) - Supercrital and Subcritical branches of Velocity. Fig. 2.1(c) - Supercrital and Subcritical branches of Froude Number. Fig. 2.1(d) - Constant Stream Head, along with Supercrital and Subcritical branches of Kinetic Height. Fig. 2.1(b) - Radiant Specific Discharge versus Height.

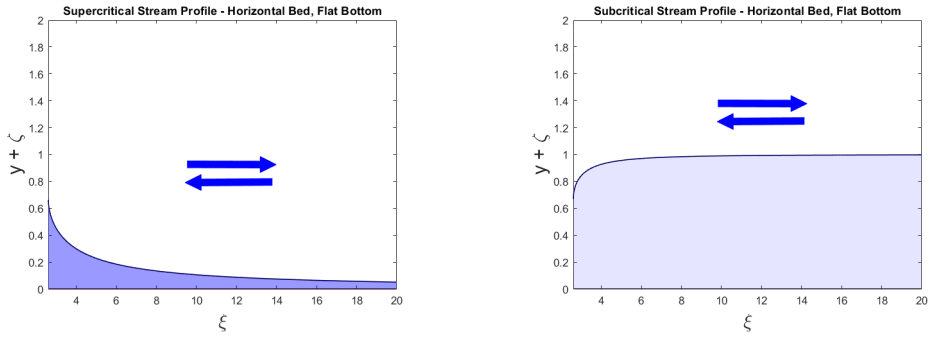

(a) (b)

Figure 2.2: **Stream Profiles - Horizontal Bed with Flat Bottom,** $\gamma_b = 0$**,** $\zeta(\xi) \equiv 0$**.** Left and right figure respectively refer to Supercritical and Subcritical Stream Profile. Blue arrows indicate that each branch of the curves represents two solutions, depending on the Convergent (along decreasing ξ) or Divergent (along increasing ξ) direction of the flow.

2.2 Case 1 - Inclined Bed with Flat Bottom

In this section, solutions of Equation 1.25 will be analyzed in the case of an inclined bed with flat bottom ($\zeta(\xi) \equiv 0$). Therefore, the reference form of the Profile Equation to be used is that reported in 2.6.

2.2.1 Structure of the Solution

In order to establish if equation (2.4) defines implicitly a single function $y = y(\xi)$ within the domain of interest $\mathcal{D} = \{\xi > 0\} \times \{y > 0\}$. In order to study the injectivity of the curve described by the equation, let fix any $\xi = \xi^* > 0$ and plug it into (2.4). Then:

$$\frac{1}{\xi^{*2} y^2} + y - 1 - \gamma_b(\xi^* - \xi_0) = 0 \tag{2.12}$$

Multiplication by y^2 holds and re-arranging of the addends hold:

$$y^3 + y^2[-1 - \gamma_b(\xi^* - \xi_0)] + \frac{1}{\xi^{*2}} = 0 \tag{2.13}$$

The last equation is algebraic of third degree of the form:

$$ay^3 + by^2 + cy + d = 0$$

where $a = 1$, $b = -1 - \gamma_b(\xi^* - \xi_0)$, $c = 0$, $d = \frac{1}{\xi^{*2}}$.
The number of real solutions strictly depends on the coefficients (therefore, on the point ξ^* and on the radius of the boundary ξ_0). Following the classical procedure to determine

the solutions of a third degree algebraic equation, let define:

$$\begin{cases} p = \frac{c}{a} - \frac{b^2}{3a^2} = -\frac{b^2}{3} \\ q = \frac{d}{a} - \frac{bc}{3a^2} + \frac{2b^3}{27a^2} = d + \frac{2b^3}{27} \end{cases}$$

where the simplified form is due to the fact that $a = 1$, $c = 0$.
Let define also:

$$\Delta_{III} = \Delta_{III}(\xi^*; \xi_0) = \frac{q^2}{4} + \frac{p^3}{27} = d\left(\frac{1}{4}d + \frac{1}{27}b^3\right) \tag{2.14}$$

If ξ^* and ξ_0 are such that $\Delta_{III} > 0$, then three solutions obtained are surely distinct, but two of them are complex and the remaining is real. It means that to an arbitrary $\xi^* > 0$ such that $\Delta_{III} > 0$, there corresponds exactly one value of y, whose sign depends on the coefficients b and d: it makes sense only if $y > 0$. If ξ^* and ξ_0 are such that $\Delta_{III} = 0$, since $d = \frac{1}{\xi^{*2}} > 0$, the only possibility is that:

$$\frac{1}{4}d + \frac{1}{27}b^3 = 0 \iff d = -\frac{4}{27}b^3 \tag{2.15}$$

In this case, referring to the solutions formulae of a third degree algebraic equation in the case $\Delta_{III} = 0$, the three solutions are real, at least two of them are equal and they all coincide if and only if $q = 0$.
Remembering the definition of q, one has:

$$q = 0 \iff d = -\frac{2}{27}b^3 \tag{2.16}$$

However, this is not consistent with condition (2.15), showing that in this specific case $q \neq 0$ necessarily. This means that in this case equation (2.13) has two coincident solutions and one distinct solution, that is, for each arbitrary ξ^* such that $\Delta_{III} = 0$ there are exactly two distinct solutions y, which are expressed in the form:

$$\begin{cases} y_1 = -2\left(\frac{q}{2}\right)^{\frac{1}{3}} - \frac{b}{3} \\ y_2 = y_3 = \left(\frac{q}{2}\right)^{\frac{1}{3}} - \frac{b}{3} \end{cases} \tag{2.17}$$

Simple algebraic passages and the use of (2.15) show that in this case the two solutions of (2.17) are strictly positive.
If instead ξ^* and ξ_0 are such that $\Delta_{III} < 0$, according to the solutions formulae for the present case, one defines:

$$z = -\frac{q}{2} + i\sqrt{-\Delta_{III}} = \rho(\cos\theta + i\sin\theta) \tag{2.18}$$

where $\rho > 0$ and $\theta \in [0,2\pi]$ are modulus and angle of the trigonometric form of the complex number z, which cannot be purely imaginary since $\Delta_{III} < 0$. Therefore θ cannot be

an integer multiple of π. In this case, the roots are expressed as follows:

$$\begin{cases} y_1 = 2\sqrt{\frac{-p}{3}}\cos\left(\frac{\theta}{3}\right) - \frac{b}{3} \\ y_2 = 2\sqrt{\frac{-p}{3}}\cos\left(\frac{\theta+2\pi}{3}\right) - \frac{b}{3} \\ y_3 = 2\sqrt{\frac{-p}{3}}\cos\left(\frac{\theta+4\pi}{3}\right) - \frac{b}{3} \end{cases}$$

where the square roots are real numbers because of $p = -\frac{b^2}{3} < 0$. The only factor which distinguishes the three solutions is the one involving cosinus. A simple study of the functions $\cos\left(\frac{\theta}{3}\right)$, $\cos\left(\frac{\theta+2\pi}{3}\right)$, $\cos\left(\frac{\theta+4\pi}{3}\right)$ shows that there not exists any point where the three graphs intersect, meaning that independently from the particular angle θ considered, at least one root is different from the others. Moreover, couple-by-couple intersections of the aforementioned cosinus functions happen at angles θ which are integer multiples of π, in contradiction with the fact that $\Delta_{III} > 0$. Therefore, the three roots y_1, y_2, y_3 are always distinct, meaning that in the case $\Delta_{III} < 0$, for any $\xi^* > 0$ one obtains three distinct values of y. About the sign of the roots, one can study the following inequalities by exploiting the fact that $p = \frac{-b^2}{3}$:

$$\begin{cases} y_1 > 0 \iff 2|\frac{b}{3}|\cos(\theta) - \frac{b}{3} > 0 \\ y_2 > 0 \iff 2|\frac{b}{3}|\cos\left(\frac{\theta+2\pi}{3}\right) - \frac{b}{3} > 0 \\ y_3 > 0 \iff 2|\frac{b}{3}|\cos\left(\frac{\theta+4\pi}{3}\right) - \frac{b}{3} > 0 \end{cases} \tag{2.19}$$

If $b > 0$, (2.19) turns into:

$$\begin{cases} \cos(\theta) > \frac{1}{2} \\ \cos\left(\frac{\theta+2\pi}{3}\right) > \frac{1}{2} \\ \cos\left(\frac{\theta+4\pi}{3}\right) > \frac{1}{2} \end{cases}$$

In particular, if $\theta \in [0, \pi]$ one has $y_1 > 0$, $y_2 < 0$, $y_3 < 0$, while if $\theta \in (\pi, 2\pi]$ one has $y_1 < 0$, $y_2 < 0$, $y_3 > 0$. Hence, in any case, when $b > 0$ there correspond a single physical $y > 0$ to ξ^*.
If $b < 0$, (2.19) turns into:

$$\begin{cases} \cos(\theta) < -\frac{1}{2} \\ \cos\left(\frac{\theta+2\pi}{3}\right) < -\frac{1}{2} \\ \cos\left(\frac{\theta+4\pi}{3}\right) < -\frac{1}{2} \end{cases}$$

In particular, for all $\theta \in [0,2\pi]$ one has $y_1 < 0$, $y_2 > 0$, $y_3 < 0$. Hence, again, when $b > 0$ there correspond a single physical $y > 0$ to ξ^*. What considered allow to conclude that points ξ^* such that $\Delta_{III} < 0$ correspond to a single physical $y > 0$.
What discussed before can be summarized in this way:

- points ξ^* such that $\Delta_{III}(\xi^*;\xi_0) > 0$ correspond to a unique y satisfying the equation, whose sign depends on ξ^* itself. Therefore, such ξ^* can correspond to at most one physical $y > 0$;
- points ξ^* such that $\Delta_{III}(\xi^*;\xi_0) = 0$ correspond to exactly two distinct values of y satisfying the equation, both positive and, thus, physical;
- points ξ^* such that $\Delta_{III}(\xi^*;\xi_0) < 0$ correspond to exactly one physical solution $y > 0$.

This suggests a structure of the solution with at most two *physical* branches, i.e., corresponding to positive heights y.

2.2.2 Critical points

Assume it is possible to explicit locally $\xi = \xi(y)$, where ξ is differentiable. Then the two members of (2.4) can be differentiated by y and evaluated along $\xi = \xi(y)$, obtaining the following:

$$-\frac{2}{\xi^2 y^3} + \frac{2}{\xi^3 y^2}\frac{d\xi}{dy} + 1 - \gamma_b \frac{d\xi}{dy} + \frac{d\zeta}{d\xi}\Big|_{\xi=\xi(y)} \frac{d\xi}{dy} = 0$$

By re-arranging:

$$\left(\frac{2}{\xi^3 y^2} - \gamma_b + \frac{d\zeta}{d\xi}\Big|_{\xi=\xi(y)}\right)\frac{d\xi}{dy} = -\left(-\frac{2}{\xi^2 y^3} + 1\right) \tag{2.20}$$

By enforcing $\frac{d\xi}{dy} = 0$ and using some algebra, one obtains the following equation:

$$-\frac{2}{\xi^2 y^3} + 1 = 0 \iff y = \left[\frac{2}{\xi(y)^2}\right]^{\frac{1}{3}} \tag{2.21}$$

Remembering (1.21), then (2.21) shows that extrema points of $\xi = \xi(y)$ are characterized by $Fr = 1$ independently from the eventual irregularities of the bed, as obtained for the plane case.

2.2.3 Numerical simulations

Since neglecting drag and considering flat bottom reduces Equation 1.25 to the algebraic equation (2.6), all the numerical simulations presented make use of such form. In particular, to plot the curve described, (2.6) is interpreted as the equation of the zero-level set

of the function

$$F(\xi, y) = \frac{1}{\xi^2 y^2} + y - 1 - \gamma_b(\xi - \xi_0) \tag{2.22}$$

in order to use a contour-plot technique, restricted to the physical domain of the problem $\mathcal{D}$.

Equation 2.6, once fixed the boundary radius ξ_0 at which unitary stream head is imposed, determines a family of orbits depending on the basal slope γ_b, which are reported in Fig. 2.3 along with the Critical Line.

Again, the orbits are sliced into a **subcritical** and a **supercritical** branch by the Critical Line, and the case of Horizontal Bed with Flat Bottom can be recovered by considering $\gamma_b = 0$. However, a novel feature emerges from the plots: while orbits corresponding to $\gamma_b > 0$ are open, those corresponding to $\gamma_b < 0$ are closed. Therefore, while the existence of a minimum radius ξ_{min} is a common feature to all the possible orbits, those obtained with $\gamma_b < 0$ also exhibit a maximum radius, ξ_{max}, and the two branches of the solution are non monotonic. Both ξ_{min} and ξ_{max} are slope dependent. As γ_b decreases for negative values, the minimum and maximum radii approach smaller values and correspond to higher maxima (minima) of the subcritical (supercritical) profile, with a consequently more abrupt decrease (increase) towards the critical height. The physical interpretation of the previous observation will be provided in Sec 2.2.4 and Sec. 2.2.6, after the description of the stream profiles that can be obtained.

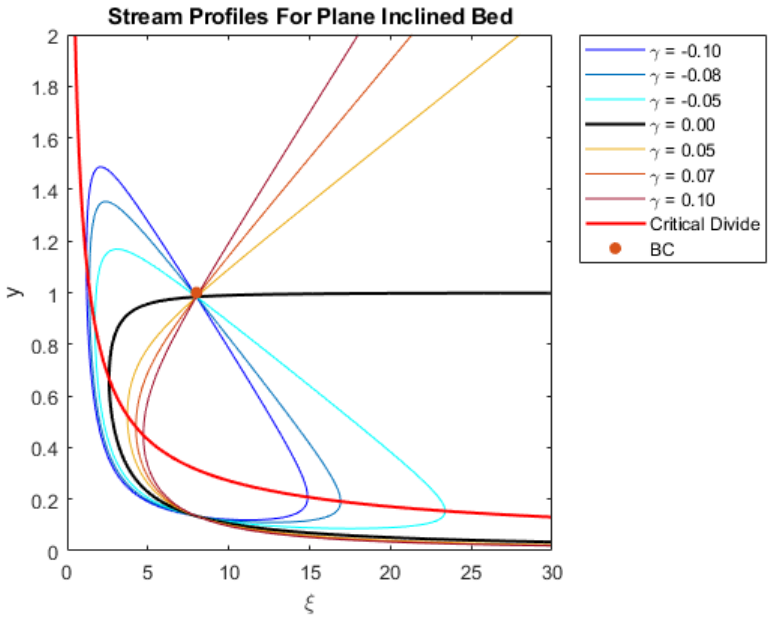

Figure 2.3: **Orbits for different values of γ_b.** Unitary stream head is imposed at $\xi_0 = 8$, corresponding to a subcritical depth $y_{0,sub} = 0.98$ and a supercritical depth $y_{0,sup} = 0.13$. Black Thick line refers to the Plane Bed with Flat Bottom ($\gamma = 0$), while the red thick line marks the Critical Divide ($Fr = 1$).

Funnel-shaped bed - $\gamma_b < 0$

The particular structure of the orbits for $\gamma_b < 0$ is responsible for two peculiar aspects. The first one is that subcritical branches of such solutions are generally non monotonic, exhibiting a maximum height y_M placed at radius ξ_M progressively smaller and nearer to the minimum radius. In particular, within the region $[\xi_{min}, \xi_M]$, the profile experiments an abrupt variation, which becomes sharper as γ_b decreases. This is well shown in Fig. 2.5, which refers to a stream starting flowing with unitary head and converging towards a central hole, on favourable slope: this is a first example of flows in which **energy increases**, as can be observed in Fig. 2.5(e), 2.5(f).

The subcritical profile starts with $Fr < 1$ and unitary stream head, then it accelerates to reach the hole in critical condition. Depth increases until reaching a maximum, then decreases to critical height, showing a non-monotonic behaviour. This can be understood by means of the radian specific discharge, at Fig. 2.6(a): indeed, the relation between y and q (the reversed graph) is non monotonic, having a maximum corresponding to the height y_M.

The flow can be also inverted, thanks to the symmetry described in Sec. 1.4.1. In this case, the flow is divergent, on opposite slope, over a funnel-shaped bed, as can be seen by the behaviour of the Stream Head: coherently, the flows described are dissipating. It starts with unitary stream head and reaches critical conditions, according to one of the two branches. Results are reported in Fig 2.4.

The supercritical profile starts instead with unitary stream head and $Fr > 1$, then depth strictly increases until reaching the hole in critical condition. Velocity, as long as Froude Number, increases until reaching a maximum, then decrease: this is explained by the fact that, in order to maintain the prescribed linear Stream Head with the depth increasing to reach critical height at the hole, kinetic energy must decrease, as reported in Fig. 2.5(f).

A second aspect of solution curves with $\gamma_b < 0$ is that they exhibit also a maximum radius $\xi = \xi_{max}$, which was also evident in the profiles reported in Fig. 2.4(a) and introduces an additional class of profiles: those enclosed between **two Froude Horizons** (in the context of Analogue Gravity, it describes a Reissner-Nordstrometric Black Hole, See [33]), as shown in Fig. 2.7. This solution is similar to that obtained for the case of plane, flat bed, in presence of friction: the novelty of this case is that this behaviour happens although friction is not considered, opening to the possibility to simulate the phenomenon also in a simpler laboratory setting. Once the flow direction is specified, one can fix a critical boundary condition upstream (downstream) and integrate downward (upward) in order to obtain the supercritical (subcritical) branch of the solution. The so obtained profiles are non-monotonical, as shown in Fig. 2.7(a). Moreover, it can be observed that the heights $y_{crit,max}$ and $y_{crit,min}$ associated to maximum and minimum respectively correspond to the minimum and maximum Radian Specific Discharge, while the minimum (maximum) height attained by the supercritical (subcritical) profile is also a minimum (maximum) height with respect to the discharge which, as a function of y, is non monotonic.

Cone-Shaped Bed - $\gamma_b > 0$

As described before, the geometry of the orbits for $\gamma_b > 0$ is significantly different, since they are open: therefore, they exhibit a minimum radius ξ_{min}, but not a maximum one

like for $\gamma_b < 0$. Such structure of the solution is similar to that of the plane case, with the exception that the minimum radius depends on the slope. Such behaviour reflects on the possible stream profiles, which are monotonic increasing if subcritical, monotonic decreasing otherwise.
When considering convergent direction, stream flows on opposite slope, thus energy decreases. This is the case of the stream reported in Fig. 2.9: subcritical (supercritical) branch starts with unitary stream head at $\xi_0 = 8$, then it accelerates (decelerates) approaching critical conditions (physically corresponding to a hole) with progressively lower (higher) depth.
Divergent direction describes instead flows on favourable slope, as the stream head increases. This is the case of the stream reported in Fig. 2.8: it starts flowing in critical condition at $\xi = \xi_0$ (physically correponding to a source), then it decelerates (accelerates) according to the subcritical (supercritical) branch attaining progressively higher(lower) depths, monotonically. In order to highlight this aspect, one can see the plot of Radiant Specific Discharge q with respect to y, reported in Fig. 2.8(e). Such relation is actually a function: q increases with the supercritical heights, reaches a maximum at $y(\xi = \xi_{min})$ (the critical height at minimum radius), then decreases to 0 as the subcritical heights increase, thus explaining the monotony of depth profiles.

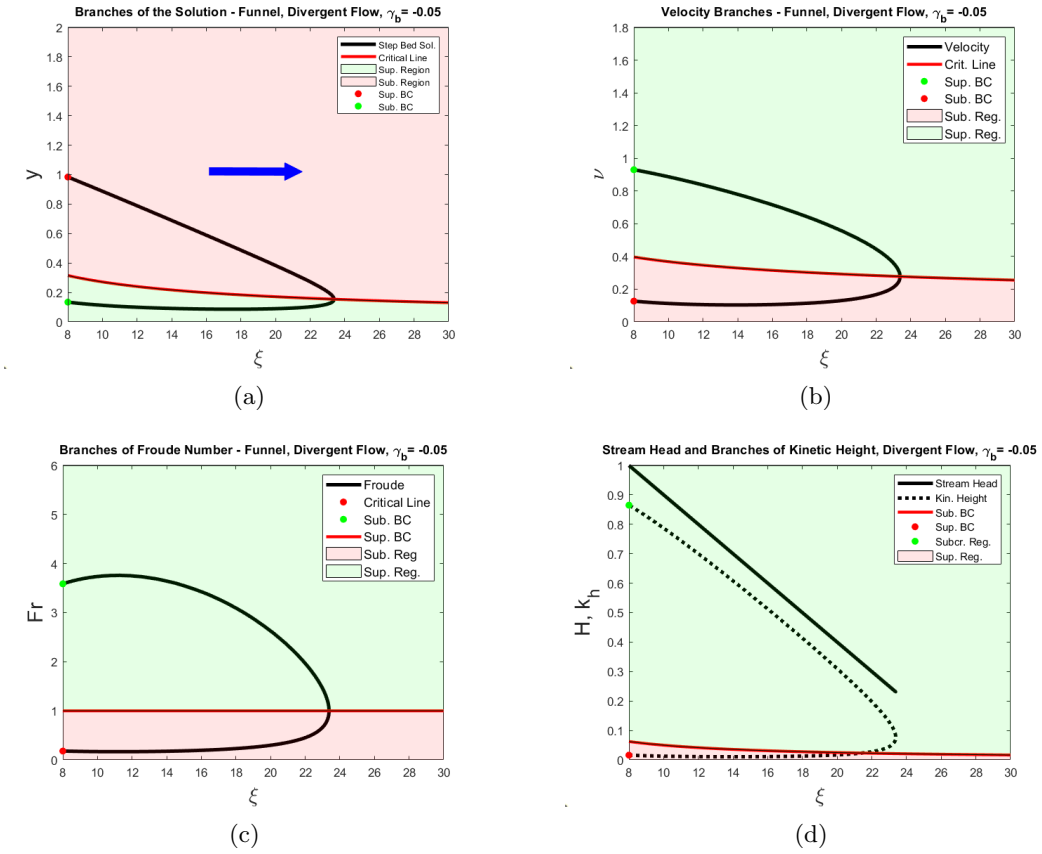

Figure 2.4: **Divergent stream flowing on opposite slope over a funnel-shaped flat bed, $\gamma_b = -0.05$.** Unitary stream head is imposed at $\xi_0 = 8$ for both supercritical and subcritical flows. Fig. 2.4(a) - Supercritical and Subcritical stream profiles. The blue arrow shows the flow direction. Fig. 2.4(b) - Supercritical and Subcritical velocities. Fig. 2.4(c) - Supercritical and Subcritical branches of the Froude Number. Fig. 2.4(d) - Stream Head, along with supercritical and subcritical branches of Kinetic Height.

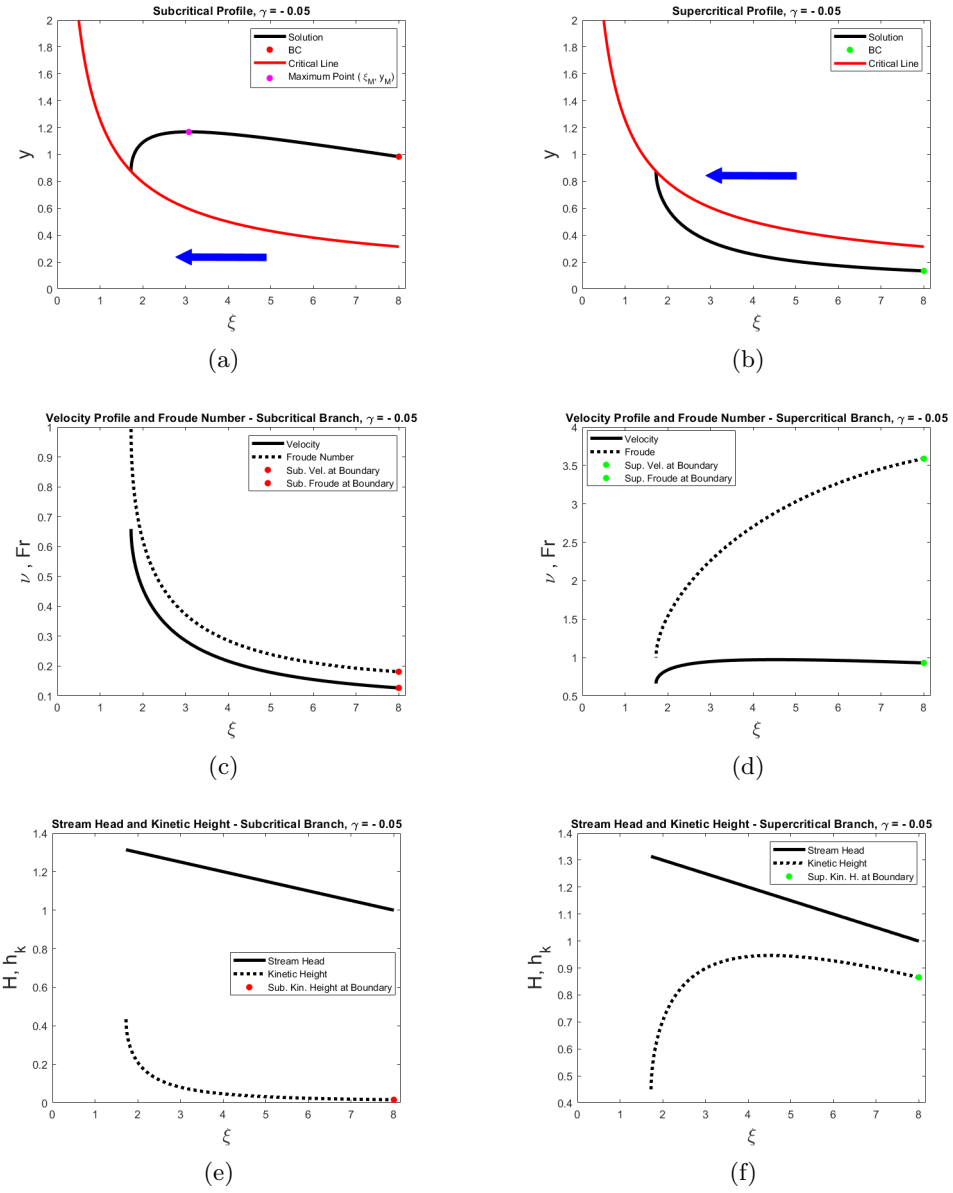

Figure 2.5: **Convergent stream flowing on favourable slope over a funnel-shaped flat bed,** $\gamma_b = -0.05$**.** Left and right column respectively refer to Subcritical and Supercritical solutions. In each column Stream Profile, Velocity and Froude number, Stream Head and Kinetic Height are reported for $\gamma_b = -0.05$. Unitary stream Head boundary condition is imposed at $\xi_0 = 8$. The blue arrow represents the convergent flow direction.

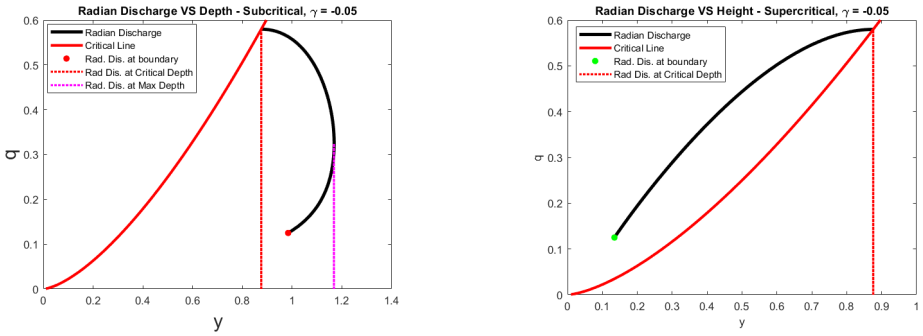

(a) (b)

Figure 2.6: **Radiant Specific Discharge -Convergent stream flowing on favourable slope over a funnel-shaped flat bed,** $\gamma_b = -0.05$**.** Left and right column respectively refer to the relation between Radiant Specific Discharge and Height for the Subcritical and the Supercritical solutions. Unitary stream Head boundary condition is imposed at $\xi_0 = 8$. Vertical lines are depicted to show that the maximum Radiant Specific Discharge is attained at the critical height associated to the minimum radius, while at the maximum subcritical height the curve has vertical tangent.

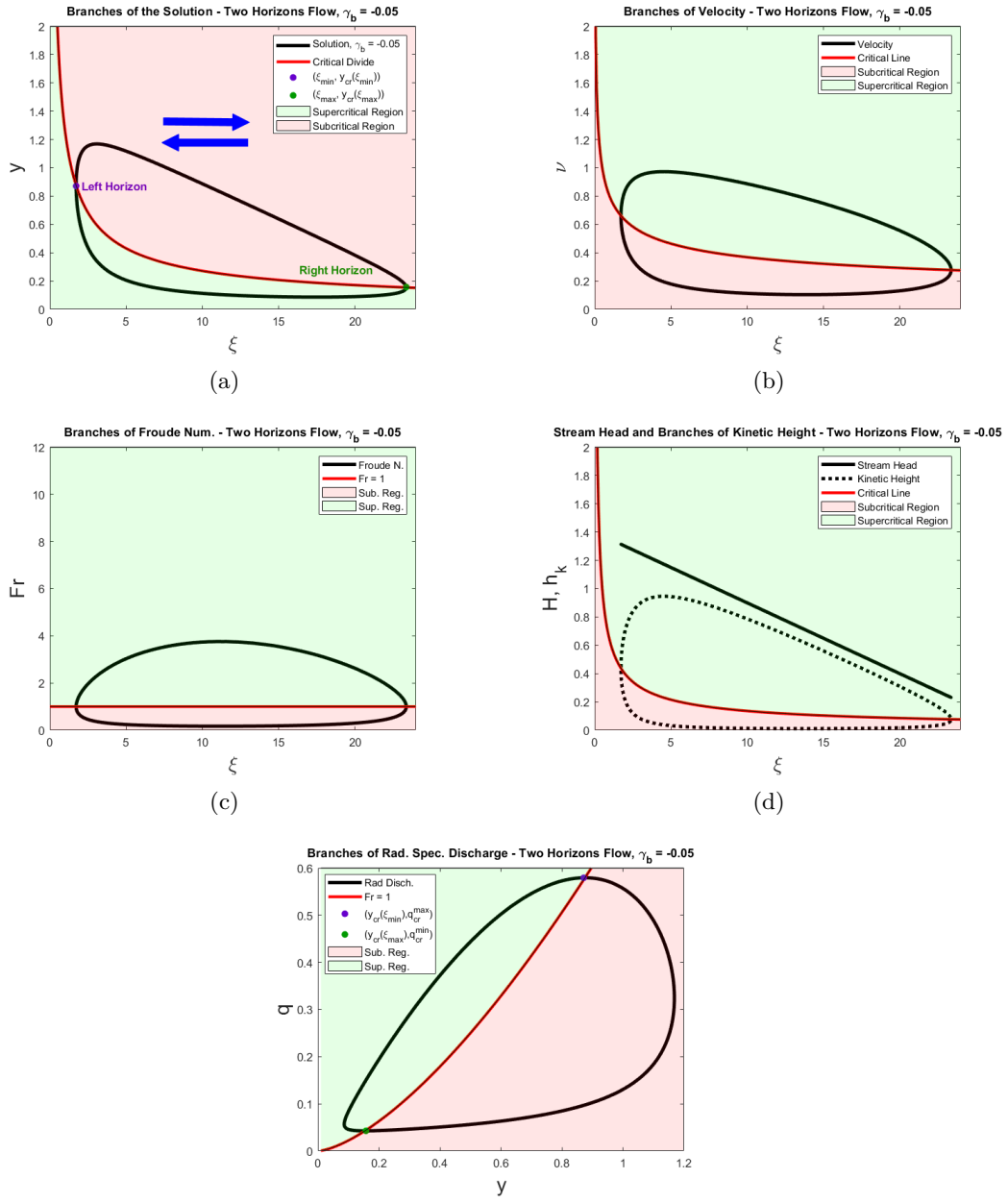

Figure 2.7: **Two Horizons Solution,** $\gamma_b = -0.05$**.** Unitary Stream Head condition is imposed at $\xi_0 = 12$. 2.7(a) - Subcritical and Supercritical branches. 2.7(b) - branches of the Velocity. 2.7(c), branches of the Froude Number. 2.7(d) - Stream Head and branches of the Kinetic Height. 2.7(e) - Branches of the Radiant Specific Discharge, along with the notable heights: the critical heights $y_{crit,max}$ and $y_{crit,min}$, corresponding to the heights attained at minimum and maximum radius; the maximum height attained by the Subcritical Profile, y_M and the minimum height attained by the Supercritical Profile, y_m.

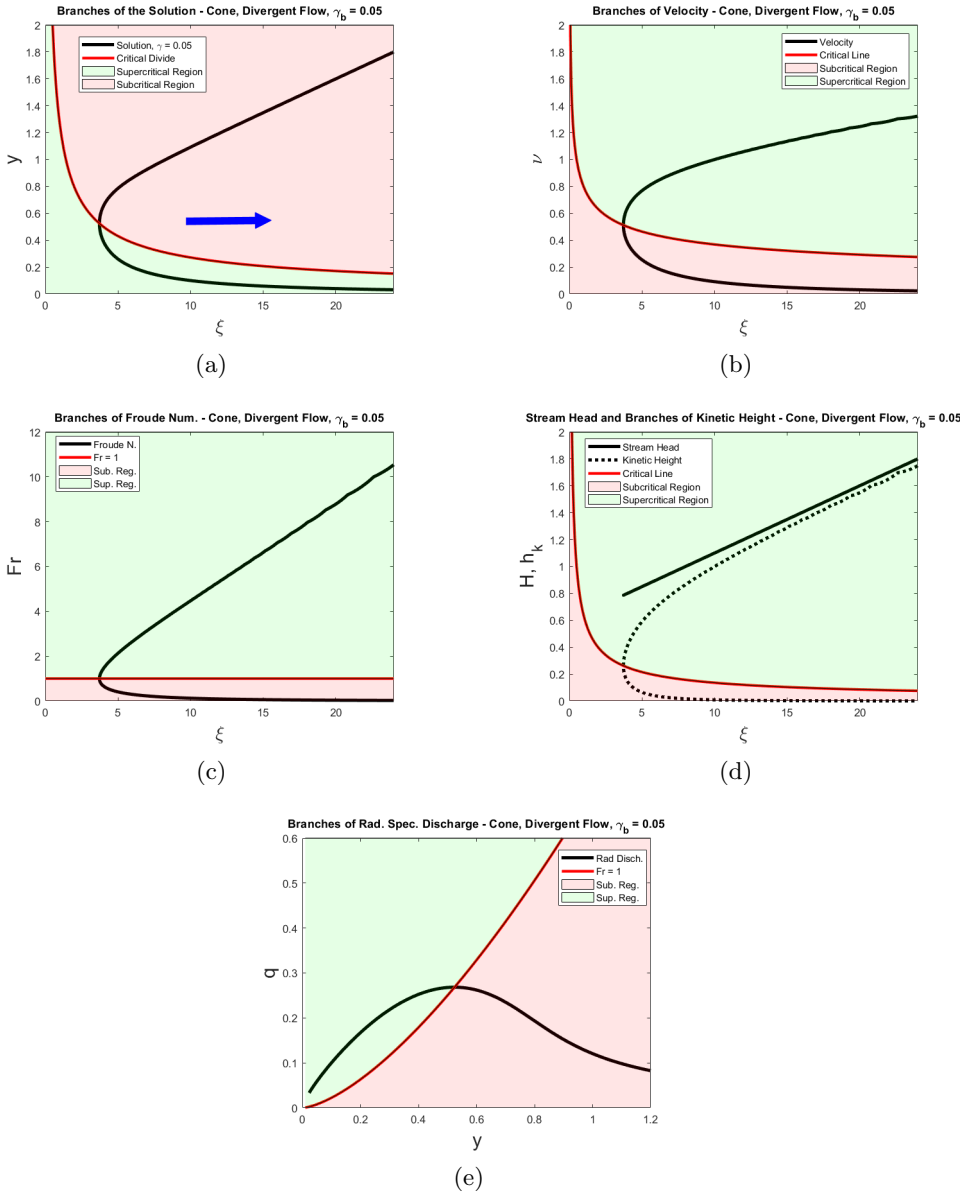

Figure 2.8: **Divergent stream flowing on favourable slope over a Cone-shaped flat bed, $\gamma_b = 0.05$.** In both regimes, flow starts in critical condition at $\xi_0 = 3.75$, physically corresponding to a source, and flows in the divergent direction. 2.8(a) - Subcritical and Supercritical Stream Profiles; the blue arrow indicates flow direction. 2.8(b), branches of the velocity. 2.8(c) - branches of the Froude Number. 2.8(d) - Stream Head along with the branches of Kinetic Height. 2.8(e), branches of the Radian Specific Discharge. Notice that the relation $q \sim y$ is actually a function.

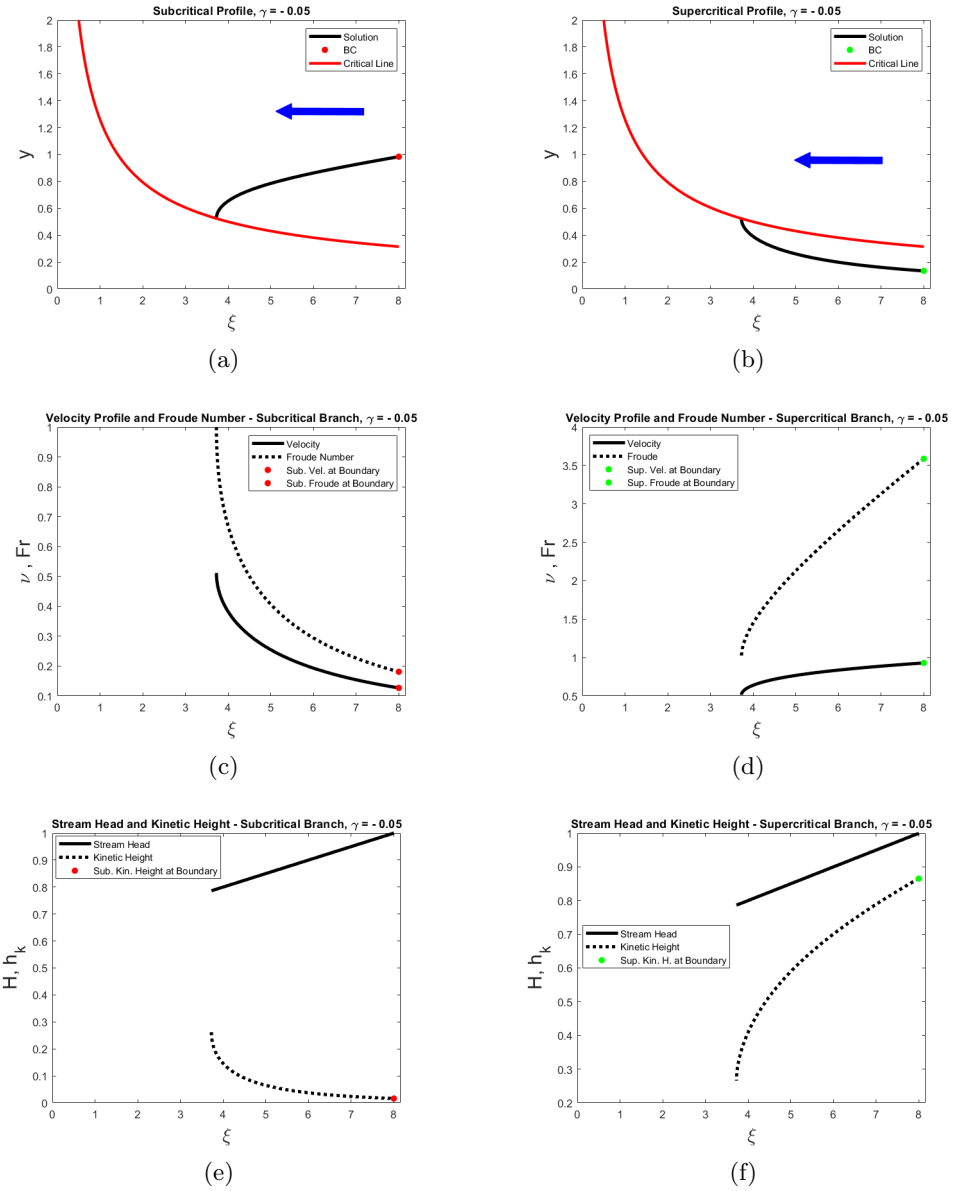

Figure 2.9: **Convergent stream flowing on opposite slope over a Cone-Shaped flat bed,** $\gamma_b = 0.05$**.** Left and right column respectively refer to Subcritical and Supercritical solutions. In each column Stream Profile, Velocity and Froude number, Stream Head and Kinetic Height and the relation between Radian Specific Discharge and the depths of the profiles are reported for $\gamma_b = 0.05$. The blue arrow represents the convergent flow direction.

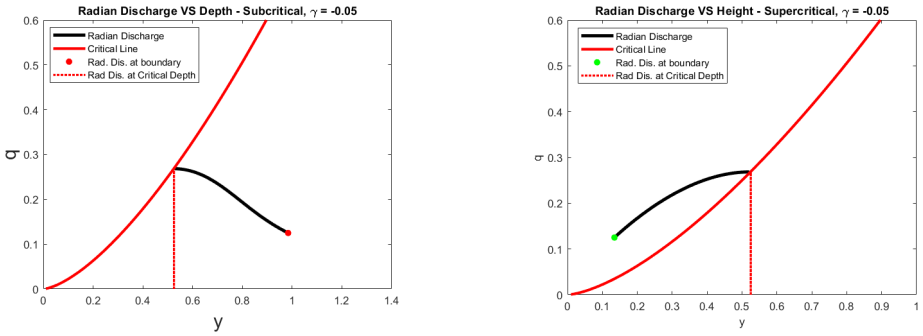

(a) (b)

Figure 2.10: **Radiant Specific Discharge -Convergent stream flowing on opposite slope over a Cone-shaped flat bed,** $\gamma_b = -0.05$**.** Left and right column respectively refer to the relation between Radiant Specific Discharge and Height for the Subcritical and the Supercritical solutions. Unitary stream Head boundary condition is imposed at $\xi_0 = 8$. Vertical lines are depicted to show that the maximum Radiant Specific Discharge is attained at the critical height associated to the minimum radius.

2.2.4 Monotony of Stream Profiles: Mathematical Point of View

A first point of view to explain the different behaviour of the orbits for positive, null and negative basal slopes γ_b (open or closed) is provided by Eq. 1.29, which in case of an Inclined Bed with Flat Bottom, with no friction, assumes the form:

$$\frac{dy}{d\xi} = \frac{\gamma_b + \frac{2}{\xi^3 y^2}}{1 - \frac{2}{\xi^2 y^3}} = \frac{\gamma_b + \frac{2}{\xi^3 y^2}}{1 - Fr^2(\xi, y)} \tag{2.23}$$

In order to discuss the sign of $dy/d\xi$, one can easily observe that the denominator of Eq. 2.23 is:

- positive for the subcritical branch;
- negative for the supercritical branch.

Regarding the nominator of Eq. 2.23, one can study its sign by means of the following inequality:

$$\frac{2}{\xi^3 y^2} \geq -\gamma_b \tag{2.24}$$

where one can observe that $-\gamma_b$ is the opposite slope and, by using the relation 1.19 for the velocity $\nu = \nu(\xi, y)$, that:

$$k_s(\xi, y) := \frac{2}{\xi^3 y^2} = 2\,\frac{\nu^2}{\xi}$$

represents *Radiant Specific Kinetic Height*, which is a measure of how Kinetic energy distributes along a specific radiant, at each radial position ξ.
Last inequality is satisfied $\forall \xi, y > 0$ if $\gamma_b \geq 0$: therefore, the nominator is positive if the bed is horizontal or Cone-shaped.
If instead one considers $\gamma_b < 0$, last inequality can be re-arranged as:

$$y \leq \sqrt{-\frac{2}{\gamma_b \xi^3}} \tag{2.25}$$

Let define:

$$y_{st,flat}(\xi) := \sqrt{-\frac{2}{\gamma_b \xi^3}} \tag{2.26}$$

Then Ineq. 2.25 tells that if the bed is Funnel-shaped ($\gamma_b < 0$), then the nominator of Eq. 2.23 is:

- positive where the height profile is lower than $y_{st,flat}(\xi)$;
- negative where the height profile is greater than $y_{st,flat}(\xi)$.

Table 2.1 combines the results just obtained to determine the sign of $dy/d\xi$ for the supercritical and the subcritical profile.
It is evident that Funnel-shaped bed gives rise to non-monotonic height profiles, since the sign of $dy/d\xi$ expressed by Eq. 2.23 can change.
Moreover, $y_{st,flat}(\xi)$ in 2.26 represents the curve where the stationary points of the height profile lie, since along it $dy/d\xi = 0$: they can be find as intersections between 2.26 and solutions curve expressed by Eq. 2.6.

2.2.5 Velocity - Gravity Interplay and Monotony of Stream Profiles

In view of what just discussed, Ineq. 2.24 can be interpreted from a physical point of view as an interplay between Kinetic and Potential Energies, which is illustrated in Fig. 2.11 and justifies what is described below.
Indeed, if the bed is Cone-shaped ($\gamma_b > 0$, Figures 2.11(b), 2.11(d)), Kinetic Energy definitively overcomes the energy subtractions given by opposite slope one and governs the behaviour of the stream profiles, granting no monotony variations: it helps the stream when flowing on both favourable slope (in order to linearly increase the Stream Head) and opposite slope, providing the fluid as much kinetic energy to go up the cone to contrast gravity until reaching the central hole at minimum radius (if the hole was not present, the stream head would abruptly decrease, being no longer linear as prescribed by 2.6, and the fluid would come back flowing on favourable slope).
Flows on Horizontal Beds ($\gamma_b = 0$) have an analogous behaviour, with the exception that

there is no slope, so the Stream Head is constantly 1.
If instead the bed is Funnel-shaped ($\gamma_b < 0$, Figures 2.11(a), 2.11(c)), such interplay shows more complex features on the supercritical and subcritical branches:

- if the stream is on favourable slope (convergent) and subcritical, kinetic energy progressively increases, balances the effects of gravity where the height profile reaches its maximum and then helps the fluid reaching the central hole (Left Horizon). If the hole was not present, Stream Head would dramatically increase breaking linear behaviour as prescribed by Eq. 2.6;
- if the flow is subcritical, but on opposite slope, kinetic energy decreases until being overbalanced by gravity, helping the flow going up the funnel until reaching the external hole (Right Horizon). If such hole was not present, the stream would come back flowing on favourable slope under the effect of gravity);
- the same holds for the supercritical flow, but the two energetic contributes balance exactly where the height profile attains its minimum. This happens because the kinetic energy is greater in the supercritical regime, implying that for supercritical flows on opposite slope gravity overbalance on kinetic energy appears at greater distances with respect to the subcritical ones, while for supercritical flows on favourable slope Radiant Specific Kinetic Energy abruptly nearby the central hole (Right Horizon), to force the flow reaching critical Conditions.

It is therefore evident the role of Radiant Specific Kinetic Energy in individuating, particularly for Beds with $\gamma_b < 0$, the regions where the flows are more influenced by the presence of the holes (Left and Right Horizon).

Table 2.1: **Sign of $dy/d\xi$.** The sign is determined according to that of the numerator and denominator of the right hand side of Eq. 2.23.

Sign of $dy/d\xi$, Inclined Bed with Flat Bottom				
	$\gamma_b > 0$	$\gamma_b = 0$	$\gamma_b < 0$	
			$y \leq y_{st,flat}(\xi)$	$y > y_{st,flat}(\xi)$
Sign of $dy/d\xi$ - Supercritical Flow	> 0	> 0	> 0	< 0
Sign of $dy/d\xi$ - Subcritical Flow	< 0	< 0	< 0	> 0

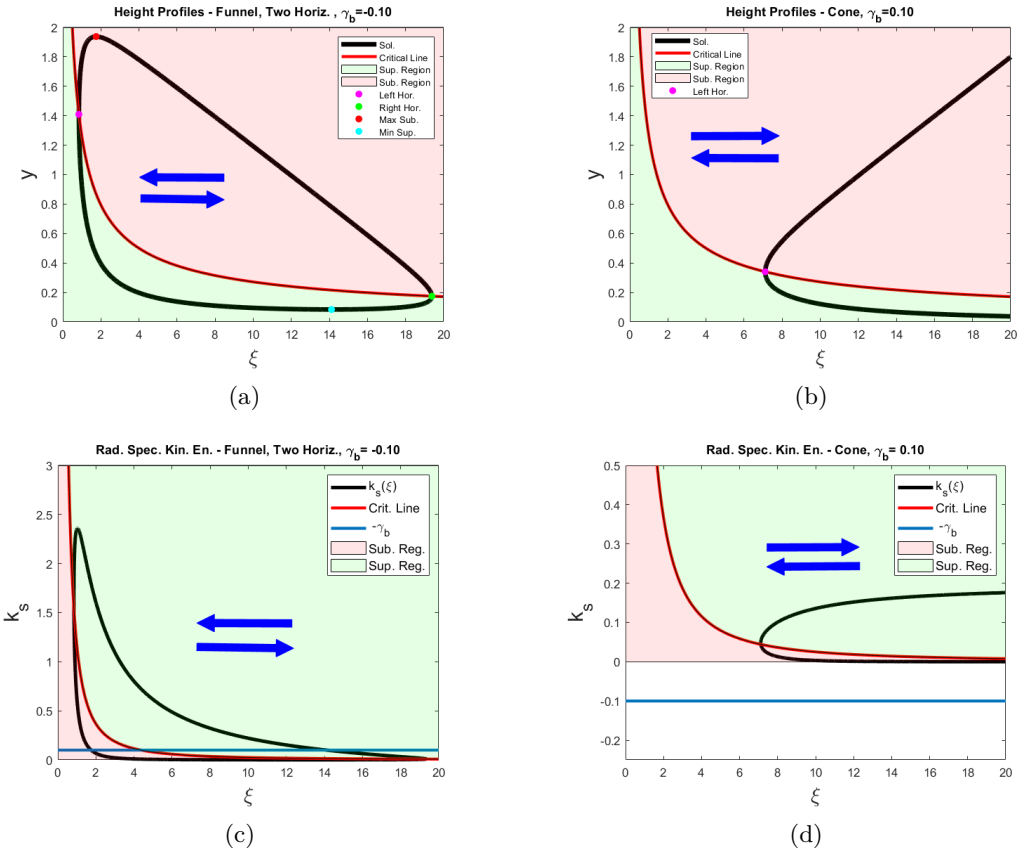

Figure 2.11: **Radiant Specific Kinetic Height $k_s(\xi)$ for Flows over Inclined Bed with Flat Bottom, $\gamma_b = \pm 0.10$.** Left panel (Figures 2.11(a),2.11(c)) refer to a Two-Horizons Flow (in both convergent and divergent direction) over a Funnel shaped Bed ($\gamma_b = -0.10$) with Flat Bottom. Right panel (Figures 2.11(b),2.11(d)) refer to a Flow over a Cone shaped Bed ($\gamma_b = 0.10$) with Flat Bottom (in both convergent and divergent direction). Both profiles are obtained by imposing unitary Stream Head at $\xi_0 = 12$.

2.2.6 Energy - Discharge Interplay and Non Monotonic Profiles

The non-monotonic behaviour of the height profiles obtained for $\gamma_b < 0$ (whose mathematical explanation was provided by the study of Eq. 2.23 at the start of Sec. 2.2.3) can be understood in physical terms by means of the Convergent and Divergent stream profiles in the framework of the governing equation 2.6, which prescribes:

- a linear Stream Head $\tilde{H}(\xi) = 1 + \gamma_b(\xi - \xi_0)$, which is exactly 1 at $\xi = \xi_0$;
- a constant Discharge Q.

Considering the Convergent Flow over Funnel shaped Bed with Flat Bottom reported in Fig. 2.5, fluid emerges from an external annular gate placed at $\xi_0 = 8$, where the stream head is enforced to be 1, and starts flowing according to the supercritical or subcritical

branch on favourable slope until converging to a central hole, located at minimum radius, which drains the fluid: for radii smaller than the minimum one (i.e., for tighter or absent central holes) and same discharge, fluid Height $y(\xi)$ and Radiant Specific Discharge $q(\xi)$ would dramatically increase, and the only possibility to maintain the Stream Head linear as prescribed by the governing equation 2.6 would be to reduce the discharge itself, in contradiction with Eq. 2.6 itself which expresses instead its conservation.
If one considers instead Divergent Flow over Funnel shaped Bed with Flat Bottom, reported in Fig. 2.4, fluid emerges from an internal annular gate placed again at $\xi_0 = 8$, where the stream head is enforced to be 1, and starts flowing on opposite slope according to one of the two branches, until reaching a maximum radius. For radii greater than the maximum one, the fluid Height $y(\xi)$ and Radiant Specific Discharge $q(\xi)$ would dramatically decrease, and the only possibility to maintain the Stream Head Linear would be instead to increase the Discharge, again in contradiction with the governing equation 2.6. The consequence of such interplay is the non monotony of the profiles, particularly evident in the two branches of the Two-Horizons Stream solutions reported in Fig. 2.7. Indeed, nearby the minimum and maximum radii (respectively Left and Right Horizons indicated in Fig. 2.7(a)) the subcritical (supercritical) flow approaches critical conditions, velocity abruptly accelerates (slows down) and consequently height decreases (increases): since the critical heights at minimum and maximum radius are different, the only possibility to connect Left and Right Critical Horizons is via a non monotonical profile, with a maximum if the flow is subcritical and a minimum if supercritical.

2.3 Case 2 - Inclined Bed with Sinusoidal Bottom

Following what has previously studied in [4] in a two-dimensional cartesian reference, let consider again a bed with general basal slope γ_b. Moreover, in order to simulate the effects of irregularities of the bed on the flow, let consider a simple sinusoidal irregularity profile:

$$\zeta(\xi) = a\cos(k_b\xi) + a \tag{2.27}$$

where:

- $a > 0$ is the amplitude of the sinusoidal bottom [2], therefore the maximum height of the bottom is given by $h_{sin,max} = 2a$;
- k_b is the wavenumber of the sinusoidal bed

Then the Solution Curve expressed by Equation 2.4, with sinusoidal bottom expressed by 2.27, assumes the following form:

$$\frac{1}{\xi^2 y^2} + y - 1 - \gamma_b(\xi - \xi_0) + a\cos(k_b\xi) - a\cos(k_b\xi_0) = 0 \tag{2.28}$$

[2] Translation by a makes the codomain of the profile described by 2.27 be [0,2a] instead of $[-a, a]$. In this way, the bed profile is completely included within the domain of interest, i.e., $D = \{(\xi, y) : \xi > 0, y > 0\}$

Again, three main cases of beds with Sinusoidal Bottom can be distinguished, depending on γ_b:

- Cone shaped Bed, $\gamma_b > 0$;
- Funnel shaped Bed, $\gamma_b < 0$;
- Horizontal Bed, $\gamma_b = 0$

However, the sinusoidal topography introduces a and k_b as additional parameters, from which depends the nature of the solutions. In order not to violate the hypothesis of gradually varied flow, small amplitude values are chosen: in particular, $ain[0.01,0.1]$, similarly to Ref. [4].
The aim of this section is to investigate the influence of a and k_b, along with γ_b, in the features of the flow.

2.3.1 Numerical Simulations

Orbits described by Eq. 2.28, again, exhibit a similar behaviour to those of the inclined bed with flat bottom: they are open with a minimum radius for $\gamma_b \geq 0$, closed for $\gamma_b < 0$. However, the sinusoidal irregularity of the bottom influences the features of both supercritical and subcritical flow. This is evident in Fig. 2.12, where orbits are obtained with amplitude $a = 0.05$, wavenumber $k_b = 5$ and basal slopes $\gamma_b = -0.1,\ 0,\ 0.1$, while unitary stream head is imposed at $\xi_0 = 12$.

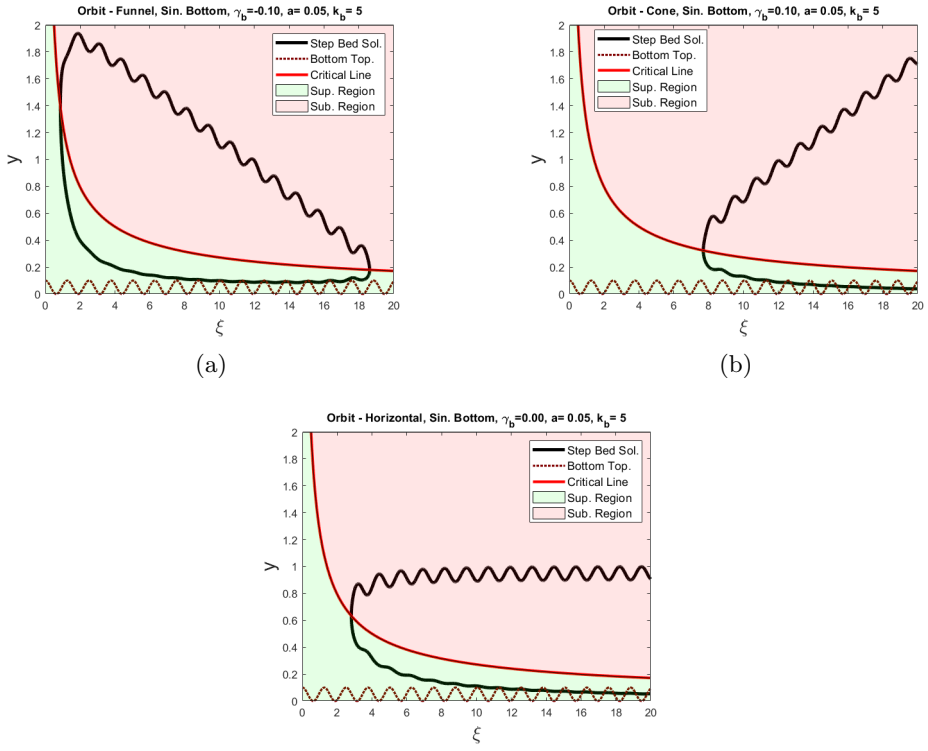

Figure 2.12: **Bed with Sinusoidal Bottom - Orbits.** In all of the three cases, unitary stream head is enforced at $\xi_0 = 12$, $a = 0.05$ and $k_b = 5$, while the basal slope, from top left figure and clockwise, assumes the values $\gamma_b = -0.1,\ 0.1,\ 0$.

Horizontal Bed with Sinusoidal Bottom, $\gamma_b = 0$

Height profiles obtained for the Horizontal Bed with Sinusoidal Bottom ($\gamma_b = 0$) are characterized, as for the case of Horizontal Bed with Flat Bottom, by bounded subcritical and supercritical branches forming an open curve, each one representing two possible solutions depending on the direction of the flow (convergent, flowing towards a central critical hole or divergent, starting from a critical source). However, the presence of the sinusoidal irregularity induces a marked non monotony, which is exhibited in both the subcritical and the supercritical branch, but with significant differences:

- the supercritical branch shows damped undulatory behaviour, with maxima and minima almost on phase with those of the bottom profile (tend to be on phase with the bed for sufficiently large ξ);
- the subcritical branch shows progressively stabilizing undulatory behaviour, with maxima and minima exhibiting a phase offset with respect to the ones of the bed profile (the phase offset tends to be $\frac{\pi}{2k_b}$).

Such behaviour is well shown in Fig. **??** and can be explained by two factors:

- the interplay between Kinetic and Potential energy, because of the sinusoidal irregularity;
- the interplay between the unitary stream head boundary condition placed at $\xi = \xi_0$ and the critical condition attained at the minimum radius.

From an energetic point of view, Mechanical Energy is not conserved and variations of the stream head are due to the sole effect of the irregularities of the bed, as it is shown by Eq. 2.8, which here assumes the following form:

$$\frac{1}{\xi^2 y^2} + y = 1 - a\cos(k_b\xi) + a\cos(k_b\xi_0) \tag{2.29}$$

Such equation expresses the fact that the Stream Head is sinusoidal and, since it contains the term $-acos(k_b\xi)$, it shows an offset of exactly $\frac{\pi}{2k_b}$ with respect to the bottom topography: if bottom topography increases, mechanical energy (the Stream Head) decreases, and vice versa. This is similar to what discussed in Sec. 2.4.2 for the effect of the Step Bottom topography: each half-oscillation of the bottom (which can be increasing or decreasing) can be "felt" by the flow as ascending or descending depending on the direction (convergent or divergent), respectively "helping" or "opposing" to the flow and therefore increasing or decreasing total Energy.
What causes the offset between the subcritical and supercritical flow features is instead the interplay between the unitary stream head boundary condition and the critical condition at the minimum radius. In order to illustrate this, let consider the case of a divergent flow starting from a critical source located at $\xi = \xi_{min} = 2.9$ and reaching unitary stream head at $\xi_0 = 12$, as reported in Fig. 2.13. The sinusoidal bottom has amplitude $a = 0.10$ and wavenumber $k_b = 5$: the convergent case can be interpreted by simply inverting flow direction and considering a hole draining the fluid (in place of the source) in critical conditions. Once barely moving from the critical source, flow is forced to accelerate (decelerate) in order to flow according to the supercritical (subcritical) regime, independently from the potential energy contribute of the sinusoidal bottom, which is felt instead by the flow starting from the first extremum point of the bottom topography faced after the minimum radius. Therefore, independently again from the behaviour of the sinusoidal bottom, in a neighbourhood of the minimum radius flow depth is forced to increase (subcritical) or decrease (supercritical) and, since the stream head must be the same for the two regimes at any radial distance ξ, the two height profiles exhibit an offset.
Mathematically, it can be explained generally by considering Profile Equation 1.25, which in the current case of Horizontal Bed with Sinusoidal Bottom and no friction (i.e., $\alpha = 0$), assumes the following form:

$$\frac{dy}{d\xi} = \frac{ak_b\sin(k_b\xi) + \frac{2}{\xi^3 y^2}}{1 - \frac{2}{\xi^2 y^3}} = \frac{ak_b\sin(k_b\xi) + \frac{2}{\xi^3 y^2}}{1 - Fr(\xi, y)^2} \tag{2.30}$$

Indeed, the denominator of Eq. 2.30 is:

- positive if the flow is subcritical;

- negative if the flow is supercritical;
- 0 if the flow is critical.

Moreover, in order to study the sign of the numerator of Eq. 2.30, one obtains by simple re-arrangement:

$$\frac{2}{\xi^3 y^2} \geq -ak_b \sin(k_b \xi) \tag{2.31}$$

Because of the physical domain [3], the previous inequality is surely satisfied when the sinus term is non-negative (since the left hand side is strictly positive, while the right hand side would be negative or zero). Therefore, the numerator is surely positive for:

$$\frac{k}{k_b}\pi \leq \xi \leq \frac{(2k+1)}{k_b}\pi \ , \ k \in \mathbb{Z}$$

Consider now the case in which sinus term is negative, i.e., when

$$\frac{2k-1}{k_b}\pi < \xi < \frac{2k}{k_b}\pi \ , \ k \in \mathbb{Z}$$

Then the right hand side of Ineq. 2.31 is positive and, by using some algebra and re-arranging, two cases can be distinguished:

- if $y \leq \sqrt{-\frac{2}{ak_b\xi^3 \sin(k_b\xi)}}$, Ineq. 2.31 is satisfied and the numerator of Eq. 2.30 is non-negative;
- if $y > \sqrt{-\frac{2}{ak_b\xi^3 \sin(k_b\xi)}}$, Ineq. 2.31 is not satisfied and the numerator of Eq. 2.30 is negative.

Table 2.2 provides an organic combination of the results just obtained, along with the sign of $\frac{dy}{d\xi}$ as a consequence, while a graphic display can be found in Fig. 2.13. It is evident that height profiles for the supercritical and subcritical branch always exhibit opposite monotony, which explains the offset which was previously detected in Fig. 2.12(c). Notice that when the sinus term at the right hand side of Ineq. 2.31 is positive, it also provides the curve along which the stationary points (minima and maxima) of both subcritical and supercritical height profiles are located, i.e., the line:

$$y_{st,sin}(\xi) := \sqrt{-\frac{2}{ak_b\xi^3 \sin(k_b\xi)}} \tag{2.32}$$

In particular, they can be found as the intersections between 2.32 and the solution curve expressed by Eq. 2.28, as it is shown in Fig. 2.13.

[3] **Recall**: The physical domain, introduced in Sec. 1.4.1, is $\mathcal{D} = \{\xi > 0\} \times \{y > 0\}$.

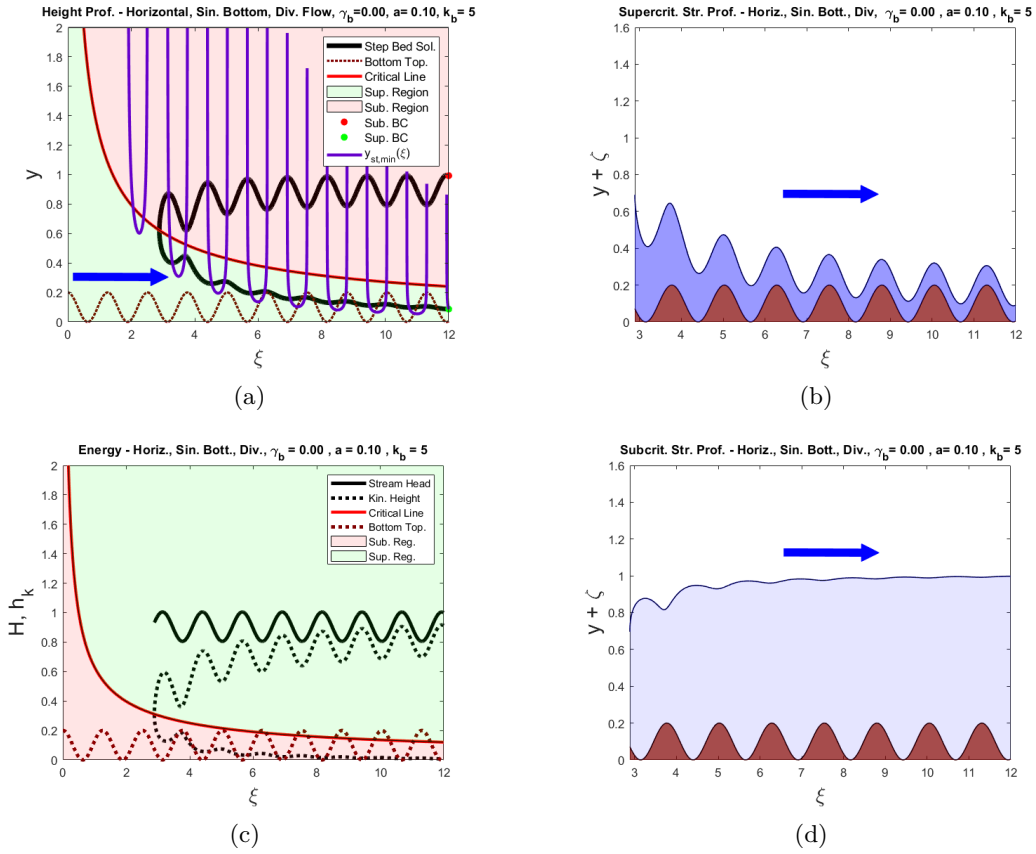

Figure 2.13: **Divergent Flow along an Horizontal Bed with Sinusoidal Bottom,** $\gamma_b = 0$**,** $a = 0.1$**,** $k_b = 5$**.** Unitary Stream Head Boundary Condition is imposed at $\xi_0 = 12$. **Fig.** 2.13(a) - Subcritical and Supercritical height profiles, along with the function $y_{st,min}(\xi)$ defined in 2.32 (purple line) to display the results summarized in Tab. 2.2. **Figures** 2.13(b), 2.13(d) - Supercritical and Subcritical Stream Profiles. **Fig.** 2.13(c)- Stream Head and Kinetic Height.

A last interesting aspect emerges from the Stream Head. Indeed the bed is horizontal ($\gamma_b = 0$), so, as described by Eq. 2.30, the Stream Head $\tilde{H}(\xi)$ is expressed by the sum of a constant mean Stream Head $H_{0,\gamma_b=0}$ due to the boundary condition imposed and a sinusoidal fluctuation $H'(\xi)$ due to the energy contribute of bottom slope:

$$\tilde{H}(\xi) = H_{0,\gamma_b=0} + H'(\xi)$$

where:

$$H_{0,\gamma_b=0} = 1 + a\cos(k_b\xi_0) = 1 + H'_0$$

can be interpreted as a mean Stream Head, while

Table 2.2: **Sign of $dy/d\xi$ and of the bottom slope $d\zeta/d\xi$.** As usual in this subsection, a and k_b respectively represent amplitude and wavenumber of the sinusoidal bottom topography. Notice that by varying $k \in \mathbb{N}_0$, the whole physical domain $\xi > 0$ is covered: in this way, the analysis shows that supercritical and subcritical height profiles always exhibit opposite monotony properties.

Sign of $dy/d\xi$ and $d\zeta/d\xi$, Sinusoidal Bottom, $\gamma_b = 0$			
	$k\pi/k_b \leq \xi \leq (2k+1)\pi/k_b$	$(2k-1)\pi/kb < \xi < 2k\pi/k_b$	
		$y \leq y_{st,sin}(\xi)$	$y > y_{st,sin}(\xi)$
Sign of $dy/d\xi$ - Supercritical Flow	< 0	≤ 0	> 0
Sign of $dy/d\xi$ - Subcritical Flow	> 0	≥ 0	< 0
Sign of $d\zeta/d\xi$= $-ak_b \sin(k_b\xi)$	<0	>0	

$$H'(\xi) = -a\cos(k_b\xi)$$

is a spatial perturbation of the mean Stream Head.
In general, one has:

$$H'_- = -a + \overline{H}_{0,\gamma_b=0} \leq \tilde{H}(\xi) \leq a + \overline{H}_{0,\gamma_b=0} = H'_+ \tag{2.33}$$

This is helpful to understand the role of the amplitude a, the wavenumber k_b and the unit stream head boundary condition:

- H'_0 is a constant perturbation of the unitary stream head, which grows in absolute value with the amplitude $a > 0$, but whose sign depends on k_b and ξ_0 by means of the cosinus term: therefore, a variation of the sole wavenumber alters the dynamics, causing an increase or decrease of energy depending on the sign of $\cos(k_b\xi_0)$;
- $H'(\xi)$ depends instead also on the radial coordinate, thus varying with the position, but is 0 on average over a period $T = 2\pi/k_b$.

Therefore, net of the fluctuations, the mean strem head $H_{0,\gamma_b=0}$ is conserved.
In order to show the role of the amplitude in determining the maxima and minima of the height profiles, Fig. 2.14 reports a comparison between the solutions obtained with Stream Head $\tilde{H}(\xi)$, $H_{0,\gamma_b=0}$ and $H'_\pm = H_{0,\gamma_b=0} \pm a$. Again, it is taken into account a Divergent Flow along an Horizontal Bed with Sinusoidal Bottom of amplitude $a = 0.1$ and wavenumber $k_b = 5$, forced to attain unitary Stream Head at $\xi_0 = 12$.
On the contrary, convergent direction, unitary stream head boundary condition and amplitude are chosen for the height profiles reported in Fig. 2.15, where instead a variable wavenumber is considered in order to show its influence: in the examples provided, $k_b = 1,\ 5,\ 10$.
Similar profiles can be obtained also by changing amplitude a and radial position ξ_0 of the

unitary stream head condition: indeed, the mean features of the flow (i.e., net of spatial perturbation expressed by $H'(\xi)$ in terms of stream head) are determined by the combination of the three parameters enclosed in $H_{0,\gamma_b=0}$. What emerges by Fig. 2.15, is that larger mean stream head $H_{0,\gamma_b=0}$ are associated to lower minimum radii at which the flow reaches critical condition. This is not surprising, since the mean stream head is conserved and therefore, on average, the behaviour is similar to that described for the Horizontal Bed with Flat Bottom in Sec. 2.2.3 [4] and reported by [29]: for radii smaller than the mimimum radius (at which critical condition is attained), Radiant Specific Discharge would increase so much that the only possibility to conserve flow rate is to decrease the mean Stream Head (which therefore is not conserved) and, conversely, the only possibility to conserve mean stream head $H_{0,\gamma_b=0}$ (mean total energy) is to reduce the flow rate (which therefore is not conserved): thus, in order to conserve both the flow rate and the mean stream head, the minimum radius behaviour arises. The larger $H_{0,\gamma_b=0}$, the larger the possible heights and velocities that can be attained by the flow, the larger the maximum radiant specific discharge, the smaller the position of the minimum radius.

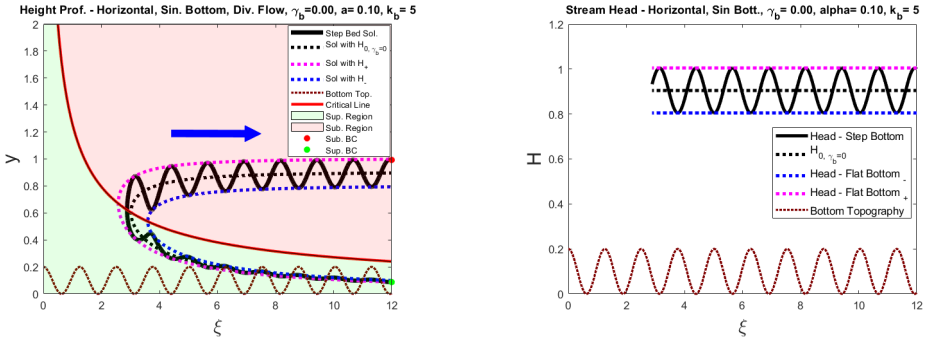

(a) (b)

Figure 2.14: **Comparison between solution with different stream heads - Horizontal Bed, Sinusoidal Bottom,** $a = 0.1$**,** $k_b = 5$**,** $\gamma_b = 0$**.** Fig. 2.14(a) reports height profiles, while 2.14(b) reports the corresponding Stream Head profiles. Solid lines refer to Height profiles for a divergent flow along an horizontal bed with sinusoidal bottom, the fluid emerging in critical condition at $\xi = 2.88$ (unitary stream head is imposed at $\xi_0 = 12$). Black dotted lines refer to the mean Stream Head $H_{0,\gamma_b=0}$ and the corresponding solution; blue and magenta dotted lines refer respectively to H'_- and H'_+ defined in 2.33 (and the corresponding solutions). It can be noticed in this way how the amplitude influences the local minima/maxima of the height profiles.

[4] **Recall:** Horizontal Bed with Flat Bottom Described in Sec. 2.2.3 is obtained for $\gamma_b = 0$ and $\zeta(\xi) \equiv 0$.

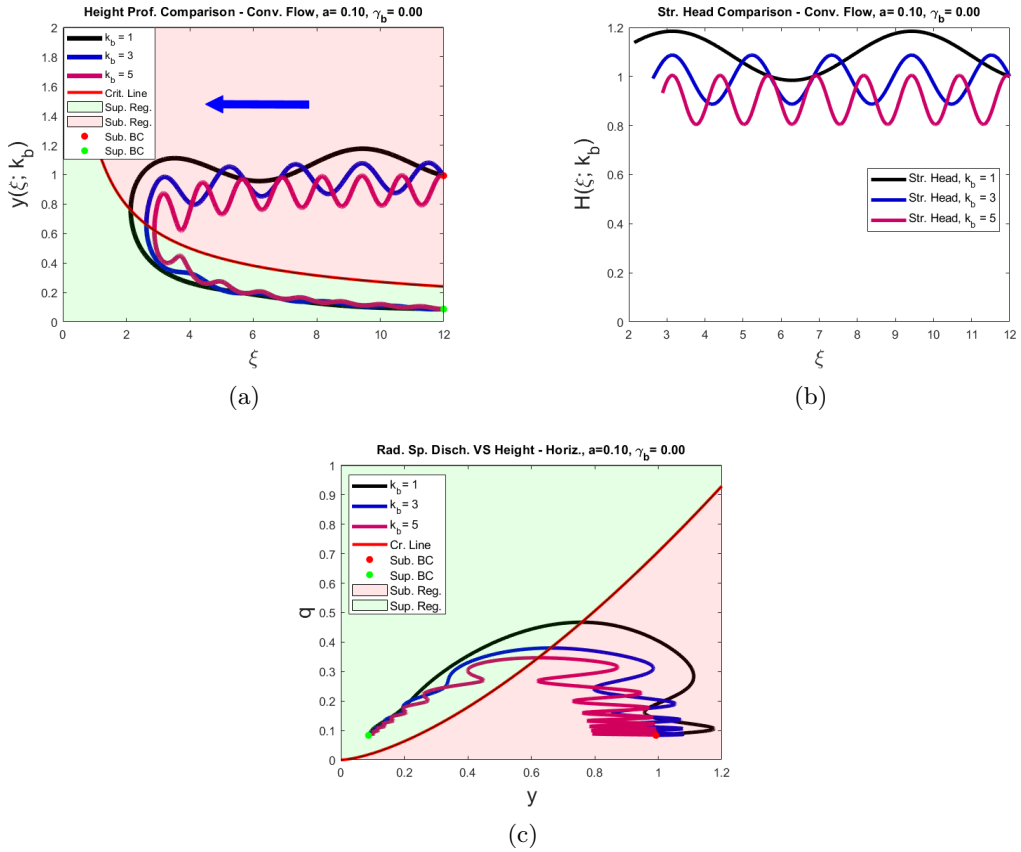

Figure 2.15: **Comparison between solutions for different wavenumbers - Horizontal Bed, Sinusoidal Bottom,** $a = 0.1$ $\gamma_b = 0$**.** Fig. 2.15(a) reports height profiles for $k_b = 1, 3, 5$. Fig. 2.15(b) reports the corresponding Stream Head profiles and Fig. 2.15(c) the corresponding relations between Height Radiant Specific Discharge. Flow is divergent along an horizontal bed with sinusoidal bottom, the fluid emerges in critical condition (unitary stream head is imposed at $\xi_0 = 12$ for all of the three profiles). Because of the different wavenumber, flows attain critical conditions at different minimum radii.

Introduction of Basal Slope $\gamma_b \neq 0$ and Stream Head Split

When a basal slope γ_b is included, solutions are described by Eq. 2.4, which in case of a sinusoidal bottom assumes the form:

$$\frac{1}{\xi^2 y^2} + y = 1 + \gamma_b(\xi - \xi_0) - a\cos(k_b\xi) + a\cos(k_b\xi_0) \tag{2.34}$$

Such equation describes a linear stream head of slope γ_b with a fluctuation expressed by the sinusoidal term, i.e.:

$$\tilde{H}(\xi) = H_{0,BC} + H_{0,\gamma_b}(\xi) + H'(\xi) \tag{2.35}$$

where:

$$H_{0,BC} := 1 + a\cos(k_b\xi_0) - \gamma_b\xi_0 \tag{2.36}$$

is the contribute to Stream Head due to boundary condition,

$$H_{\gamma_b}(\xi) := \gamma_b\xi \tag{2.37}$$

is the energy contribute due to the basal slope γ_b, giving positive or negative slope to Stream Head if respectively γ_b is positive or negative.
Finally,

$$H'(\xi) := -a\cos(k_b\xi) \tag{2.38}$$

represents the fluctuation due to the energy contribute of the sinusoidal bottom.
It can then be defined the mean Stream Head (i.e., the stream head net to the sinusoidal fluctuation $H'(\xi)$) similarly to the case of Horizontal Bed with Sinusoidal Bottom:

$$H_{0,\gamma_b}(\xi) := H_{0,BC} + H_{\gamma_b}(\xi) = 1 + a\cos(k_b\xi_0) + \gamma_b(\xi - \xi_0) \tag{2.39}$$

Therefore, the following split of the Stream Head $\tilde{H}(\xi)$ holds:

$$\tilde{H}(\xi) = H_{0,BC} + H_{\gamma_b}(\xi) + H'(\xi) = H_{0,\gamma_b} + H'(\xi) \tag{2.40}$$

Notice that $H_{0,\gamma_b}(\xi)$ is associated to the following Equation:

$$\frac{1}{x^2 + y^2} + y = 1 + a\cos(k_b\xi_0) + \gamma_b(\xi - \xi_0) \tag{2.41}$$

which is of the same form of Eq. 2.6, with boundary stream Head:

$$1 + a\cos(k_b\xi_0)$$

instead of 1. Therefore, the behaviour of the mean solution, i.e., the solution net of the perturbation $H'(\xi)$ which satisfies Eq. 2.41, is the same of the cases of Inclined (Cone or Funnel) Bed with Flat Bottom described in Sec. 2.2, as expected.
The behaviour of the Stream Head $\tilde{H}(\xi)$ and, particularly, of the mean Stream Head has implications in the solutions that will be discussed within the next two subsections.

Cone shaped Bed with Sinusoidal Bottom, $\gamma_b > 0$

Similarly to the case of Cone shaped Bed with Flat or Step bottom, the orbits are open and characterized by a subcritical and a supercritical branch, while critical condition is attained at a minimum radius, as reported in Fig. 2.12(b). Each branch, as for the previous cases, represents two possible solutions depending on the direction (convergent or divergent):

- in case of convergent direction, stream flows on opposite basal slope γ_b attaining unitary stream head at $\xi = \xi_0$ and until reaching a critical hole, thus the mean stream head $H_{0,\gamma_b}(\xi)$ decreases;
- in case of divergent direction, stream emerges from a critical source and flows on favourable basal slope, attaining again unitary stream head at $\xi = \xi_0$, thus $H_{0,\gamma_b}(\xi)$ grows indefinitely.

Fig. 2.16 reports the stream profiles and features for both convergent and divergent direction: there, $\gamma_b = 0.10$, $a = 0.10$ and $k_b = 5$, while unitary stream head is enforced at $\xi_0 = 12$. As already observed for the case of Horizontal Bed with Sinusoidal Bottom, subcritical height profiles exhibit an offset with respect to supercritical ones and to the bottom topography.
Moreover, while the supercritical profiles exhibit the already seen damped undulatory behaviour, the subcritical profiles amplifies the effects of the amplitude of bottom topography, due to interplay between the energy contribute of basal slope and bottom slope. This is particularly evident in Fig. 2.16(c), where the stream Head is reported for the diverging case (thus, the stream flows on favourable slope):

- the sinusoidal fluctuations given by the bottom topography, expressed by contribute $H'(\xi)$ to the Stream Head, help or hamper the flow in terms of potential energy depending on whether the bottom topography is felt as ascending or descending by the flow direction;
- however, the favourable basal slope $\gamma_b > 0$, expressed by the contribute $H_{\gamma_b}(\xi)$, helps the flow in terms of potential energy, reducing the decrease and amplifying the increase of the Stream Head $\tilde{H}(\xi)$ due to the fluctuation $H'(\xi)$.

The interplay between the two potential energy contributes is mathematically described by:

$$H_{\gamma_b}(\xi) + H'(\xi) = \gamma_b \xi - a\cos(k_b \xi)$$

The interaction with the kinetic energy, expressed by the kinetic height in Fig. 2.16(c), gives rise to the height behaviours described for the supercritical and subcritical profiles (divergent case):

- for the subcritical profile, velocity tends to decrease as ξ increases and so the kinetic height does, thus height tends to increase with progressively larger amplitude in order to maintain the increasing oscillations of the Stream Head $\tilde{H}(\xi)$;

- for the supercritical profile, velocity tends to increase as ξ increases and so the kinetic height does, thus height tends to decrease with progressively damping amplitude in order not to exceed the increasing oscillations of the Stream Head $\tilde{H}(\xi)$.

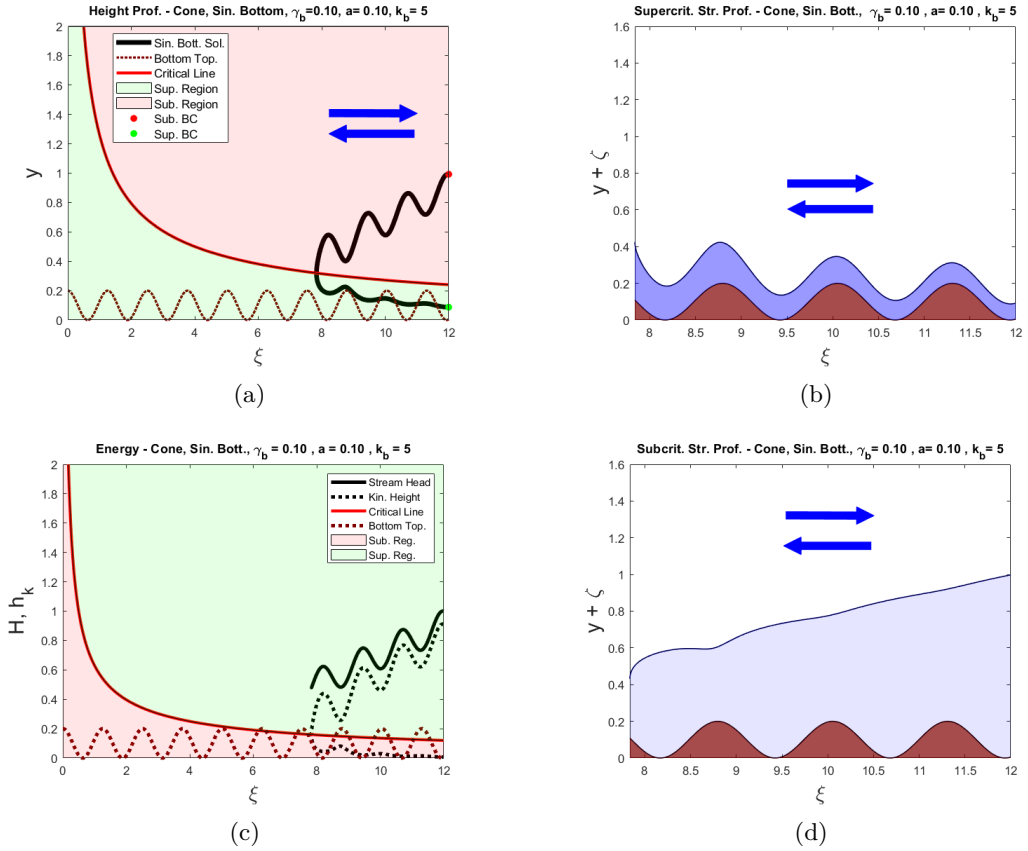

Figure 2.16: **Flow along a Cone shaped bed with Sinusoidal Bottom,** $\gamma_b = 0.10$**,** $a = 0.10$**,** $k_b = 5$**.** Unitary Stream Head is imposed at $\xi_0 = 12$. Fig. 2.16(a) - Subcritical and Supercritical height profiles. Figures 2.16(b), 2.16(d) - Supercritical and Subcritical stream profiles (blue colored areas), along with bottom topography (brown colored area). Fig. 2.16(c) - Stream Head along with supercritical and subcritical branches of Kinetic Height. Double blue arrows indicates that Stream and Height profiles can be interpreted in both convergent and divergent direction, as well as the branches of the Kinetic Height and the Stream Head in Fig. 2.16(c) (although arrows are not depicted in this figure).

Funnel shaped Bed with Sinusoidal Bottom, $\gamma_b < 0$

Also for the case of Funnel Shaped Bed with Sinusoidal Bottom, solutions can be obtained by solving Eq. 2.34, which now represents a linear stream Head of negative slope γ_b with a fluctuation induced by the sinusoidal bottom topography, again expressed by the cosinus term of the aforementioned Equation.

As for the cases of Funnel bed with flat or step bottom, orbits obtained for $\gamma_b < 0$ are closed, therefore both supercritical and subcritical profiles are characterized by a "Two horizons" behaviour, with a minimum and a maximum radius. Again, each branch can represent two solutions depending on the flow direction (convergent or divergent). In particular, using the same notation introduced in 2.36, 2.37, 2.38 and 2.39 (which leads to the splitting of the Stream Head 2.40) four main physical situation can be described:

- a stream flowing on favourable basal slope along convergent direction, starting from an external annular source located at $\xi = \xi_0$ (where the Stream Head is enforced to be unitary) until reaching a central hole where the fluid is drained (Fig. 2.17);
- a stream flowing on opposite basal slope along divergent direction, starting from an internal annular source located at $\xi = \xi_0$ (where the Stream Head is enforced to be unitary) until reaching an external hole where the fluid is drained (Fig. 2.17);
- a stream flowing on favourable basal slope along convergent direction which emerges from a critical source placed at a maximum radius $\xi = \xi_{max}$, attains unitary Stream Head at $\xi = \xi_0$ and enters a critical hole at minimum radius placed at $\xi = \xi_{min}$;
- a stream flowing on opposite slope along divergent direction which emerges at a critical source placed at minimum radius $\xi = \xi_{min}$, attains unitary stream head at $\xi = \xi_0$ and enters a critical hole at maximum radius $\xi = \xi_{max}$.

It is not surprising that, net of the fluctuations, the overall behaviour is non monotonical: this is indeed due to the mean Stream Head $H_{0,\gamma_b}(\xi)$, which thanks to Eq. 2.41 and negative γ_b gives rise to a mean solution with analogous behaviour to the case of Funnel-shaped Bed with Flat Bottom in Section 2.2, including the presence of two Froude Horizons.
What is interesting is the behaviour of the height profiles, which is well depicted for the case of Two-Horizons stream reported in Fig. **??** (but can be recovered also for the Convergent and Divergent case in Fig. 2.17. Indeed, the subcritical profile behaves as follows:

- in a neighbourhood of the left horizon (i.e., nearby the minimum radius), abruptly decreases as it approaches critical condition, appearing almost not influenced by the sinusoidal bottom;
- within the left and right horizons, after reaching the absolute maximum, amplitude constantly decreases;
- nearby the right horizon, amplitude decreases more rapidly towards critical height.

Regarding the supercritical profile, instead:

- in a neighbourhood of the left horizon (i.e., nearby the minimum radius), abruptly increases as it approaches critical condition, appearing almost not influenced by the sinusoidal bottom;
- within the left and right horizons, the effect of bottom topography appears rapidly damped until the profile reaches its absolute minimum; from this point, amplitude increases until reaching the right horizon, where the increase is more abrupt.

The damping or amplifying response of the height profile to the sinusoidal bed topography has an interesting connection with the behaviour of Radiant Specific Kinetic Height and will be discussed into the next Section.

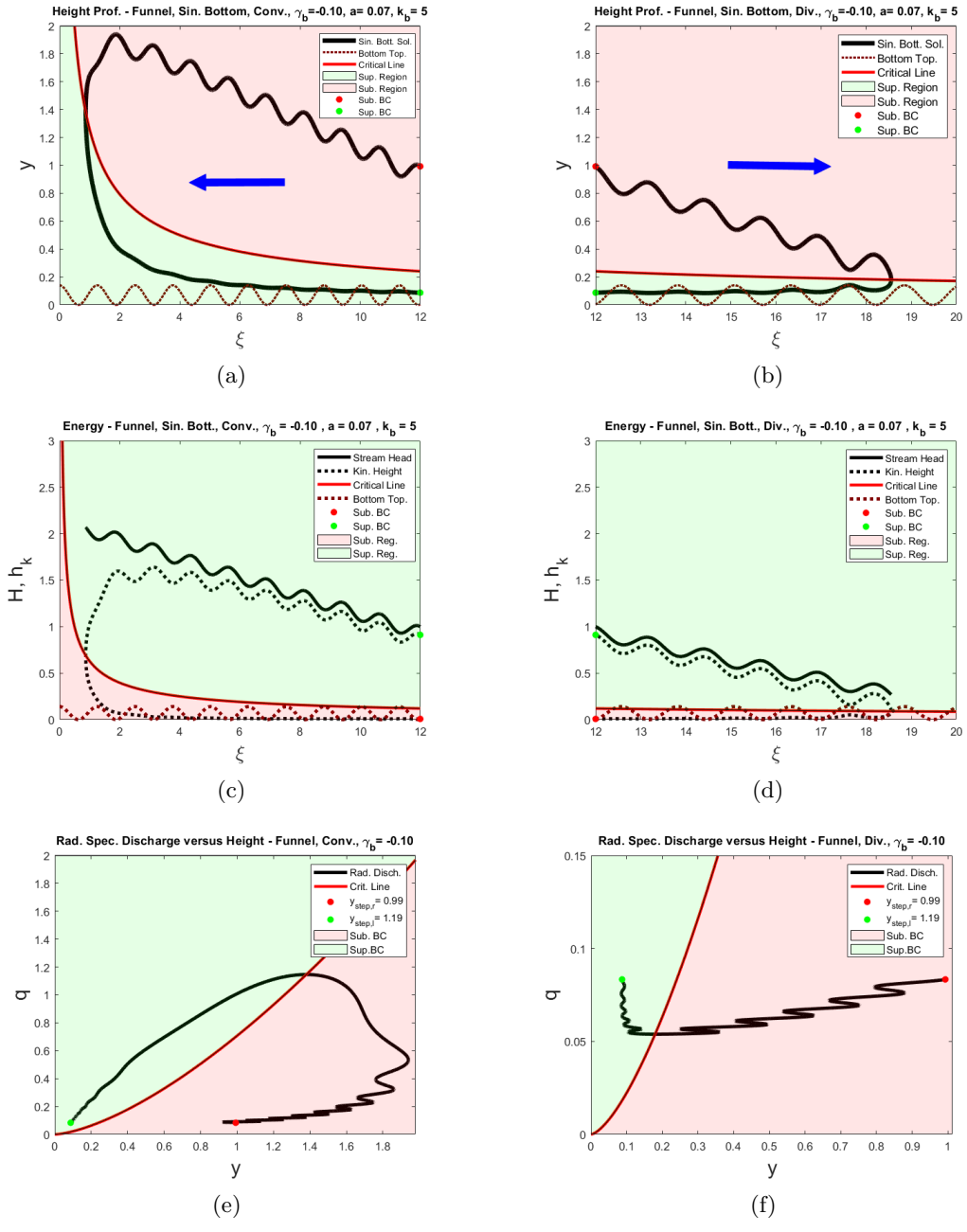

Figure 2.17: **Flow along a Funnel shaped bed with Sinusoidal Bottom, Convergent and Divergent directions,** $\gamma_b = 0.10$**,** $a = 0.10$**,** $k_b = 5$**.** Unitary Stream Head is imposed at $\xi_0 = 12$. Left panel and right panel respectively refer to Convergent and Divergent Flow, as indicated by the blue arrows. First row (Figures 2.17(a), 2.17(b)) report height profiles. Second row (Figures 2.17(c), 2.17(d)) report Stream Head, along with Kinetic Height. Third row (Figures 2.17(e), 2.17(f)) report Radiant Specific Discharge.

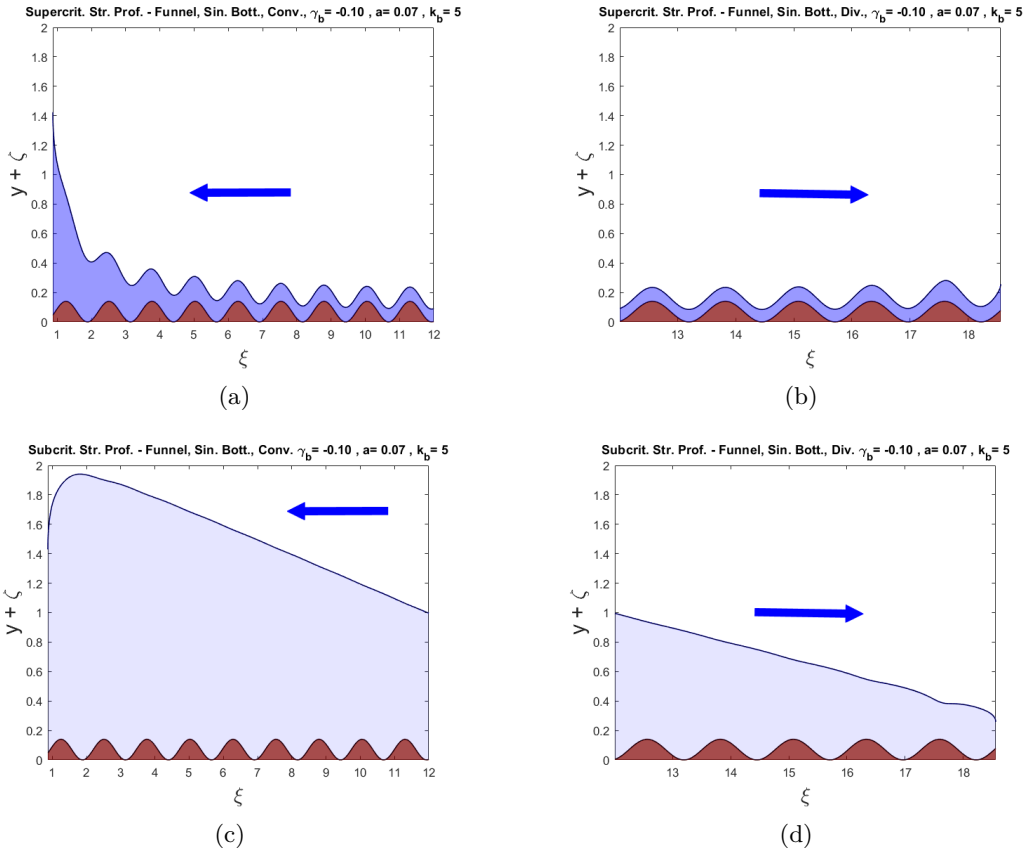

Figure 2.18: **Flow along a Funnel shaped bed with Sinusoidal Bottom, Convergent and Divergent directions,** $\gamma_b = 0.10$**,** $a = 0.10$**,** $k_b = 5$**.** Unitary Stream Head is imposed at $\xi_0 = 12$. Left panel and right panel respectively refer to Convergent and Divergent Flow, as indicated by the blue arrows. First row (Figures 2.18(a), 2.18(b)) report Supercritical Stream Profiles. Second row (Figures 2.18(c), 2.18(d)) report instead Subcritical Stream Profiles.

2.3.2 Velocity - Gravity Interplay and Flow Response to Sinusoidal Bed Topography

The Stream Profiles obtained in Sec. 2.3.1 have a different response to the Sinusoidal Bottom Topography, which from a qualitative point of view appears to vary with the sign of bottom slope γ_b and the regime (supercritical or subcritical).
Results are summarized in Table 2.3 and graphically displayed in Fig. 2.19. As can be observed, the profiles of Radiant Specific Kinetic Height $k_s(\xi)$ appear very similar to those obtained with Flat Bottom, except for the presence of the sinusoidal perturbation and the

reason comes from a re-organization of the governing Profile Equation 1.29 [5] similar to that operated to obtain Eq. 2.30:

$$\frac{dy}{d\xi} = \frac{\gamma_b + ak_b \sin(k_b\xi) + \frac{2}{\xi^3 y^2}}{1 - \frac{2}{\xi^2 y^3}} = \frac{\gamma_b + ak_b \sin(k_b\xi) + \frac{2}{\xi^3 y^2}}{1 - Fr^2(\xi, y)} \tag{2.42}$$

It is straightforward to conclude that the denominator of Eq. 2.42 is positive or negative if the flow is, respectively, subcritical or supercritical (and 0 at critical conditions). The study of the sign of its nominator, instead, leads to the following Inequality:

$$k_s(\xi, y) = \frac{2}{\xi^3 y^2} \geq -\gamma_b - ak_b \sin(k_b\xi) \tag{2.43}$$

Notice that the right hand side of 2.43, as displayed in Fig. 2.19, describes nothing but a sinusoidal oscillating around the basal opposite slope $-\gamma_b$ with amplitude ak_b.
Ineq. 2.43 not only provides the monotony variations of the height profiles, but similarly to what discussed in Sec. 2.2.5 encloses the interplay between velocity (Kinetic Energy) and gravity (Potential Energy), whose contribute in terms of slope can be found at the right hand side: where Ineq. 2.43 is satisfied, kinetic contribute overbalances the gravitational one and vice versa.
The behaviour of the Height profiles obtained appears intimately connected with that of the corresponding $k_s(\xi, y(\xi))$ (see Fig. 2.19):

- for couples $(\xi, y(\xi))$ satisfying Ineq. 2.43, i.e., where kinetic contribute overbalances that of gravity, the amplitudes of subcritical profiles grow (linearly or, for the Horizontal Bed, until a stabilization), while supercritical profiles dampen;
- for couples $(\xi, y(\xi))$ not satisfying Ineq. 2.43, i.e., where the kinetic contribute is overbalanced by that of gravity, the amplitudes of subcritical profiles dampen, while those of the supercritical profiles grow.

It is interesting to notice that the transition from damping to amplifying regime (or vice versa) which is observed for supercritical and subcritical height profiles with $\gamma_b < 0$ takes place only and exactly at, respectively, their absolute minimum and absolute maximum (there, Ineq. 2.43 reduces to the corresponding equality): therefore, the sinusoidal perturbation at the right hand side of Ineq. 2.43 influences the location of the absolute minimum and maximum, however the distinction between the two regimes remains perfectly dichotomous (instead of having, for example, an alternation of zones with amplification or damping as expected by the graphical solution of Ineq. 2.43 evident by the graphs of $k_s(\xi, y(\xi))$ in Fig. 2.19).)
Such transition does not happen for supercritical and subcritical height profiles with $\gamma_b \geq 0$ where, although Ineq. 2.43 shows that there exists multiple zones where gravity contribute

[5] Considering $\alpha = 0$ and $\zeta'(\xi) = -ak_b \sin(k_b\xi)$ due to the absence of of bottom friction and the Sinusoidal Bottom Topography.

overbalances the kinetic one, both subcritical and supercritical brances of $k_s(\xi, y(\xi)$ overcome the opposite basal slope.
What just discussed suggests that the damping and amplifying behaviour depends mostly on γ_b, independently from the characteristics of the sinusoidal perturbation which only affect the position of the absolute minimum and maximum for $\gamma_b < 0$.

Table 2.3: **Amplitude response of Flow to Sinusoidal Bottom Topography**. Here, "AMP", "DAMP" and "STAB" stand respectively for "AMPLIFYING", "DAMPING", "STABILIZING". The notation "Min/Max" has to be interpreted as "Minimum" for the Supercritical Flow and "Maximum" for the Subcritical Flow. The Table must be read in the divergent flow direction (increasing ξ): for the convergent one, it suffices to invert "DAMP" with "AMP" and "Before" with "After".

	$\gamma_b > 0$	$\gamma_b = 0$	$\gamma_b < 0$	
			Before Abs. Min/Max	**After Abs. Min/Max**
Supercritical	DAMP	DAMP	DAMP	AMP
Subcritical	AMP	AMP $\rightarrow$ STAB	AMP	DAMP

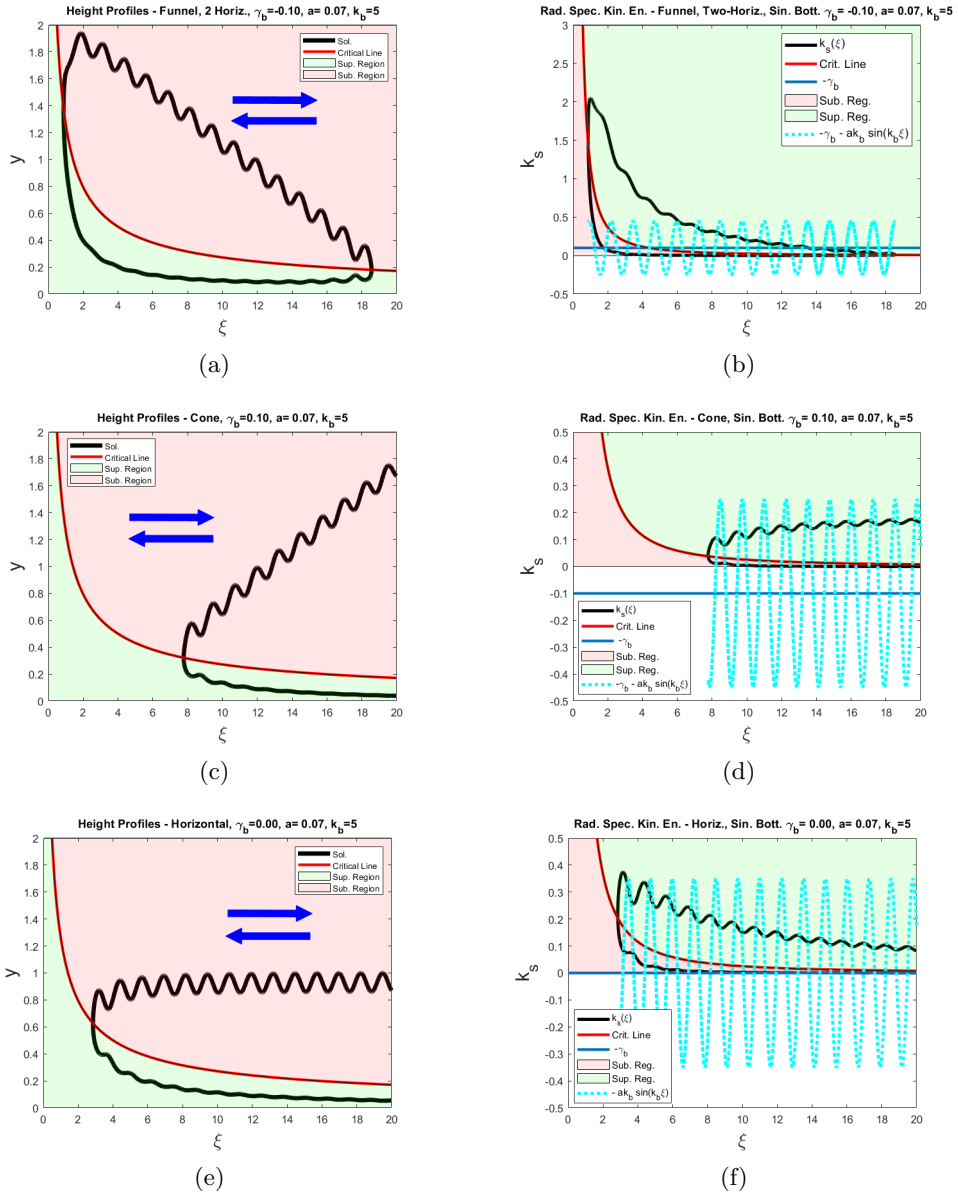

Figure 2.19: **Radiant Specific Kinetic Height and Amplitude Response of Stream Profiles to Sinusoidal Bottom Topography.** Left column (Figures 2.19(a), 2.19(c), 2.19(e)) reports Height profiles for respectively (from top to bottom) $\gamma_b = -0.10$,$\gamma_b = 0.10$,$\gamma_b = 0$, while right column report the corresponding profiles of Radiant Specific Kinetic Height. For all the profiles, unitary stream Head condition is imposed at $\xi_0 = 12$.

2.4 Case 3 - Inclined Bed with Step Bottom

In order to obtain a simple model for the presence of a step along the bed, let consider the following irregularity profile:

$$\zeta(\xi) = h_s \tanh[\sigma_s(\xi - \xi_s)] + h_s \tag{2.44}$$

where $h_s > 0$ controls the step height (which is given by $h_{step} = 2h_s$) [6], $|\sigma_s|$ controls the steepness of the step and $\mathrm{sgn}(\sigma_s)$ controls the direction of the step (increasing or decreasing): this is shown in Fig. 2.20. This kind of function, which is $C^\infty(\mathbb{R})$, represents a suitable choice to represent the step geometry without loosing regularity, since its derivative

$$\zeta'(\xi) = h_s\sigma_s \,\mathrm{sech}^2[\sigma_s(\xi - \xi_s)] \tag{2.45}$$

is almost 0 everywhere except for a straight interval around the maximum, which is $h_s\sigma_s$ and is attained at $\xi = \xi_s$ [7]. For this purpose, $|\sigma_s|$ will be considered as a prescribed, sufficiently large number and Eq. 2.4 now depends on:

- basal slope γ_b;
- step height h_s;
- steepness sign $\mathrm{sgn}(\sigma_s)$.

The aim of this section, in particular, is to investigate the energetic role of the step topography. It is worth to notice, however, that the presence of a sort of discontinuity at the step, although the regularity of the bottom topography, can lead to solution violating the hypothesis of gradually varied flow. In order to limit such violation only in the step region, the parameter h_s is chosen in such a way it is sufficiently small compared to the unitary stream head. Typical values will be in the range $[0.01, 0.2[$.

---

[6] Translation by h_s makes the codomain of the profile described by 2.44 be $[0,2h_s]$ instead of $[-h_s, h_s]$. In this way, the bed profile is completely included within the domain of interest, i.e., $D = \{(\xi, y) : \xi > 0, y > 0\}$

[7] It can be proved (Ref. [13]) that, if $\{\sigma_n\}_{n=1}^{\infty}$ is a strictly increasing sequence in absolute value, then

$$\lim_{n\to+\infty} h_s\sigma_n \,\mathrm{sech}^2[\sigma_n(\xi - \xi_s)] = \delta(\xi_s)$$

in the sense of distributional convergence, therefore such a bed profile well approximates the presence of a step for sufficiently large values of σ.

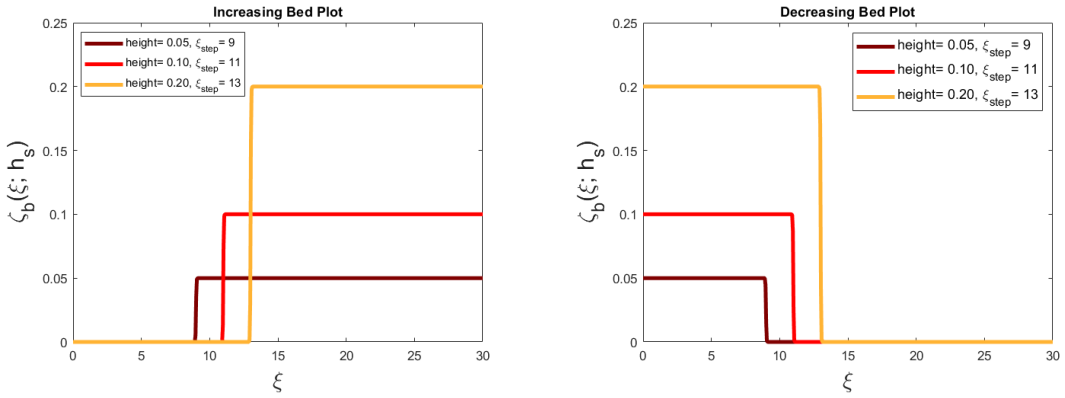

(a) (b)

Figure 2.20: **Step Bed configurations.** For both panels, same step heights are used, as long as for the value $|\sigma_s| = 100$. The only difference is given by $\text{sgn}(\sigma_s)$, which is 1 for the increasing step (left) and -1 for the decreasing step (right).

2.4.1 Numerical Simulations

Orbits described by Eq. 2.4, with the bottom topography $\zeta(\xi) = h_s tanh(\sigma_s[\xi - \xi_0)]$, exhibit a similar behaviour to those of the inclined bed with flat bottom: they are open with a minimum radius for $\gamma_b \geq 0$, closed for $\gamma_b < 0$. However, the presence of the step reflects on both profiles, particularly the subcritical one. This is evident in Fig. 2.21, where orbits are obtained by imposing unitary stream head at $\xi_0 = 8$ and considering a decreasing step located at $\xi_s = 9$, with height $h_s = 0.1$. The reason of this behaviour will be clear within the next subsections, were specific solutions will be illustrated.

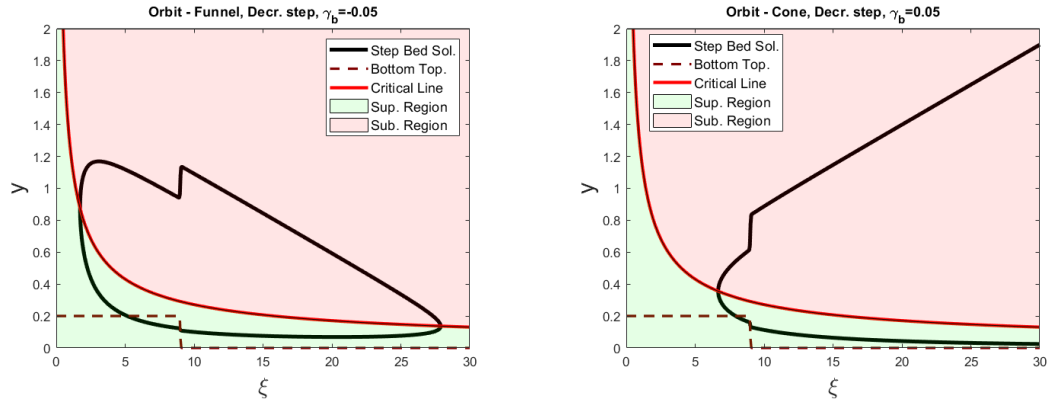

(a) (b)

Figure 2.21: **Orbits for Inclined Bed with Step Bottom.** Left and right figure respectively refer to $\gamma_b = -0.05$, $\gamma_b = 0.05$. For both cases, decreasing step of the bottom is located at $\xi_s = 12$ and unitary Stream Head is imposed at $\xi_0 = 12$.

Convergent Flow over Funnel-shaped Bed with Step Bottom - $\gamma_b < 0$

Fig. 2.22 reports the main features of a convergent flow down a cone-like bed with step bottom, increasing or decreasing depending on $\text{sgn}(\sigma_s)$ as described earlier. Stream flows in convergent direction, on favourable step, starting with unitary stream head at $\xi_0 = 12$, then faces a step at $\xi_s = 9$ and finally reaches a hole in critical condition. In case of **increasing step**, i.e., $\text{sgn}(\sigma_s) = 1$, the subcritical height experiments an abrupt increase, while supercritical heights slightly reduces. This behaviour is the consequence of the combination of two factors: the step, which is "felt" as descending by the flow, increases the stream energy (as shown by the stream head in Fig. 2.22(c)), while the Radian Discharge remains constant across the step (see Fig. 2.22(e)). A perfectly opposite behaviour is shown instead if, maintaining all the other features, one considers **decreasing step** ($\text{sgn}(\sigma_s) = -1$): indeed, the step is "felt" as ascending by the flow, causing an energy decrease. The stream profiles obtained, showing water surface, are shown in Fig. 2.23.

Divergent Flow over Funnel-shaped Bed with Step Bottom - $\gamma_b < 0$

Fig. 2.24 reports the main features of a divergent flow over a funnel bed with step bottom: the flow starts with unitary stream head at $\xi_0 = 5$, then faces a step and ends up in critical condition, represented by a hole. Also divergent flow is affected by the presence of the step, for the same reasons (variation of the energy and conservation of radian discharge) described for the convergent flow. The only changes are due to the direction of the flow, which now is dissipating. The effect of the increasing step will be to enlarge dissipation, since will be felt by the flow as ascending while, on the contrary, to reduce dissipation if decreasing. The corresponding stream profiles are shown in Fig. 2.25.

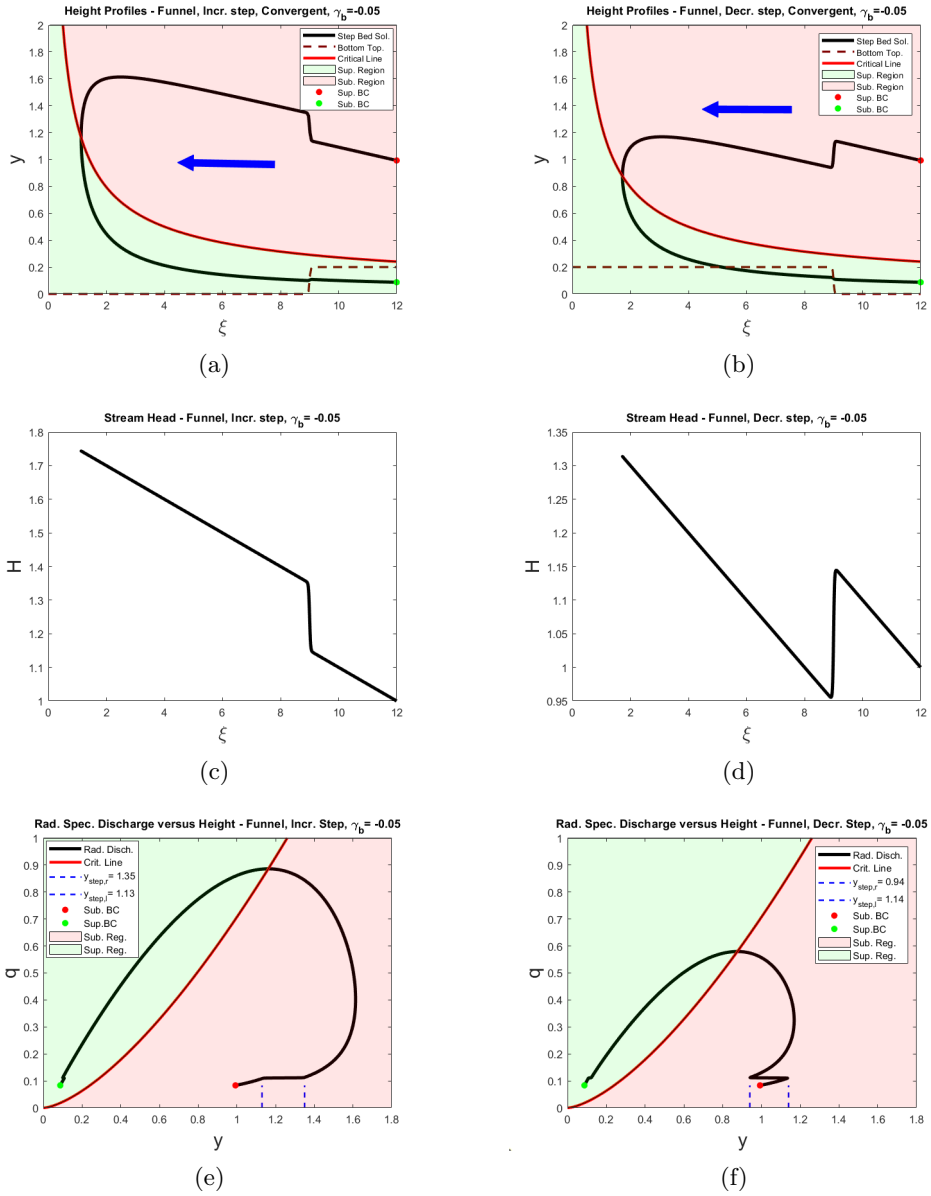

Figure 2.22: **Convergent stream flowing on favourable slope over a funnel-shaped bed with step bottom, $\gamma_b = -0.05$.** Left panel refers to an increasing step, while right panel refers to a decreasing one. Blue arrow, as usual, indicates flow direction.

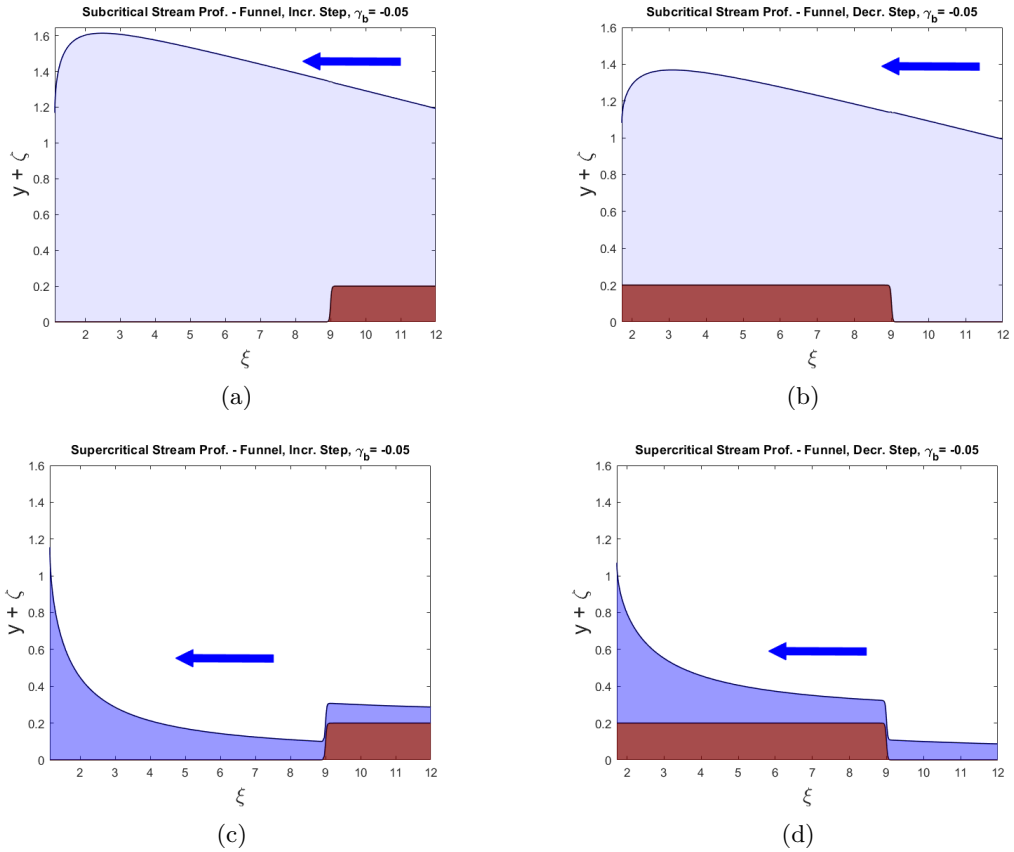

Figure 2.23: **Convergent stream flowing on favourable slope over a funnel-shaped bed with step bottom - Stream Profiles and Free Surface,** $\gamma_b = -0.05$**.** Left column refers to an increasing step, right column to a decreasing one.

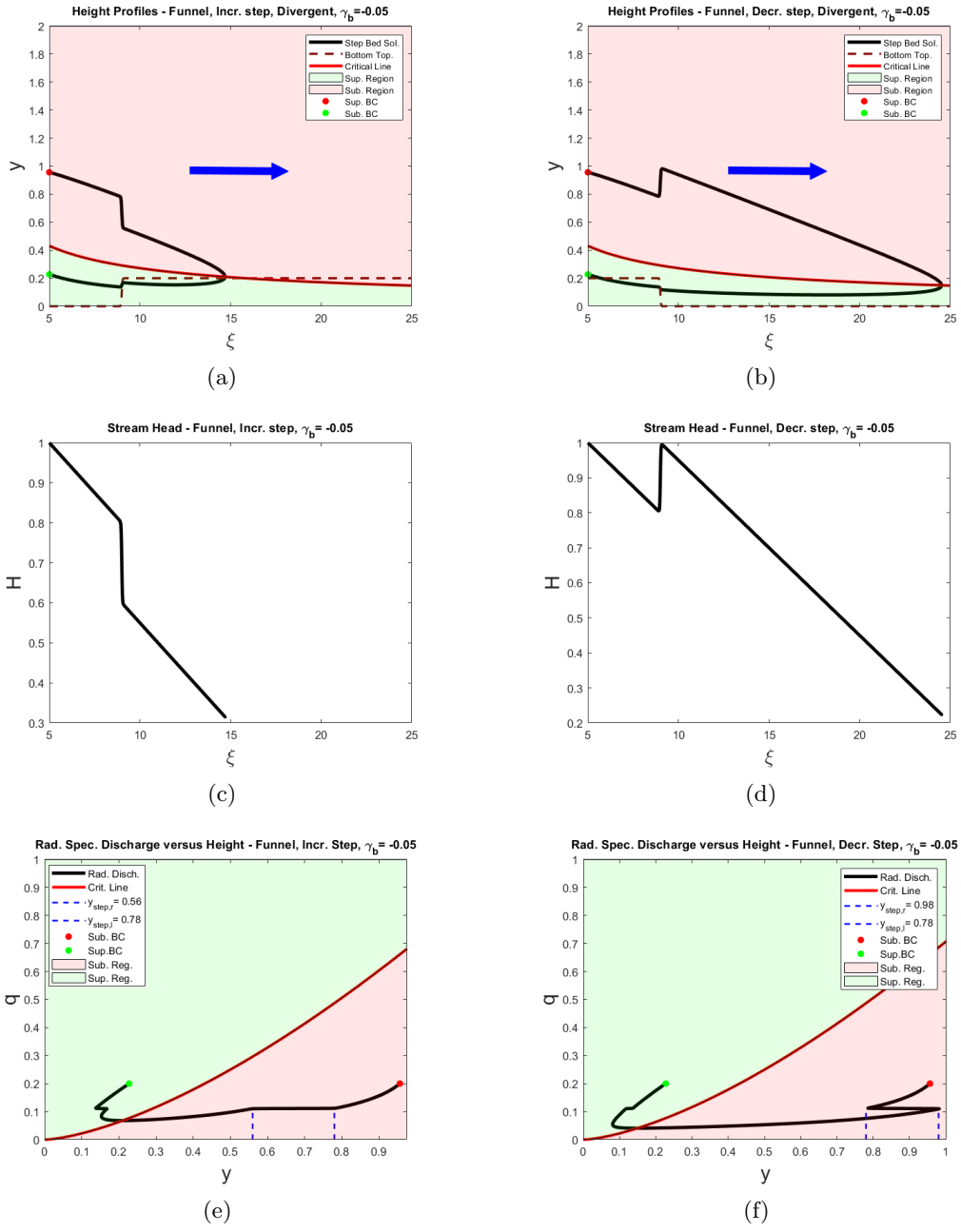

Figure 2.24: **Divergent stream flowing on opposite slope over a funnel-shaped bed with step bottom,** $\gamma_b = -0.05$**.** Left panel refers to an increasing step, while right panel refers to a decreasing one. Blue arrow, as usual, indicates flow direction.

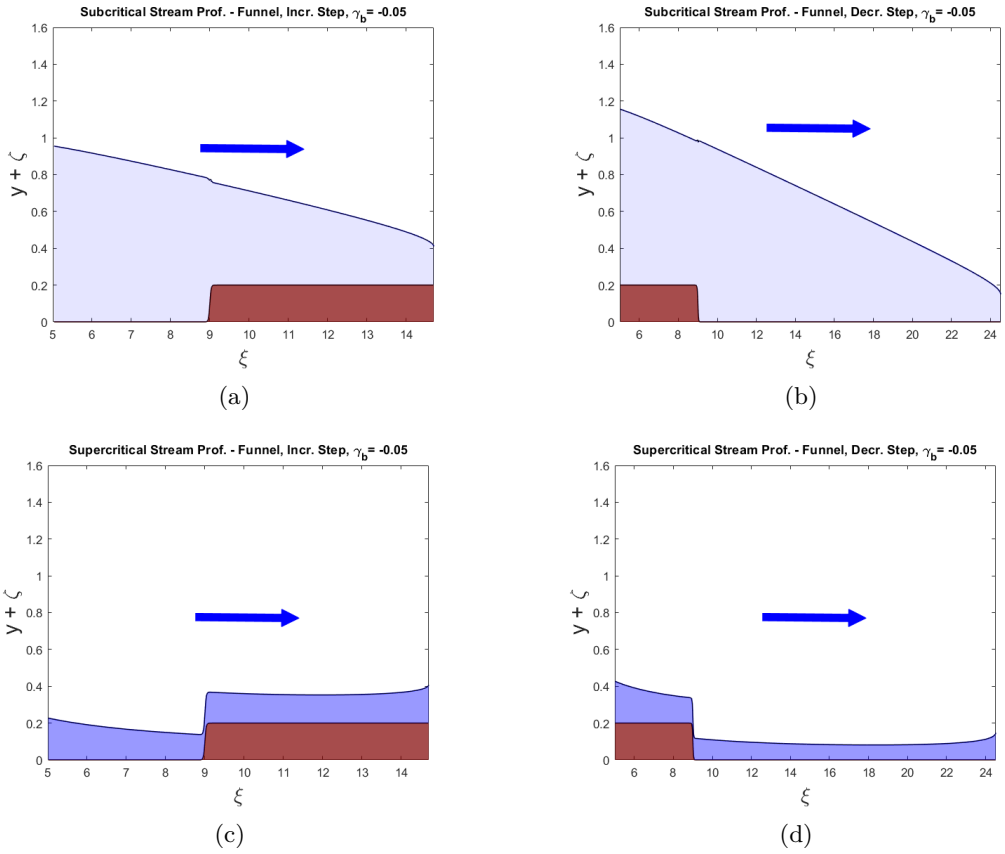

Figure 2.25: **Divergent stream flowing on opposite slope over a funnel-shaped bed with step bottom - Stream Profiles and Free Surface,** $\gamma_b = -0.05$**.** Left column refers to an increasing step, right column to a decreasing one.

Flow over a Cone-shaped Bed with Step Bottom, $\gamma_b > 0$

As described before, orbits are open for $\gamma_b > 0$, with the supercritical branch approaching to 0 and the supercritical branch growing indefinitely as ξ increases. Therefore, analogously to the cone-shaped bed with flat bottom, two possible solutions can be represented by each branch, depending on the convergent or divergent direction:

- stream starting from a source in critical condition and flowing on favourable slope along divergent direction in subcritical (supercritical) conditions, with the heights increasing (approaching 0) as ξ grows;
- stream starts with unitary stream head and flows on opposite slope along convergent direction in subcritical (supercritical) conditions, decreasing (increasing) to reach critical conditions at the edge of a hole, located at a minimum radius.

The main features of such flows are described in Fig. 2.26, while the stream profiles are reported in Fig. 2.27. As expected, the role of the step is the same as before: it increases

or decreases energy depending on the direction at which is felt by the flow (ascending or descending).

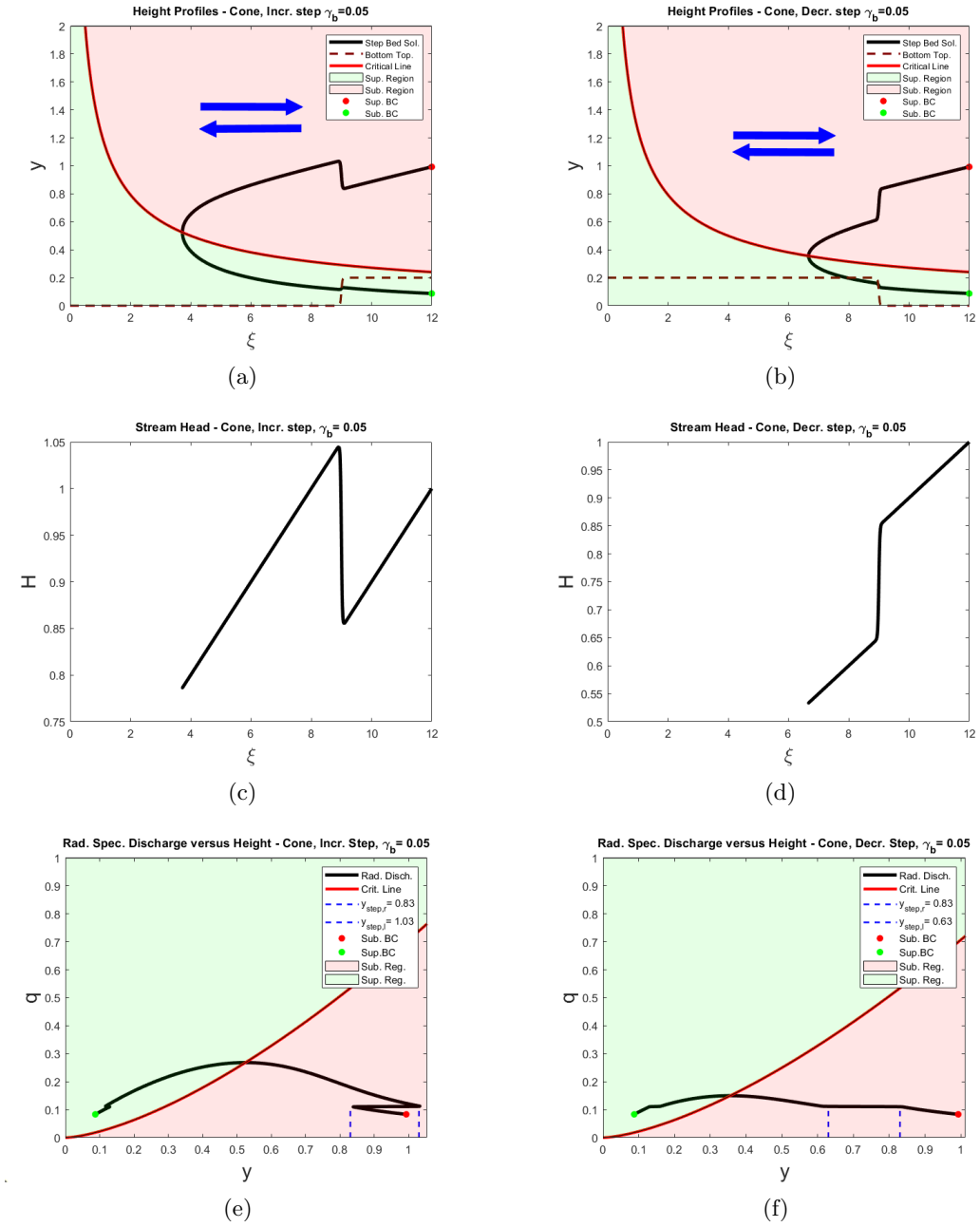

Figure 2.26: **Stream flowing on over a Cone-shaped bed with step bottom,** $\gamma_b = 0.05$**.** Left column refers to an increasing step, while right panel refers to a decreasing one. Double blue arrows, indicates that each branch can represent flows on both converging and diverging direction. Boundary Conditions placed are to be intended for the converging flow

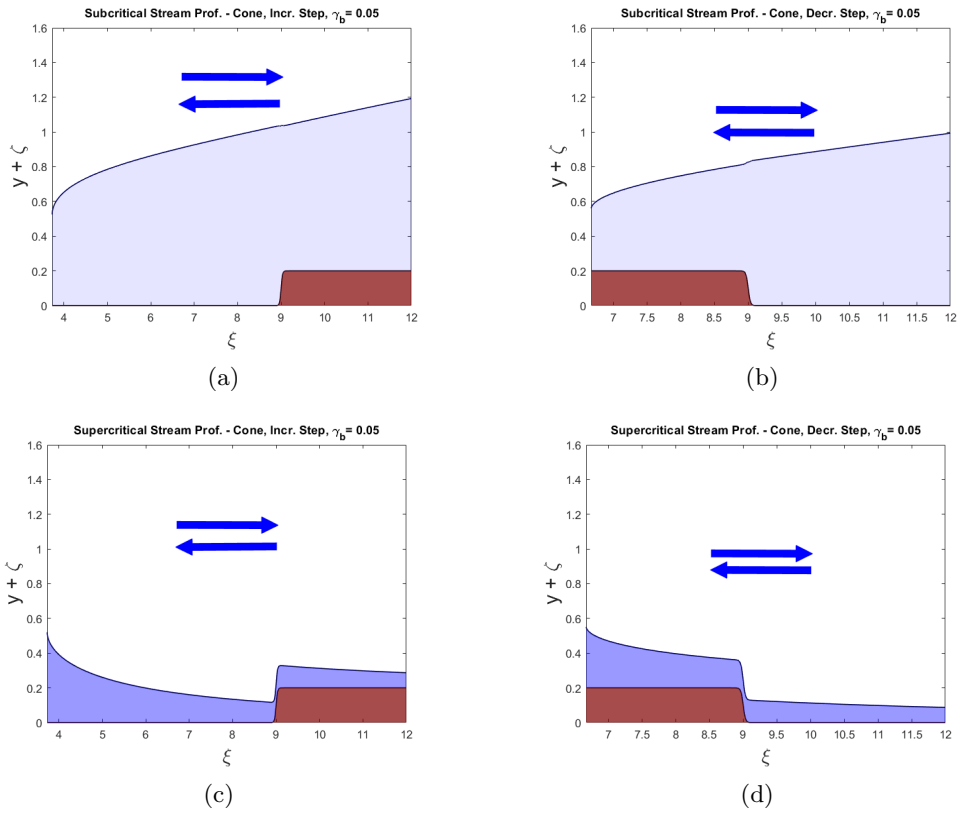

Figure 2.27: **Flow down a Cone-Shaped bed with Step Bottom- Stream Profiles and Free Surface,** $\gamma_b = -0.05$**.** Left column refers to an increasing step, right column to a decreasing one.

Horizontal Bed with Step Bottom - $\gamma_b = 0$

As for the case $\gamma_b > 0$, solutions with $\gamma_b = 0$ (horizontal bed with step bottom) correspond to open curves, with the supercritical branch lower bounded by 0. Each branch of the solution, again, describes two possible solution depending on the direction of the flow:

- stream starts from a source in critical condition, flows on favourable slope along divergent direction in subcritical (supercritical) conditions and faces a step;
- stream starts with unitary stream head and flows on opposite slope along convergent direction in subcritical (supercritical) conditions and faces a step; the height decreases (increases) then to reach critical conditions at the edge of a hole, located at a minimum radius.

The main difference with respect to the Horizontal Bed with flat bottom ($\gamma_b = 0$, $\zeta(\xi) \equiv 0$) is that energy is no longer conserved. This is evident by the behaviour of the Stream Head, reported in Fig. 2.28, where a discontinuity located at $\xi = \xi_{step}$ connects two branches:

- a constant branch corresponding to a unitary stream head;

- a constant branch corresponding to a stream head $1 \pm 2h_s$, the sign depending on whether, respectively, the step is increasing or decreasing.

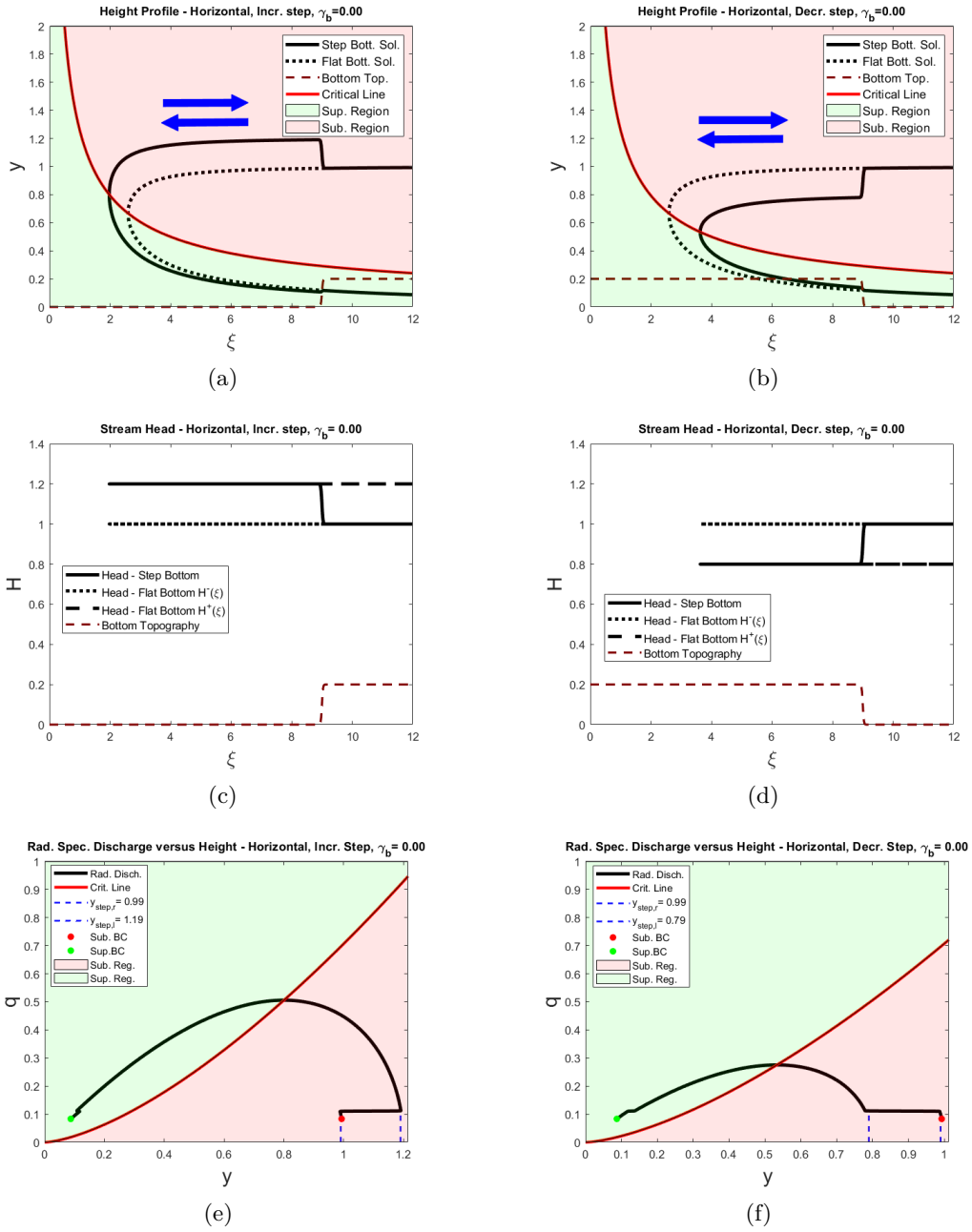

Figure 2.28: **Stream flowing over a Horizontal Bed with Step Bottom ,** $\gamma_b = 0$**.** Left column refers to the case of Increasing Step, the right one to the case of Decreasing Step.Figures 2.28(a), 2.28(b) - Comparison between height profiles obtained for the horizontal bed with step and flat bottom, respectively for increasing and decreasing step. Step is located at $\xi_s = 9$, while the solution with step bottom is obtained by imposing unitary stream head at $\xi_0 = 12$. Figures 2.28(c), 2.28(d) - Stream Head of the solutions with increasing and decreasing step, along with the extensions $\tilde{H}^+(\xi)$ and $\tilde{H}^-(\xi)$ of the two branches connected by the discontinuity at ξ_s. Figures 2.28(c), 2.28(d) - Relation between Radiant Specific Discharge and Height Profiles.

The energetic role of the bottom step, which will be described in details in Section 2.4.2, is determined by the flow direction (convergent or divergent) and the step shape (increasing or decreasing), according to Table 2.4: an increasing step will be felt as "ascending" from a divergent flow and "descending" from a convergent flow, causing respectively an increase or a decrease in terms of energy; the contrary holds for the decreasing step. The main features of the flows are reported in Fig. 2.28, while the corresponding Stream Profiles are reported in Fig. 2.29.

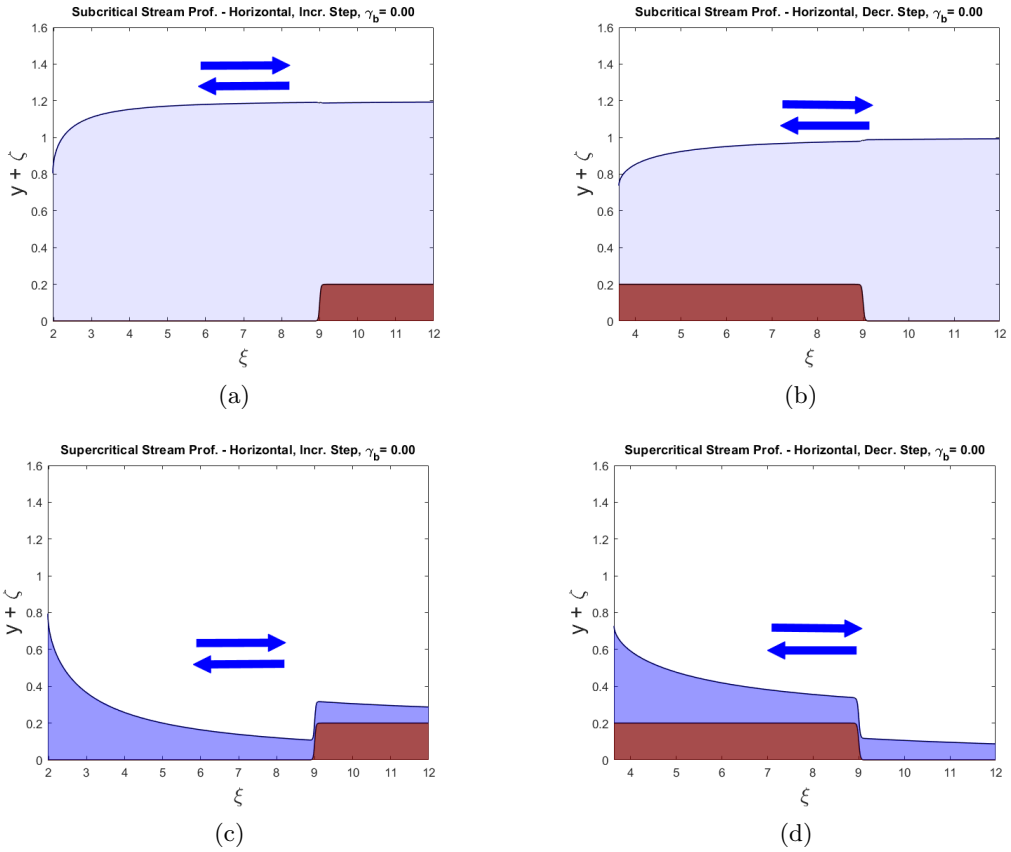

Figure 2.29: **Horizontal bed with Step bottom, $\gamma_b = 0$ - Stream Profiles.** Left column refers to the case of Increasing Step, Right column to the case of Decreasing Step. In both cases, step is located at $\xi_s = 9$ and the orbits are obtained by imposing unitary Stream Head at $\xi_0 = 8$.

2.4.2 Role of the Step: Orbit Jump

As seen in the previous subsections by the behaviour of the stream head, the presence of the step bottom affects the energy of the stream, while the Radian Specific Discharge is conserved across the step. The results obtained are summarized in Table 2.4. The step reflects on all the kinematic and dynamic features of the flow, and alters the behaviour of both supercritical and subcritical height (and free surface) profiles.

Table 2.4: **Energetic Role of the Step.** Positive sign "+" means that the step causes an energy increase, the contrary holds for the negative sign "-".

Step - Energy Variations				
	$\gamma_b > 0$		$\gamma_b < 0$	
	Incr. Step	**Decr. Step**	**Incr. Step**	**Decr. Step**
Conv. Flow	+	-	+	-
Div. Flow	-	+	-	+

To explain this, Fig. 2.30 and Fig. 2.31 reports a comparison between the height profiles obtained for inclined bed with flat bottom and step bottom, considering the same value of γ_b. It is evident, from all the figures reported, that depending on the increasing (decreasing) direction of the step, the two orbits are coincident within the left (right) region delimited by the step, which acts as a discontinuity and marks a difference between the behaviour of the orbits within the respective opposite regions. This happens because if one considers Eq. 2.4 with step topography [8], one has:

$$\frac{1}{\xi^2 y^2} + y = 1 + \gamma_b(\xi - \xi_0) - \{h_s \tanh[(\sigma_s(\xi - \xi_s)] - h_s \tanh[\sigma_s(\xi_0 - \xi_s)]\} \tag{2.46}$$

One can observe that except for a small neighbourhood around the step position:

- at the left (right) of the increasing (decreasing) step $\tanh[\sigma_s(\xi - \xi_s)]$ abruptly approaches -1 [9];
- at the right (left) of the increasing (decreasing) step $\tanh[\sigma_s(\xi - \xi_s)]$ abruptly approaches 1 [10].

Therefore, if the bed is increasing (decreasing), immediately at the left (right) of the step Eq. 2.46 approximates as:

[8] **Recall:** the function chosen to represent step bottom topography is the following:

$$\zeta(\xi) = h_s \tanh[\sigma_s(\xi - \xi_s)]$$

where h_s is the non-dimensional step height, $\mathrm{sgn}(\sigma_s)$ determines step direction ($+1$ if increasing, -1 if decreasing), $|\sigma_s|$ controls steepness of the step (the higher $|\sigma_s|$, the steeper is the step).

[9] Precisely, $\lim_{\xi \to 0^+} \tanh[\sigma_s(\xi - \xi_s)] = -1$ if $\sigma_s > 0$ (increasing), while $\lim_{\xi \to +\infty} \tanh[\sigma_s(\xi - \xi_s)] = -1$ if $\sigma_s < 0$ (decreasing).

[10] Precisely, $\lim_{\xi \to +\infty} \tanh[\sigma_s(\xi - \xi_s)] = 1$ if $\sigma_s > 0$ (increasing), while $\lim_{\xi \to 0^+} \tanh[\sigma_s(\xi - \xi_s)] = 1$ if $\sigma_s < 0$ (decreasing).

$$\frac{1}{\xi^2 y^2} + y \approx 1 + \gamma_b(\xi - \xi_0) + h_s\{1 + \tanh[\sigma_s(\xi_0 - \xi_s)]\} = \tilde{H}_-(\xi) \tag{2.47}$$

while, on the contrary, immediately at the right (left) of the step Eq. 2.46 approximates as:

$$\frac{1}{\xi^2 y^2} + y \approx 1 + \gamma_b(\xi - \xi_0) - h_s\{1 - \tanh[\sigma_s(\xi_0 - \xi_s)]\} = \tilde{H}_+(\xi) \tag{2.48}$$

Such approximations motivate the structure of the Stream Head represented in Fig. 2.30 and Fig. 2.31, which exhibits two branches separated by a discontinuity located at the step position $\xi = \xi_s$: functions $\tilde{H}_-(\xi)$ and $\tilde{H}_+(\xi)$ can be respectively interpreted as :

- the right and left branches of the Stream Head if the step is increasing ($\sigma_s > 0$);
- the left and right branches of the Stream Head if the step is decreasing ($\sigma_s < 0$).

The difference between the two branches is given by:

$$\Delta H(\xi) = |\tilde{H}_-(\xi) - \tilde{H}_+(\xi)| = 2h_s$$

which, as explained at the top of this subsection, corresponds to the height of the step: therefore, the higher h_s (i.e., the higher step height), the higher the energy difference across the step. Since it is independent on the radial position ξ, such difference is the same at both step position and boundary radial position $\xi = \xi_0$. Considering separately the two linear branches, one can find therefore that each one is associated to a specific orbit of those obtained in the case of Inclined bed with flat bottom, already discussed previously. The two orbits have the same value of γ_b, but different stream heads at the boundary ξ_0:

- $\tilde{H}_-(\xi = \xi_0) = 1 + h_s \tanh[\sigma_s(\xi_0 - \xi_s)]$;
- $\tilde{H}_+(\xi = \xi_0) = 1 - h_s + h_s \tanh[\sigma_s(\xi_0 - \xi_s)]$.

This is also justified by the fact that Equations 2.47, 2.48 have the same form of Eq. 2.6, which describes the Stream Head for the case of an inclined bed with flat bottom, and explains why the presence of the step modifies the position of the minimum and maximum radius: the step causes an energy jump, represented by a discontinuity, which also causes an orbit jump giving rise to the profiles described in Fig. 2.30 and Fig. 2.31.
Another interesting aspect emerging by Equations 2.47 and 2.48 is the dependence on the relative position between step and unitary stream head boundary condition, by means of the term:

$$\tanh[\sigma_s(\xi_0 - \xi_s)]$$

Indeed, since hyperbolic tangent is an odd function, a sign change between the relative

distance $\xi_0 - \xi_s$ turns into a sign change of the hole aforementioned term. This means that the stream head branches $\tilde{H}_-(\xi)$ and $\tilde{H}_+(\xi)$ described by Equations 2.47 and 2.48 vary according to whether $\xi_0 > \xi_s$ or $\xi_0 < \xi_s$: it can increase or decrease, giving rise to different orbits which exhibit different minimum or maximum radius if compared to the solutions obtained with same γ_b, but flat bottom.

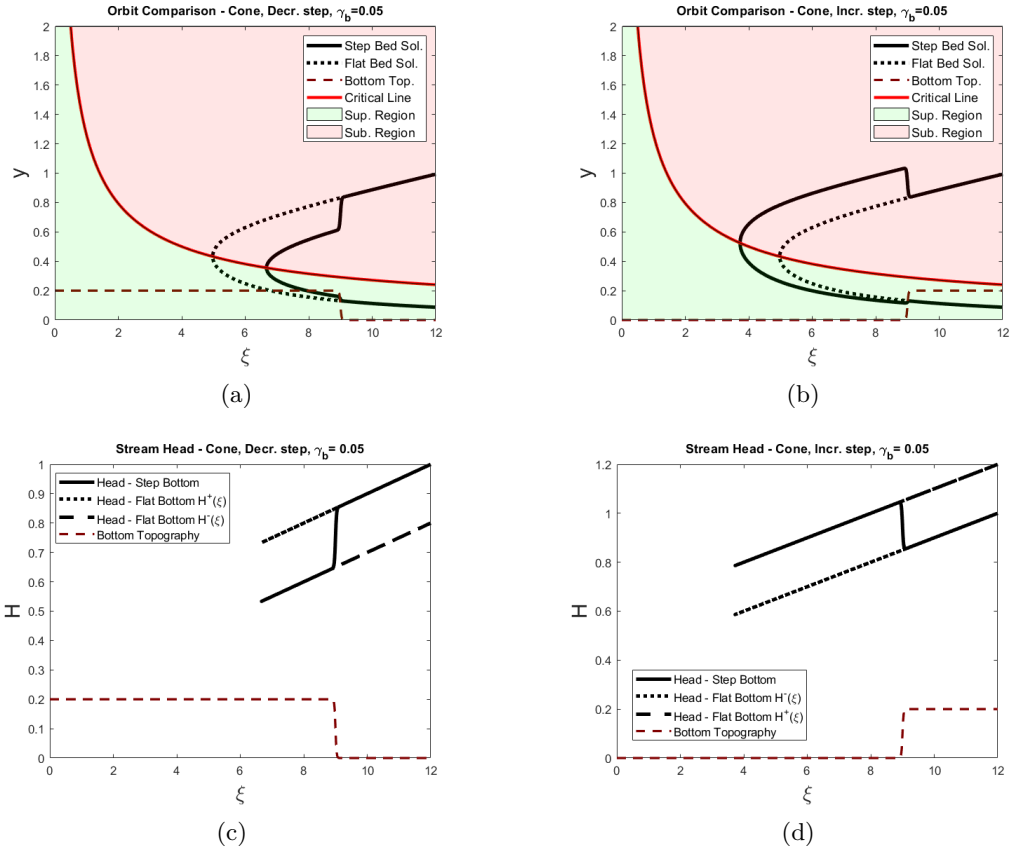

Figure 2.30: **Cone - Orbit comparison between step and flat bottom,** $\gamma_b = 0.05$**.** textcaption

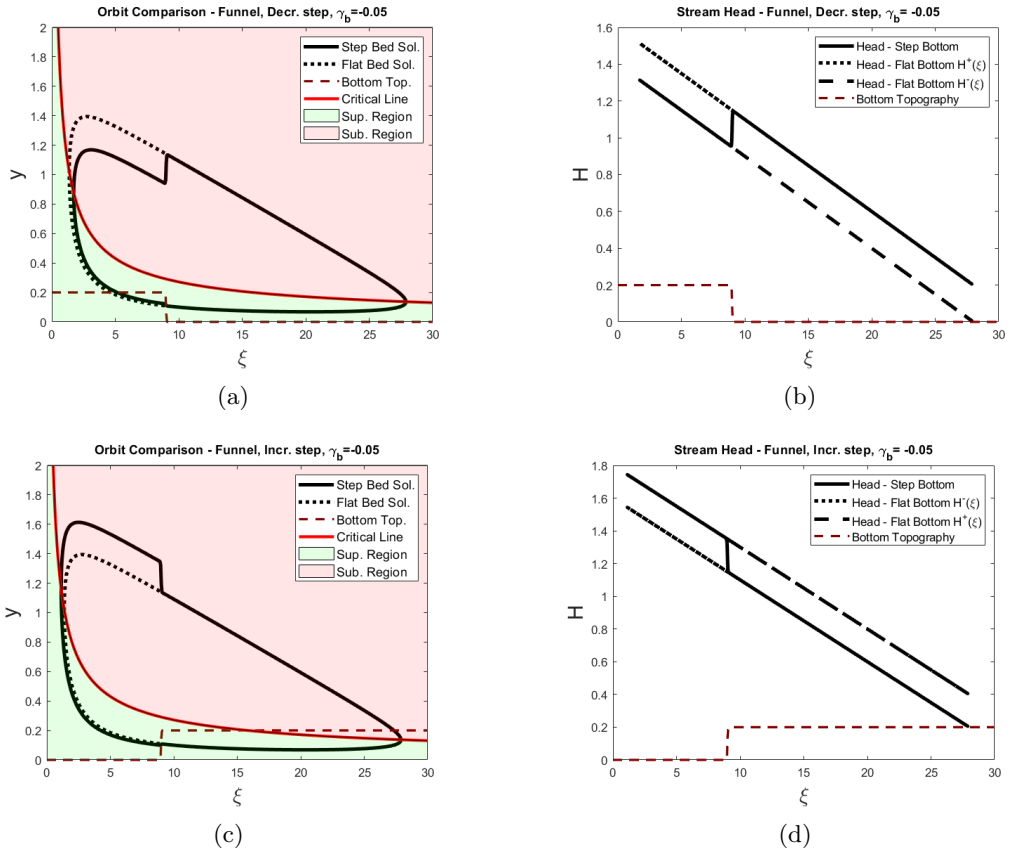

Figure 2.31: **Funnel - Orbit comparison between step and flat bottom,** $\gamma_b = -0.05$**,** $\xi_0 > \xi_s$**.** Left column shows orbits for **decreasing** (top left) and **increasing** (bottom left), the right one the corresponding stream head. The step of bed topography is located at $\xi_s = 9$. Unitary stream head is enforced at $\xi_0 = 12 > \xi_s$, showing that in this case only the minimum radius is different with respect to that of the orbits obtained with same γ_b, but flat bottom. The maximum radius remains instead the same.

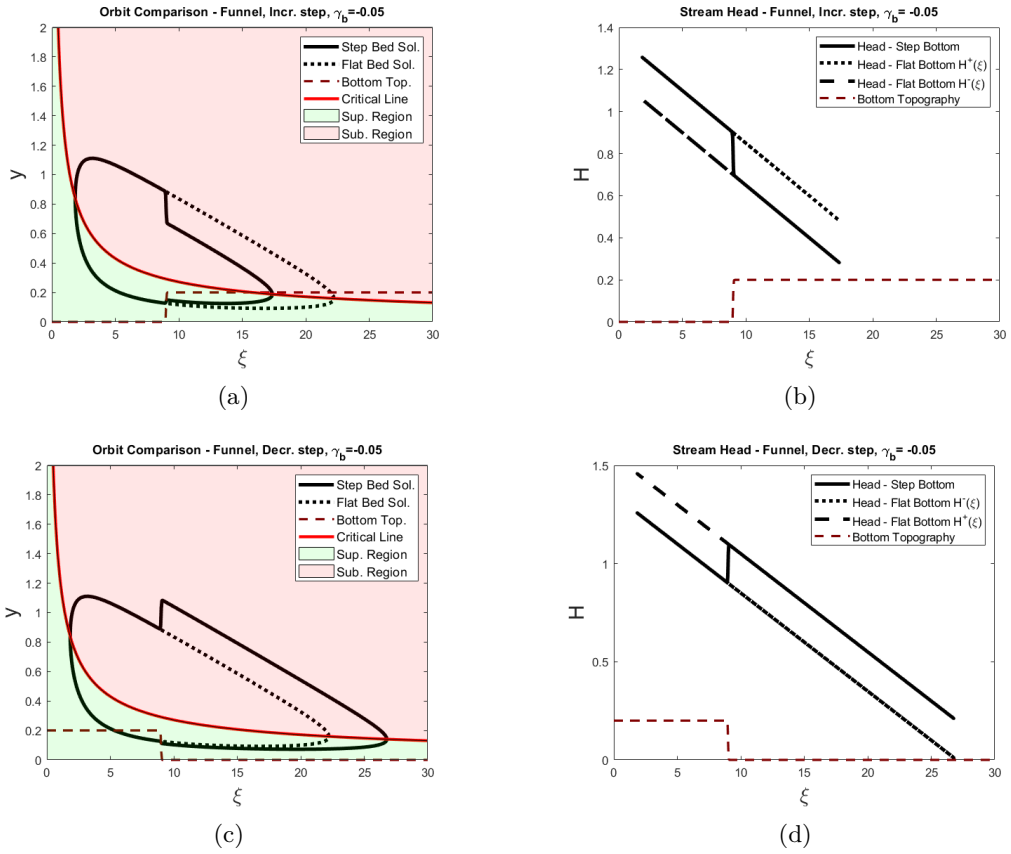

Figure 2.32: **Funnel - Orbit comparison between step and flat bottom,** $\gamma_b = -0.05$**,** $\xi_0 < \xi_s$**.** Left column shows orbits for **increasing** (top left) and **decreasing** (bottom left), the right one the corresponding stream head. The step of bed topography is located at $\xi_s = 9$. Unitary stream head is enforced at $\xi_0 = 7 < \xi_s$, showing that in this case only the minimum radius is different with respect to that of the orbits obtained with same γ_b, but flat bottom. The maximum radius remains instead the same.

Chapter 3

Stream Profiles for de Saint-Venant's Equations Including Drag

In this chapter, an analysis of de Saint-Ventant's Equations in circular symmetry will be performed, taking into account also the contribution of bottom friction. For this reason, the general model introduced in Chapter 1 in its complete form is taken into account by means of Eq. 1.25, here reported again to facilitate reading:

$$\frac{dy}{d\xi}(1-\frac{2}{\xi^2 y^3}) = \gamma_b - \frac{d\zeta}{d\xi} + \frac{2}{\xi^3 y^2} - \frac{\alpha}{\xi^2 y^3} \tag{3.1}$$

Friction introduces an additional degree of complexity with respect to the models previously discussed [1] , interacting in terms of energy with basal slope, bottom topography and Kinetic Energy to determine height profiles $y(\xi)$: by varying one of such contributes, mathematically expressed at the right hand side of Eq. 3.1, one can obtain different stream profiles.
Before investigating the effect of Bottom Topography in the stream profiles obtained (which is the main purpose of the whole current Chapter), it is interesting to find and analyze bottom topographies that ensure particular features to the flow.
Therefore, the current Chapter organizes into two macro-studies, according to the objectives to be pursued. The first study, reported in Sec. 3.1, is dedicated to find bottom topographies ensuring:

- constant stream head;
- constant depth;

[1] Compared to the models obtained in absence of friction in Chapter 2, governed by Eq. 2.4, now representing a particular case of Eq. 3.1 that can be recovered by considering $\alpha \to 0$.

- everywhere critical conditions.

The second study, involving Sections 3.3, 3.5, 3.4, is instead devoted to study the energetic role of Bottom Friction for the same bottom topographies introduced in Chapter 2, namely:

- flat bottom, Sec. 3.3;
- step bottom, Sec. 3.5;
- sinusoidal bottom, Sec. 3.4.

The link between the two studies is provided by the choice of the Boundary Conditions, which are briefly reported and discussed in Sec. 3.2.

3.1 Notable Bed Topographies

In this section, differently to what done before, the bottom topography $\zeta(\xi)$ is unknown. The goal is to find bottom topographies which ensure specific features to the stream: constant Stream Head, Constant Height and everywhere Critical Height. Such configurations provide steady state profiles that can be useful also to perform Linear Stability Analysis, as will be discussed next in Chapter 5.

3.1.1 Constant Stream Head Topography

Assume constant, given stream head $H(r) = H_0$, which in non-dimensional terms reads as $\tilde{H}(\xi) \equiv 1$. Then $d\tilde{H}/d\xi \equiv 0$, as well as the left hand side of Eq. 3.1 which therefore assumes the following form:

$$\frac{d\zeta}{d\xi} = \gamma_b - \frac{\alpha}{\xi^2 y^3} \tag{3.2}$$

On the other hand, as described by [29], the solution $y = y(\xi)$ related to constant stream head satisfies:

$$\xi = \frac{1}{y\sqrt{1-y}}$$

By plugging such solution into the right hand side of Eq. 3.2, one finally obtains the following equation:

$$\frac{d\zeta}{d\xi} = \gamma_b - \frac{\alpha[1-y(\xi)]}{y(\xi)} \tag{3.3}$$

where is to be intended that $y(\xi)$ is the supercritical or subcritical constant stream head solution, therefore by fixing α and γ_b one obtains two different bottom topographies depending on the regime. Eq. 3.3 describes the behaviour of the bottom slope ensuring

constant stream head, due to a balance between friction dissipation and energy gain because of slope. Indeed, it can be formulated also in the following way:

$$\gamma(\xi) = \frac{\alpha(1-y)}{y} \tag{3.4}$$

where:

$$\gamma(\xi) = \gamma_b - \frac{d\zeta}{d\xi} \tag{3.5}$$

is the topographic slope "felt" by the stream while flowing, which takes into account the contributes of both basal slope and bottom topography.
Equation 3.3 opens to an additional class of profiles which can be both monotonic or not, depending on the values of α and γ_b and the supercritical or subcritical solution $y(\xi)$. Indeed, one can easily find by the equation itself that bottom topography :

- increases where the right hand side of Eq. 3.3 is positive, i.e., where basal slope energy gain overbalances energy loss due to friction;
- decreases where the right hand side of Eq. 3.3 is negative, i.e., where basal slope energy gain is overbalanced by energy loss due to friction;
- attains stationary points (maxima or minima) where the right hand side of Eq. 3.3 where basal slope energy gain balances energy loss due to friction.

Such behaviour is well illustrated in Figures 3.1(e), 3.1(f), 3.2(e), 3.2(f), 3.3(e), 3.3(e), where friction contribute $\alpha[1-y(\xi)]/y(\xi)$ is reported along with γ_b.
Notice that non-monotonical bottom topographies are possible only if $\gamma_b \neq 0$. Indeed, if $\gamma_b = 0$, then Eq. 3.3 modifies as:

$$\frac{d\zeta}{d\xi} = -\frac{\alpha[1-y(\xi)]}{y(\xi)} \tag{3.6}$$

Since the Constant Stream Head Solution 2.10 is such that $0 < y(\xi) < 1$ for all $\xi > \xi_{min}$ [2], then the right hand side of Eq. 3.6 only depends on α, therefore it does not vary with ξ.
Remembering that both supercritical and subcritical solutions $y(\xi)$ are well defined and continuous for $\xi \geq \xi_{min}$, one can fix a point $\xi_0 > \xi_{min}$ and integrate Eq. 3.3 within $[\xi, \xi_0]$, where $\xi \geq \xi_{min}$, to obtain the bottom topography $\zeta(\xi)$. Using Torricelli-Barrow's Fundamental Theorem of Calculus and re-defining $\zeta(\xi)$ as $\zeta_{CH}(\xi)$ [3], one obtains the

[2] **Recall**: ξ_{min} is the minimum radius arising in the Height Solution for the Horizontal Bed with Flat Bottom, see Sec. 2.1

[3] The subscript "CH" stands for "Constant Head".

following expression for the topography ensuring Constant Stream Head solution:

$$\zeta_{CH}(\xi) = \zeta(\xi_0) + \gamma_b(\xi - \xi_0) - \alpha \int_{\xi_0}^{\xi} \frac{1 - y(\xi')}{y(\xi')} d\xi' \tag{3.7}$$

The integral term of 3.7 can be numerically computed for each value of $\xi \geq \xi_{min}$, by means of the Trapezoidal Numerical Integration and by using the numerical values of the function $y(\xi)$, according to the supercritical or subcritical branch. The previous analysis expresses therefore that Stream Energy Conservation is possible also in presence of bottom friction, provided that the related dissipation is balanced by bottom topography.
Figures 3.1, 3.2 and 3.3 illustrate some examples of monotonic topographies ensuring Constant Stream Head, respectively obtained for Funnel-shaped, Cone-shaped and Horizontal Bed: each one reports supercritical and subcritical stream profiles, along with the basal line (black dot-dashed line) indicating the flat bottom. It is evident, from the Stream Profiles obtained, the role of the topography in trying to maintain the Stream Head constant, particularly from those related to the subcritical profile:

- for convergent flows along Funnel-shaped Bed (Fig. 3.1(c)) or divergent flows along Cone-shaped bed (Fig. 3.2(d)), where in case of flat bottom the Stream Head would increase due to the flow on favourable slope, the bottom topography increases, opposing to the stream in order not to increase the Stream Head and keeping it constant;
- for divergent flows along Funnel-shaped Bed (Fig. 3.1(d)) or convergent flows along Cone-shaped bed (Fig. 3.2(c)), where in case of flat bottom the Stream Head would decrease due to the flow on opposite slope, the bottom topography decreases, helping the stream in order not to decrease the Stream Head and keeping it constant.

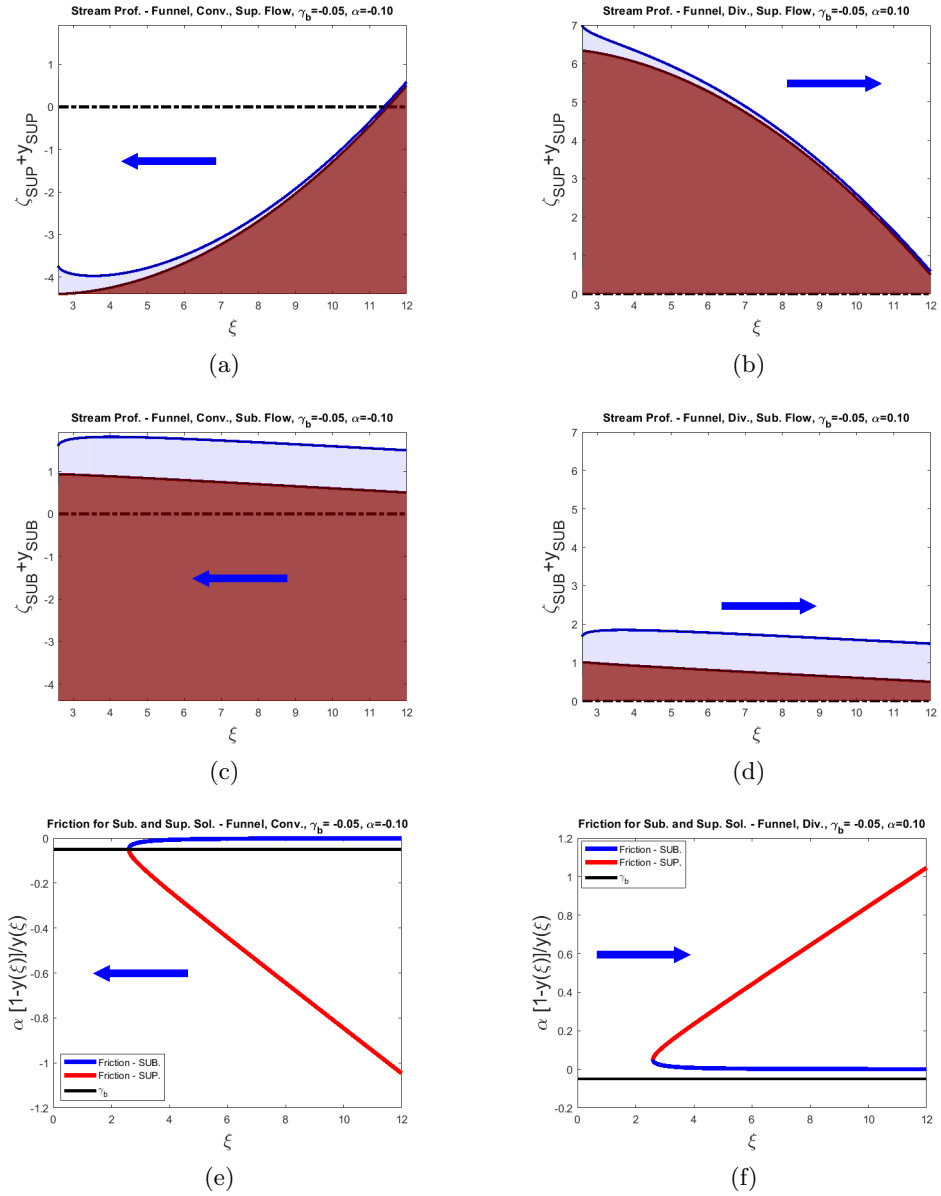

Figure 3.1: **Bottom Topographies ensuring Constant Stream Head for Funnel-shaped Bed in presence of Bottom Friction, $\gamma_b = -0.05$, $\alpha = \pm 0.1$.** Left column (Figures 3.1(a), 3.1(c), 3.1(e)) refer to a stream flowing down a Funnel-shaped bed along convergent direction ($\gamma_b = -0.05$, $\alpha = -0.1$). Right column (Figures 3.1(b), 3.1(d), 3.1(f)) refer to a stream flowing over a Funnel-shaped bed along divergent direction ($\gamma_b = -0.05$, $\alpha = 0.1$). In each column, top and middle figures respectively report supercritical and subcritical stream profiles and related topographies (the black dashed-dotted line stands for the flat bottom), while bottom figure reports friction for both supercritical and subcritical profiles, along with γ_b, in order to show the behaviour of the right hand side of Eq. 3.3.

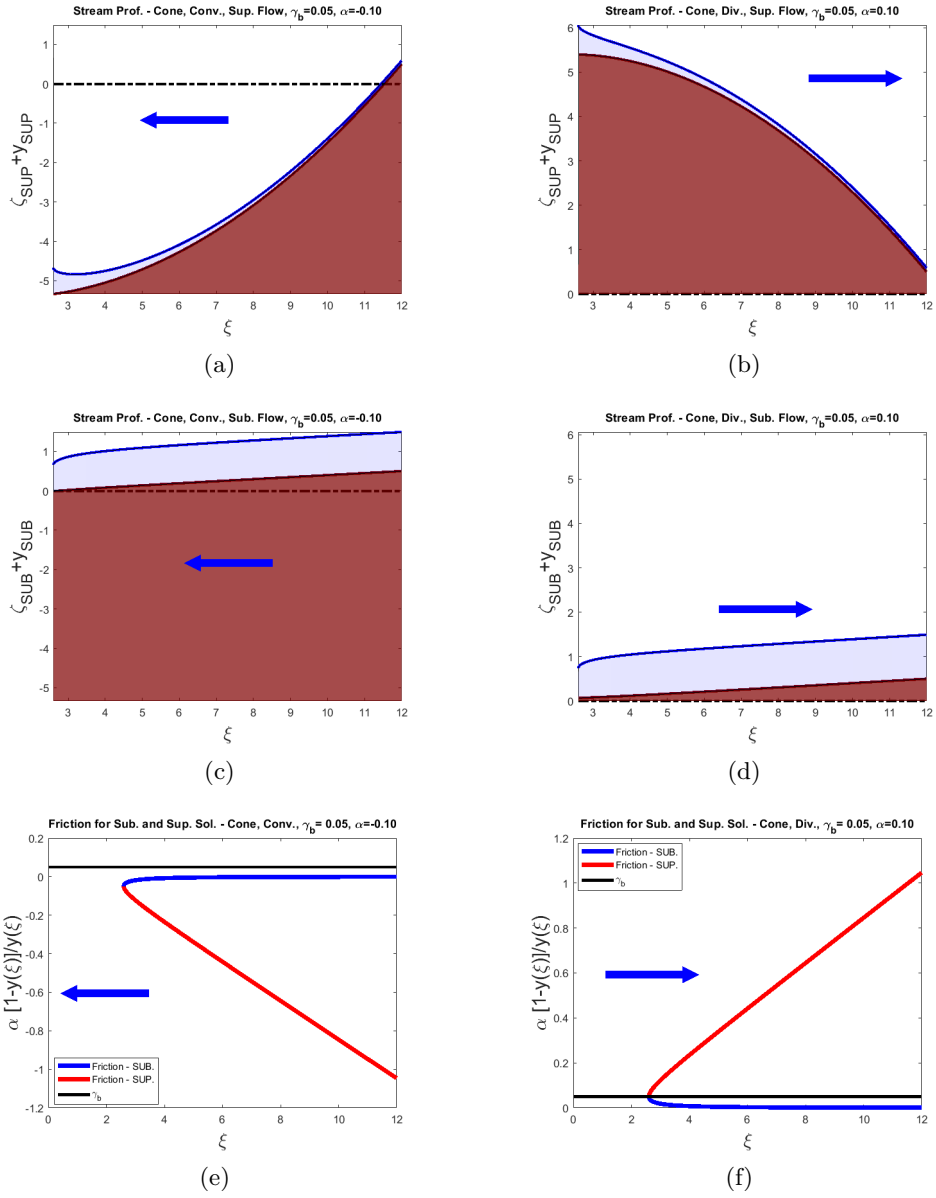

Figure 3.2: **Bottom Topographies ensuring Constant Stream Head for Cone-shaped Bed in presence of Bottom Friction, $\gamma_b = 0.05$, $\alpha = \pm 0.1$.** Left column (Figures 3.2(a), 3.2(c), 3.2(e)) refer to a stream flowing over a Cone-shaped bed along convergent direction ($\gamma_b = 0.05$, $\alpha = -0.1$). Right column (Figures 3.2(b), 3.2(d), 3.2(f)) refer to a stream flowing down a Cone-shaped bed along divergent direction ($\gamma_b = 0.05$, $\alpha = 0.1$). In each column, top and middle figures respectively report supercritical and subcritical stream profiles and related topographies (the black dashed-dotted line stands for the flat bottom), while bottom figure reports friction for both supercritical and subcritical profiles, along with γ_b, in order to show the behaviour of the right hand side of Eq. 3.3.

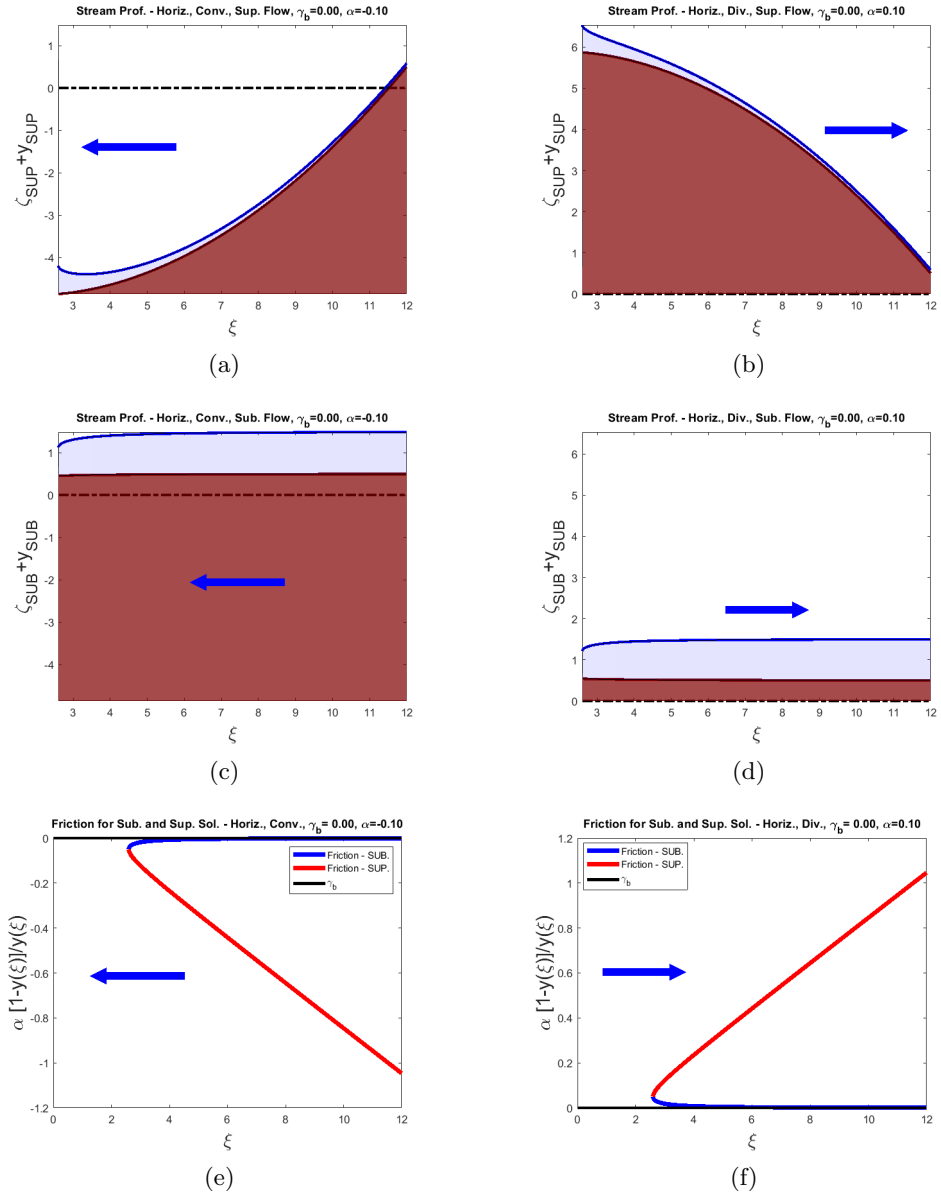

Figure 3.3: **Bottom Topographies ensuring Constant Stream Head for Horizontal Bed in presence of Bottom Friction, $\gamma_b = 0$, $\alpha = \pm 0.1$.** Left column (Figures 3.3(a), 3.3(c), 3.3(e)) refer to a stream flowing along convergent direction ($\gamma_b = 0$, $\alpha = -0.1$). Right column (Figures 3.3(b), 3.3(d), 3.3(f)) refer to a stream flowing along divergent direction ($\gamma_b = 0$, $\alpha = 0.1$). In each column, top and middle figures respectively report supercritical and subcritical stream profiles and related topographies (the black dashed-dotted line stands for the flat bottom), while bottom figure reports friction for both supercritical and subcritical profiles, along with γ_b, in order to show the behaviour of the right hand side of Eq. 3.3.

3.1.2 Constant Flow Depth Topography

In this Section, bottom topography will be obtained by imposing uniform stream depth y_0, followed by a discussion about the stream profile and the choice of the boundary conditions.

Bottom Topography

Assume everywhere constant flow depth $y(\xi) = y_0$, with y_0 given constant. Then $\frac{dy}{d\xi} = 0$ and Eq. 3.1 modifies as:

$$\frac{d\zeta}{d\xi} = \gamma_b + \frac{2}{\xi^3 y_0^2} - \frac{\alpha}{\xi^2 y_0^3} \tag{3.8}$$

The stationary points of $\zeta(\xi)$ can be found by imposing the right hand side member of Eq. 3.8 as null, obtaining the following third degree algebraic equation with no quadratic term which can be solved for $\xi > 0$ by using the well known Cardano's formulae ([9]):

$$\xi^3 - \frac{\alpha}{\gamma_b y_0^3}\xi + \frac{2}{\gamma_b y_0^2} = 0 \tag{3.9}$$

For the purpose of this work, eventual computation of the stationary points from Eq. 3.9 is demanded to classical numerical algorithms, instead of the exact formulae, while basics results of third degree equations show that:

- profiles in which α and γ_b have different sign (i.e., convergent flows over a cone-shaped bed or divergent flows over a funnel-shaped bed) are characterized by at most one stationary point;
- profiles in which α and γ_b have both negative sign (i.e., convergent flows over a funnel-shaped bed) are characterized by at most one stationary point too;
- profiles in which α and γ_b have both positive sign (i.e., divergent flows down a cone-shaped bed) are characterized by at most one stationary point if $0 < \alpha \leq \sqrt[3]{27\,\gamma_b\, y_0^5}$, up to two otherwise, and in this latter case they are a maximum and a minimum (they cannot be of the same nature).

It is interesting, here, to observe how the presence of friction introduces physical and computational complexity, giving rise to a variety of monotonic or non-monotonic bottom configurations. Neglecting friction (i.e., $\alpha \to 0$) reduces such complexity. Indeed, in order to study the sign of the right hand side of Eq. 3.8, one obtains the inequality:

$$\gamma_b + \frac{2}{\xi^3 y^2} \geq 0 \tag{3.10}$$

which allows to conclude that, in the domain $\{\xi > 0\}$:

- profiles with $\gamma_b > 0$ (cone-shaped bed) are monotonic;

- profiles with $\gamma_b < 0$ have a maximum point located at $\xi = \sqrt[3]{-\frac{2}{\gamma_b y_0^2}}$.

On the other hand, also considering horizontal beds ($\gamma_b = 0$) reduces complexity, as the study of the sign of the right hand side in Eq. 3.8 reduces to the following inequality:

$$\frac{2}{\xi^3 y^2} + \frac{\alpha}{\xi^2 y_0^3} \geq 0 \tag{3.11}$$

In this case, one has that, in the domain $\{\xi > 0\}$:

- profiles with $\alpha < 0$ (i.e., flowing on convergent direction) are monotonic;
- profiles with $\alpha > 0$ are non-monotonic and exhibit exactly one maximum located at $\xi = \frac{2y_0}{\alpha}$.

Finally, considering horizontal beds with no friction ($\gamma_b = 0$, $\alpha = 0$), the sign study of the right hand side of Eq. 3.8 brings to the following inequality:

$$\frac{2}{\xi^3 y_0^2} \geq 0 \tag{3.12}$$

which is always verified within the domain $\{\xi > 0\}$, therefore the bottom topographies obtained are monotonic.
The start point for the interpretation of the bottom topographies just obtained, which are illustrated in Figures 3.5, 3.6 and 3.7, is to find a closed analytical expression for the bottom topography. Given a boundary radius ξ_0, such expression is found by direct integration in the variable ξ of the two members of Eq. 3.8 (assume for simplicity $\xi > \xi_0 > 0$) and re-naming of $\zeta(\xi)$ as $\zeta_{UH}(\xi)$ [4], thus obtaining:

$$\zeta_{UH}(\xi) = \zeta_{UH}(\xi_0) + \gamma_b(\xi - \xi_0) + \frac{\alpha}{\xi y_0^3} - \frac{1}{\xi^2 y_0^2} - \frac{\alpha}{\xi_0 y_0^3} + \frac{1}{\xi_0^2 y_0^2} \tag{3.13}$$

Notice that for large ξ the last two addends defining the solution 3.13 assume small values, so the following approximation holds:

$$\zeta_{UH}(\xi) \approx \zeta_{UH}(\xi_0) + \gamma_b(\xi - \xi_0) - \frac{\alpha}{\xi_0 y_0^3} + \frac{1}{\xi_0^2 y_0^2} = \gamma_b(\xi - \xi_0) + \Delta\zeta \tag{3.14}$$

where $\Delta\zeta$ is the intercept:

$$\Delta\zeta := \zeta_{UH}(\xi_0) + \frac{1}{\xi_0^2 y_0^2} - \frac{\alpha}{\xi_0 y_0^3} \tag{3.15}$$

This is coherent with the fact that, by studying Eq. 3.13 for sufficiently large values of ξ,

[4] The subscript "UH" stands for "Uniform Height".

one obtains, independently from α:

$$\frac{d\zeta}{d\xi} \to \gamma_b$$

that is, the bottom tends to be flat as the friction dissipation, as well as Radiant Kinetic Height, tends to vanish. Notice that if friction is absent, then:

$$\Delta\zeta_{\alpha=0} := \zeta_{UH}(\xi_0) + \frac{1}{\xi_0^2 y_0^2} \tag{3.16}$$

therefore:

- if $\alpha < 0$ (convergent flows), then $\Delta\zeta$ is greater than in the case in which $\alpha = 0$;
- if $\alpha > 0$ (divergent flows), then $\Delta\zeta$ is lower than in the case in which $\alpha = 0$.

Supercritical to Subcritical Smooth Transition

A second important aspect, emerging instead from the constant height solution $y(\xi) = y_0$ itself, is that flows on divergent direction experience a smooth transition from supercritical to subcritical regime, without hydraulic jump. Indeed, remembering the expression 1.20, the Froude Number is:

$$Fr(\xi, y_0) = \sqrt{\frac{2}{\xi^2 y_0^3}} \tag{3.17}$$

which now only depends on the radial position ξ (notice that the Froude Number is also not explicitly dependent on friction coefficient α). Such behaviour is reported in Fig. 3.4 for different values of y_0.

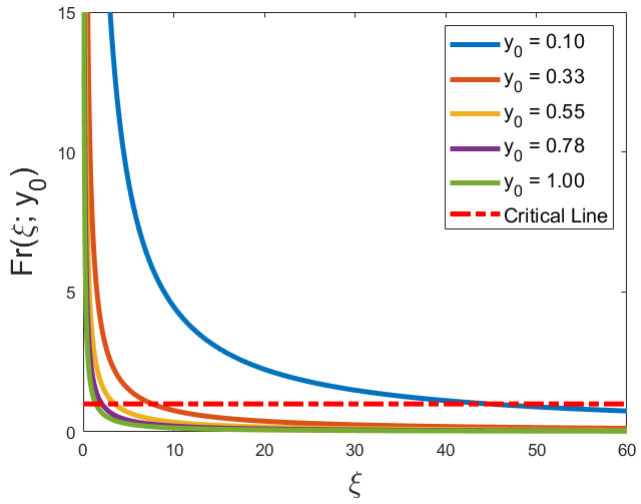

Figure 3.4: **Froude Number for Constant Depth Solution** $y(\xi) \equiv y_0$**.** Froude Number is reported for equally spaced values of y_0 between 0.1 and 1, along with the Critical Line

Therefore, the flow is:

- supercritical for $\xi < \sqrt{\frac{2}{y_0^3}}$;
- critical if $\xi = \sqrt{\frac{2}{y_0^3}}$;
- subcritical for $\xi > \sqrt{\frac{2}{y_0^3}}$;

This is a peculiar difference with respect to all of the other profiles obtained in the previous chapters, where the supercritical and subcritical branches of the stream attained critical condition at singular points and a transition was possible only through an hydraulic jump. Indeed, the important difference between Eq. 3.1 (where $y = y(\xi)$ is one of the solutions obtained in Chapter 2) and Eq. 3.13, where $y(\xi) \equiv y_0$, is that now $\frac{dy}{d\xi} \equiv 0$, therefore the singular term:

$$(1 - Fr^2)\,\frac{dy}{d\xi}$$

vanishes.
For the same reason, there is no longer a two-branches behaviour of the solution nor the presence of a minimum radius: the Froude Number, indeed, blows up as ξ approaches 0, as well as velocity, while on the contrary bottom topography decreases unbounded in order to maintain constant depth.
At the same time, $y(\xi) \equiv y_0$ is an admissible solution because, thanks to the balance between basal slope γ_b, friction (by means of α) and Radiant Specific Kinetic Height $2/\xi^3 y_0^2$ described by Eq. 3.13, there exist topographies (those described in this section) that ensure its existence in physical terms. Examples of curved bed giving rise to smooth supercritical to subcritical transition of the flow are also described in [2], [17].

Interpretation of the Bottom Topography

In view of the previous discussion, supported by the stream profiles in Figures 3.5, 3.6 and 3.7, Eq. 3.8 explains the monotony characteristics obtained for the bottom topography. The interaction of the terms appearing at its right hand side can be analyzed within three main areas, which are evident in Figures 3.8 and 3.9:

- for sufficiently small radii, i.e., $\xi \to 0$, where Kinetic Energy and Friction dominate;
- for sufficiently large radii, i.e., $\xi \to +\infty$, where Basal Slope dominates;
- a central area where the three contributes into r.h.s. of Eq. 3.13 are comparable.

Indeed, one can observe that since no minimum radius arises, the stream profile, as well as the bottom topography, is well defined for $\{\xi > 0\}$: in order to visualize this fact in physical terms, one can figure out a stream starting from an external annular gate located at ξ_0 and flowing continuously along convergent direction, with no central hole draining the fluid [5], as reported in Figures 3.5(a), 3.5(c). In mathematical terms, this is described by the fact that for $\xi \to 0$ the dominant term on the right hand side of Eq. 3.8 is that of Radiant Specific Kinetic Height, i.e.,

$$k_s(\xi; y_0) = \frac{2}{\xi^3 y_0^2} = 2\,\frac{\nu(\xi; y_0)}{\xi} \tag{3.18}$$

which represents nothing but the Head Slope $\frac{d\tilde{H}}{d\xi}|_{y=y_0}$, where as usual $\tilde{H}(\xi, y)$ is the Stream Head: in absence of a hole draining the fluid and with a constant discharge at the boundary, the Stream Head would grow indefinitely as well as the flow depth (which is imposed instead to be constant) if no energy sinks are present. On the other hand, both basal slope γ_b and the boundary energy contributes on the right hand side of Eq. 3.8 are constant and bounded, so the only way to contrast the strong energy increase given by the term 3.18 for radii approaching zero and maintain constant depth y_0 is via a strong energy decrease given by the slope of bottom topography. This explains why, in all the cases, $\zeta(\xi) \to -\infty$ as $\xi \to 0$.
As described in the approximation 3.14, for sufficiently large ξ the topography tends instead to be linear, with slope γ_b: indeed, thanks to the Chézy formula and the geometry chosen, both $k_s(\xi; y_0)$ and the friction term of Eq. 3.8 approach 0 as $\xi \to +\infty$. In this case, the effects of friction and boundary are only enclosed into the intercept $\Delta\zeta$ of Eq. 3.14.
The most important range to understand the monotony properties of bottom topography is that in which $k_s(\xi; y_0)$, friction term and basal slope become progressively comparable and give rise to the eventual stationary points of the bottom topography $\zeta(\xi)$, depending on the sign of α and γ_b. In order to illustrate this, it suffices to remember that the right

[5] **Recall**: for the flows described in Chapter 2, the minimum radius ξ_{min} arising in the solutions could be interpreted as the edge of a central hole which, in case of convergent flows, drained the fluid acting as a control on the increase or decrease of the Stream Head. In this case, it is like the minimum radius is located at $\xi = 0$, thus being described by a hole of zero radius.

hand side of Eq. 3.13 is nothing but a sum of energy contributes, taken with their sign. Figures 3.8, 3.9 report the behaviour of the tree terms separately and their sum (i.e., the right hand side) for all of the possible sign combinations of α and γ_b: the cases in which $\gamma_b = 0$ (horizontal bed) or $\alpha = 0$ (no bottom friction) can be easily derived and interpreted, so they are not reported. It is peculiar the presence of a maximum followed by a minimum for $\alpha > 0$ and $\gamma_b > 0$: the first appears to be connected to a balance between Radiant Specific Height and Friction, while the second seems to be related to the balance between friction and basal slope. It is now clear how the bottom topography drives the maintenance of the constant height y_0, giving rise to the topographies illustrated in Figures 3.5, 3.6: for small radii, it rapidly increases (decreases) to add (subtract) energy in case of divergent (convergent) flow for small ξ, independently from the basal slope γ_b. The same happens for large ξ , where instead:

- if $\gamma_b < 0$, it linearly decreases (increases) in order to help (control) the flow on opposite (favourable) slope maintaining constant depth y_0;
- the contrary happens if $\gamma_b > 0$.

The uniform depth stream profile will be useful in Chapter 5, to write the perturbation equation derived from Linear Stability Analysis.

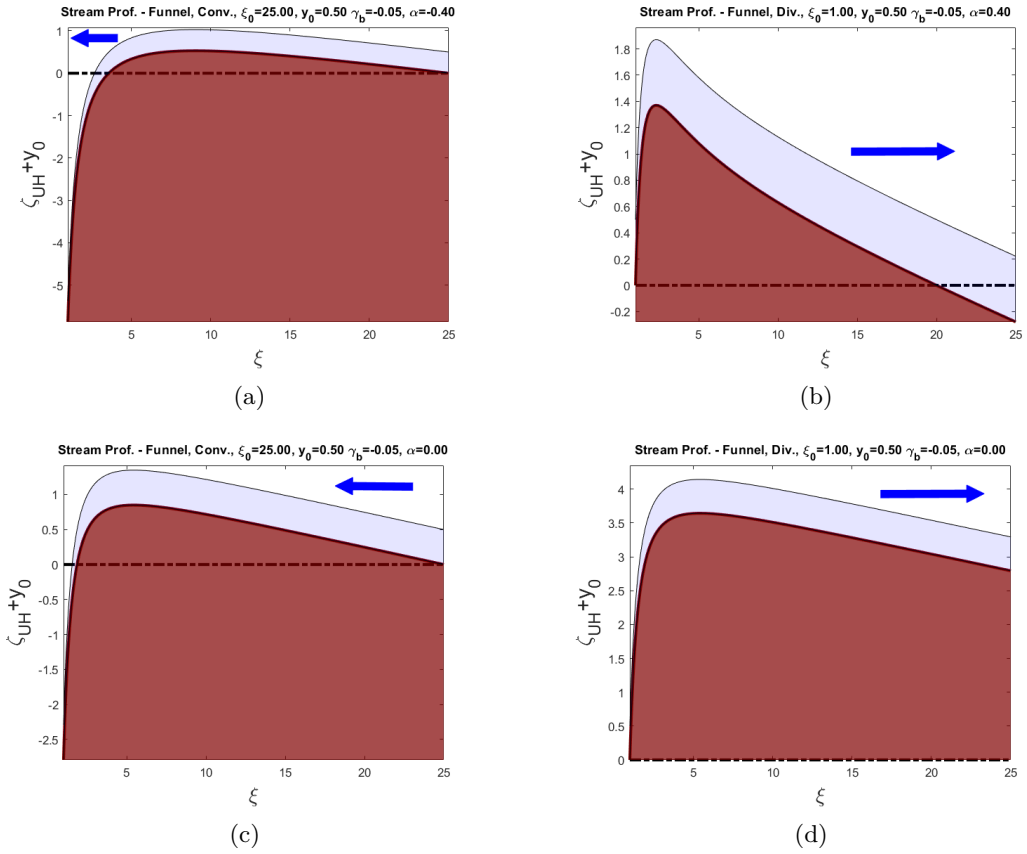

Figure 3.5: **Bottom Topography ensuring Uniform Depth Stream flowing along a Funnel-Shaped bed.** Left and right column respectively refer flows along Convergent and Divergent direction, as indicated by the blue arrows. For all of the stream profiles reported, the bottom topography at boundary $\zeta_{UH}(\xi_0)$ is imposed to be 0. Each figure reports boundary radius ξ_0, uniform depth y_0, basal slope γ_b and friction coefficient α are reported: in particular, bottom figures (Fig. 3.5(c) and 3.5(d)) report the case in which friction is absent, i.e., $\alpha = 0$. Finally, the dot-dashed line indicates the level of the flat bottom. Plot range is $\xi \in$ [1,25].

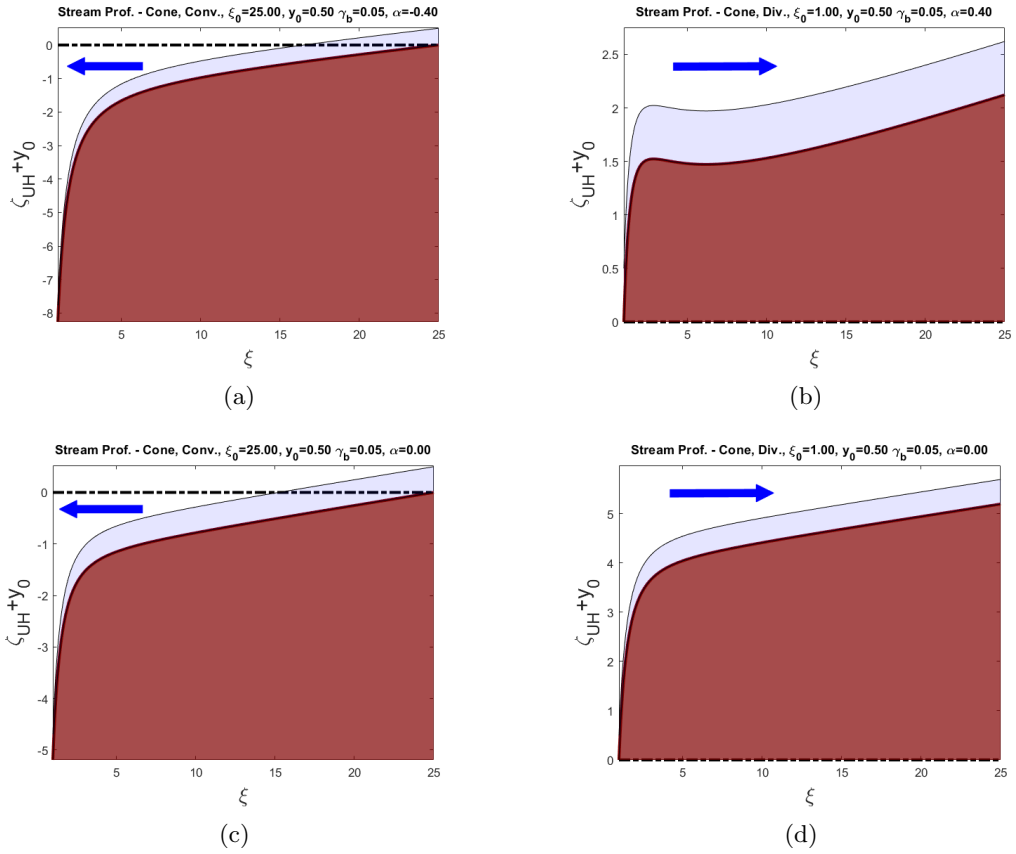

Figure 3.6: **Bottom Topography ensuring Uniform Depth Stream flowing along a Cone-Shaped bed.** Left and right column respectively refer flows along Convergent and Divergent direction, as indicated by the blue arrows. For all of the stream profiles reported, bottom topography at boundary $\zeta_{UH}(\xi_0)$ is imposed to be 0. Each figure reports boundary radius ξ_0, uniform depth y_0, basal slope γ_b and friction coefficient α are reported: in particular, bottom figures (Fig. 3.6(c) and 3.6(d)) report the case in which friction is absent, i.e., $\alpha = 0$. Finally, the dot-dashed line indicates the level of the flat bottom. Plot range is $\xi \in$ [1,25].

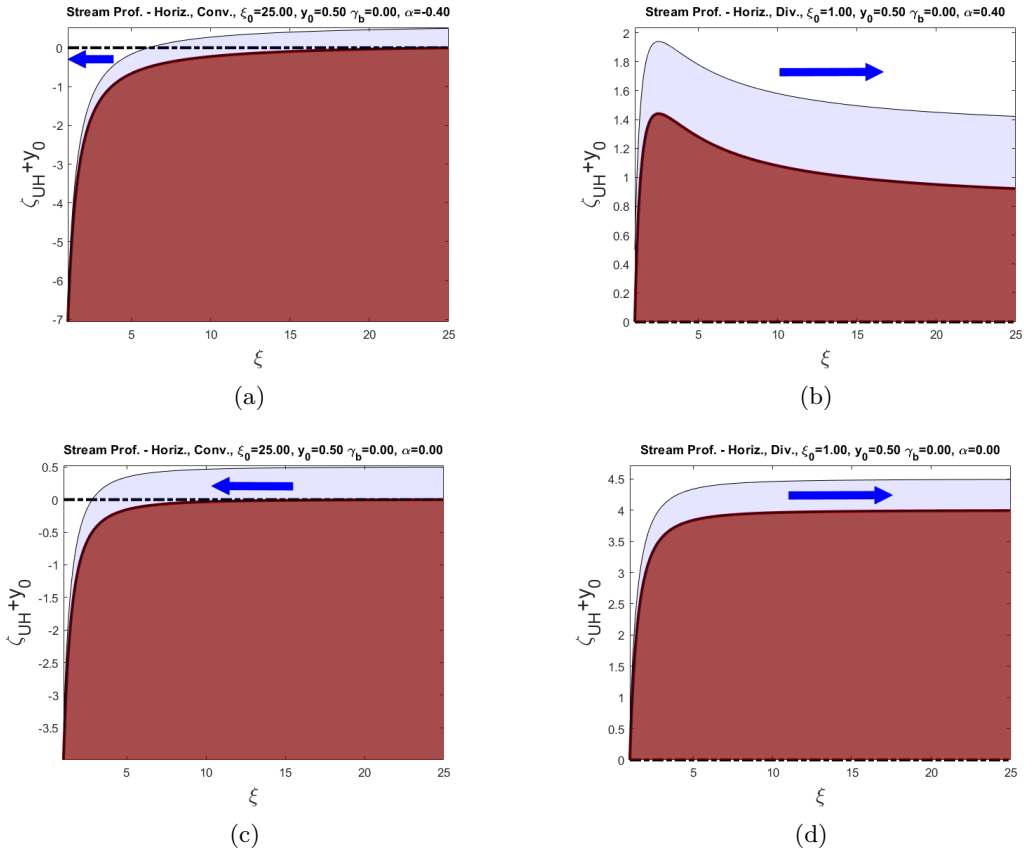

Figure 3.7: **Bottom Topography ensuring Uniform Depth Stream flowing along a Horizontal Bed.** Left and right column respectively refer to flows along Convergent and Divergent direction, as indicated by the blue arrows. For all of the stream profiles reported, bottom topography at boundary $\zeta_{UH}(\xi_0)$ is imposed to be 0. Each figure reports boundary radius ξ_0, uniform depth y_0, basal slope γ_b and friction coefficient α are reported: in particular, bottom figures (Fig. 3.7(c) and 3.7(d)) report the case in which friction is absent, i.e., $\alpha = 0$. Finally, the dot-dashed line indicates the level of the flat bottom. Plot range is $\xi \in$ [1,25].

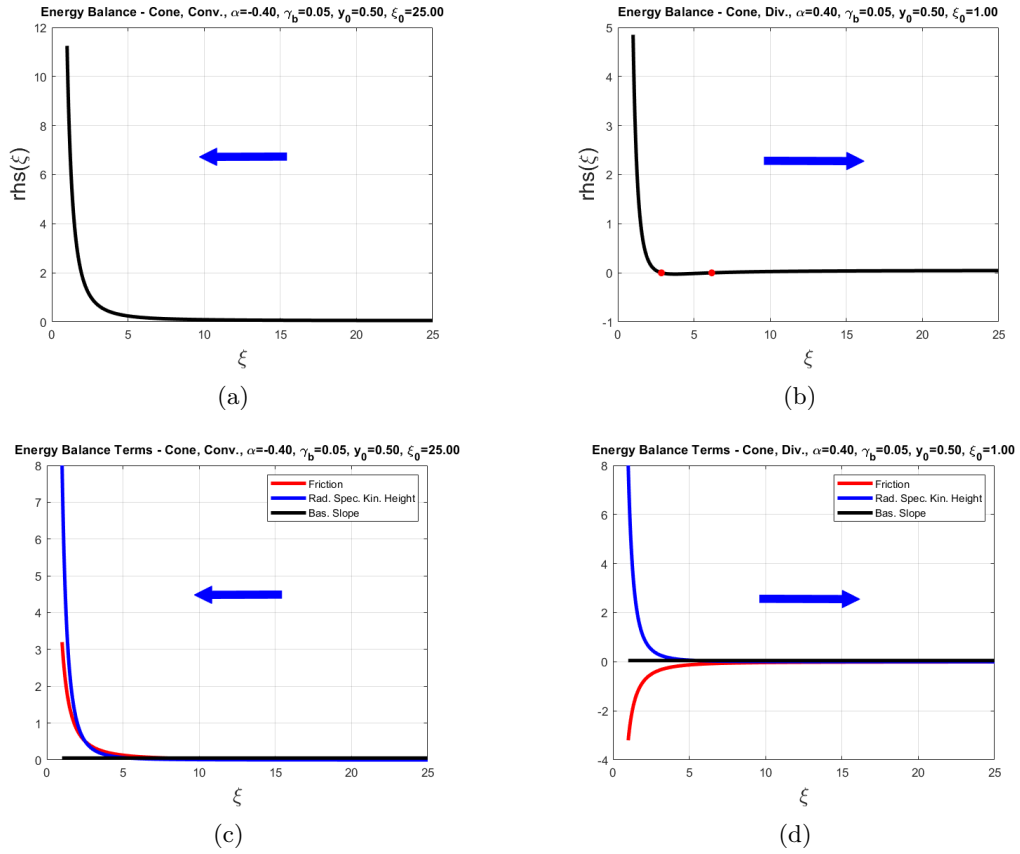

Figure 3.8: **Monotony of Bottom Topographies ensuring Constant Depth for Cone-shaped Beds in presence of Bottom Friction,** $\gamma_b = 0.05$**,** $\alpha = \pm 0.4$**,** $y_0 = 0.5$**.** Boundary radius ξ_0 is imposed to be 1 for the divergent flow ($\alpha = 0.4$, right column), 25 for the convergent flow ($\alpha = -0.4$, left column). Top figures (3.8(a), 3.8(b)) report the overall behaviour of the right hand side $rhs(\xi)$ of Eq. 3.13, while bottom figures (3.8(c), 3.8(d)) report the behaviour of its specific terms: Friction $-\alpha/\xi^2 y_0^3$, Radiant Specific Kinetic Height $2/\xi^3 y_0^2$ and Basal Slope γ_b. The two red dots reported in Fig. 3.8(b) are the zeros of the right hand side of Eq. 3.8, corresponding (in increasing order) to a maximum and a minimum of the bottom topography $\zeta(\xi)$. Plot range is $\xi \in$ [1,25].

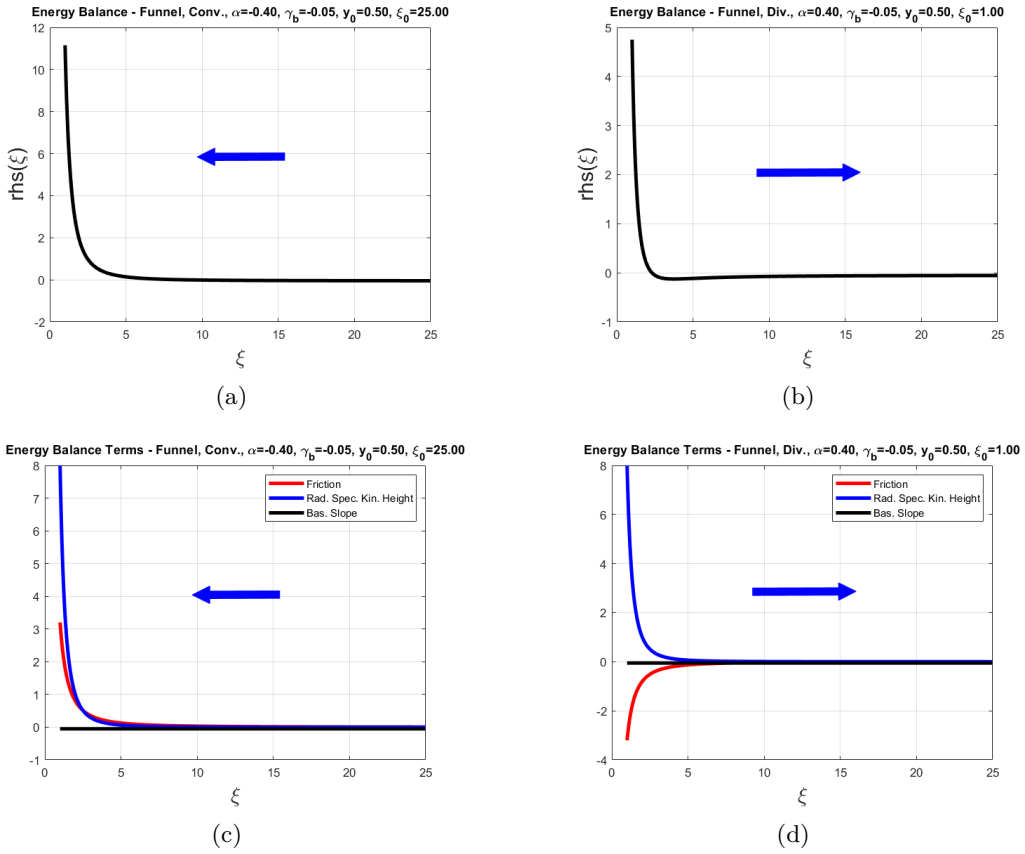

Figure 3.9: **Monotony of Bottom Topographies ensuring Constant Depth for Funnel-shaped Beds in presence of Bottom Friction,** $\gamma_b = -0.05$**,** $\alpha = \pm 0.4$**,** $y_0 = 0.5$**.** Boundary radius ξ_0 is imposed to be 1 for the divergent flow ($\alpha = 0.4$, right column), 25 for the convergent flow ($\alpha = -0.4$, left column). Top figures (3.9(a), 3.9(b)) report the overall behaviour of the right hand side $rhs(\xi)$ of Eq. 3.13, while bottom figures (3.9(c), 3.9(d)) report the behaviour of its specific terms: Friction $-\alpha/\xi^2 y_0^3$, Radiant Specific Kinetic Height $2/\xi^3 y_0^2$ and Basal Slope γ_b. Plot range is $\xi \in$ [1,25].

Choice of the Boundary Conditions

Unlike what done the previous Chapters, where the boundary conditions were chosen differently for the supercritical and subcritical regime in order to ensure unitary Stream Head at the boundary (according to the benchmark case of Horizontal Bed with Flat Bottom described in Sec. 2.1), here the following methods are used to impose boundary conditions:

- choose the height y_0 and the Froude Number at the boundary in order to obtain, by inverting expression 3.17, the coordinate ξ_0 at which imposing the boundary bottom height $\zeta_{UH}(\xi_0)$;
- choose the radial position ξ_0 at which imposing not only the boundary bottom height

$\zeta_{UH}(\xi_0)$, but also the boundary Froude Number from which y_0 is determined by using again 3.17;

- simply choose the uniform height y_0 and the radial position ξ_0 at which imposing boundary bottom height $\zeta_{UH}(\xi_0)$, the Froude Number being them a consequence by 3.17.

Such three ways are identically useful and suitable for the problem analyzed.

3.1.3 Everywhere Critical Flow Topography

Let consider the problem of finding a bottom topography $\zeta(\xi)$ such that the flow is everywhere critical. It is recalled here that the critical depth $y_cr(\xi)$ is described by expression 1.21, here reported for the sake of clearness:

$$y_{cr}(\xi) = \sqrt[3]{\frac{2}{\xi^2}} \tag{3.19}$$

By plugging such expression into Eq. 3.1 and re-organizing the two members, one obtains:

$$\frac{d\zeta}{d\xi} = \gamma_b - \frac{\alpha}{2} + \sqrt[3]{\frac{2}{\xi^5}} \tag{3.20}$$

where at the right hand side, from left to right, one can find the energetic contributes of basal slope, friction and kinetic energy, this latter one being easily recognized by the following chain of equalities :

$$\sqrt[3]{\frac{2}{\xi^5}} = \frac{d}{d\xi}\left[\tilde{H}(\xi, y_{cr}(\xi))\right] = \frac{2}{\xi^3[y_{cr}(\xi)]^2} = k_s(\xi, y_{cr}(\xi))$$

where $\tilde{H}(\xi, y_{cr}(\xi)) = \tilde{H}(\xi, y)|_{y=y_{cr}(\xi)}$ and $k_s(\xi, y_{cr}(\xi))$ are respectively the Stream Head and the Radiant Specific Kinetic Height associated to the critical solution $y_{cr}(\xi)$.
In order to study the monotony of the bottom topography $\zeta(\xi)$ one obtains by the right hand side of Eq. 3.20 the following inequality, in the domain $\{\xi > 0\}$:

$$\sqrt[3]{\frac{2}{\xi^5}} \geq \frac{\alpha}{2} - \gamma_b \tag{3.21}$$

Two cases can be distinguished, giving rise to two different kinds of bottom topography:

- if $\alpha < 2\gamma_b$, then $\frac{d\zeta}{d\xi} > 0$ for all possible $\xi > 0$, giving rise to monotonic bottom topographies;
- if $\alpha \geq 2\gamma_b$, then the bottom topographies so obtained are non-monotonic and exhibit a maximum point located at $\xi = \sqrt[5]{\frac{(\alpha-2\gamma_b)^3}{2}}$

The monotony properties for topographies ensuring critical depth when bottom friction is negligible ($\alpha = 0$) or the stream flows along a horizontal bed ($\gamma_b = 0$) can be easily studied by interpreting these as particular cases of Ineq. 3.21.
An important difference with respect to Equations 3.2, 3.8 (respectively describing bottom topographies ensuring Constant Stream Head and Constant Stream Depth) is that here friction dissipation contribute does not depend on ξ: this reflects on the linear part of the bottom topographies, obtained by direct integration Eq. 3.20 and re-naming of $\zeta(\xi)$ as $\zeta_{CR}(\xi)$ [6], as follows:

$$\zeta_{CR}(\xi) = \zeta_{CR}(\xi_0) + (\gamma_b - \frac{\alpha}{2})(\xi - \xi_0) - \sqrt[3]{\frac{27}{4\xi^2}} + \sqrt[3]{\frac{27}{4\xi_0^2}} \tag{3.22}$$

Examples of bottom topographies obtained with different values of α and γ_b are reported in Figures 3.10, 3.11, 3.12.
Notice that also Critical Stream Profile does not exhibit singular behaviour at a minimum or maximum radius like for the profiles obtained in Chapter 2, but for a different reason with respect to what discussed in Section 3.1.2 for the Constant Depth Solution. Indeed, while in that case the singularity was eliminated by imposing $y(\xi) \equiv y_0$, here for $y(\xi) = y_{cr}(\xi)$ the left hand side of the general governing Equation 3.1 is null because it is studied exactly at the singularity, i.e., when the Froude Number is exactly 1, having from Eq. 3.1:

$$\left[\frac{dy}{d\xi}(1 - Fr^2(\xi, y))\right]|_{y=y_{crit}(\xi)} \equiv 0$$

Therefore, it makes sense to study the Critical Solution, as well as the Bottom Topography and all of the other terms involved into Eq. 3.20 for all $\xi > 0$.
In order to investigate the interaction between basal slope, friction and kinetic energy gain or dissipation to determine bottom topography according to the balance expressed by Eq. 3.20, one can again figure out a stream flowing on convergent direction starting from an external reservoir located at radial position $\xi = \xi_0$ which is not drained by any central hole (Fig. **??**), and visualize the energetic contributes into two areas:

- for sufficiently small ξ, where kinetic energy dominates while basal slope and friction have barely no effect;
- for larger ξ, where kinetic energy contribute decays to 0, being overbalanced by the interplay between friction dissipation and energy gain/loss due to basal slope γ_b, both independent on ξ according to Eq. 3.20.

For sufficiently small radii, i.e., $\xi \to 0$, the dominant term of Eq. 3.20 is that connected to Kinetic Energy, which blows up to $+\infty$: it is expected, since the fluid is not drained from any hole and the bounded contribute of basal slope γ_b and dissipation α is not

[6] The subscript "CR" stands for "Critical".

enough to control such a high energy increase in order to maintain critical conditions. The equilibrium term required comes instead from bottom topography which, by means of its opposite energetic contribute, counterbalances that of Kinetic Height and is responsible for the characteristic strongly decreasing behaviour down to $-\infty$, independently from the values of α and γ_b, as reported in Figures 3.10, 3.11, 3.12.
Looking instead at the behaviour of $\zeta_{CR}(\xi)$ for sufficiently large values of ξ, it can be observed that while the contribute of Kinetic Height in Eq. 3.20 decays to 0, those of friction and basal slope become progressively more significant and both determine the asymptotic slope of the bottom topography, since they are both independent on the radial position ξ. In particular:

$$\zeta_{CR}(\xi) \approx \zeta_{CR}(\xi_0) + (\gamma_b - \frac{\alpha}{2})(\xi - \xi_0) \tag{3.23}$$

Also in this case, the bed shape which determines everywhere critical flux is approximately linear at sufficiently large ξ, but the dominant term is governed not only by the bottom angle (γ_b), but also by friction, by means of the parameter α: it regulates increasing or decreasing in order to maintain critical depth, that for sufficiently large ξ decays to 0. The overall behaviour of the right hand side of Eq. 3.20 and of its terms separately is reported in Figures 3.13, 3.14 in order to illustrate their balance giving rise to the monotony properties of the so obtained bottom topographies.

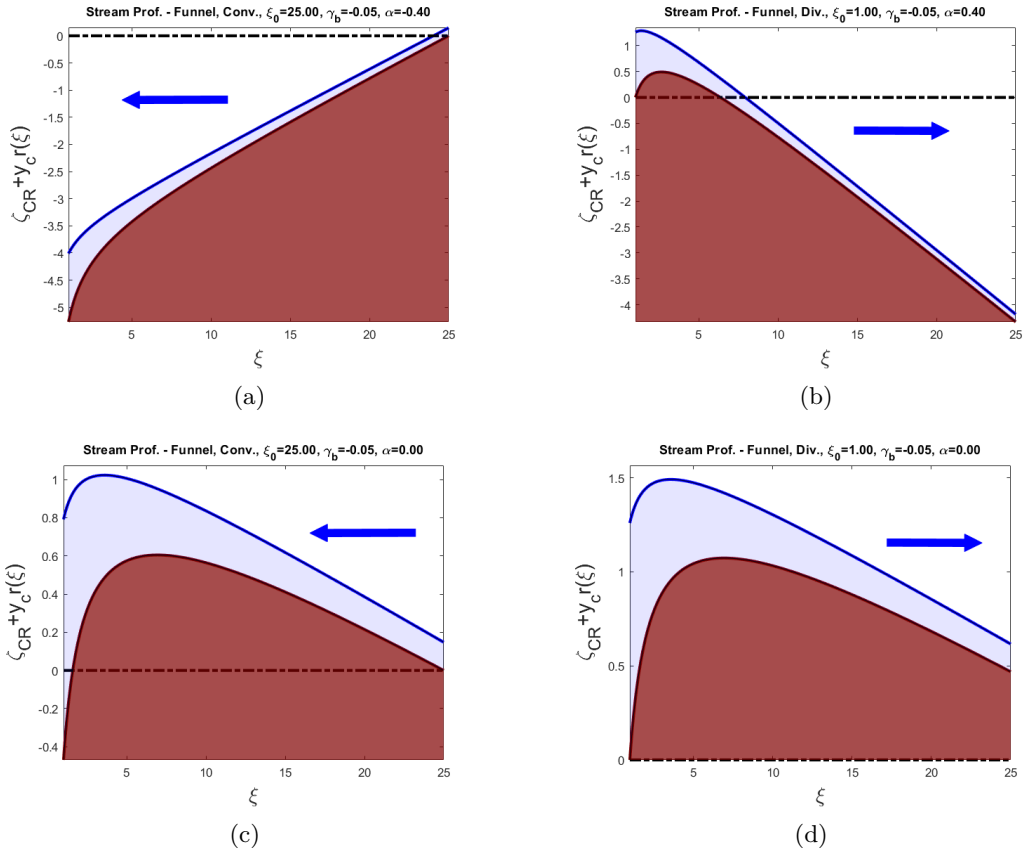

Figure 3.10: **Bottom Topography ensuring Critical Depth Stream flowing along a Funnel-Shaped bed.** Left and right column respectively refer to flows along Convergent and Divergent direction, as indicated by the blue arrows. For all of the stream profiles, the bottom topography at boundary $\zeta_{UH}(\xi_0)$ is imposed to be 0. For each figure boundary radius ξ_0, basal slope γ_b and friction coefficient α are reported: in particular, bottom figures (Fig. 3.5(c) and 3.5(d)) report the case in which friction is absent, i.e., $\alpha = 0$. Finally, the dot-dashed line indicates the level of the flat bottom. Plot range is $\xi \in$ [1,25].

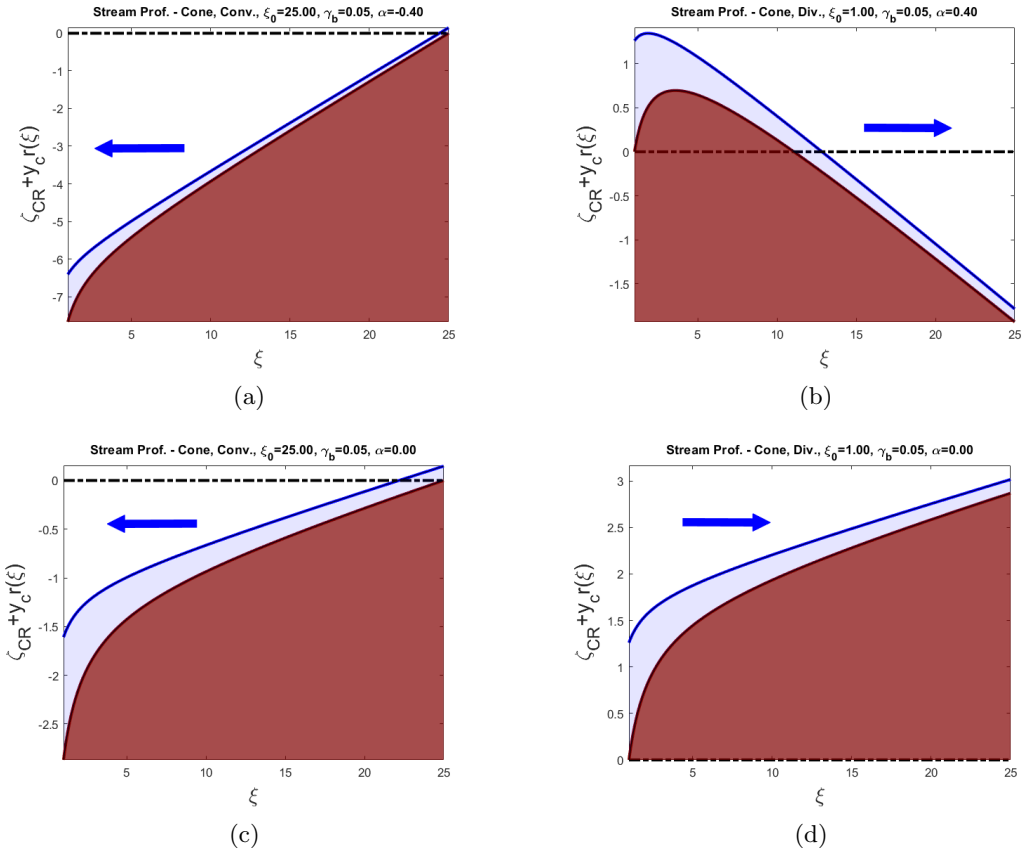

Figure 3.11: **Bottom Topography ensuring Critical Depth Stream flowing along a Cone-Shaped bed.** Left and right column respectively refer flows along Convergent and Divergent direction, as indicated by the blue arrows. For all of the stream profiles, bottom topography at boundary $\zeta_{UH}(\xi_0)$ is imposed to be 0. For each figure boundary radius ξ_0, basal slope γ_b and friction coefficient α are reported: in particular, bottom figures (Fig. 3.11(c) and 3.11(d)) report the case in which friction is absent, i.e., $\alpha = 0$. Finally, the dot-dashed line indicates the level of the flat bottom. Plot range is $\xi \in [1,25]$.

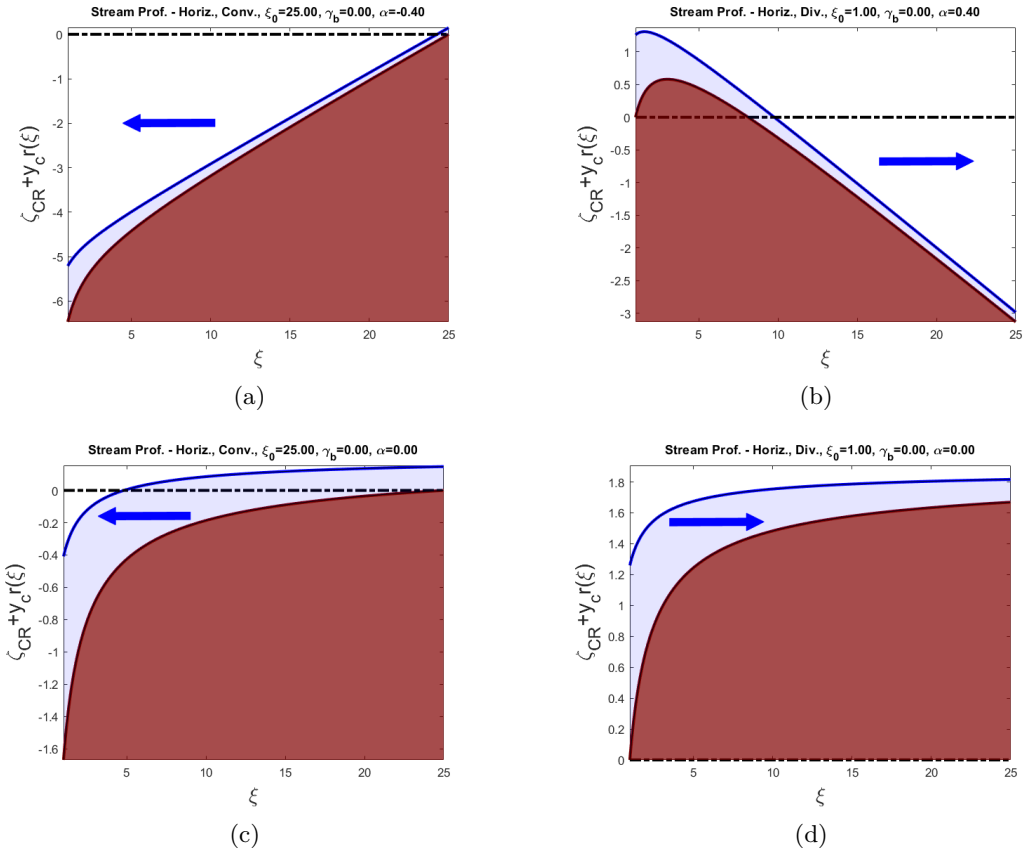

Figure 3.12: **Bottom Topography ensuring Critical Depth Stream flowing along a Horizontal Bed.** Left and right column respectively refer to flows along Convergent and Divergent direction, as indicated by the blue arrows. For all of the stream profiles reported, bottom topography at boundary $\zeta_{UH}(\xi_0)$ is imposed to be 0. For each figure boundary radius ξ_0, basal slope γ_b and friction coefficient α are reported: in particular, bottom figures (Fig. 3.12(c) and 3.12(d)) report the case in which friction is absent, i.e., $\alpha = 0$. Finally, the dot-dashed line indicates the level of the flat bottom. Plot range is $\xi \in$ [1,25]

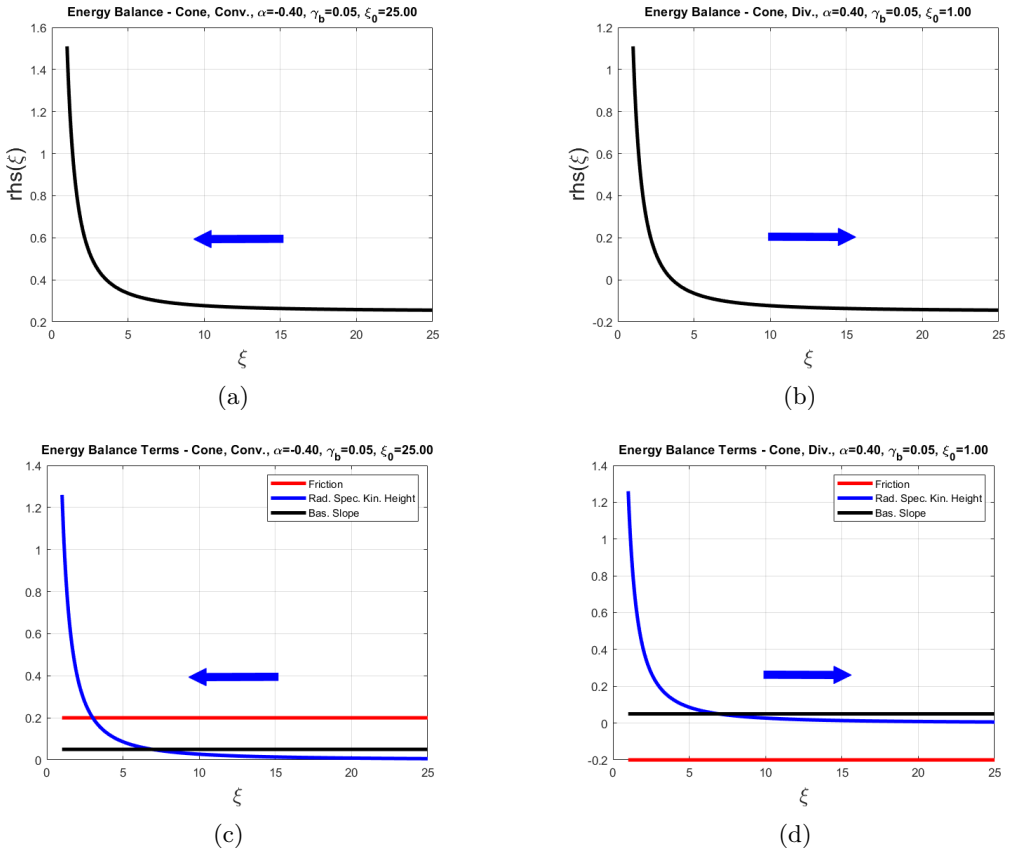

Figure 3.13: **Monotony of Bottom Topographies ensuring Critical Depth for Cone-shaped Beds in presence of Bottom Friction,** $\gamma_b = 0.05$**,** $\alpha = \pm 0.4$**.** Boundary radius ξ_0 is imposed to be 1 for the divergent flow ($\alpha = 0.4$, right column), 25 for the convergent flow ($\alpha = -0.4$, left column). Top figures (3.13(a), 3.13(b)) report the overall behaviour of the right hand side $rhs(\xi)$ of Eq. 3.20, while bottom figures (3.13(c), 3.13(d)) report the behaviour of its specific terms: Friction $-\alpha/2$, Radiant Specific Kinetic Height $\sqrt[3]{2/\xi^5}$ and Basal Slope γ_b.

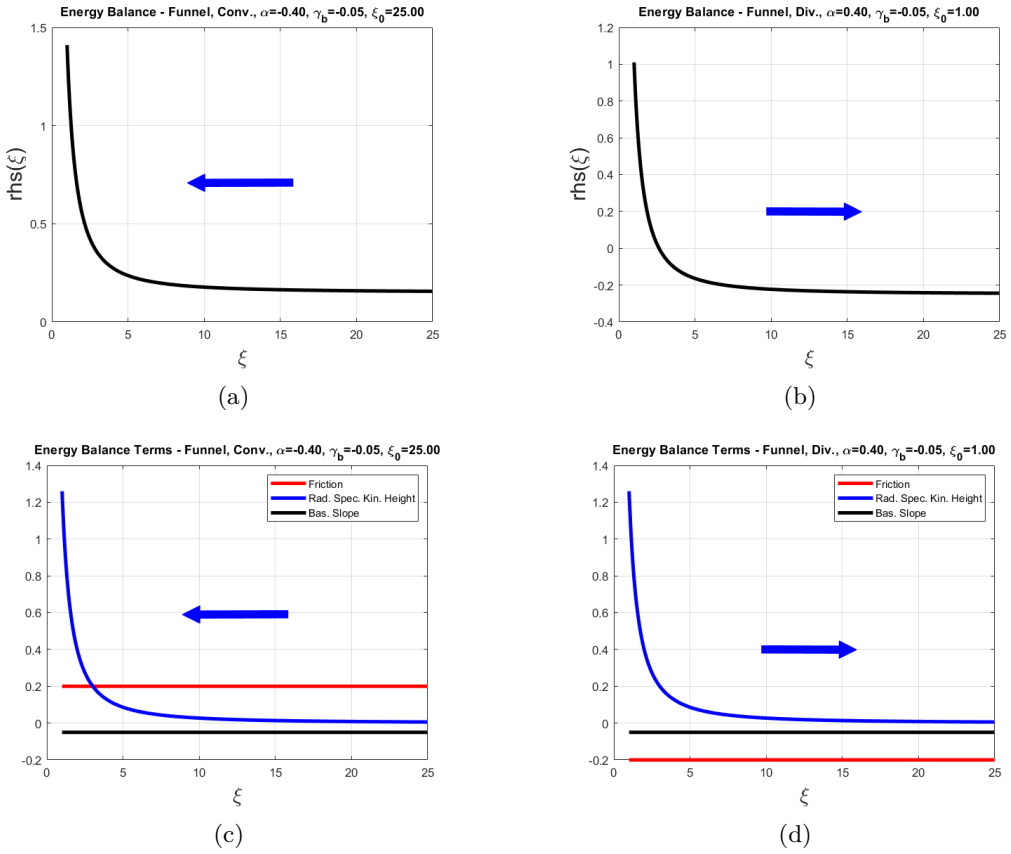

Figure 3.14: **Monotony of Bottom Topographies ensuring Critical Depth for Funnel-shaped Beds in presence of Bottom Friction,** $\gamma_b = -0.05$**,** $\alpha = \pm 0.4$**.** Boundary radius ξ_0 is imposed to be 1 for the divergent flow ($\alpha = 0.4$, right column), 25 for the convergent flow ($\alpha = -0.4$, left column). Top figures (3.14(a), 3.14(b)) report the overall behaviour of the right hand side $rhs(\xi)$ of Eq. 3.20, while bottom figures (3.14(c), 3.14(d)) report the behaviour of its specific terms: Friction $-\alpha/2$, Radiant Specific Kinetic Height $\sqrt[3]{2/\xi^5}$ and Basal Slope γ_b.

3.2 Boundary Conditions

According to the analysis performed in Sec. 3.1, Constant Stream Head solution is obtained by imposing a balance between the energy contributes of topographical slope (i.e., cumulative of the slope contributes due to both basal angle ϕ and bottom topography $d\zeta/d\xi$) and friction. Therefore, assuming bottom topography $\zeta(\xi) = \zeta_{CH}(\xi)$ as found in 3.7, Eq. 3.1 reduces to Eq. 2.7, obtained for the Horizontal Bed with Flat Bottom and expressing Stream Energy conservation.
Therefore, the stream height solution $y(\xi)$ is given by:

$$\xi = \frac{1}{y\sqrt{1-y}}$$

For all of the cases that will be discussed throughout the rest of this chapter, such solution will be used (as for Chapter 2) to impose supercritical and subcritical boundary conditions (although differently specified, as will be done in several cases) for the stream heights, in the way described in Sec. 2.1.2, remarking the important benchmark role of the case of Horizontal Bed with Flat Bottom.

3.3 Flat Bottom Topography

This section is devoted to the study of the Shallow-water model with general formulation expressed by 1.33 in the particular case of flat bottom, which is expressed by the following bottom topography:

$$\zeta(\xi) \equiv 0 \tag{3.24}$$

Then Eq. 1.33 describing the height profile assumes the following form:

$$\frac{dy}{d\xi} = \frac{\gamma_b \xi^3 y^3 + 2y - \alpha\xi}{\xi^3 y^3 - 2\xi} = \frac{N(\xi, y)}{D(\xi, y)} \tag{3.25}$$

or, equivalently:

$$\frac{d}{ds}\begin{bmatrix}\xi \\ y\end{bmatrix} = \begin{bmatrix}\xi^3 y^3 - 2\xi \\ \gamma_b \xi^3 y^3 + 2y - \alpha\xi\end{bmatrix} \tag{3.26}$$

where $(\xi, y) = (\xi(s), y(s))$ is a parametrization of the orbits in the parameter $s \in A \subseteq \mathbb{R}$, as in 1.42. , Since the goal of this study is to investigate how taking into account friction alters the dynamics with respect to the same case in absence of friction, discussed in Sections 2.1, 2.2, the section organizes as follows:

- analysis of the geometry of the phase plane;
- solutions for different values of bottom slope γ_b.

3.3.1 Geometry of the Phase Plane

The study of the geometry of the Phase Plane when friction is taken into account in the Shallow-water model described by 3.26 is focused on two main aspects: the intersections of the nullclines of Eq. 3.25 [7], equivalent to the equilibrium points of System 3.26 and the structure of the trajectories, by varying bottom slope γ_b (particularly its sign) and friction coefficient α, actually the only parameters of the model.

[7] The nullclines of Eq. 3.25 are expressed by the equations $N(\xi, y) = 0$ and $D(\xi, y)$=0, the last one corresponding to the Critical Line $y = \sqrt[3]{2/\xi^2}$

Intersections of the Nullclines

The starting point is to study the intersections of the nullclines of Eq. 1.33, i.e., $N(\xi, y) = 0$ and $D(\xi, y = 0)$. Indeed, at these points one has $dy/d\xi = [0/0]$, thus the trajectories (describing the height profiles) can pass through these points with either finite or infinite gradient, as described by [4]. The only intersection can be easily computed exactly, according to 1.46, as:

$$\begin{cases} \xi_* = 2^{\frac{1}{5}} t_*^{-\frac{3}{5}} \\ y_* = 2^{\frac{1}{3}} \xi_*^{-\frac{2}{3}} = 2^{\frac{1}{5}} t_*^{\frac{2}{5}} \end{cases} \tag{3.27}$$

where t_* is the generalized slope at the equilibrium points as defined in 1.44, which for the specific case of flat bottom topography assumes the following form:

$$t_* = -\gamma_b + \frac{\alpha}{2} \tag{3.28}$$

It is worth to notice that such intersection lies within the physical domain $\{\xi > 0\} \times \{y > 0\}$ if and only if $t_* > 0$, i.e.:

$$\alpha > 2\gamma_b$$

In order to investigate the internal stability properties of such point as equilibrium point of System 3.26, one can use 1.50 and 1.51 to respectively determine the Trace and Determinant of the corresponding Jacobian Matrix evaluated at (ξ_*, y_*) as follows:

$$(\text{tr } \mathbf{J_F})|_{(\xi_*, y_*)} = 3\alpha t_*^{-1} = \frac{6\alpha}{\alpha - 2\gamma_b} \tag{3.29}$$

and:

$$(\det \mathbf{J_F})|_{(\xi_*, y_*)} = 4(5 + 6 \cdot 2^{\frac{1}{5}} \zeta_*'' t_*^{-\frac{3}{5}}) = 20 \tag{3.30}$$

since $\zeta_*'' = \frac{d^2\zeta}{d\xi^2}|_{\xi=\xi^*} = 0$. Therefore, at a physically meaningful intersection, one has:

- sign of the Jacobian Trace equal to that of α;
- positive determinant, independently from the values of α and γ_b.

Moreover, one can compute the discriminant of the characteristic polynomial associated to the Jacobian Matrix as:

$$\Delta_* = [(\text{tr } \mathbf{J_F})|_{(\xi_*, y_*)}]^2 - 4(\det \mathbf{J_F})|_{(\xi_*, y_*)} = (\alpha/2 - \gamma_b)^2 - 80 \tag{3.31}$$

Mathematically, it is possible to choose α and γ_b such that $\Delta_* \geq 0$. However, according

to the values chosen for γ_b and α [8], the quantity $\alpha/2 - \gamma_b$ is typically two up to three orders of magnitude below 80, therefore it can be assumed that $\Delta_* < 0$.

Thanks to this, one can conclude that the point $(\xi_*, y_*) = \left(\sqrt[5]{\frac{2}{(\alpha/2-\gamma_b)^3}}, \sqrt[5]{2(\alpha/2-\gamma_b)^2} \right)$ is a focus, in particular:

- if $\alpha > 0$, it is an unstable focus;
- if $\alpha > 0$, it is a stable focus.

Phase portraits containing the focus are reported in Fig. 3.15.
A finest range for the values of α and a specific region where the focus should be located to produce effect on the solutions will be provided after the description of the trajectories, when the energetic point of view will be highlighted.

[8] **Recall**: suitable values for γ_b used in this work to maintain the hypothesis of gradually varied flow are $-0.10 \leq \gamma_b \leq 0.10$, while typical values of friction coefficients range between -1 and 1.

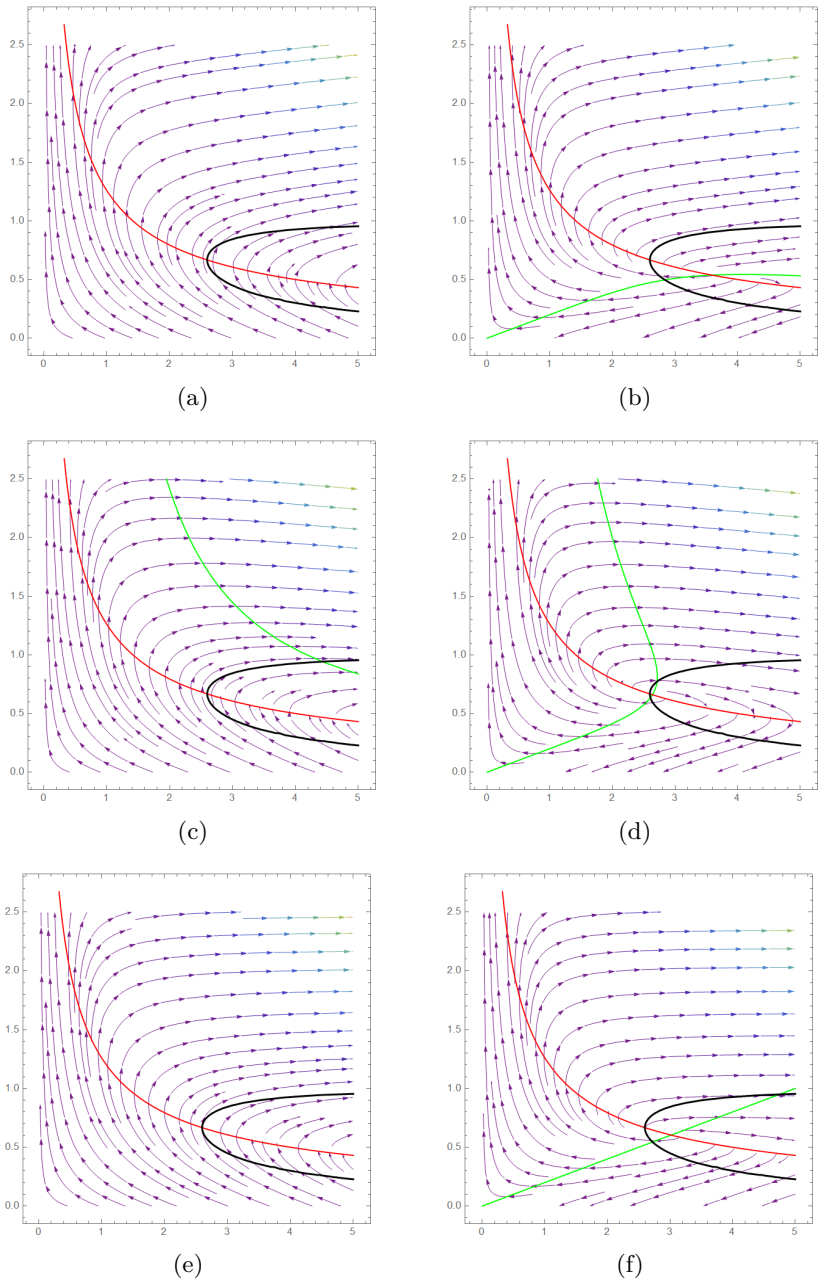

Figure 3.15: $\xi - y$ **Phase Portrait** Horizontal axis reports the radius ξ, the vertical one reports the corresponding values of height y, based on Eq. 3.25. Red line marks Critical conditions: subcr. trajectories lie under the red line, while supercr. ones lie above. Green line is the nullcline $N(\xi, y) = 0$ of Eq. 3.25. Black line depicts $y(\xi)$ for the Conservative Solution (Hor. Bed with Flat Bott. with no friction, Sec. 2.1). Left column, Figures 3.15(a), 3.15(c), 3.15(e) - Flows on Convergent direction ($\alpha = -0.4$) for Cone, Funnel and Horiz. Bed (resp., $\gamma_b = 0.05, -0.05, 0$). Right column, Figures 3.15(b), 3.15(d), 3.15(f) - Flows on Divergent direction ($\alpha = 0.4$) for Cone, Funnel and Horiz. Bed (resp., $\gamma_b = 0.05, -0.05, 0$).

Trajectories

A first novel aspect with respect to the case of flat bottom without including friction discussed in Sections 2.1, 2.2 emerges by looking at the trajectories, some examples of which are reported in Fig. 3.15 for $\alpha = \pm 0.4$ and $\gamma_b = 0.05, -0.05, 0$. Indeed, it appears that:

- the subcritical trajectories are mainly governed by the basal slope γ_b, and exhibit a similar behaviour with respect to the inviscid case: for $\gamma_b \geq 0$, they collide with the Critical Line at exactly one point, showing a *one Froude Horizon* behaviour, while if $\gamma_b < 0$ they meet the Critical Line at a minimum and a maximum point, thus exibiting a *two Froude Horizons* behaviour;
- the supercritical trajectories, on the contrary, are mainly governed by friction, showing a completely different behaviour with respect to the inviscid case: independently from γ_b, supercritical streams flowing on convergent directions ($\alpha < 0$) collide with the Critical Line at exactly one point (*one Froude Horizon* behaviour), while those flowing on divergent direction ($\alpha > 0$) collide with the Critical Line at a minimum and a maximum radius (*two Froude Horizon* behaviour).

The reason of this different behaviour resides again in the behaviour of the Radiant Specific Discharge q with respect to the stream height y. Their relation, however, is no longer algebraic as for the case with no friction, but differential. In order to obtain it, one can remember by the definition 1.23 itself that:

$$q(\xi) = \frac{1}{\xi}$$

from which the differential $d\xi$ can be expressed as:

$$d\xi = -\xi^2 dq = -\frac{1}{q^2}\, dq$$

and Eq. 3.25 assumes the following form [9]:

$$\frac{dq}{dy} = \frac{2q^4 - y^3 q^2}{\gamma_b y^3 + 2q^3 y - \alpha q^2} = \frac{N_q(q,y)}{D_q(q,y)} \tag{3.32}$$

One can then compute the intersections between the nullclines $N_q(q,y) = 0$ [10] and

[9] It is worth to notice that this can be done only by assuming that the Inverse Function Theorem holds for $y = y(q)$ separately for the supercritical and the subcritical branch of each orbit, since only the restriction to one of the branches is actually a function.

[10] The nullcline $N_q(q,y) = 0$ is represented by the line $q(y) = \sqrt{\frac{y^3}{2}}$ and it is nothing but the Critical Line in terms of q and y.

$D_q(q, y) = 0$ to obtain, as expected, that the only one is given by:

$$\begin{cases} q_* = \sqrt[5]{\frac{(\alpha/2-\gamma_b)^3}{2}} = \frac{1}{\xi_*} \\ y_* = \sqrt[3]{2q_*^2} \end{cases} \tag{3.33}$$

The point (y_*, q_*) represents a focus (for the typical values of α and γ_b used in this work) and, as seen for the focus (ξ_*, y_*) in the $y - \xi$ diagram, it lies in the physical region $\{y > 0\} \times \{q > 0\}$ only when $\alpha/2 > \gamma_b$, i.e., when friction dissipation overcomes the energy contribute of basal slope. Again, if one restricts to the typical values of γ_b and α used, the focus lies in the physical regions for almost all $\alpha > 0$, that is, for divergent flows, which in the $q - y$ plane are those on decreasing q direction [11].
Fig. 3.16 reports the phase planes $q-y$ obtained for different couples (α, γ_b), where $\alpha \neq 0$. It is evident that:

- for $\gamma_b < 0$, $\alpha > 0$, where the flow is divergent on opposite slope, the trajectories start at a maximum discharge (minimum radius), that can be thought as a central source and flow along decreasing q (increasing radius), with the friction dissipation amplifying the contrasting effect due to the opposite slope. The focus than forces both supercritical and subcritical reaches to collide again with the Critical Line at a minimum q (maximum radius), that can be exemplified by the edge of the plate: for smaller radii, flow would not be so energetic to continue;

- for $\gamma_b > 0$, $\alpha > 0$, where the flow is divergent on favourable slope, both supercritical and subcritical trajectories start in critical condition; however, while the subcritical trajectories continue helped by favourable slope along decreasing q (increasing ξ), which is asymptotically 0, the supercritical trajectories accelerate until reaching a maximum velocity at the minimum height, than decelerate to collide again with the Critical Line at a minimum q (maximum ξ).

By considering $\alpha = 0$, one can mathematically explain also the case of Flat Bottom with no friction discussed in Sec. 2.2.3. Indeed, the only equilibrium point is given by:

$$\begin{cases} q_* = \sqrt[5]{\frac{-\gamma_b^3}{2}} = \frac{1}{\xi_*} \\ y_* = \sqrt[3]{2q_*^2} \end{cases} \tag{3.34}$$

and lies within the physical region $\{y > 0\} \times \{q > 0\}$ only if $\gamma_b < 0$, that is, for funnel-shaped beds, which effectively are those exhibiting the *two Froude Horizons* behaviour.

[11] Since divergent flows are along increasing ξ and $q = 1/\xi$.

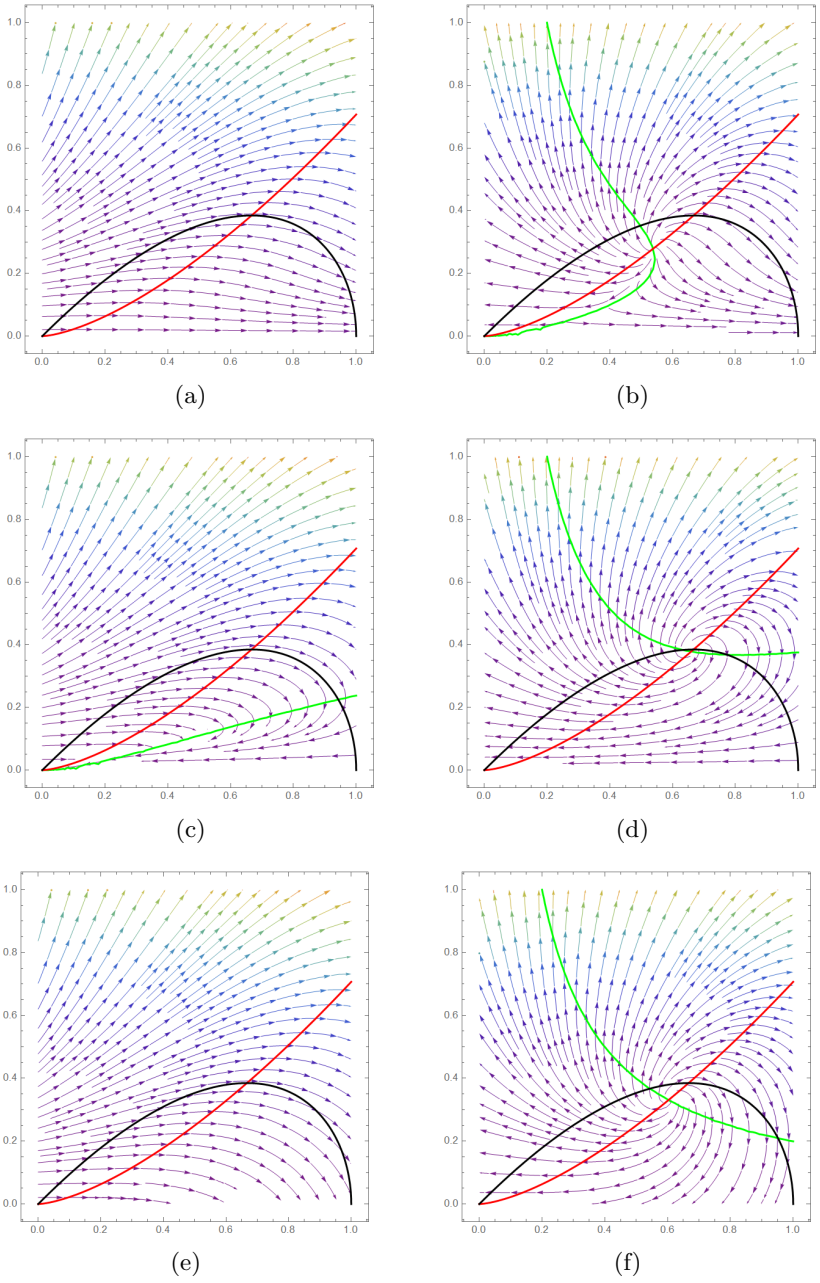

Figure 3.16: $q - y$ **Phase Portrait** Horizontal axis reports the Height values y, the vertical one reports the corresponding values of Radiant Specific Discharge $q = q(y)$, based on Eq. 3.32. Red line marks Critical conditions: subcr. trajectories lie under the red line, while supercr. ones lie above. Green line is the nullcline $N_q(y, q) = 0$ of Eq. 3.32. Black line depicts $q(y)$ for the Conservative Solution (Hor. Bed with Flat Bott. with no friction, Sec. 2.1), $q(y) = y\sqrt{1-y}$. Left column, Figures 3.16(a), 3.16(c), 3.16(e) - Flows on Convergent direction ($\alpha = -0.4$) for Cone, Funnel and Horiz. Bed (resp., $\gamma_b = 0.05, -0.05, 0$). Right column, Figures 3.16(b), 3.16(d), 3.16(f) - Flows on Divergent direction ($\alpha = 0.4$) for Cone, Funnel and Horiz. Bed (resp., $\gamma_b = 0.05, -0.05, 0$).

3.3.2 Energetic Point of View and Restricted Ranges for α

Looking at the physics of the problem, one can observe that when the stream flows on opposite slope and friction is considered its energy, expressed by the Stream Head $\tilde{H}(\xi, y(\xi)) = \frac{1}{\xi^2[y(\xi)]^2}$, once fixed a prescribed boundary value, can only diminish. In Sections 2.1.2 and 3.2 has been emphasized the benchmark role of the case of the Horizontal Bed with Flat Bottom to impose boundary condition, since it expresses energy conservation $H(\tilde{\xi}, y) \equiv 1$. The curve $H(\tilde{\xi}, y) = 1$, which in the plane $\xi - y$ describes the orbit expressing energy conservation, separates therefore two regions:

- the internal region, where $H(\tilde{\xi}, y) < 1$;
- the internal region, where $H(\tilde{\xi}, y) > 1$.

Therefore, solutions for which the Stream Head can only diminish with respect to that imposed at the boundary must lie into the internal region. This particularly holds for flows along Horizontal Bed (independently from the convergent or divergent direction of the flow), along convergent direction over a Cone-shaped Bed and along divergent direction over a Funnel-shaped Bed. In these cases, in order for the focus $(\xi_*, y_*) = \left(\sqrt[5]{\frac{2}{(\alpha/2-\gamma_b)^3}}, \sqrt[5]{2(\alpha/2-\gamma_b)^2}\right)$ to be included into the internal region, α must vary into a more restricted range. Indeed, by plugging the expression of (ξ_*, y_*) into the inequality $\tilde{H}(\xi, y) < 1$ and few algebraic computation, one obtains that:

$$\alpha < \frac{8}{9\sqrt{3}} + 2\gamma_b \tag{3.35}$$

This is coherent with previous literature for the Horizontal Bed, since by imposing $\gamma_b = 0$ one recovers the same inequality reported in [29], Sec. IV.

3.3.3 Solutions

In view of what discussed about the geometry of the Phase Plane $\xi - y$, the energetic point of view and the possibility of having hydraulic jump, solutions are obtained for different values of basal slope γ_b and friction coefficient α, which also encloses in its sign the direction of the flow. In particular, the following values will be used:

- $\gamma_b = -0.05,\ 0,\ 0.05$;
- $\alpha = -0.1, 0.1$

Such ranges are coherent with those adopted in [19, 29], i.e., small bottom slopes and small values of friction coefficient α. Moreover, $\alpha = \pm 0.1$ lies within the range discussed previously in Sec. 3.3.2. The stream profiles and features are reported, for both convergent and divergent direction, in the following figures:

- Figures 3.17, 3.18 for the Horizontal Bed, $\gamma_b = 0$, $\alpha = \pm 0.1$;
- Figures 3.19, 3.20 for the Cone-shaped Bed, $\gamma_b = 0.05$, $\alpha = \pm 0.1$;
- Figures 3.21, 3.22 for the Funnel-shaped Bed, $\gamma_b = -0.05$, $\alpha = \pm 0.1$.

Flow along a Horizontal Bed, $\gamma_b = 0$, $\alpha = \pm 0.1$

Height Profiles and Specific Forces are reported in Fig. 3.17, while Froude Number, Stream Head and Stream Profiles are reported in Fig. 3.18.
This case has been widely discussed in [29], with a numerical approach analogous to that pursued in this work and by [42], with a first order perturbation procedure to obtain an approximate analytical solution.
For the convergent case ($\alpha = -0.1$), the stream starts flowing with unitary Stream Head, in supercritical condition, from an external annular gate; before reaching critical conditions, a hydraulic jump connects the supercritical reach to the subcritical one, and the flow proceeds until reaching a central hole draining the fluid, whose edge is located at a minimum radius, in critical conditions.
For the divergent case ($\alpha = 0.1$), the stream starts flowing with unitary Stream Head, in supercritical condition, from a central source, which can be thought for example as originating from a jet impinging the bed; before reaching critical conditions, a hydraulic jump connects the supercritical reach to the subcritical one, and the flow proceeds along the plate indefinitely, in subcritical conditions.

Flow along a Cone-shaped Bed, $\gamma_b = 0.05$, $\alpha = \pm 0.1$

Height Profiles and Specific Forces are reported in Fig. 3.19, while Froude Number, Stream Head and Stream Profiles are reported in Fig. 3.20.
For the convergent case ($\alpha = -0.1$), the stream starts flowing with unitary Stream Head from an external annular source and proceeds over the cone decelerating, while consequently increasing height; before reaching critical conditions, a hydraulic jump connects the supercritical reach to the subcritical one, and the flow proceeds over the cone until reaching a central hole which drains the fluid, whose edge is located at a minimum radius.
For the divergent case ($\alpha = 0.1$), the stream springs from a central source in critical conditions and, after an acceleration, it decelerates although decreasing height; before reaching critical conditions, a hydraulic jump connects the supercritical reach to the subcritical one and then, helped by favourable slope, continues flowing down the cone indefinitely. The reason why the supercritical trajectories manifest this novel trajectory is the presence of the focus, as shown in Fig. 3.16(b) in the $q - y$ Phase Portrait, which attracts all of the supercritical trajectories if the flow is divergent, forcing them to meet critical conditions. Indeed, the flow proceeds along increasing ξ, i.e., for decreasing Radiant Specific Discharge q, thus the arrows reported in the Phase Portrait in Fig. 3.16(b) must be read in the inverse direction. Moreover, they are all forced to cross the Conservative Solution (that obtained for Horizontal Bed, Flat Bottom and no friction) and enter the internal region, where the Stream Head becomes minor of 1.

Flow along a Funnel-shaped Bed, $\gamma_b = -0.05$, $\alpha = \pm 0.1$

Height Profiles and Specific Forces are reported in Fig. 3.21, while Froude Number, Stream Head and Stream Profiles are reported in Fig. 3.22.
For the convergent case ($\alpha = -0.1$) the flow starts in supercritical condition (with Stream

Head greater than 1) from an external source; before reaching critical condition, a hydraulic jump connects the supercritical branch to the subcritical one, which flows with non monotonic profile until reaching a central hole draining the fluid, in critical conditions. Also in this case, the action of friction manifests in the presence of the focus in the Phase Portrait, from which the trajectories escape in case of Divergent Direction in such a way they exhibit a *two Froude Horizons* behaviour and are forced to cross the Conservative Solution Line, as shown in Fig. 3.16(c). Where they meet Critical Line, radiant specific discharge q attains its minimum (at the maximum radius) and its maximum (at the minimum radius): for radii greater than the maximum one, q would be too small for the stream to start flowing, while for radii smaller than the minimum one q would be too high to contemporary maintain total discharge Q conservation (Continuity Equation) while satisfying the Stream Head (Energy) described by Eq. 3.25. For the divergent case ($\alpha = 0.1$), instead, flow starts in supercritical condition from a central source (jet impinging the bed) and flows in supercritical conditions, on opposite slope; before reaching critical conditions, a hydraulic jump connects the supercritical reach to the subcritical one, that flows until reaching the external edge of the bed and the fluid is drained.

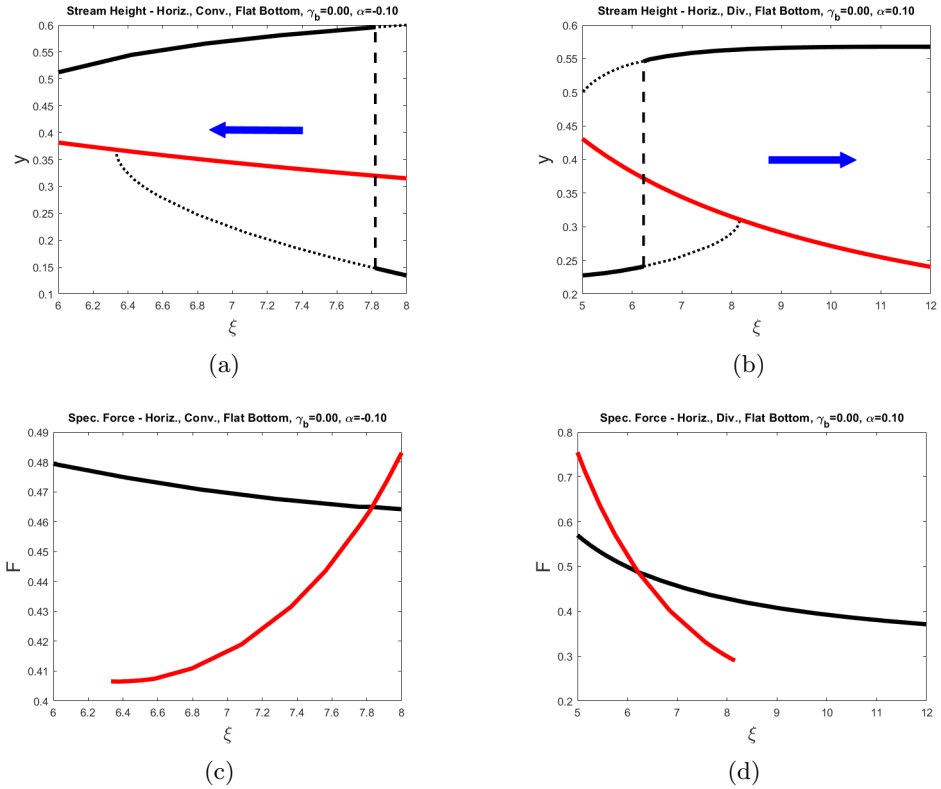

Figure 3.17: **Hydraulic Jump Solution - Stream flowing along a Horizontal Bed with Flat Bottom.** In each column Height Profile, Specific Force, Froude Number and Stream Head are reported for $\gamma_b = 0$ and $\alpha = -0.1$ (convergent flow, left column) and $\alpha = 0.1$ (divergent flow, right column) . Figures 3.17(a), 3.17(b): solid lines represent the solution with hydraulic jump (black and red respectively for the subcritical and supercritical branch), dotted line represent subcritical and supercritical solutions without jump, black dashed line represents the hydraulic jump. Figures 3.17(c), 3.17(d) show the behaviour of the specific force for the supercritical (red) and subcritical (black) branches of the solution.

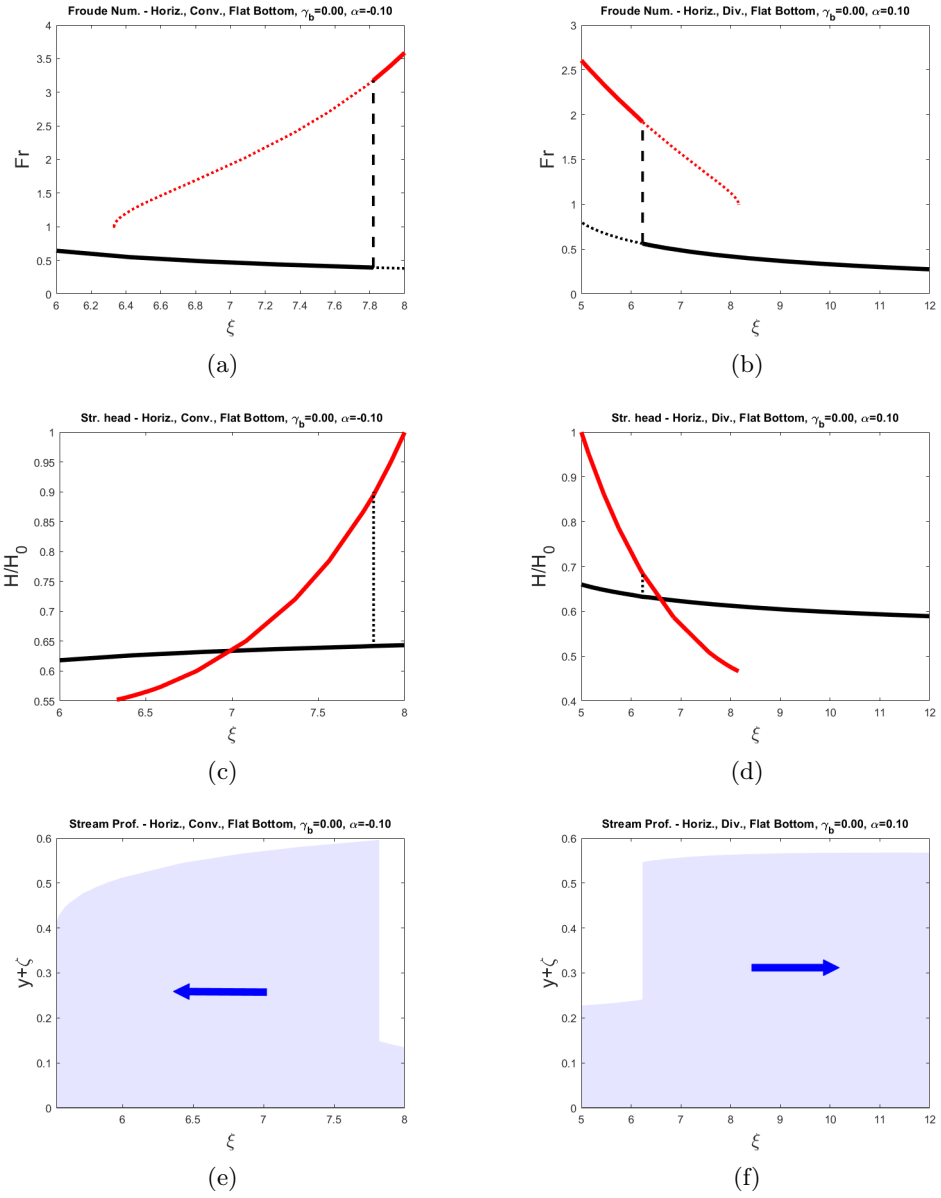

Figure 3.18: **Stream Flowing along a Horizontal Bed with Flat Bottom - Flow features.** In each column (top to bottom) Froude Number, Stream Head and Stream Profile are reported for $\gamma_b = 0$ and $\alpha = -0.1$ (convergent flow, left column) and $\alpha = 0.1$ (divergent flow, right column), basing on Fig. 3.17 . Figures 3.18(a), 3.18(b) (Froude Number) and Fig. 3.18(c), 3.18(d) (Stream Head) : solid lines represent the solution with hydraulic jump (black and red respectively for the subcritical and supercritical branch), dotted line represent subcritical and supercritical reach without jump, black dashed line represents the hydraulic jump. Figures 3.18(e), 3.18(f) show the stream profiles, i.e., the free surface of the fluid.

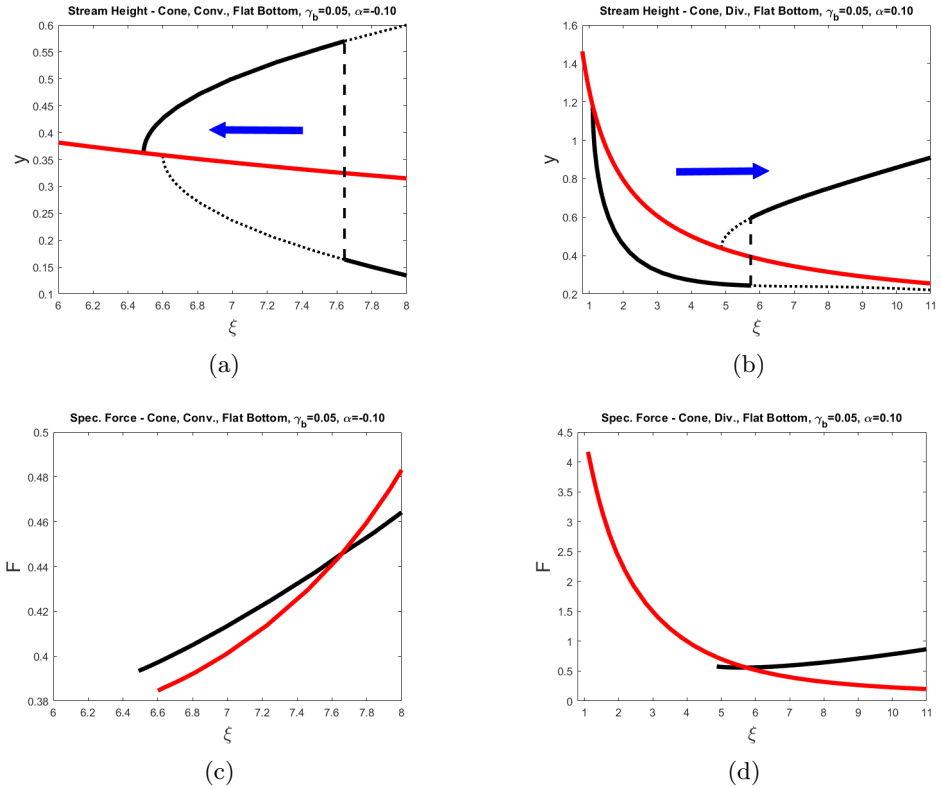

Figure 3.19: **Hydraulic Jump Solution - Stream flowing along a Cone-shaped Bed with Flat Bottom.** In each column Height Profile, Specific Force, Froude Number and Stream Head are reported for $\gamma_b = 0.05$ and $\alpha = -0.1$ (convergent flow, left column) and $\alpha = 0.1$ (divergent flow, right column) . Figures 3.19(a), 3.19(b): solid lines represent the solution with hydraulic jump (black and red respectively for the subcritical and supercritical branch), dotted line represent subcritical and supercritical solutions without jump, black dashed line represents the hydraulic jump. Figures 3.19(c), 3.19(d) show the behaviour of the specific force for the supercritical (red) and subcritical (black) branches of the solution.

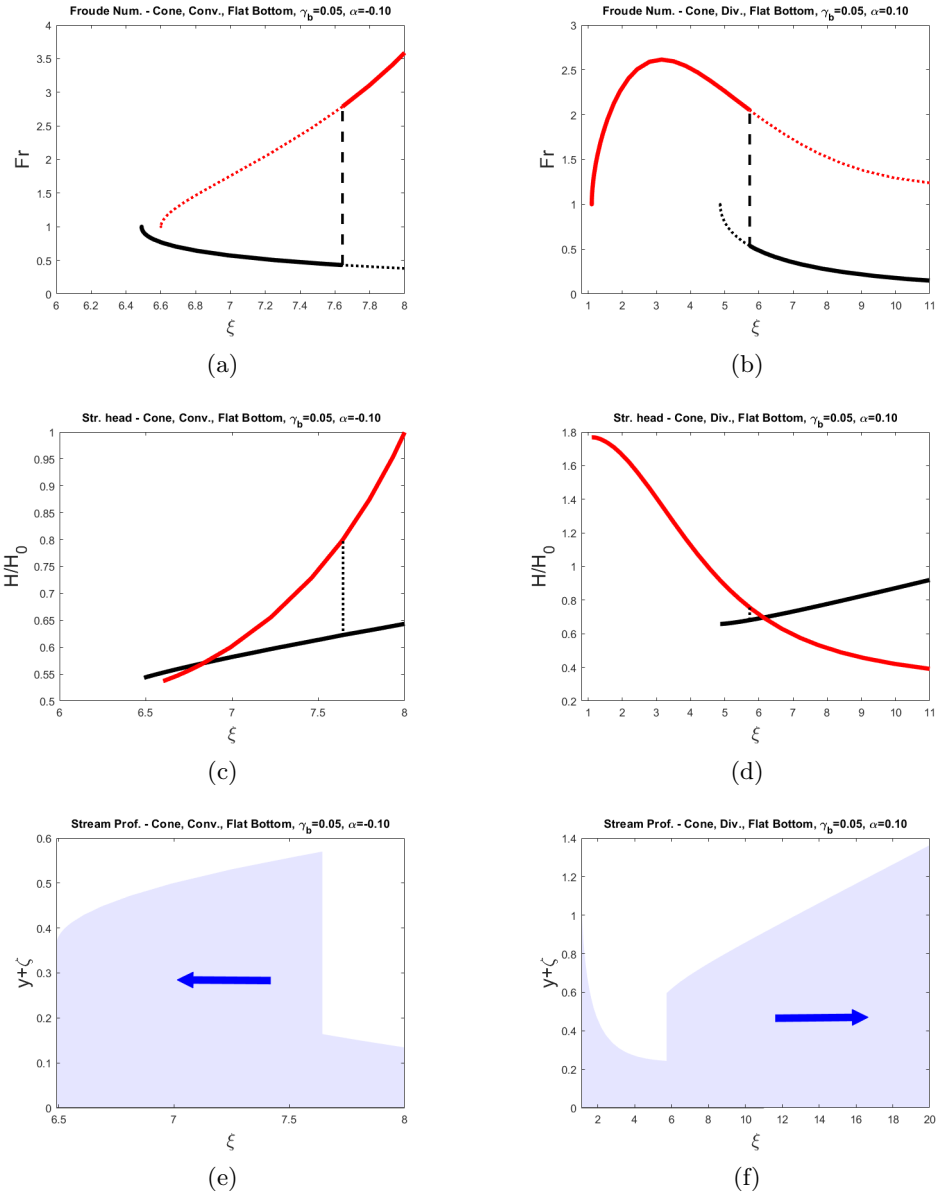

Figure 3.20: **Stream Flowing along a Cone-shaped Bed with Flat Bottom - Flow features.** In each column (top to bottom) Froude Number, Stream Head and Stream Profile are reported for $\gamma_b = 0.05$ and $\alpha = -0.1$ (convergent flow, left column) and $\alpha = 0.1$ (divergent flow, right column), basing on Fig. 3.19 . Figures 3.20(a), 3.20(b) (Froude Number) and Fig. 3.20(c), 3.20(d) (Stream Head) : solid lines represent the solution with hydraulic jump (black and red respectively for the subcritical and supercritical branch), dotted line represent subcritical and supercritical reach without jump, black dashed line represents the hydraulic jump. Figures 3.20(e), 3.20(f) show the stream profiles, i.e., the free surface of the fluid.

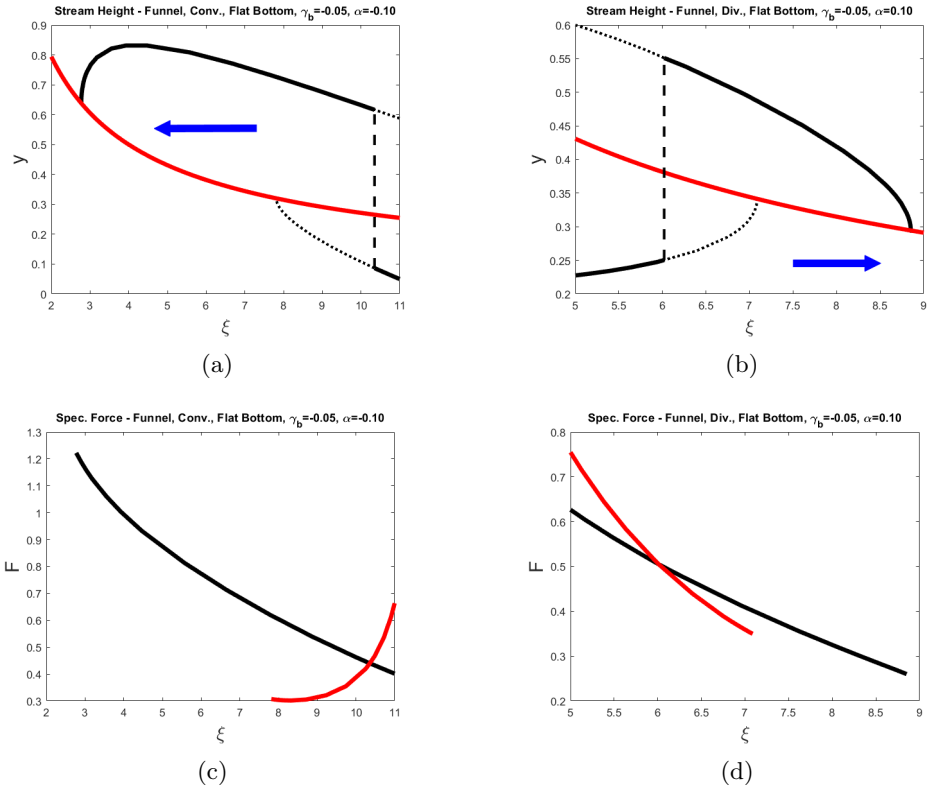

Figure 3.21: **Hydraulic Jump Solution - Stream flowing along a Funnel-shaped Bed with Flat Bottom.** In each column Height Profile, Specific Force, Froude Number and Stream Head are reported for $\gamma_b = -0.05$ and $\alpha = -0.1$ (convergent flow, left column) and $\alpha = 0.1$ (divergent flow, right column) . Figures 3.21(a), 3.21(b): solid lines represent the solution with hydraulic jump (black and red respectively for the subcritical and supercritical branch), dotted line represent subcritical and supercritical solutions without jump, black dashed line represents the hydraulic jump. Figures 3.21(c), 3.21(d) show the behaviour of the specific force for the supercritical (red) and subcritical (black) branches of the solution.

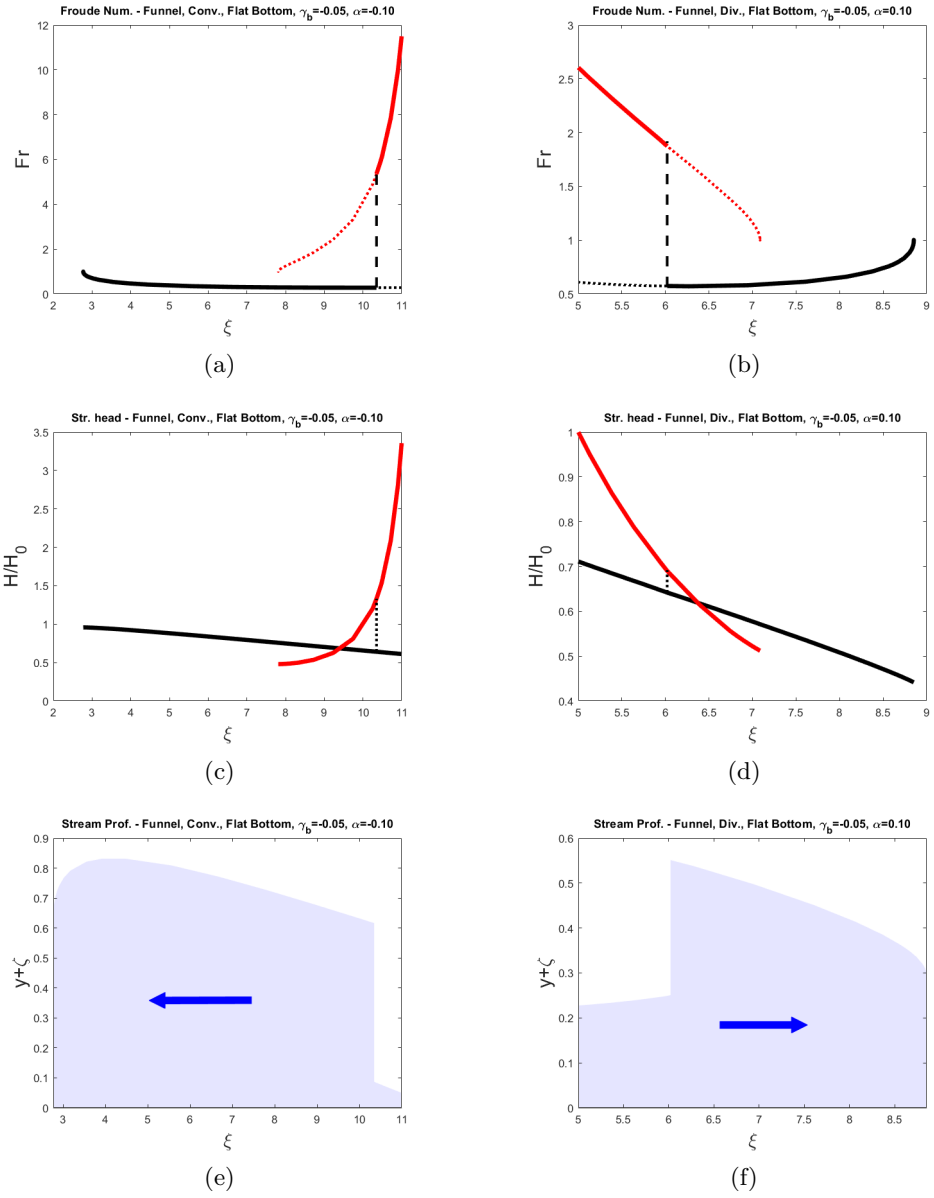

Figure 3.22: **Stream Flowing along a Funnel-shaped Bed with Flat Bottom - Flow features.** In each column (top to bottom) Froude Number, Stream Head and Stream Profile are reported for $\gamma_b = -0.05$ and $\alpha = -0.1$ (convergent flow, left column) and $\alpha = 0.1$ (divergent flow, right column), basing on the solution in Fig. 3.21. Figures 3.22(a), 3.22(b) (Froude Number) and Fig. 3.22(c), 3.22(d) (Stream Head) : solid lines represent the solution with hydraulic jump (black and red respectively for the subcritical and supercritical branch), dotted line represent subcritical and supercritical reach without jump, black dashed line represents the hydraulic jump. Figures 3.22(e), 3.22(f) show the stream profiles, i.e., the free surface of the fluid.

3.4 Sinusoidal Bottom Topography

This section is devoted to the study of the sinusoidal bottom topography in presence of friction. Again, let consider the following sinusoidal bottom topography:

$$\zeta(\xi) = a\cos(k_b\xi) \tag{3.36}$$

recalling that $a > 0$ is the amplitude and $k_b > 0$ is the wavenumber. The goal here is to understand how the introduction of friction coefficient α influences the stream features already seen in Sec. 2.3, in the framework of Eq. 3.1, formulated as in 1.33 and here assuming the following form:

$$\frac{dy}{d\xi} = \frac{[\gamma_b + ak_b\sin(k_b\xi)]\xi^3y^3 + 2y - \alpha\xi}{\xi^3y^3 - 2\xi} = \frac{N(\xi, y)}{D(\xi, y)} \tag{3.37}$$

where $N(\xi, y)$ and $D(\xi, y)$ respectively represent the numerator and the denominator of the right hand side of Eq. 3.37, useful for the study of the corresponding Phase Portrait (as done in Sec. 1.4.4) since the lines $N(\xi, y) = 0$ and $D(\xi, y) = 0$ represent the nullclines of the equivalent system:

$$\frac{d}{ds}\begin{bmatrix}\xi\\ y\end{bmatrix} = \begin{bmatrix}\xi^3y^3 - 2\xi\\ [\gamma_b + ak_b\sin(k_b\xi)]\xi^3y^3 + 2y - \alpha\xi\end{bmatrix} \tag{3.38}$$

where $(\xi, y) = (\xi(s), y(s))$ is nothing but a parametrization of the orbits in the parameter $s \in A \subseteq \mathbb{R}$.

3.4.1 Geometry of the Phase Space

This section is devoted to the study of the Phase Portrait when a sinusoidal bottom topography is considered, in presence of bottom friction and a basal slope γ_b, as described by System 3.38 or, equivalently, by Eq. 3.37. The aim of is to understand the influence of the model parameters γ_b, α, a and γ_b in determining:

- the number of intersections points of the nullclines of System 3.38, which are the points where $dy/d\xi$ is undetermined;
- the nature of the aforementioned intersections points, as equilibrium points of System 3.38;
- the main geometric features of the orbits.

Such aspects connected to the Phase Portrait will be analyzed in the order they have just been reported.

Number of Intersection Points of the Nullclines

As can be observed by Eq. 3.37, the geometry of the phase space depends not only on γ_b and α, but also on a and k_b. The first step to understand the behaviour of the orbits in presence of bottom friction is to find possible crossing points of the nullclines described by Eq. 1.34, 1.35 [12], i.e., points where $\frac{dy}{d\xi} = \begin{bmatrix} 0 \\ 0 \end{bmatrix}$ and so the slope of the stream depth can be either finite or infinite [13], as described in [4]. In order to do this, one has to plug Eq. 1.34 into Eq. 1.35 (this time using the specific definition of $\zeta(\xi)$ given in 3.4), thus obtaining:

$$2\xi\left[\gamma_b - \frac{\alpha}{2} + ak_b \sin(k_b\xi)\right] + 2\sqrt[3]{\frac{2}{\xi^2}} = 0 \tag{3.39}$$

This equation is in general implicit and can be easily solved numerically. However, by simple re-arrangement, the following equivalent form is obtained:

$$\sin(k_b\xi) = \frac{\frac{\alpha}{2} - \gamma_b - 2^{\frac{1}{3}}\xi^{-\frac{5}{3}}}{ak_b} \tag{3.40}$$

The number of the solutions of Eq. 3.40 within the physical domain depends strictly on the parameters of the model. Indeed, it can be observed that while the function $\sin(\xi)$ periodically oscillates within $[-1,1]$ for all $\xi > 0$, the function at the right hand side of Eq. 3.40 (which is continuous for $\xi > 0$) has instead the following behaviour, for $\xi \to 0^+$:

$$\lim_{\xi\to 0^+} \frac{\frac{\alpha}{2} - \gamma_b - 2^{\frac{1}{3}}\xi^{-\frac{5}{3}}}{ak_b} = -\infty$$

For $\xi \to +\infty$, instead:

$$\lim_{\xi\to +\infty} \frac{\frac{\alpha}{2} - \gamma_b - 2^{\frac{1}{3}}\xi^{-\frac{5}{3}}}{ak_b} = \frac{\frac{\alpha}{2} - \gamma_b}{ak_b}$$

Moreover, such function results to be strictly increasing for all $\xi > 0$, therefore the value $\frac{\frac{\alpha}{2}-\gamma_b}{ak_b}$ results to be an upper bound (never reached as a maximum by the function). Let define the non-dimensional coefficient:

$$A := \frac{\frac{\alpha}{2} - \gamma_b}{ak_b} \tag{3.41}$$

[12] They coincide with the equilibrium points of System 3.38.

[13] **Recall**: as described in Sec. 1.4.4, at points where $D(\xi, y) = 0$ and $N(\xi, y) \neq 0$ the stream height profile exhibit vertical tangent, as they lie in the Critical Line, which is the locus of the singularities of Eq. 1.33. On the contrary, points where $N(\xi, y) = 0$ and $D(\xi, y) \neq 0$ represent stationary points for the stream height, so they are not singular.

where it can be recognized that:

- at the numerator of A, one has the energy gain/loss due to the basal slope γ_b net of the dissipation, which in terms of slope is given by $\alpha/2$;
- at the denominator of A, one has the maximum gain/loss (in absolute value) in terms of slope due to sinusoidal bottom topography.

Therefore, A can be used to compare the energetic contribute of bottom topography with the stream energy in absence of bottom topography, for large ξ. By means of A, three cases can be distinguished:

- $A \leq -1$ for which no intersections are possible;
- $-1 < A \leq 1$ for which infinitely (countable) many intersections arise;
- $A > 1$ for which only a finite number of intersections arises.

The first of the inequalities just seen can be re-arranged (taking into account that $ak_b > 0$) in order to obtain:

$$\frac{\alpha}{2} \leq \gamma_b - ak_b$$

By observing that $ak_b = \max_{\xi>0} \zeta'$ and using the properties of minimum and maximum operators [14] with extension to the constant γ_b, one concludes that physical intersections are not possible if and only if:

$$\frac{\alpha}{2} \leq \min_{\xi>0}[\gamma_b - \zeta'(\xi)] = \min_{\xi>0}[\gamma(\xi)] \tag{3.42}$$

where $\gamma(\xi)$ is the slope "felt" by the stream while flowing, defined in 3.5.
Thus, nullclines of Sys. 3.38 does not intersect if friction dissipation does not exceed the energetic contribute given by slope and topography. An analogous re-arrangement with similar usage of the properties of min and max operators brings to the following inequality:

$$\frac{\alpha}{2} > -\min_{\xi>0}[\gamma_b - \zeta'] = \max_{\xi>0}[-\gamma(\xi)]$$

This allows to conclude that if friction dissipation definitely overbalances the one of the topographic counter-slope, one has only a finite number of crossing points.
Therefore, it appears immediate that the presence of intersection points of the nullclines and, consequently, the possibility of having multiple hydraulic jumps, strictly depends on friction coefficient α.

[14] Indeed, one has that $\max_{\xi>0}[\zeta'(\xi)] = -\min_{\xi>0}[-\zeta'(\xi)]$, while $\min_{\xi>0}[\zeta'(\xi)] = -\max_{\xi>0}[-\zeta'(\xi)]$

Nature of the Intersection Points of the Nullclines

The three possible cases for the number of intersections determines several geometries of the phase space, which are displayed in Fig. 3.26 and summarized in Tab. 3.2, here discussed more in details.
In particular, as expected, combinations of the model parameters resulting in $A < -1$ give no intersections of the nullclines, therefore the trajectories exhibit local stationary points (minima or maxima) where they cross the line $N(\xi, y) = 0$ and infinite gradient at points where they cross the Critical Divide Line $D(\xi, y) = 0$, which separates subcritical and supercritical branches of the solutions.
Interesting and novel geometries emerge instead when considering the cases in which $A > -1$ (infinitely many countable intersections), as illustrated in Fig. 3.26(a). Indeed, it can be observed that the orbits exhibit an alternation of unstable focus followed by saddle points: the trajectories move out from the unstable focus, then enter the saddle point following the stable direction and leaves it following the unstable direction to join the repulsion basin of the next unstable focus, which enlarges as ξ increases. It is worth to notice that, although from Fig. 3.26(a) it looks like focus arise nearby the minimum points of bed topography and saddles around the maxima, this is only due to the fact that, as in this case, a small value of A is used. Therefore, by using Eq. 3.40, one can find that intersections are located at points where sinus function assumes values very close to 0 and in any case no more than A, which is the upper-bound of the function at the right hand side member. Therefore, at that points, the slope of the sinusoidal bottom topography function is very close to 0, that is, bottom topography assumes values very close to the extremum points.
The geometry just described is coherent with the study of the Phase Space reported in Sec. 1.4.4 for the general model (Eq. 1.25), particularly for what concerns the signs of the Jacobian Trace 1.50 and Determinant 1.51. Indeed, the alternation of unstable focuses and saddles obtained for $A > -1$ is due to the fact that while the sign of the Jacobian Trace is constant (as it is the same sign of α), that of the determinant alternates, as it is well shown in Fig. 3.27. Particular is the case $\alpha = 0$ (no bottom friction), corresponding to a null Jacobian Trace: the sole sign of the determinant governs the nature of the crossing point, which can be saddles (negative determinant) or centres (positive determinant).
In principle, the case of a sinusoidal bottom topography exhibits six possible geometries, which are summarized in Tab. 3.2. However, some of these are hard to obtain (as for the stable focus) because of the choice of the parameters that, since they are non-dimensional, will be in general between 0 and 1 (except for the wavenumber k_b) in absolute value : typical values used for α and γ_b are $-1 < \alpha < 1$, $-0.1 \leq \gamma_b \leq 0.1$ (as in [29]) , while a spans in the range $0.01 \leq a \leq 1$ (as in [4]). Geometries requiring values of α and a out of the aforementioned ranges

Main Geometric Features of the Orbits

A last interesting aspect is that the sign of the basal slope γ_b is no longer the sole model parameter in dictating the general behaviour of the trajectories. Indeed, it appears that while the geometry of the subcritical branches of the trajectories is mostly governed by

γ_b (similarly to what obtained in Sec. 2.3), that of the supercritical branches is closely related to the flow direction (i.e., to the sign of α). In particular

- if $\gamma_b \geq 0$, subcritical trajectories diverge (or stabilize oscillating around an asymptotic value if $\gamma_b = 0$) as ξ increases, while if $\gamma_b < 0$ they exhibit overall non-monotonical behaviour, starting and terminating on the critical line at respectively minimum and maximum radius, as it was observed for the Sinusoidal Bottom Topography in absence of friction, in Sec. 2.3;
- the supercritical branches, instead, are described by non-monotonic curves starting and ending in critical condition (with a minimum and maximum radius, i.e., a *two Froude Horizons* behaviour) if $\alpha > 0$ (i.e., for flows on divergent direction), while if $\alpha < 0$ (convergent flows) they result described by curves that meet Critical Line only at a minimum radius (i.e., only one Froude Horizon).

The overall behaviour just described for the supercritical branches with $\alpha < 0$ seems to be qualitatively independent on basal slope γ_b, amplitude a and wavenumber k_b, novel geometries for the case of Sinusoidal Bottom with respect to the case in which turbulent friction is not included (Sec. 2.3), as reported in Table 3.1. Care has to be taken, in the current case, while imposing boundary condition and during integration, since such trajectories cross the ξ-axis and then, net of the sinusoidal fluctuation, converge to 0 (if $\gamma_b \geq 0$) or diverge to $-\infty$ (if $\gamma_b > 0$) [15], therefore giving rise to non-physical solutions [16]. Results are summarized in Table 3.1, while examples of the aforementioned trajectories are reported in Fig. 3.23.

[15] If one considers the trajectories without excluding the sinusoidal fluctuation, they oscillate indefinitely, thus it is a mathematical mistake to talk about convergence to 0 or divergence to $-\infty$. In particular, 0 is only an upper bound in case $\gamma_b \geq 0$.

[16] As they exceed the physical domain $\mathcal{D} = \{\xi > 0\} \times \{y > 0\}$.

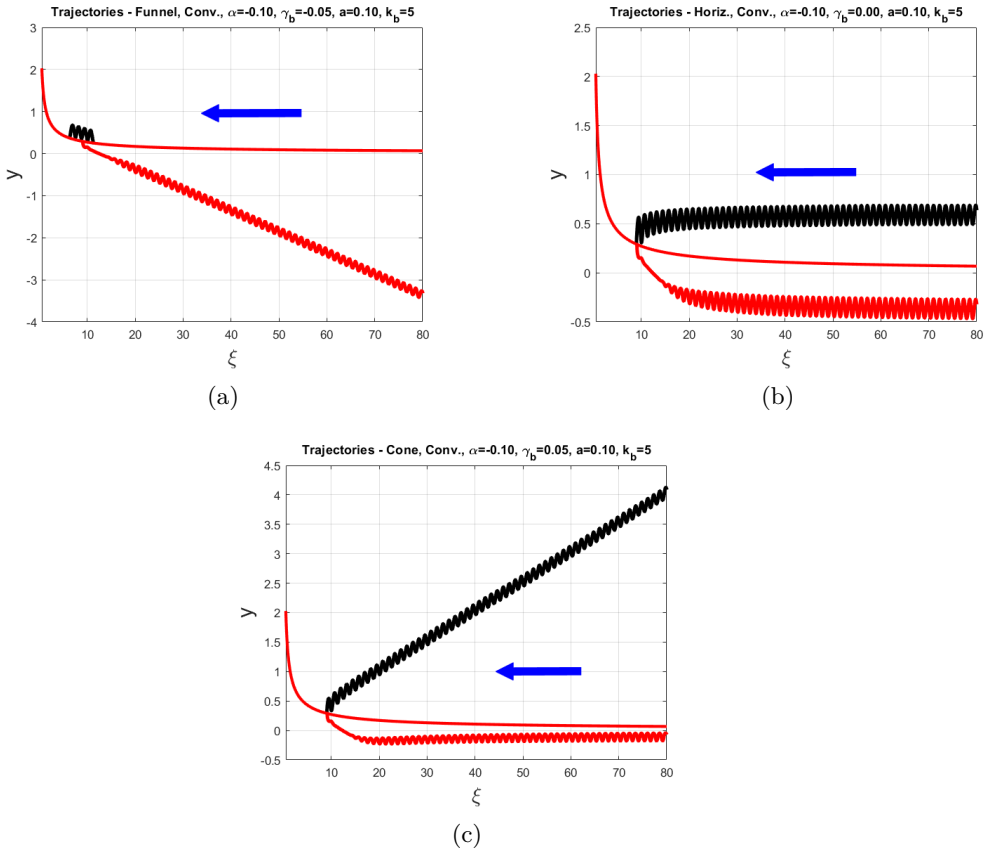

(a) (b) (c)

Figure 3.23: **Supercritical Trajectories with one Froude Horizon for Convergent Streams along Cone, Funnel and Horizontal bed,** $\alpha = -0.1$, $\gamma_b = -0.05, 0, 0.05$, $a = 0.1$, $k_b = 0.05$. In all the figures: red line separating the two branches is the Critical Divide Line; supercritical and subcritical profiles are respectively the red and black branches.

Table 3.1: **Geometric Structure of the Trajectories in the Phase Plane in case of Sinusoidal Bottom including friction** . The table highlights the dependence of the geometric structure of trajectories described by Sys. 3.38 (equivalently, Eq. 3.37) on the main model parameters: basal slope γ_b and friction coefficient α. The abbreviations "SUB" and "SUP" respectively stand for "Subcritical branch" and "Supercritical branch", while "1 F.H." and "2 F.H." stand respectively for *one Froude Horizon* (i.e. only a minimum radius where the stream meets Critical conditions) and *two Froude Horizons* (i.e., both a minimum and a maximum radius where the stream meets Critical conditions). In order to make a comparison with the current case in which turbulent friction is included in the model (i.e., $\alpha \neq 0$), the case in which friction is not included (see Sec. 2.3) is reported.

Friction					No Friction (Sec. 2.3)	
	$\gamma_b \geq 0$		$\gamma_b < 0$		$\gamma_b \geq 0$	$\gamma_b < 0$
	$\alpha > 0$	$\alpha < 0$	$\alpha > 0$	$\alpha < 0$	$\alpha = 0$	
SUB	1 F.H.		2 F.H.		1 F.H.	2 F.H.
SUP	2 F.H.	1 F.H.	2 F.H.	1 F.H.	1 F.H.	2 F.H.

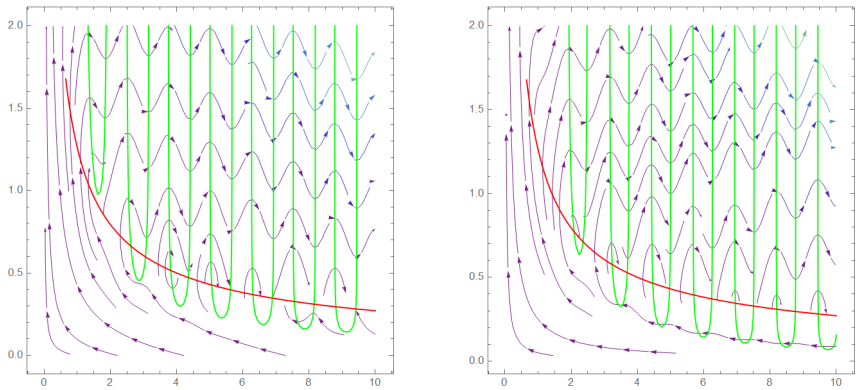

(a) (b)

Figure 3.24: **Orbits in presence of Sinusoidal Bottom Topography for Positive and Negative Basal Slope,** $\alpha = 0.4$**,** $\gamma_b = \pm 0.05$. In both figures: red line is the Critical Divide Line; green line is the Numerator Divide Line; arrows represent the stream lines. Fig. 3.24(a) corresponds to orbits obtained for negative $\gamma_b = -0.05$, while Fig. 3.24(b) corresponds to those obtained for positive $\gamma_b = 0.05$.

Table 3.2: **Geometries of the Phase Space for Sinusoidal Bottom Topography**. The table highlights the dependence of the nature of the equilibrium points of Sys. 3.38 (i.e., crossing points of the corresponding nullclines) on the sign of the Jacobian Trace (equivalently, of α), Jacobian Determinant and Discriminant $\Delta = \mathrm{tr}^2 - 4 \det$ of the characteristic polynomial associated to the Jacobian Matrix 1.49. The abbreviations "Un." and "St." respectively stand for "Unstable" and "Stable", while "Foc.", "Sad." and Cen." respectively stand for "Focus", "Saddle" and "Center".

	$\alpha > 0$			$\alpha < 0$			$\alpha = 0$		
$\mathrm{tr}(\xi_*, y_*)$	> 0			< 0			0		
$\det(\xi_*, y_*)$	> 0		< 0	> 0		< 0	> 0		< 0
$\Delta(\xi_*, y_*)$	<0	>0	>0	<0	>0	>0	<0	>0	>0
Eq. Point	Un. Foc.	Un. Node	Sad.	St. Foc.	St. Node	Sad.	Cen.		Sad.

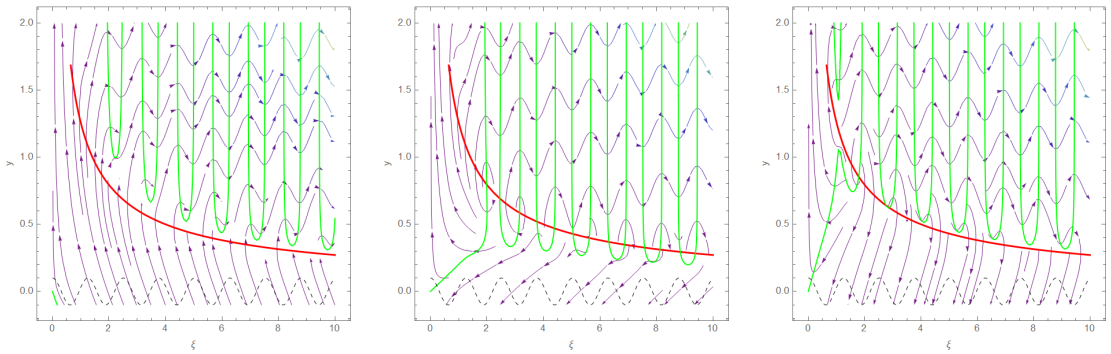

(a) (b) (c)

Figure 3.25: **Orbits in presence of Sinusoidal Bottom Topography depending on the number of crossing points of the nullclines** A. In all the figures: red line is the Critical Divide Line; green line is the Numerator nullcline $N(\xi, y) = 0$; black dashed line is the bottom topography; the arrows represent the stream lines. Fig. 3.25(a) corresponds to the case $A = -1.3$ (no intersections); Fig. 3.25(b) corresponds to the case $A = 0.3$ (infinitely many intersections); Fig. 3.25(c) corresponds to the case $A = 1.4$ (finitely many intersections).

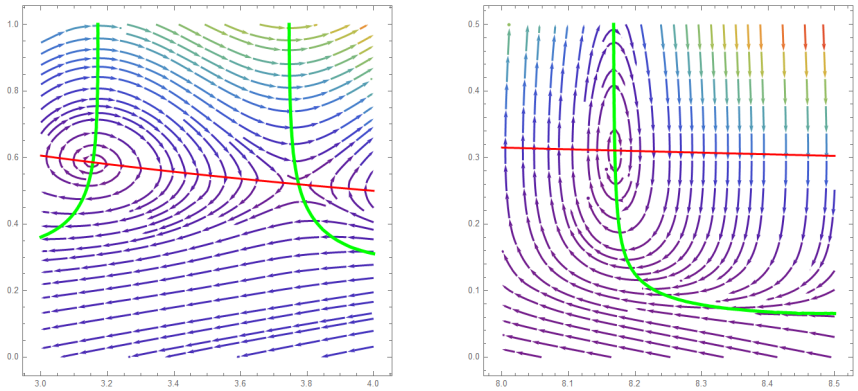

(a)

(b)

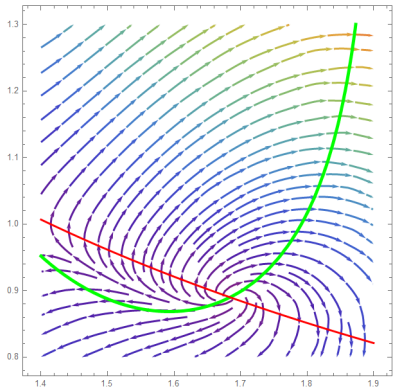

(c)

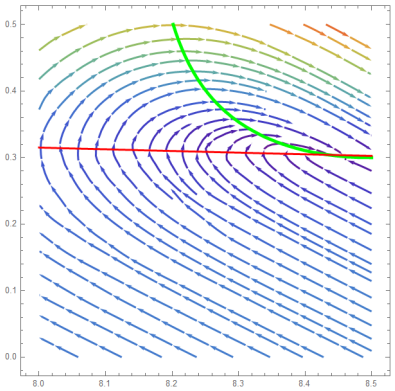

(d)

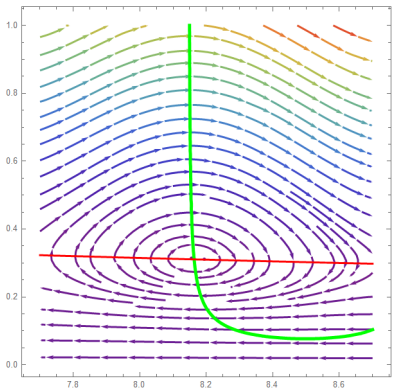

(e)

Figure 3.26: **The six possible geometries of the Phase Space**. Fig. 3.26(a) - Unstable Focus at $\xi \approx 3.13$ followed by a Saddle Point at $\xi \approx 3.81$, $\alpha = 0.4$, $\gamma_b = 0.05$, $a = 0.1$, $k_b = 5$. Fig. 3.26(b) - Stable Focus at $\xi \approx 8.16$, $\alpha = -0.4$, $\gamma_b = -0.1$, $a = 4$ (this value is out of range for the applications here), $k_b = 5$. Fig. 3.26(c) - Source located at $\xi \approx 1.63$, $\alpha = 2$ (out of range), $\gamma_b = 0.05$, $a = 0.1$, $k_b = 5$. Fig. 3.26(d) - Sink located at $\xi \approx 8.44$, $\alpha = -1$, $\gamma_b = -0.05$, $a = 0.1$, $k_b = 5$. Fig. 3.26(e) - Centre located at $\xi \approx 8.16$, $\alpha = 0$, $\gamma_b = -0.05$, $a = 0.1$, $k_b = 5$.

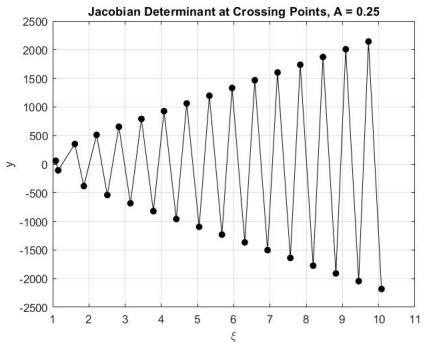

(a)

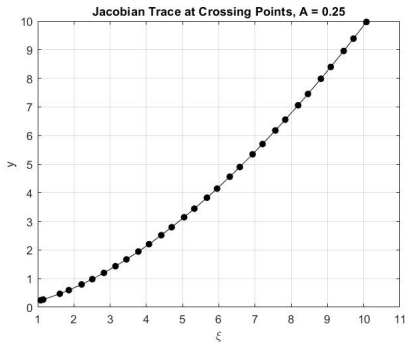

(b)

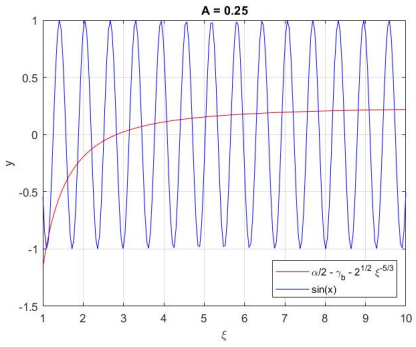

(c)

Figure 3.27: In all the panels: $\alpha = 0.4$, $\gamma_b = -0.05$, $a = 0.1$, $k_b = 5$, therefore $A = 0.25$. Fig. 3.27(a) shows the behaviour of the Jacobian Determinant for $0 \leq \xi \leq 10$: black dots represents the value of the determinant at crossing points, while solid black line is plotted to better underline, by simple piecewise linear interpolation, the alternate change in sign. Fig. 3.27(b) shows the behaviour of the Jacobian Trace for $0 \leq \xi \leq 10$: as before, black dots represent the values of the trace at crossing points, while the interpolating black line is to better represent the behaviour as ξ increases. Finally, Fig. 3.27(c) shows crossing points by graphical solution of Eq. 3.40.

3.4.2 Solutions

Such a variety of possible geometries reflects on the possible solutions of Eq. 1.33, whose structure depends on the nature of the equilibrium points and boundary conditions.
What is interesting is that, because of the sinusoidal structure of bed topography and, consequently, of the numerator $N(x, y)$ of Eq. 1.33, if $A > -1$ (when the energetic contribute of friction is not definitely overbalanced by the one of topographic slope) one can have up to infinitely many countable crossing points, opening to the possibility of a stream profile with multiple shock discontinuities, physically corresponding to hydraulic jumps. Such kinds of solutions are in principle possible also in absence of friction as shown in Tab. 3.2, where for $\alpha = 0$ the Focus degenerate to Centres, therefore opening to the possibility of having shock discontinuities. Here, hydraulic jump stream profiles are

obtained including turbulent friction α and their position, as done in previous sections for the cases of Flat Bottom and Step Bottom, is obtained as intersection of the specific forces of the supercritical and subcritical branch.
The different cases analyzed within the next subsections have been chosen coherently with the general behaviour of the trajectories in the phase portrait (as discussed at the end of Sec. 3.4.1): after considering the case $A \leq -1$ (no crossing points), convergent ($\alpha < 0$) and divergent ($\alpha < 0$) flows will be analyzed for both cone ($\gamma_b > 0$), funnel ($\gamma_b < 0$) and horizontal ($\gamma_b = 0$) shaped beds, for different amplitudes a of the bottom topography. The goal is to understand how the presence of friction influences the response of the flow to the amplitude of the sinusoidal bottom topography, compared to the results obtained in absence of friction and summarized in Tab. 2.3.

Solutions in absence of crossing points ($A \leq -1$)

In case $A \leq -1$, Eq. 3.40 has no solution and therefore there not exists any physical point at which nullclines intersect. Thus, according to Eq. 1.33, the trajectories join critical line with vertical tangent and exhibit horizontal tangent where they meet the nullcline $N(\xi, y) = 0$: there, the subcritical profiles attain local stationary points. On the contrary, supercritical profiles are monotonic within the physical domain $\{\xi > 0\} \times \{y > 0\}$, since in this case the line $N(\xi, y) = 0$ always remains above the Critical Line). This is well shown in Fig. 3.28, where stream profiles are reported for different parameter combinations resulting in $A \leq -1$.
As expected from the discussion at the end of Sec. 3.4.1, the overall behaviour of the subcritical branch is determined by the sign of basal slope γ_b, similarly to the inviscid case in Sec. 2.3: diverging oscillating if $\gamma_b > 0$, oscillating and confined between two critical horizons if $\gamma_b < 0$.
Variations over negative α values (opposite slope) does not produce significant differences of supercritical trajectories. Such a behaviour of the supercritical profiles can be explained by the fact when $A \leq -1$ friction energetic contribute is definitively lower than the one given by topographic slope, as expressed by the inequality 3.42.

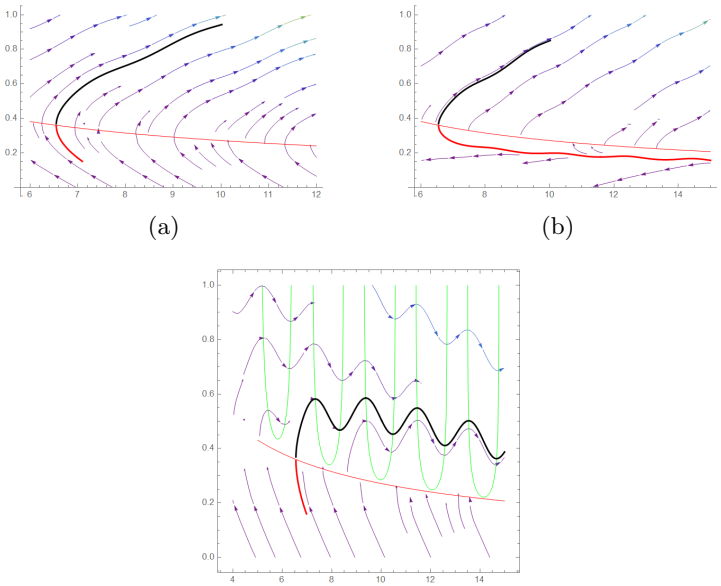

(a) (b)

(c)

Figure 3.28: Three possible solutions for parameter combinations resulting in $A \leq -1$. In all the figures: thick black and red lines represent respectively subcritical and supercritical profiles, thin red and green lines represent the nullclines (the red one is the Critical Line), arrows represent streamlines. Fig. 3.28(a) and 3.28(b) refer to positive γ_b and, respectively, negative and positive α, while Fig. 3.28(c) illustrates the case of negative α and γ_b.

Convergent Stream on Opposite Slope over a Cone-shaped Bed ($\gamma_b > 0$, $\alpha < 0$)

Interesting stream profiles emerge by considering the case $\alpha = -0.1$, $\gamma_b = 0.05$ and the tree values of amplitude $a = 0.1, 0.05, 0.01$. Fig. 3.29 reports height profiles, along with specific force in order to determine the radius at which hydraulic jump takes place (shock discontinuity of 0 length) and the corresponding sinusoidal bottom topography. Fig. 3.30 displays instead the main flow features: stream profile (free surface and bottom), Froude Number and non-dimensional Stream Head $\tilde{H}(\xi) = H(\xi)/H_0$.
The fluid springs from an external circular gate located at $\xi = \xi_0$ in supercritical conditions and flows along convergent direction ascending the cone-shaped bed, while increasing depth to join critical conditions. Then a hydraulic jump located at $\xi = \xi_{jump} < \xi_0$ connects the supercritical profile to the subcritical one, which oscillates decreasing in height until reaching critical conditions at a hole which drains the fluid.
The oscillations of the subcritical height profile progressively decrease in amplitude and exhibit a variable phase offset with respect to the bottom topography, more evident for higher values of α and smaller radii ξ. On the contrary, that of the supercritical branch are almost on phase with bottom topography and increase as the stream flows on convergent direction.
Notice in Figures 3.30(g), 3.30(h), 3.30(i) the role of the amplitude in determining the energy jump intensity, which is lower for lower values of a. This appears coherent with

the behaviour of stream energy: indeed, while the supercritical stream (where inertia dominates) appears less affected by variations of a, it is not the same for the subcritical one, where gravity dominates and greater values of amplitude provide an additional contribute contrasting the stream, which moreover flows along opposite basal slope. Therefore, the higher a, the less energetic tends to be the subcritical branch and, as a consequence, the higher the energy jump tends to be.

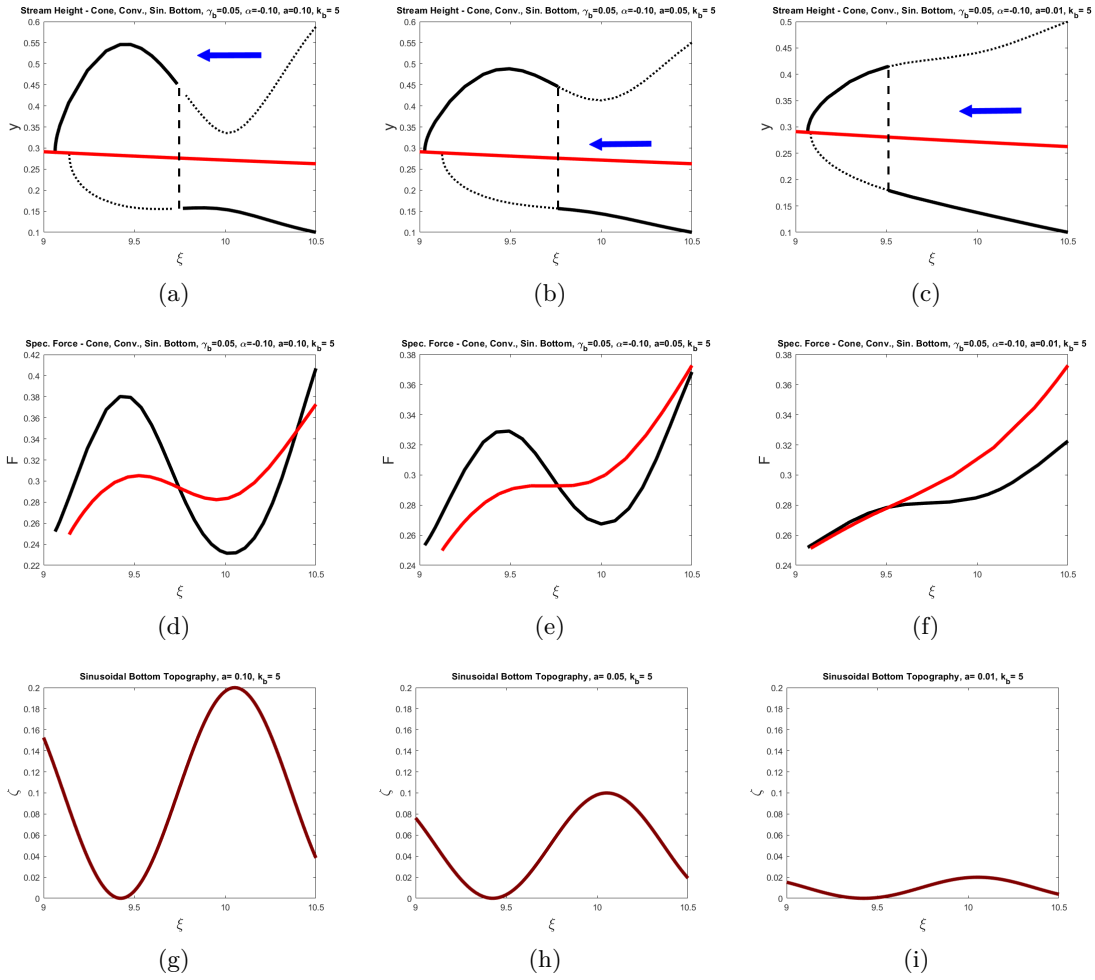

Figure 3.29: **Height Profiles with Hydraulic Jump - Convergent Stream flowing on opposite slope over a Cone-shaped Bed with Sinusoidal Bottom.** In each column Height Profile, Specific Force and Bottom Topography are reported for $\gamma_b = 0.05$, $\alpha = -0.1$, $k_b = 5$ and different values of amplitude: from left to right column, $a = 0.1,\ 0.05,\ 0.01$. Figures 3.29(a), 3.29(b), 3.29(c): solid lines represent the solution with hydraulic jump (black and red respectively for the subcritical and supercritical branch), thick dotted line represent subcritical and supercritical solutions without jump, black dashed line represents the hydraulic jump as a discontinuity (shock). Figures 3.29(d), 3.29(e), 3.29(f) show the behaviour of the specific force for the supercritical (red) and subcritical (black) branches of the solution, the radial position of the hydraulic jump being the intersection of the two branches. Figures 3.29(g), 3.29(h), 3.29(i) depict instead the bottom topography for the different values of amplitude a.

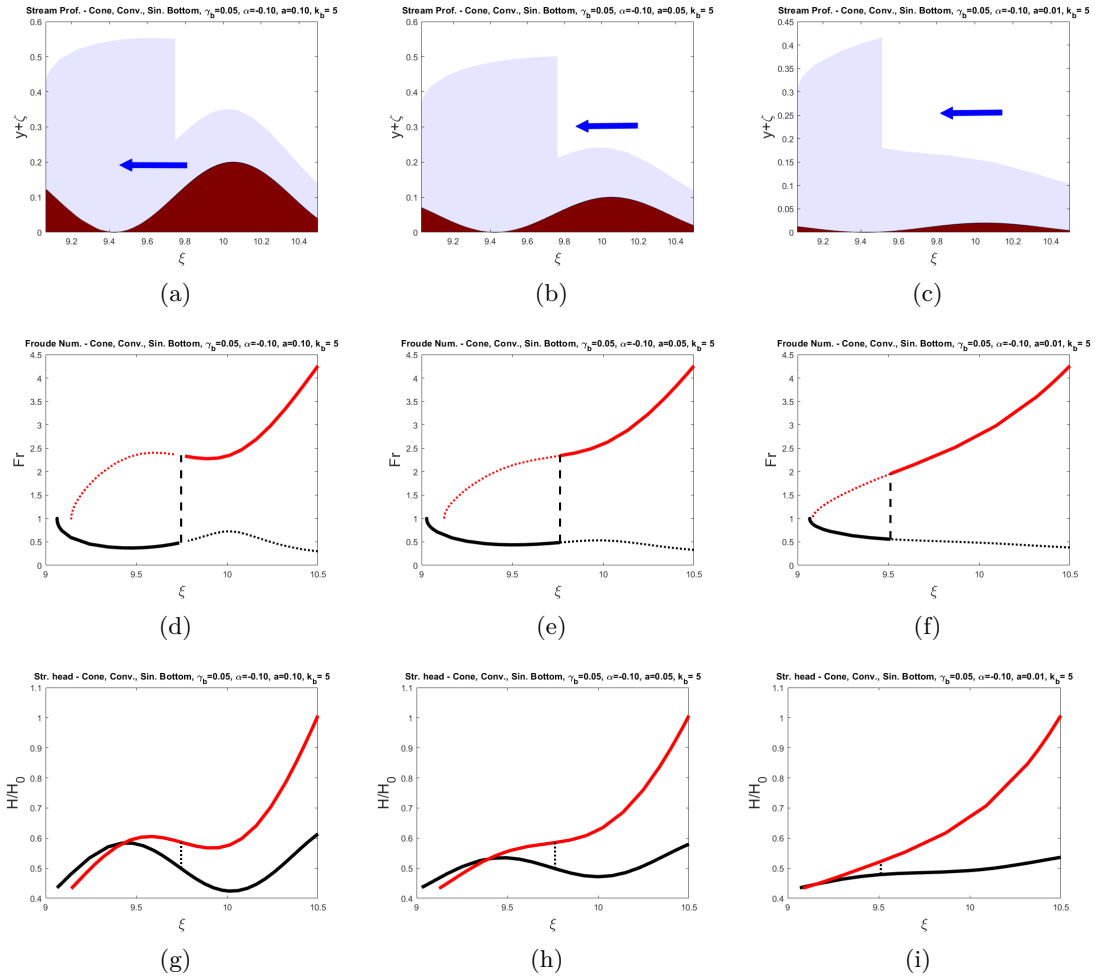

Figure 3.30: **Stream Profiles and features of the Hydraulic Jump - Convergent Stream flowing on opposite slope over a Cone-shaped Bed with Sinusoidal Bottom.** In each column Height Profile, Specific Force and Bottom Topography are reported for $\gamma_b = 0.05$, $\alpha = -0.1$, $k_b = 5$ and different values of amplitude: from left to right column, $a = 0.1,\ 0.05,\ 0.01$, basing on the hydraulic jump height profiles in Fig. 3.29. Figures 3.30(a), 3.30(b), 3.30(c) report Free Surfaces and Bottom Topographies: the blue arrows indicate flow direction and the hydraulic jump is represented as a sharp discontinuity. Figures 3.30(d), 3.30(e), 3.30(f) show the behaviour of the Froude Number for the supercritical (red) and subcritical (black) branches of the solution. Figures 3.30(g), 3.30(h), 3.30(i) reports finally the Stream Head for the supercritical (red) and subcritical (black) branches: the dotted line reports the energy discontinuity at the hydraulic jump in order to illustrate dissipation.

Divergent Stream on Favourable Slope down a Cone-shaped Bed ($\gamma_b > 0$, $\alpha > 0$)

Let consider the case $\alpha = 0.1$, $\gamma_b = 0.05$, for the tree different values of amplitude $a = 0.1,\ 0.05,\ 0.01$. Fig. 3.31 reports height profiles, along with specific force in order

to determine the radius at which hydraulic jump takes place (shock discontinuity of 0 length) and the corresponding sinusoidal bottom topography. Fig. 3.32 displays instead the main flow features: stream profile (free surface and bottom), Froude Number and non-dimensional Stream Head $\tilde{H}(\xi) = H(\xi)/H_0$.
The fluid springs from a central source in critical conditions (described by the presence of a minimum radius) and flows along divergent direction descending the cone-shaped bed, oscillating with an overall non-monotonic trend. Before re-joining critical conditions at a maximum radius, a hydraulic jump located at $\xi = \xi_{jump} < \xi_0$ connects the supercritical profile to the subcritical one, which oscillates with increasing amplitude.
The oscillations of the subcritical and supercritical height profiles maintains the same phase offsets with respect to bottom topography described for the convergent case.
Notice in Figures 3.32(g), 3.32(h), 3.32(i) the role of the amplitude in determining the energy jump intensity, which is higher for lower values of a. Again, it is coherent with the behaviour of the stream energy: although the the "ascending" parts [17] of the bottom topography contrast the stream in terms of energy, they are overbalanced by the "descending" parts [18], which are also helped by the fact that the flow is on favourable slope: the more the amplitude, the more the bottom topography helps the flow in energetic terms. Therefore, the subcritical flow is more energetic as a increases and the supercritical flow needs less energy dissipation at the jump to reach it.

[17] Increasing taking as a reference the flow direction, thus contrasting the stream that in such parts goes on opposite slope.

[18] Decreasing taking as a reference the flow direction, thus helping the stream that in such parts goes on favourable slope.

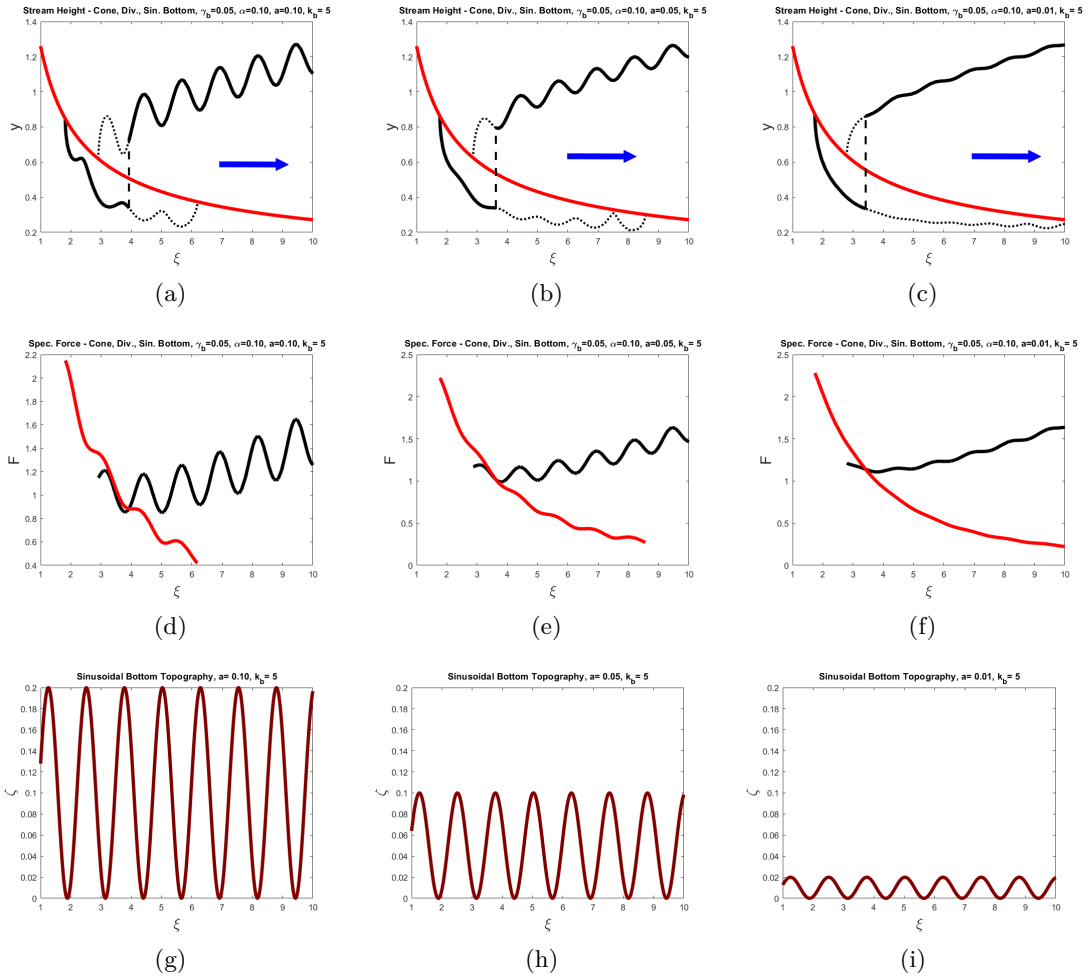

Figure 3.31: **Height Profiles with Hydraulic Jump - Divergent Stream flowing on favourable slope down a Cone-shaped Bed with Sinusoidal Bottom.** In each column Height Profile, Specific Force and Bottom Topography are reported for $\gamma_b = 0.05$, $\alpha = 0.1$, $k_b = 5$ and different values of amplitude: from left to right column, $a = 0.1,\ 0.05,\ 0.01$. Figures 3.31(a), 3.31(b), 3.31(c): solid lines represent the solution with hydraulic jump (black and red respectively for the subcritical and supercritical branch), thick dotted line represent subcritical and supercritical solutions without jump, black dashed line represents the hydraulic jump as a discontinuity (shock). Figures 3.31(d), 3.31(e), 3.31(f) show the behaviour of the specific force for the supercritical (red) and subcritical (black) branches of the solution, the radial position of the hydraulic jump being the intersection of the two branches. Figures 3.31(g), 3.31(h), 3.31(i) depict instead the bottom topography for the different values of amplitude a.

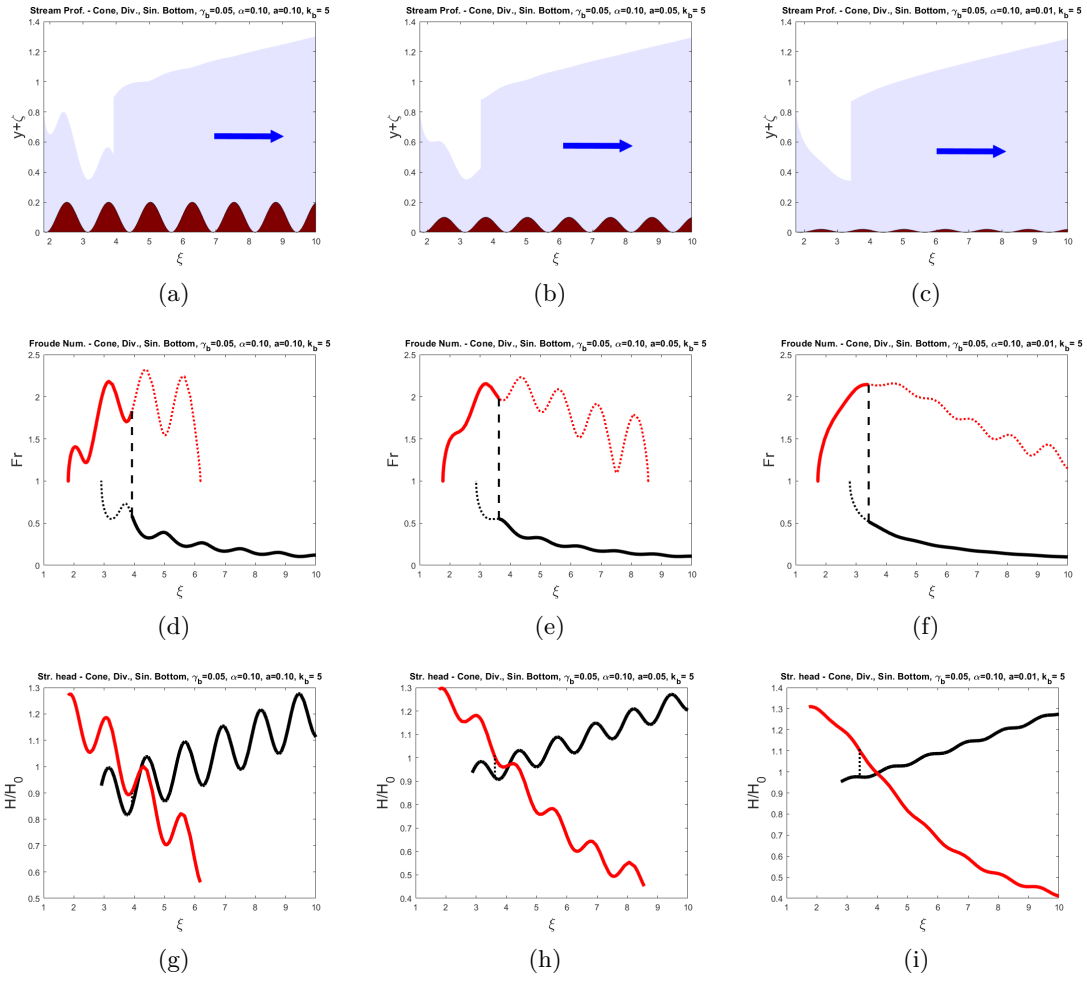

Figure 3.32: **Stream Profiles and features of the Hydraulic Jump - Divergent Stream flowing on favourable slope down a Cone-shaped Bed with Sinusoidal Bottom.** In each column Height Profile, Specific Force and Bottom Topography are reported for $\gamma_b = 0.05$, $\alpha = 0.1$, $k_b = 5$ and different values of amplitude: from left to right column, $a = 0.1,\ 0.05,\ 0.01$, basing on the hydraulic jump height profiles in Fig. 3.31. Figures 3.32(a), 3.32(b), 3.32(c) report Free Surfaces and Bottom Topographies: the blue arrows indicate flow direction and the hydraulic jump is represented as a sharp discontinuity. Figures 3.32(d), 3.32(e), 3.32(f) show the behaviour of the Froude Number for the supercritical (red) and subcritical (black) branches of the solution. Figures 3.32(g), 3.32(h), 3.32(i) reports finally the Stream Head for the supercritical (red) and subcritical (black) branches: the dotted line reports the energy discontinuity at the hydraulic jump in order to illustrate dissipation.

Convergent Stream on Favourable Slope down a Funnel-shaped Bed ($\gamma_b < 0$, $\alpha < 0$)

Let consider the case $\alpha = -0.1$, $\gamma_b = -0.05$, for the tree different values of amplitude $a = 0.1, 0.05, 0.01$. Fig. 3.33 reports height profiles, along with specific force in order to determine the radius at which hydraulic jump takes place (shock discontinuity of 0 length) and the corresponding sinusoidal bottom topography. Fig. 3.34 displays instead the main flow features: stream profile (free surface and bottom), Froude Number and non-dimensional Stream Head $\tilde{H}(\xi) = H(\xi)/H_0$.
The fluid springs in supercritical conditions from an external circular gate located at $\xi = \xi_0$ (where a supercritical boundary condition is imposed) and flows along convergent direction descending the funnel-shaped bed, oscillating with an overall increasing trend. Before joining critical conditions, a hydraulic jump located at $\xi = \xi_{jump} < \xi_0$ connects the supercritical profile to the subcritical one, which oscillates with increasing amplitude until reaching the edge of a central hole draining the fluid, located at a minimum radius that identifies the diameter of the hole.
The oscillations of the subcritical and supercritical height profiles maintains the same phase offsets with respect to bottom topography described for the previous cases.
Notice in Figures 3.34(g), 3.34(h), 3.34(i) the role of the amplitude in determining the energy jump intensity, which is lower for lower values of a. Again, it is coherent with the behaviour of the stream energy: although the the "ascending" parts [19] of the bottom topography contrast the stream in terms of energy, they are overbalanced by the "descending" parts [20], which are also helped by the fact that the flow is on favourable slope: the more the amplitude, the more the bottom topography helps the flow in energetic terms. Therefore, the subcritical flow is more energetic as a increases and the supercritical flow needs less energy dissipation at the jump to reach it.

[19] Increasing taking as a reference the flow direction, thus contrasting the stream that in such parts goes on opposite slope.

[20] Decreasing taking as a reference the flow direction, thus helping the stream that in such parts goes on favourable slope.

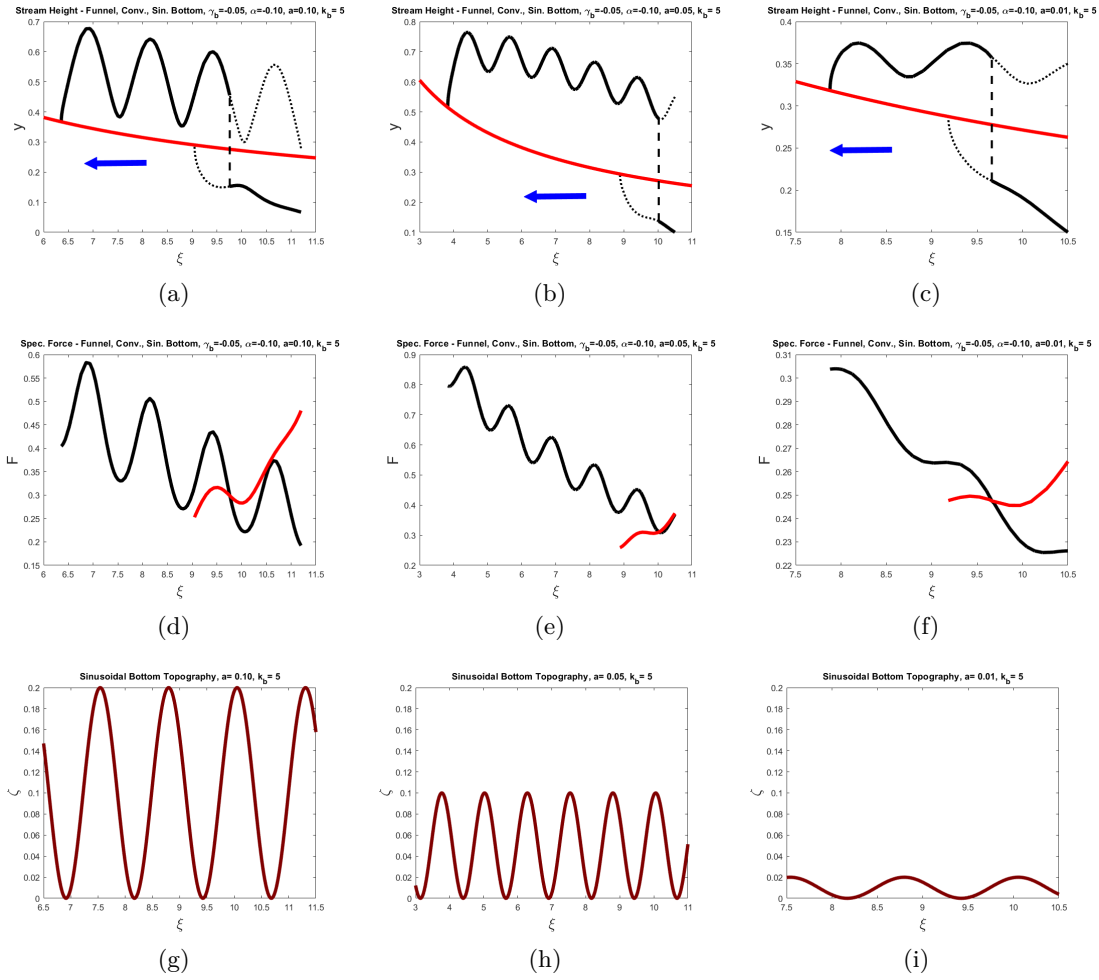

Figure 3.33: **Height Profiles with Hydraulic Jump - Convergent Stream flowing on favourable slope down a Funnel-shaped Bed with Sinusoidal Bottom.** In each column Height Profile, Specific Force and Bottom Topography are reported for $\gamma_b = -0.05$, $\alpha = -0.1$, $k_b = 5$ and different values of amplitude: from left to right column, $a = 0.1,\ 0.05,\ 0.01$. Figures 3.33(a), 3.33(b), 3.33(c): solid lines represent the solution with hydraulic jump (black and red respectively for the subcritical and supercritical branch), thick dotted line represent subcritical and supercritical solutions without jump, black dashed line represents the hydraulic jump as a discontinuity (shock). Figures 3.33(d), 3.33(e), 3.33(f) show the behaviour of the specific force for the supercritical (red) and subcritical (black) branches of the solution, the radial position of the hydraulic jump being the intersection of the two branches. Figures 3.33(g), 3.33(h), 3.33(i) depict instead the bottom topography for the different values of amplitude a.

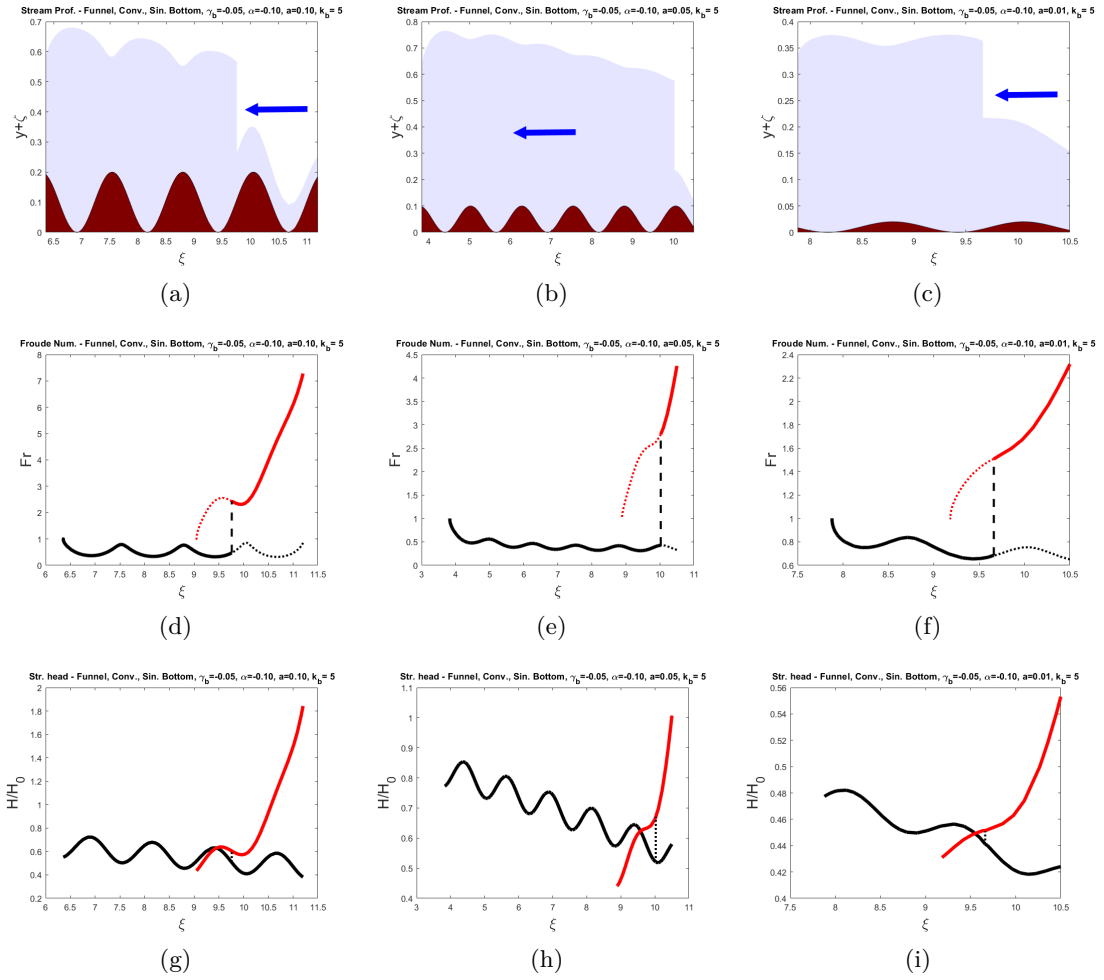

Figure 3.34: **Stream Profiles and features of the Hydraulic Jump - Convergent Stream flowing on favourable slope down a Funnel-shaped Bed with Sinusoidal Bottom.** In each column Height Profile, Specific Force and Bottom Topography are reported for $\gamma_b = -0.05$, $\alpha = -0.1$, $k_b = 5$ and different values of amplitude: from left to right column, $a = 0.1,\ 0.05,\ 0.01$, basing on the hydraulic jump height profiles in Fig. 3.33. Figures 3.34(a), 3.34(b), 3.34(c) report Free Surfaces and Bottom Topographies: the blue arrows indicate flow direction and the hydraulic jump is represented as a sharp discontinuity. Figures 3.34(d), 3.34(e), 3.34(f) show the behaviour of the Froude Number for the supercritical (red) and subcritical (black) branches of the solution. Figures 3.34(g), 3.34(h), 3.34(i) reports finally the Stream Head for the supercritical (red) and subcritical (black) branches: the dotted line reports the energy discontinuity at the hydraulic jump in order to illustrate dissipation.

Divergent Stream on Opposite Slope over a Funnel-shaped bed ($\gamma_b < 0$, $\alpha > 0$)

Let consider the case $\alpha = 0.1$, $\gamma_b = -0.05$, for the tree different values of amplitude $a = 0.1,\ 0.05,\ 0.01$. Fig. 3.35 reports height profiles, along with specific force in order

to determine the radius at which hydraulic jump takes place (shock discontinuity of 0 length) and the corresponding sinusoidal bottom topography. Fig. 3.36 displays instead the main flow features: stream profile (free surface and bottom), Froude Number and non-dimensional Stream Head $\tilde{H}(\xi) = H(\xi)/H_0$.
The fluid springs in critical conditions from a central source located at a minimum radius (which identifies the diameter of the source) and flows along divergent direction ascending the funnel-shaped bed, oscillating with an overall non monotonic trend (also net of the sinusoidal fluctuation). Before re-joining critical conditions, a hydraulic jump connects the supercritical profile to the subcritical one, which oscillates with decreasing amplitude until reaching critical conditions at a maximum radius, which can be exemplified as the external border of the bed and after which the fluid falls down.
The oscillations of the subcritical and supercritical height profiles maintains the same phase offsets with respect to bottom topography described for the previous cases.
Notice in Figures 3.36(g), 3.36(h), 3.36(i) the role of the amplitude in determining the energy jump intensity, which is lower for lower values of a. Again, it is coherent with the behaviour of the stream energy: although the "descending" parts [21] of the bottom topography help the stream in terms of energy, they are overbalanced by the "ascending" parts [22], which are also helped by the fact that the flow is on opposite slope: the more the amplitude, the more the bottom topography contrasts the flow in energetic terms. Therefore, the subcritical flow is less energetic as a increases and the supercritical flow needs more energy dissipation at the jump to reach it.

[21] Decreasing taking as a reference the flow direction, thus helping the stream that in such parts goes on favourable slope.

[22] Increasing taking as a reference the flow direction, thus contrasting the stream that in such parts goes on opposite slope.

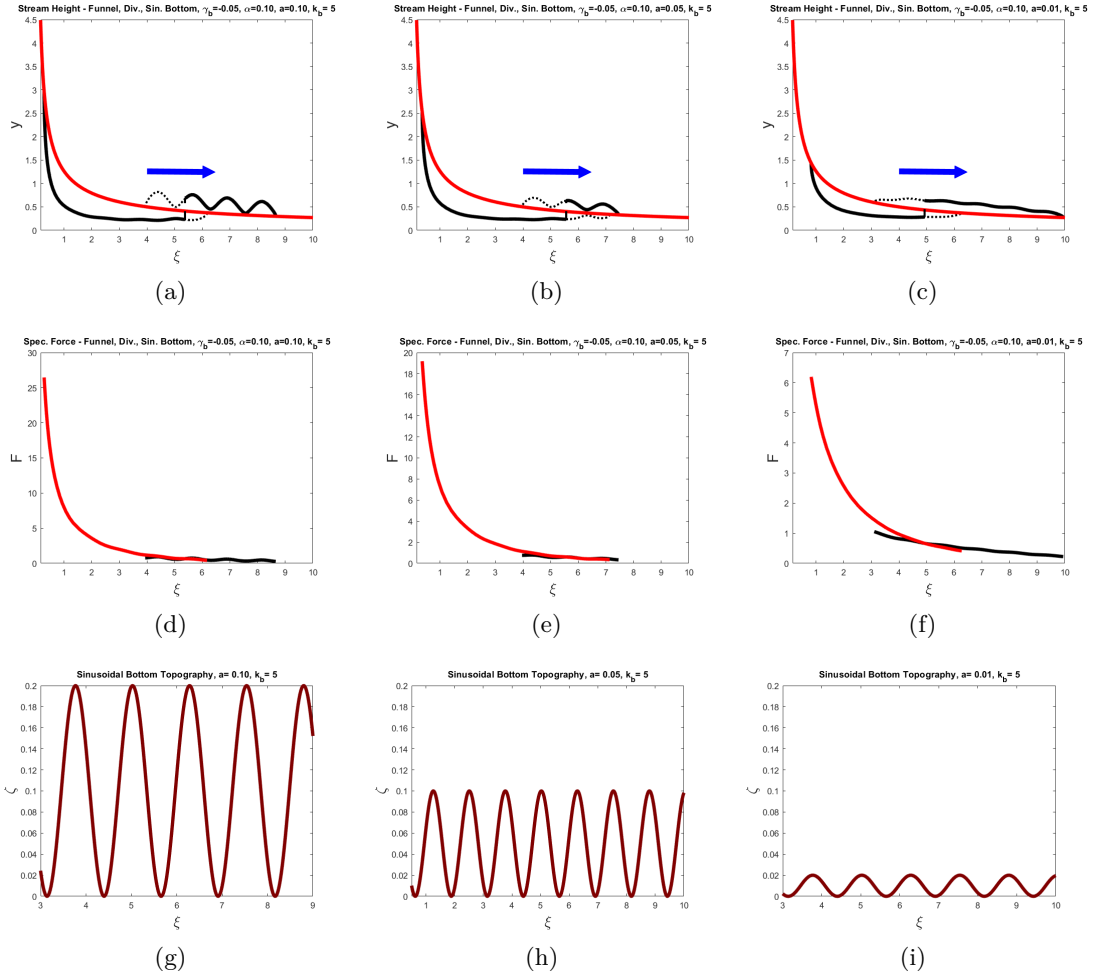

Figure 3.35: **Height Profiles with Hydraulic Jump - Divergent Stream flowing on opposite slope over a Funnel-shaped Bed with Sinusoidal Bottom.** In each column Height Profile, Specific Force and Bottom Topography are reported for $\gamma_b = -0.05$, $\alpha = 0.1$, $k_b = 5$ and different values of amplitude: from left to right column, $a = 0.1,\ 0.05,\ 0.01$. Figures 3.35(a), 3.35(b), 3.35(c): solid lines represent the solution with hydraulic jump (black and red respectively for the subcritical and supercritical branch), thick dotted line represent subcritical and supercritical solutions without jump, black dashed line represents the hydraulic jump as a discontinuity (shock). Figures 3.35(d), 3.35(e), 3.35(f) show the behaviour of the specific force for the supercritical (red) and subcritical (black) branches of the solution, the radial position of the hydraulic jump being the intersection of the two branches. Figures 3.35(g), 3.35(h), 3.35(i) depict instead the bottom topography for the different values of amplitude a.

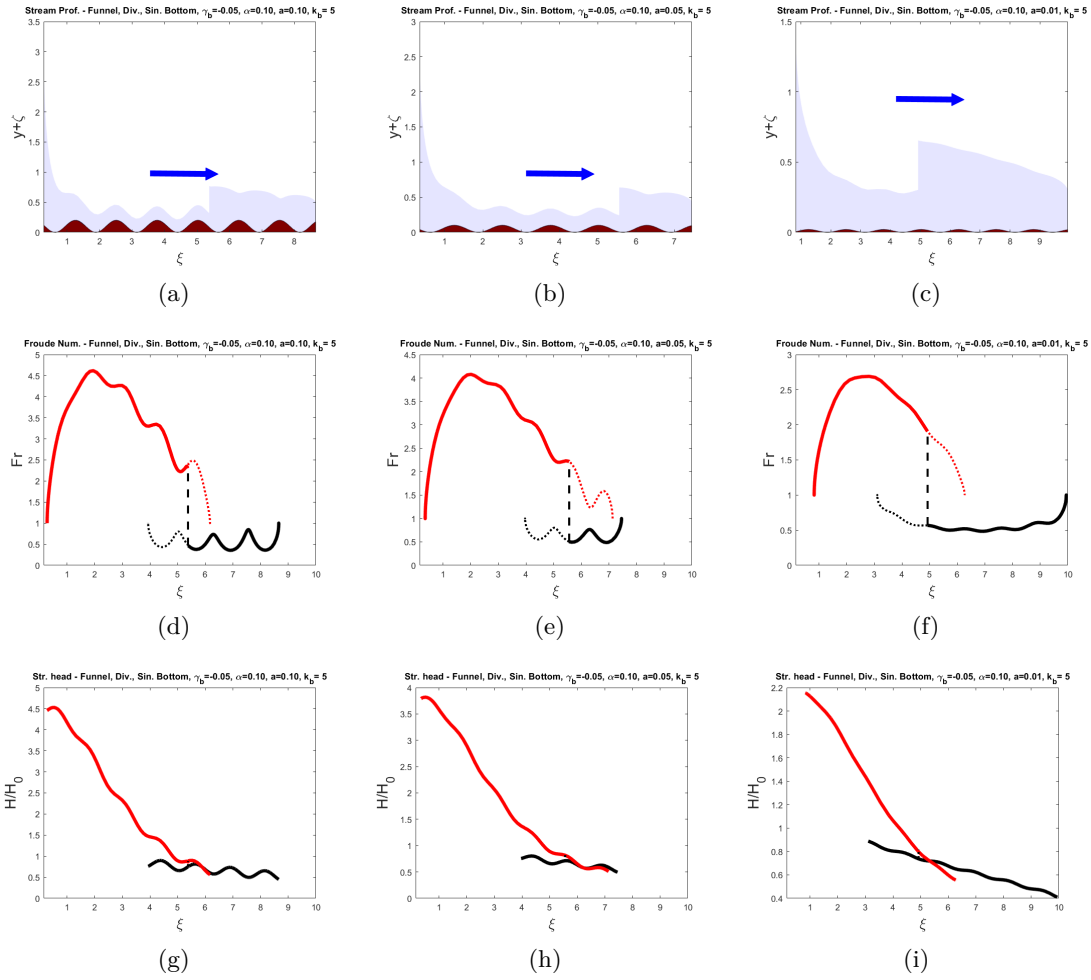

Figure 3.36: **Stream Profiles and features of the Hydraulic Jump - Divergent Stream flowing on opposite slope over a Funnel-shaped Bed with Sinusoidal Bottom.** In each column Height Profile, Specific Force and Bottom Topography are reported for $\gamma_b = -0.05$, $\alpha = 0.1$, $k_b = 5$ and different values of amplitude: from left to right column, $a = 0.1,\ 0.05,\ 0.01$, basing on the hydraulic jump height profiles in Fig. 3.35. Figures 3.36(a), 3.36(b), 3.36(c) report Free Surfaces and Bottom Topographies: the blue arrows indicate flow direction and the hydraulic jump is represented as a sharp discontinuity. Figures 3.36(d), 3.36(e), 3.36(f) show the behaviour of the Froude Number for the supercritical (red) and subcritical (black) branches of the solution. Figures 3.36(g), 3.36(h), 3.36(i) reports finally the Stream Head for the supercritical (red) and subcritical (black) branches: the dotted line reports the energy discontinuity at the hydraulic jump in order to illustrate dissipation.

Divergent Stream along a Horizontal Bed, ($\gamma_b = 0$, $\alpha > 0$)

Let consider the case $\alpha = 0.1$, $\gamma_b = 0$, for the tree different values of amplitude $a = 0.1, 0.05, 0.01$. Fig. 3.37 reports height profiles, along with specific force in order to determine the radius at which hydraulic jump takes place (shock discontinuity of 0 length)

and the corresponding sinusoidal bottom topography. Fig. 3.38 displays instead the main flow features: stream profile (free surface and bottom), Froude Number and non-dimensional Stream Head $\tilde{H}(\xi) = H(\xi)/H_0$.
The fluid springs in critical conditions from a central source located at a minimum radius (which identifies the diameter of the source) and flows along divergent direction along the horizontal bed, oscillating with an overall non monotonic trend (also net of the sinusoidal fluctuation). Before re-joining critical conditions, a hydraulic jump connects the supercritical profile to the subcritical one, which oscillates with increasing, but progressively stabilizing amplitude.
The oscillations of the subcritical and supercritical height profiles maintains the same phase offsets with respect to bottom topography described for the previous cases.
Notice in Figures 3.38(g), 3.38(h), 3.38(i) that the energy jump is not significantly affected by differences in the amplitude a, whose effects are quiet evident in the jump position. This is due to the fact that the bed is horizontal, therefore the increasing or decreasing parts of the bottom topography are not amplified by the additional effect of bottom slope and each increasing half oscillation is perfectly balanced by the decreasing one. On average, keeping same friction coefficient α and boundary conditions, supercritical and subcritical branches are not affected by changes in the amplitude a in terms of energy, as well as the energy jump.

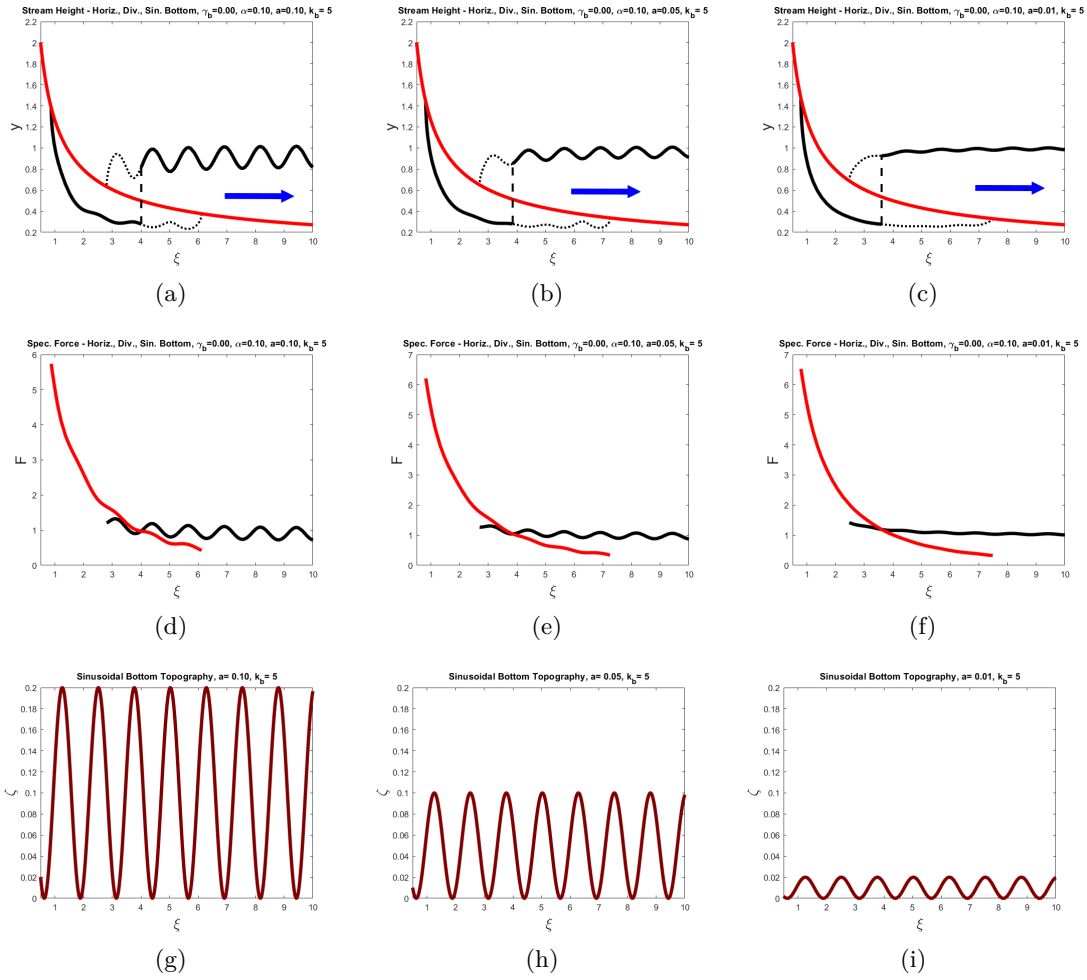

Figure 3.37: **Height Profiles with Hydraulic Jump - Divergent Stream flowing along a Horizontal Bed with Sinusoidal Bottom.** In each column Height Profile, Specific Force and Bottom Topography are reported for $\gamma_b = 0$, $\alpha = 0.1$, $k_b = 5$ and different values of amplitude: from left to right column, $a = 0.1,\ 0.05,\ 0.01$. Figures 3.37(a), 3.37(b), 3.37(c): solid lines represent the solution with hydraulic jump (black and red respectively for the subcritical and supercritical branch), thick dotted line represent subcritical and supercritical solutions without jump, black dashed line represents the hydraulic jump as a discontinuity (shock). Figures 3.37(d), 3.37(e), 3.37(f) show the behaviour of the specific force for the supercritical (red) and subcritical (black) branches of the solution, the radial position of the hydraulic jump being the intersection of the two branches. Figures 3.37(g), 3.37(h), 3.37(i) depict instead the bottom topography for the different values of amplitude a.

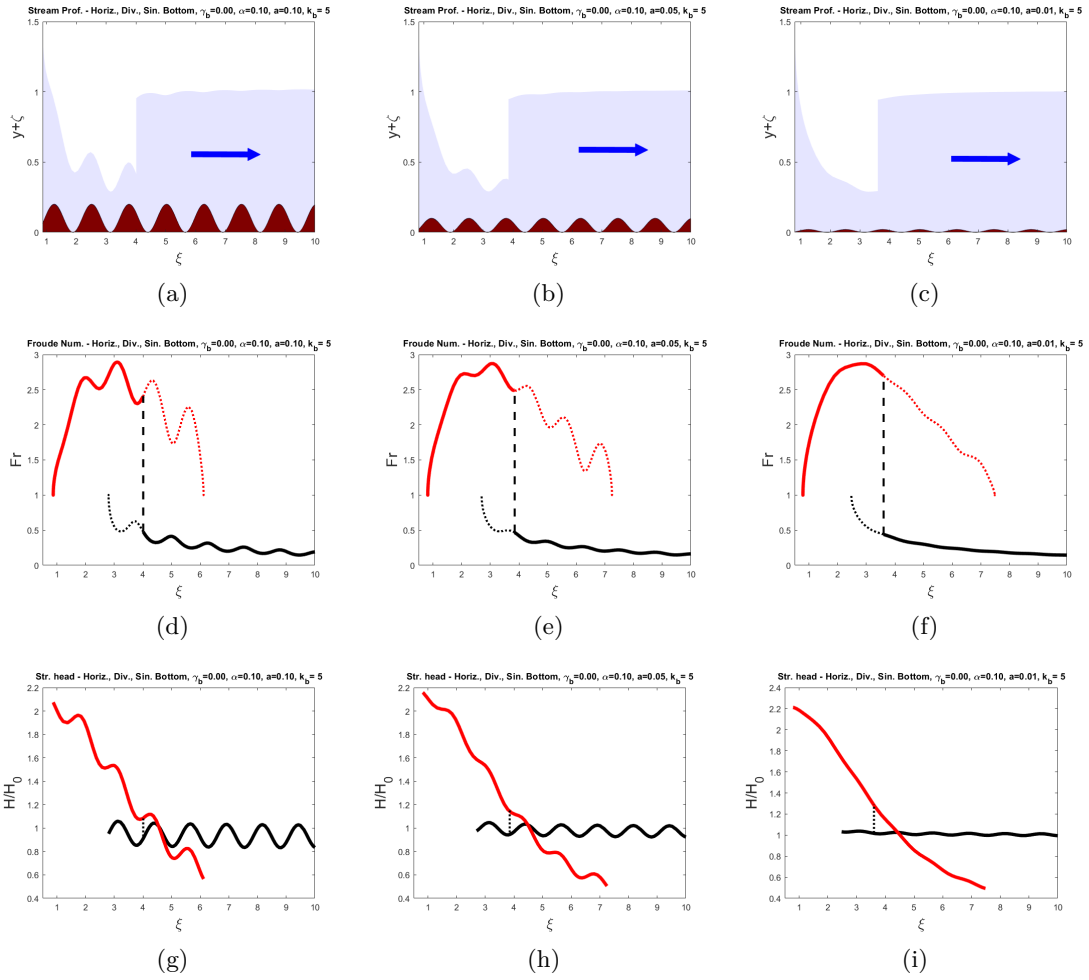

Figure 3.38: **Stream Profiles and features of the Hydraulic Jump - Divergent Stream flowing along a Horizontal Bed with Sinusoidal Bottom.** In each column Height Profile, Specific Force and Bottom Topography are reported for $\gamma_b = 0$, $\alpha = 0.1$, $k_b = 5$ and different values of amplitude: from left to right column, $a = 0.1,\ 0.05,\ 0.01$, basing on the hydraulic jump height profiles in Fig. 3.37. Figures 3.38(a), 3.38(b), 3.38(c) report Free Surfaces and Bottom Topographies: the blue arrows indicate flow direction and the hydraulic jump is represented as a sharp discontinuity. Figures 3.38(d), 3.38(e), 3.38(f) show the behaviour of the Froude Number for the supercritical (red) and subcritical (black) branches of the solution. Figures 3.38(g), 3.38(h), 3.38(i) reports finally the Stream Head for the supercritical (red) and subcritical (black) branches: the dotted line reports the energy discontinuity at the hydraulic jump in order to illustrate dissipation.

Convergent Stream along a Horizontal Bed, ($\gamma_b = 0$, $\alpha < 0$)

Let consider the case $\alpha = -0.1$, $\gamma_b = 0$, for the tree different values of amplitude $a = 0.1, 0.05, 0.01$. Fig. 3.39 reports height profiles, along with specific force in order to determine the radius at which hydraulic jump takes place (shock discontinuity of 0

length) and the corresponding sinusoidal bottom topography. Fig. 3.40 displays instead the main flow features: stream profile (free surface and bottom), Froude Number and non-dimensional Stream Head $\tilde{H}(\xi) = H(\xi)/H_0$.
The fluid springs in supercritical conditions from an external gate and flows along convergent direction along the horizontal bed, oscillating with increasing amplitude. Before joining critical conditions, a hydraulic jump connects the supercritical profile to the subcritical one, which oscillates with decreasing amplitude.
The oscillations of the subcritical and supercritical height profiles maintains the same phase offsets with respect to bottom topography described for the previous cases.
Notice in Figures 3.40(g), 3.40(h), 3.40(i) that the energy jump is not significantly affected by differences in the amplitude a, for the same reasons discussed for the Divergent case.

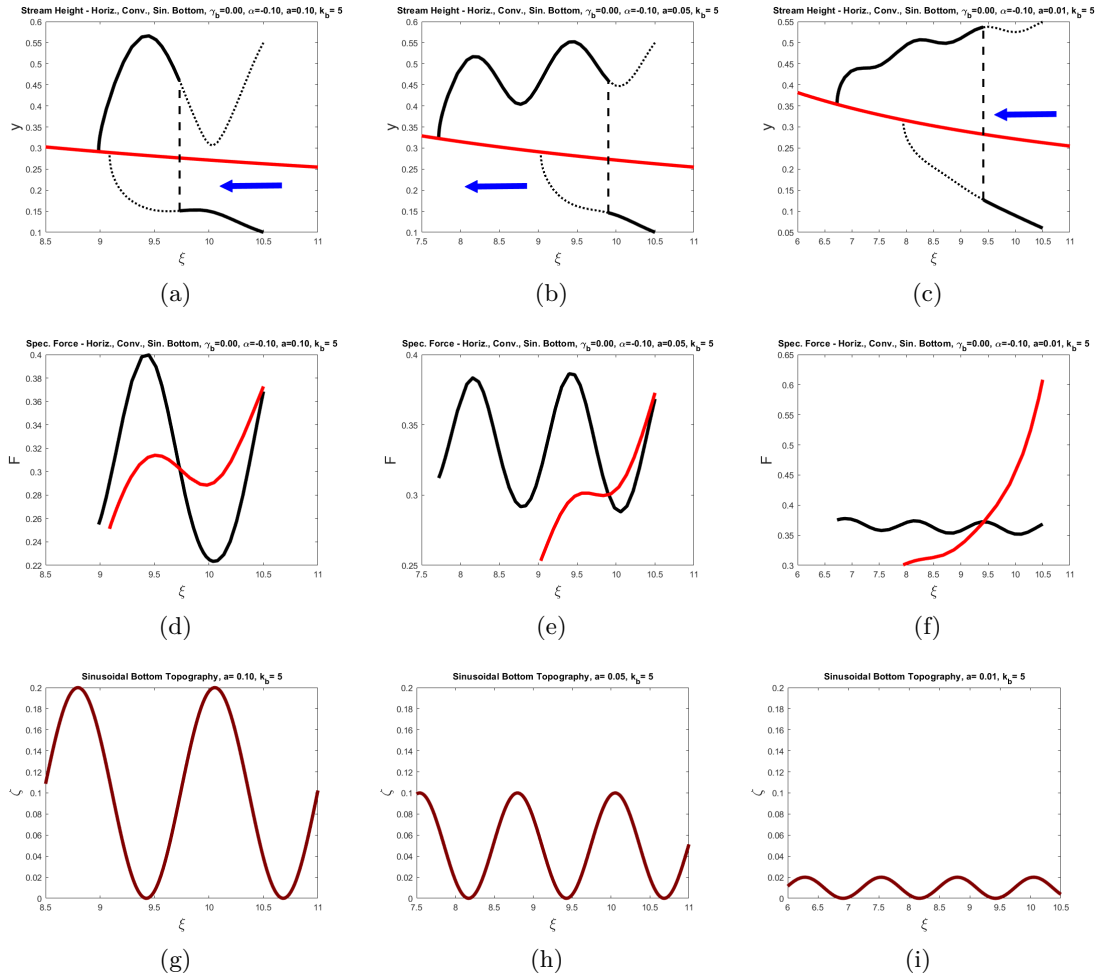

Figure 3.39: **Height Profiles with Hydraulic Jump - Convergent Stream flowing along a Horizontal Bed with Sinusoidal Bottom.** In each column Height Profile, Specific Force and Bottom Topography are reported for $\gamma_b = 0$, $\alpha = -0.1$, $k_b = 5$ and different values of amplitude: from left to right column, $a = 0.1,\ 0.05,\ 0.01$. Figures 3.39(a), 3.39(b), 3.39(c): solid lines represent the solution with hydraulic jump (black and red respectively for the subcritical and supercritical branch), thick dotted line represent subcritical and supercritical solutions without jump, black dashed line represents the hydraulic jump as a discontinuity (shock). Figures 3.39(d), 3.39(e), 3.39(f) show the behaviour of the specific force for the supercritical (red) and subcritical (black) branches of the solution, the radial position of the hydraulic jump being the intersection of the two branches. Figures 3.39(g), 3.39(h), 3.39(i) depict instead the bottom topography for the different values of amplitude a.

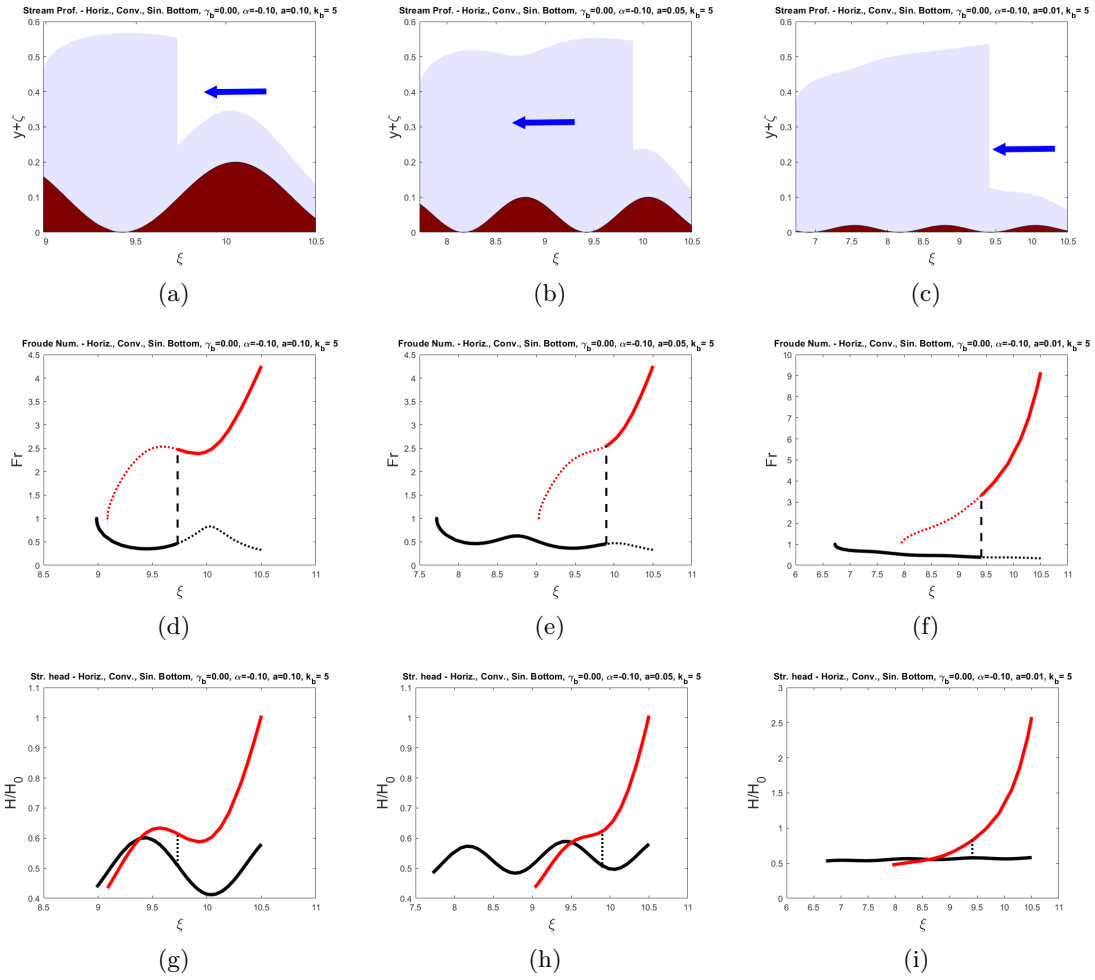

Figure 3.40: **Stream Profiles and features of the Hydraulic Jump - Convergent Stream flowing along a Horizontal Bed with Sinusoidal Bottom.** In each column Height Profile, Specific Force and Bottom Topography are reported for $\gamma_b = 0$, $\alpha = -0.1$, $k_b = 5$ and different values of amplitude: from left to right column, $a = 0.1,\ 0.05,\ 0.01$, basing on the hydraulic jump height profiles in Fig. 3.39. Figures 3.40(a), 3.40(b), 3.40(c) report Free Surfaces and Bottom Topographies: the blue arrows indicate flow direction and the hydraulic jump is represented as a sharp discontinuity. Figures 3.40(d), 3.40(e), 3.40(f) show the behaviour of the Froude Number for the supercritical (red) and subcritical (black) branches of the solution. Figures 3.40(g), 3.40(h), 3.40(i) reports finally the Stream Head for the supercritical (red) and subcritical (black) branches: the dotted line reports the energy discontinuity at the hydraulic jump in order to illustrate dissipation.

3.4.3 Friction-Gravity Interplay and Phase Offset

The height profiles obtained for the Sinusoidal Bottom Topography when friction is taken into account show a common feature:

- subcritical profiles exhibit a variable phase offset with respect to bottom topography, which is more evident for small radii ξ and higher values of α in absolute value;
- on the contrary, supercritical profiles are almost on phase with bottom topography, although slight offsets can be observed for small radii.

This is similar to what observed for the Sinusoidal Bottom in the Inviscid case (Sec. 2.3) and finds a natural explanation in the behaviour of the stream energy (Stream head), with the difference that now it is affected by friction dissipation: bottom topography still help or contrast the stream where it respectively decrease or increase, due to gravity, but friction amplifies the contrasting effect which, due to the Chèzy parametrization, the shallow-water model used and the radial symmetry, are more felt for smaller radii. In view of this, one can conjecture an offset of the Stream Head with respect to bottom topography, but no longer constant as described in Sec. 2.3 due to friction. This is actually confirmed by the model formulation described by Eq. 1.29, here reported for the specific case of sinusoidal bottom:

$$\frac{dy}{d\xi} = \frac{\gamma_b + ak_b \sin(k_b\xi) + \frac{2}{\xi^3 y^2} - \frac{\alpha}{\xi^2 y^3}}{1 - Fr^2} \tag{3.43}$$

or, equivalently, by using the non-dimensional Stream Head $\tilde{H}(\xi) = 1/\xi^2 y(\xi)^2$:

$$\frac{d\tilde{H}}{d\xi} = \gamma_b + ak_b \sin(k_b\xi) - \frac{\alpha}{\xi^2 y(\xi)^3} \tag{3.44}$$

Indeed, since the bottom topography slope is $\zeta'(\xi) = -ak_b sin(k_b\xi)$, one can conclude that the sinusoidal term of Eq. 3.44 exhibits an offset with respect to bottom topography, which is modulated (as well as amplitude) by the linear term due to basal slope γ_b and the friction term. The different response of the fluid height is then evident from Eq. 3.43 and depends on the Froude Number, which determines the sign of the denominator and reflects how inertia and gravity dominate the flow:

- subcritical flows ($Fr < 1$, where gravity dominates) maintain the marked offset observed for the Stream Head;
- supercritical flows ($Fr < 1$, where intertia dominates) are almost on phase with bottom topography, the slight offsets being determined by the presence of basal slope and friction.

Such results are evident in Figures 3.30, 3.32, 3.34, 3.36.

3.5 Step Bottom Topography

Let consider a step in the bed topography. For the sake of simplicity, this is represented by the function:

$$\zeta(\xi) = h_s \tanh[\sigma_s(\xi - \xi_s)] \tag{3.45}$$

where, as already discussed in Sec. 2.4, $h_s > 0$ controls the step height (which is given by $h_{step} = 2h_s$), $|\sigma_s|$ controls the steepness of the step, $\text{sgn}(\sigma_s)$ determines the direction of the step (increasing or decreasing) and ξ_s determines the radial position of the jump, as shown in Fig. 2.20.
As done previously, in order to simplify the model:

- $|\sigma_s|$ is assumed as an arbitrarily high number in order for the step to be sufficiently steep, but it is not considered as a parameter of the model;
- ξ_s would not be considered a parameter too, since eventual changes of the radial positions are not relevant for the economy of this work.

Finally, the expression of the first derivative $\zeta'(\xi)$ is recalled:

$$\zeta'(\xi) = h_s\sigma_s \,\text{sech}^2[\sigma_s(\xi - \xi_s)] \tag{3.46}$$

By plugging bed topography function 3.45 into Profile Equation 1.33, one obtains the following:

$$\frac{dy}{d\xi} = \frac{(\gamma_b - h_s\sigma_s \,\text{sech}^2[\sigma_s(\xi - \xi_s)])\xi^3y^3 + 2y - \alpha\xi}{\xi^3y^3 - 2\xi} = \frac{N(\xi, y)}{D(\xi, y)} \tag{3.47}$$

which is also equivalent to the following system:

$$\frac{d}{ds}\begin{bmatrix}\xi \\ y\end{bmatrix} = \begin{bmatrix}\xi^3y^3 - 2\xi \\ (\gamma_b - h_s\sigma_s \,\text{sech}^2[\sigma_s(\xi - \xi_s))\xi^3y^3 + 2y - \alpha\xi\end{bmatrix} \tag{3.48}$$

where, again, $(\xi, y) = (\xi(s), y(s))$ represent a parametrization of an orbit with respect to the parameter $s \in A \subset \mathbb{R}$.
The goal of this study is to investigate how the interaction between the step bottom and friction alter the dynamics with respect to the same case in absence of friction, as discussed in Sec. 2.4.

3.5.1 Phase Portrait

This section is devoted to the study of the $\xi - y$ Phase Portrait described by Eq. 3.47, whose geometry is again organized by the corresponding nullclines $N(\xi, y) = 0$ and $D(\xi, y) = 0$, this last one representing the Critical Line as usual. The section is organized as follows:

- first two subsections, in which the number and nature of the intersections of the nullcines are determined;
- qualitative appearence of the trajectories.

Number of Intersections of the Nullclines

By plugging the current expression of $\zeta'(\xi)$ into Eq. 1.36, some algebra leads to the following implicit equation to determine the number of possible intersections between the null-clines of Eq. 1.33:

$$\operatorname{sech}^2[\sigma_s(\xi - \xi_s)] = \frac{\gamma_b - \frac{\alpha}{2} + 2^{\frac{1}{3}}\xi^{-\frac{5}{3}}}{h_s\sigma_s} \tag{3.49}$$

The right hand side member of Eq. 3.49 defines a strictly increasing or decreasing function depending on whether, respectively $\sigma_s < 0$ or $\sigma_s > 0$.
Moreover:

$$\lim_{\xi\to 0} \frac{\gamma_b - \frac{\alpha}{2} + 2^{\frac{1}{3}}\xi^{-\frac{5}{3}}}{h_s\sigma_s} = \pm\infty$$

for, respectively, $\sigma_s > 0$ or $\sigma_s < 0$, while:

$$\lim_{\xi\to +\infty} \frac{\gamma_b - \frac{\alpha}{2} + 2^{\frac{1}{3}}\xi^{-\frac{5}{3}}}{h_s\sigma_s} = \frac{\gamma_b - \frac{\alpha}{2}}{h_s\sigma_s}$$

The left hand side of Eq. 3.49 defines instead a positive function, which exhibits the only absolute maximum 1 at $\xi = \xi_s$ and is symmetric with respect to such point. The number of intersections is governed by the monotony of the right hand side member of Eq. 3.49 and by the ratio A defined below:

$$A := \frac{\gamma_b - \frac{\alpha}{2}}{h_s\sigma_s} \tag{3.50}$$

The number of solutions of Eq. 3.49, which is consequence of the structure of the functions defining its two members, is reported in Chapter A of the Appendix, along with a discussion motivating the results summarized in Table A.1. As can be seen, the maximum number of intersections obtainable is three.
There are three cases in which intersections do not arise. The first one is the case in which $\sigma_s > 0$ and $A_s \geq 1$, that is:

$$\frac{\gamma_b - \frac{\alpha}{2}}{h_s\sigma_s} \geq 1$$

which can be re-arranged into:

$$\gamma_b - \frac{\alpha}{2} \geq h_s\sigma_s = \max_{\xi>0} \zeta'(\xi)$$

Last inequality suggests that intersections of the nullclines, potentially representing discontinuities, do not arise if the potential energy given by the basal slope, net of the energy

dissipation, exceeds the energy contribution given by the step (which is increasing, since $\sigma_s > 0$). The second is the case in which $\sigma_s < 0$ and $A_s < 0$, that is:

$$\frac{\gamma_b - \frac{\alpha}{2}}{h_s \sigma_s} < 0$$

which corresponds to the case $\gamma_b < \frac{\alpha}{2}$, that is, when friction dissipation dominates and the effect of the step (which is decreasing, since $\sigma_s < 0$) does not affect the dynamics. The last case is the one in which $0 \leq A_s < 1$, but according to what discussed in Chapter A, the function defining right hand side evaluated at $\xi = \xi_s$ exceeds 1, that is:

$$\frac{\gamma_b - \frac{\alpha}{2} + 2^{\frac{1}{3}} \xi_s^{-\frac{5}{3}}}{h_s \sigma_s} \geq 1$$

This can be interpreted similarly to the case in which $\sigma_s > 0$ and $A_s \geq 1$, but with the additional contribute $2^{\frac{1}{3}} \xi_s^{-\frac{5}{3}}$ which appears because here $0 \leq A_s < 1$.

Nature of the intersections of the Nullclines

Assume (ξ_*, y_*) being an intersection point of the nullclines, $\xi_* > 0$. By plugging the current expressions of $\zeta(\xi)$, $\zeta'(\xi)$ and $\zeta''(\xi)$ [23] into 1.44, 1.50, 1.51, the corresponding expressions for the Jacobian Trace and Determinant of system 1.4.4 are obtained:

$$(\text{tr } \mathbf{J_F})|_{(\xi_*, y_*)} = 3\alpha t_*^{-1} \tag{3.51}$$

$$(\det \mathbf{J_F})|_{(\xi_*, y_*)} = 5 + 6 \cdot 2^{1/5} t_*^{-3/5} \{-2 h_s \sigma_s^2 \tanh[\sigma_s(\xi_* - \xi_s)] \operatorname{sech}^2[\sigma_s(\xi_* - \xi_s)]\} \tag{3.52}$$

where, according to 1.46, in order to have $\xi_* > 0$ it must be satisfied:

$$t_* = -\gamma_b + \alpha/2 + h_s \sigma_s \operatorname{sech}^2[\sigma_s(\xi_* - \xi_s)] > 0$$

Then the sign depends on the relative position between ξ and ξ_* by means of $\tanh[\sigma_s(\xi_* - \xi_s)]$. One can thus conclude that $(\det \mathbf{J_F})|_{(\xi_*, y_*)}$ is positive for $\xi_* \gtrless \xi_s$ when respectively $\sigma_s \lessgtr 0$, and equals 5 when $\xi = \xi_s$.
The resulting geometries are displayed in Fig. 3.41 and summarized in Tables 3.3, 3.4, 3.5, respectively referred to the case $\alpha > 0$ (divergent flow), $\alpha < 0$ (convergent flow), $\alpha = 0$ (no friction).

[23] **Remark**: $\zeta''(\xi) = h_s \sigma_s^2 \, tanh[\sigma_s(\xi - \xi_s)] \, \operatorname{sech}[\sigma_s(\xi - \xi_s)]$

Trajectories

Figures 3.41, 3.42 show the behaviour of the orbits in the Phase Plane $\xi - y$, for $\gamma_b = 0.05, -0.05, 0$, $\alpha = \pm 0.4$ and step height $2h_s = 0.1$. The step is said to be Positive if it represents an increase of the bottom topography as ξ increases ($\sigma_s > 0$), otherwise it is said to be Negative ($\sigma_s > 0$). The case $\sigma_s > 0$ will be useful to determine the solutions.
In case of **Positive Step** ($\sigma_s > 0$, reported in Fig. 3.41), similarly to what observed for the inviscid case with same topography (Sec. 2.4), the trajectories result affected by the presence of the step in the bottom in proximity of its position. In particular, there is always at least one intersection, which is a focus that, in case friction coefficient or steepness are sufficiently small in absolute value, it is followed by a saddle.
Sufficiently far from the step position and the intersection points, the trajectories exhibit instead the same features observed for the flat case, as they represent nothing but a jump between two orbits obtained with flat bottom (see Sec. 2.4.2) due to a discontinuity in the height of the bottom.
Finally, it is interesting to observe the energetic role of the step, already discussed in Sec. 2.4: in case of convergent flows, where the step is felt as "descending" by the flow and helps adding favourable slope, the trajectories experiment an energy boost and can overcome the Conservative Solution reaching a Stream Head that is major of 1. On the other hand, in case of divergent flows, the step is felt as "ascending" by the flow and subtracts energy, being on opposite slope. Therefore, the trajectories experiment an abrupt reduction and can enter the internal region delimited by the Conservative Solution, reaching a Stream Head that is minor of 1.
Similar arguments can be used to explain the trajectories in case of Negative Step ($\sigma_s > 0$), reported in Fig. 3.42 where, as for the Positive Step case, a focus can arise but, on the contrary, it appears followed by a saddle only by increasing the step height $2h_s$ or the friction coefficient α.

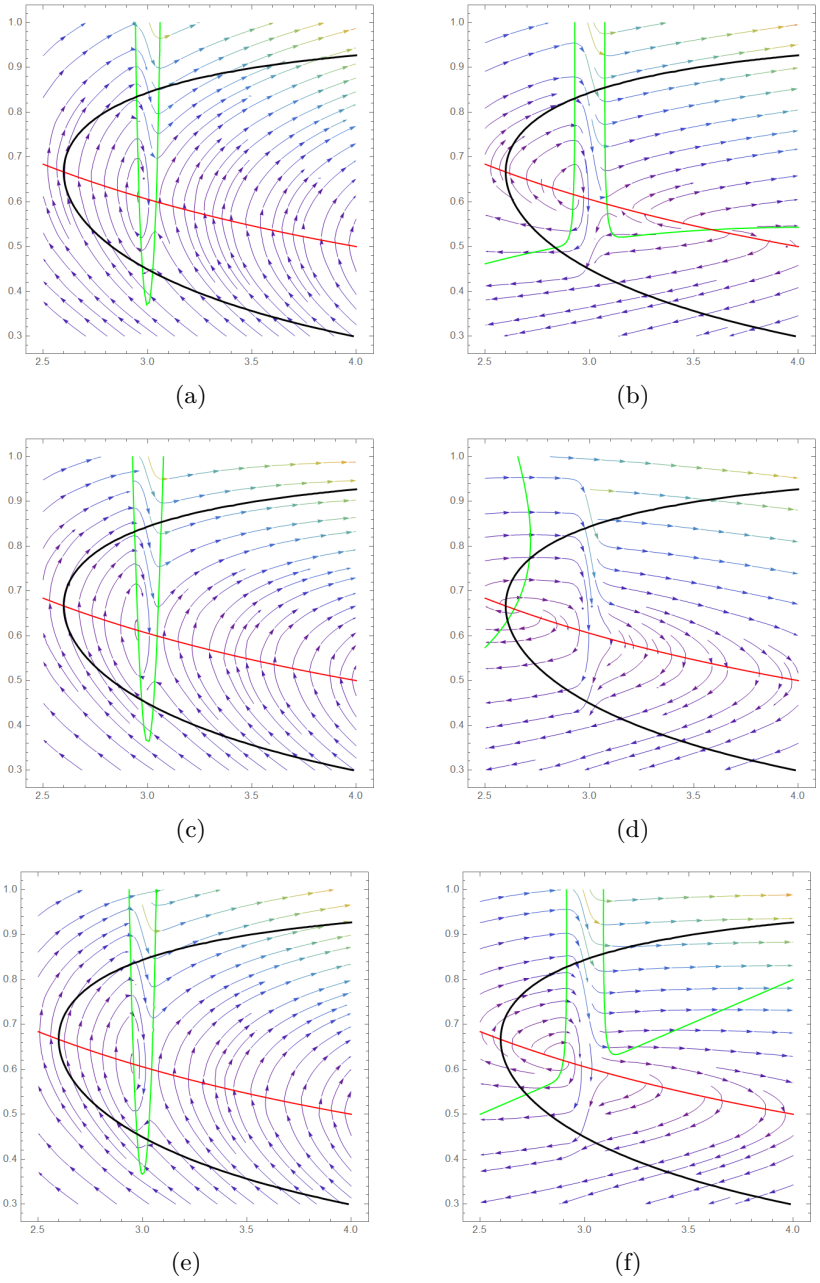

Figure 3.41: $\xi - y$ **Phase Portrait for Positive Step Bottom Topography** In all of the figures, $h_s = 0.05$, $\sigma_s = +30$, while the step is located at $\xi_s = 3$. Horizontal axis reports the radius ξ, the vertical one the height y, based on Eq. 3.47. Red line marks Critical conditions: subcr. trajectories lie under the red line, while supercr. ones lie above. Green line is the nullcline $N(\xi, y) = 0$ of Eq. 3.47. Black line represents the Conservative Solution (see Sec. 2.1). Left column, Figures 3.41(a), 3.41(c), 3.41(e) - Flows on Convergent direction ($\alpha = -0.4$) for Cone, Funnel and Horiz. Bed (resp., $\gamma_b = 0.05, -0.05, 0$). Right column, Figures 3.41(b), 3.41(d), 3.41(f) - Flows on Divergent direction ($\alpha = 0.4$) for Cone, Funnel and Horiz. Bed (resp., $\gamma_b = 0.05, -0.05, 0$).

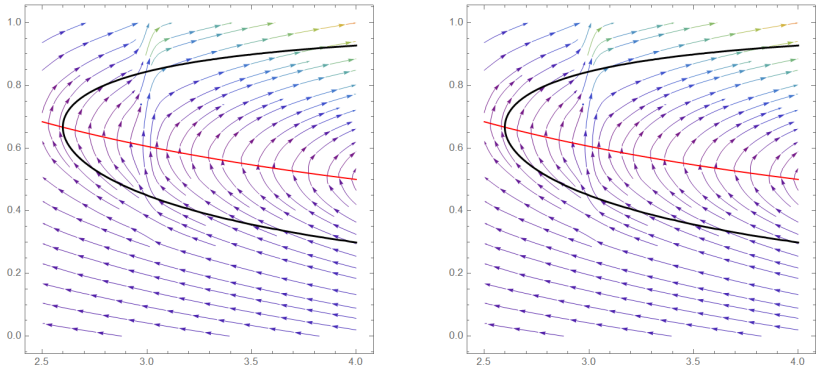

(a)

(b)

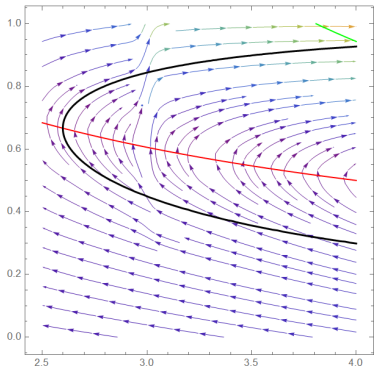

(c)

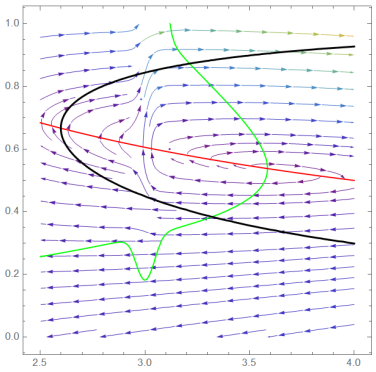

(d)

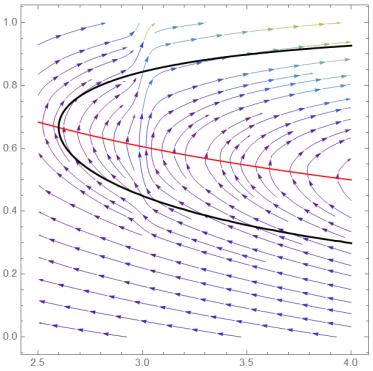

(e)

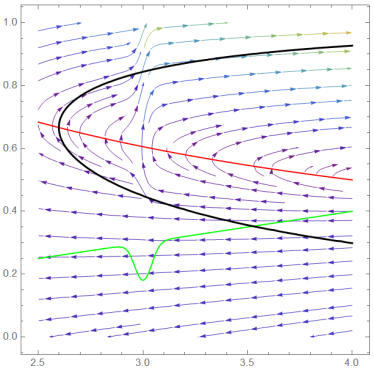

(f)

Figure 3.42: $\xi - y$ **Phase Portrait for Negative Step Bottom Topography** In all of the figures, $h_s = 0.05$, $\sigma_s = -30$, while the step is located at $\xi_s = 3$. Horizontal axis reports the radius ξ, the vertical one the height y, based on Eq. 3.47. Red line marks Critical conditions: subcr. trajectories lie under the red line, while supercr. ones lie above. Green line is the nullcline $N(\xi, y) = 0$ of Eq. 3.47. Black line represents the Conservative Solution (see Sec. 2.1). Left column, Figures 3.42(b), 3.42(b), 3.42(e) - Flows on Convergent direction ($\alpha = -0.4$) for Cone, Funnel and Horiz. Bed (resp., $\gamma_b = 0.05, -0.05, 0$). Right column, Figures **??**, 3.42(d), 3.42(f) - Flows on Divergent direction ($\alpha = 0.4$) for Cone, Funnel and Horiz. Bed (resp., $\gamma_b = 0.05, -0.05, 0$).

$\alpha > 0$										
$\text{tr}(\xi^*, y^*)$	> 0									
	$\sigma_s > 0$					$\sigma_s < 0$				
	$\xi^* > \xi_s$		$\xi^* < \xi_s$			$\xi^* > \xi_s$		$\xi^* < \xi_s$		
$\det(\xi^*, y^*)$	> 0		< 0	> 0		> 0		> 0		< 0
$\Delta(\xi^*, y^*)$	< 0	> 0	> 0	< 0	> 0	< 0	> 0	< 0	> 0	> 0
Equilibrium Point	U.F.	U.N.	Saddle	U.F.	U.N.	U.F.	U.N	U.F	U.N	Saddle

Table 3.3: **Possible geometries of the Phase Plane with step bottom topography for** $\alpha > 0$. The classification depends on the Jacobian Determinant and Discriminant $\Delta_* = [(\text{tr } \mathbf{J_F})|_{(\xi_*, y_*)}]^2 - 4(\det \mathbf{J_F})|_{(\xi_*, y_*)}$ of the characteristic polynomial associated to the Jacobian Matrix 1.49. Here, "U.F." and "U.N." respectively stand for "Unstable Focus" and "Unstable Node".

$\alpha < 0$										
$\text{tr}(\xi^*, y^*)$	< 0									
	$\sigma_s > 0$					$\sigma_s < 0$				
	$\xi^* > \xi_s$		$\xi^* < \xi_s$			$\xi^* > \xi_s$		$\xi^* < \xi_s$		
$\det(\xi^*, y^*)$	> 0		< 0	> 0		> 0		> 0		< 0
$\Delta(\xi^*, y^*)$	< 0	> 0	> 0	< 0	> 0	< 0	> 0	< 0	> 0	> 0
Equilibrium Point	S.F.	S.N.	Saddle	S.F.	S.N.	S.F.	S.N.	S.F.	S.N.	Saddle

Table 3.4: **Possible geometries of the Phase Plane with step bottom topography and**$\alpha < 0$. The classification depends on the Jacobian Determinant and Discriminant $\Delta_* = [(\text{tr } \mathbf{J_F})|_{(\xi_*, y_*)}]^2 - 4(\det \mathbf{J_F})|_{(\xi_*, y_*)}$ of the characteristic polynomial associated to the Jacobian Matrix 1.49. Here, "S.F." and "S.N." respectively stand for "Stable Focus" and "Stable Node".

3.5.2 Solutions

Since the purpose is to investigate the effect of a step topography, but described by an infinitely many times differentiable function, the parameter σ_s will be consider as fixed and sufficiently high in order for the first derivative to represent a slope of about 90°: in this work, $|\sigma_s| = 100$. Also the position of the step, for the sake of simplicity, will be fixed to $\xi_s = 4$.

$\alpha = 0$						
$\mathrm{tr}(\xi^*, y^*)$	0					
	$\sigma_s > 0$			$\sigma_s < 0$		
	$\xi^* > \xi_s$		$\xi^* < \xi_s$	$\xi^* > \xi_s$	$\xi^* < \xi_s$	
$\det(\xi^*, y^*)$	> 0	< 0	> 0	> 0	> 0	< 0
Equilibrium Point	Centre	Saddle	Centre	Saddle	Centre	Saddle

Table 3.5: **Possible geometries of the Phase Plane with Step Bottom topography in case friction is absent**. The classification depends on the sign of the Jacobian Determinant associated to the Jacobian Matrix 1.49.

Further simplifications arise from the geometry considered: $\sigma_s < 0$ (Negative Step) is assumed, in order to describe a bottom topography which decreases as ξ grows. Therefore, the step will be felt by the stream as "descending" if it flows on divergent direction, otherwise it will be felt as "ascending", helping or contrasting it in terms of energy depending on if it constitutes a favourable or an opposite slope variation.
Finally, in order to be more reliable with practical situations, only three cases will be discussed, that is, those for which the step is on favourable slope, helping the flow with an additional energy boost:

- Divergent stream flowing down a Cone-shaped Bed with Negative Step Bottom;
- Convergent stream flowing down a Funnel-shaped Bed with Negative Step Bottom;
- Divergent stream flowing along a Horizontal Bed with Negative Step Bottom.

Solutions for the case of Positive Step ($\sigma_s > 0$) are not discussed here, although the trajectories are reported in Fig. 3.41, as they do not provide further information to the description of the physical point of view carried out in this work. In view of this, Eq. 3.47 depends only on h_s, α and γ_b.

Divergent Stream flowing down a Cone-shaped bed with Negative Step Bottom, $\gamma_b = 0.05$, $\alpha = 0.2$

Fig. 3.43 reports the stream profile and features for the case of divergent flow down a cone-shaped bed and negative step bottom of height $2h_s = 0.2$. Boundary conditions are imposed at $\xi_0 = 3$ in order to obtain the supercritical and subcritical height profiles $y(\xi)$. In particular, the following heights are imposed:

- the subcritical height corresponding to unitary stream head;
- an arbitrary supercritical height corresponding to a Stream Head greater than 1.

The flow starts in supercritical condition. Then, immediately after the step position, a hydraulic jump connects it with the subcritical profile, which continues indefinitely, flowing on favourable slope.

Convergent Stream flowing down a Funnel-shaped bed with Negative Step Bottom, $\gamma_b = -0.05$, $\alpha = -0.2$

Fig. 3.44 reports the stream profile and features for the case of convergent flow down a funnel-shaped bed and negative step bottom of height $2h_s = 0.1$. Boundary conditions are imposed at $\xi_0 = 6$ in order to obtain the supercritical and subcritical height profiles $y(\xi)$. In particular, the following heights are imposed:

- the subcritical height corresponding to unitary stream head;
- an arbitrary supercritical height corresponding to a Stream Head greater than 1.

The flow starts in supercritical condition. Then, immediately after the step position, a hydraulic jump connects it with the subcritical profile, which continues until reaching critical condition at the edge of a central hole draining the fluid, located at the minimum radius.

Divergent Stream flowing along a Horizontal Bed with Negative Step Bottom, $\gamma_b = 0$, $\alpha = 0.2$

Fig. 3.45 reports the stream profile and features for the case of divergent flow along a horizontal bed with negative step bottom of height $2h_s = 0.2$. Boundary conditions are imposed at $\xi_0 = 3$ in order to obtain the supercritical and subcritical height profiles $y(\xi)$. In particular, the following heights are imposed:

- the subcritical height corresponding to unitary stream head;
- an arbitrary supercritical height corresponding to a Stream Head greater than 1.

The flow starts in supercritical condition. Then, immediately after the step position, a hydraulic jump connects it with the subcritical profile, which continues indefinitely preserving the stream head which results from the energy boost given by the step.

3.5.3 On the Froude Number and the Validity of the Zero Lenght Shock Approximation of Hydraulic Jump

It is immediate to observe, from Figures 3.43(b), 3.44(b), 3.45(b), that high Froude Numbers at the boundary are required for the supercritical profiles in order to be such energetic to generate hydraulic jump. This is mostly due to the behaviour of the supercritical trajectories, which experiment a rapid decrease in Stream Head while proceeding along Divergent (for Cone-shaped and Horizontal Bed) or Convergent (for Funnel-shaped Bed) direction in order to satisfy the Hydraulic constraint to reach critical conditions at, respectively, the external edge of the bed (maximum radius) or a central hole (minimum radius).

Such values Froude Numbers (from 10 to 40) are not usual in open channel experiments, but are documented and experimentally obtained, in the research topic of Cavitation (See [24, 45]). However, such Froude Numbers are proper of Strong Hydraulic Jump ([36]), which typically exhibit a roller of a certain length and is characterised by a significant amount of air bubbles incorpored, due to the fluid-air interaction ([31, 12]). Therefore, the theory adopted in this work of describing the hydraulic jump as a shock discontinuity fails in describing such a situation, which needs more detailed description including in the mass balance also lateral forces and bed friction ([29, 42]).

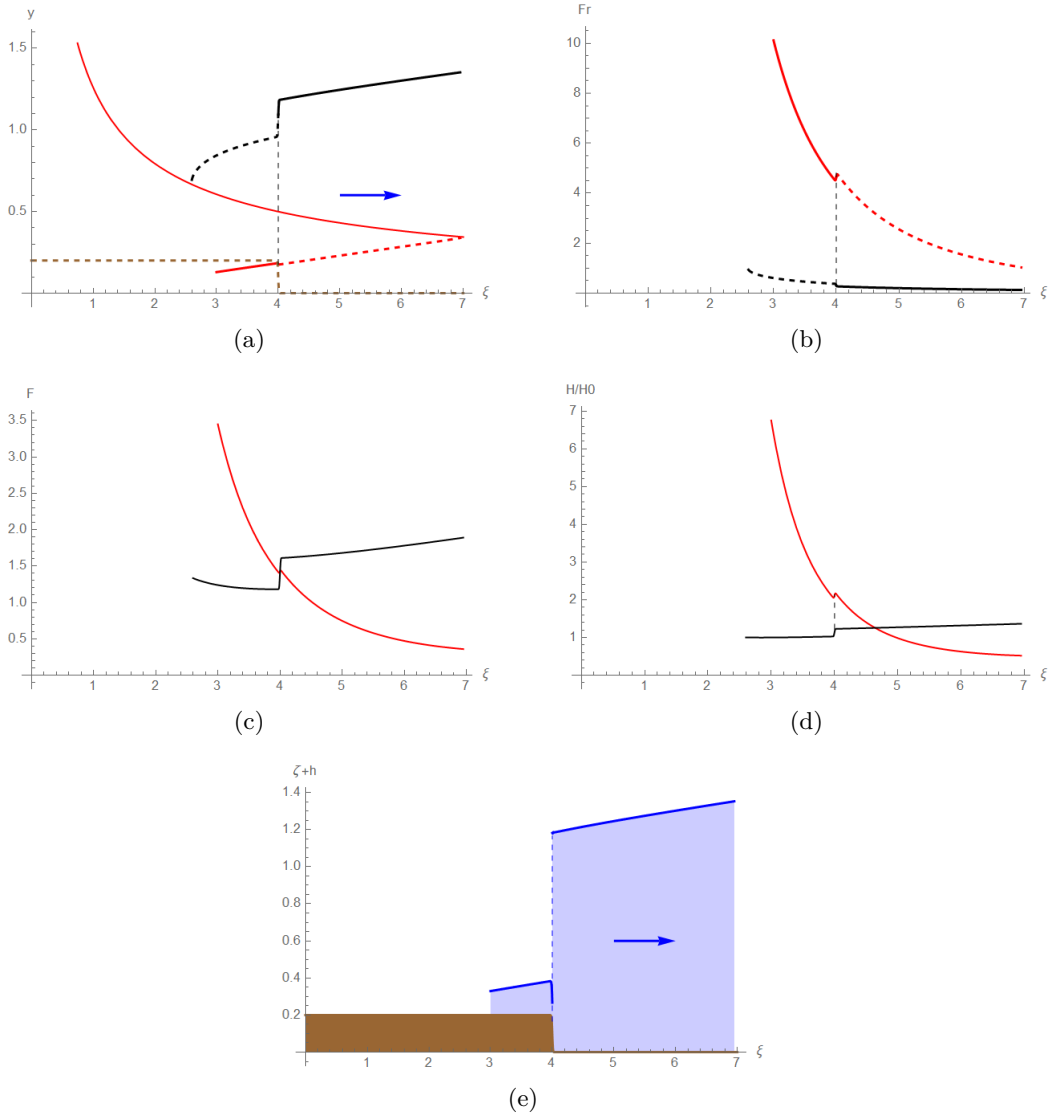

(a) (b) (c) (d) (e)

Figure 3.43: $\xi - y$ **Divergent Stream flowing down a Cone-shaped Bed with Negative Step Bottom,** $\gamma_b = 0.05$**,** $\alpha = 0.2$. Solution is obtained for $h_s = 0.1$, $\sigma_s = 100$, $\xi_s = 4$. In all of the figures, supercritical and subcritical reaches are respectively represented by red and black line. Solid lines in Figures 3.43(a) (Height Profile) and 3.43(b) (Froude Number) represent the jump solution, black and red dashed lines the solutions without jump. In Fig. 3.43(a), brown dashed line represents bottom topography, while solid line separating supercritical and subcritical reaches is the Critical Line. The blue arrow indicates the flow direction. Fig. 3.43(c) reports the branches of the Specific Force. Fig. 3.43(d) reports the branches of the Stream Head, along with jump discontinuity. Fig. 3.43(e) depicts the free surface of the fluid, along with the step bottom.

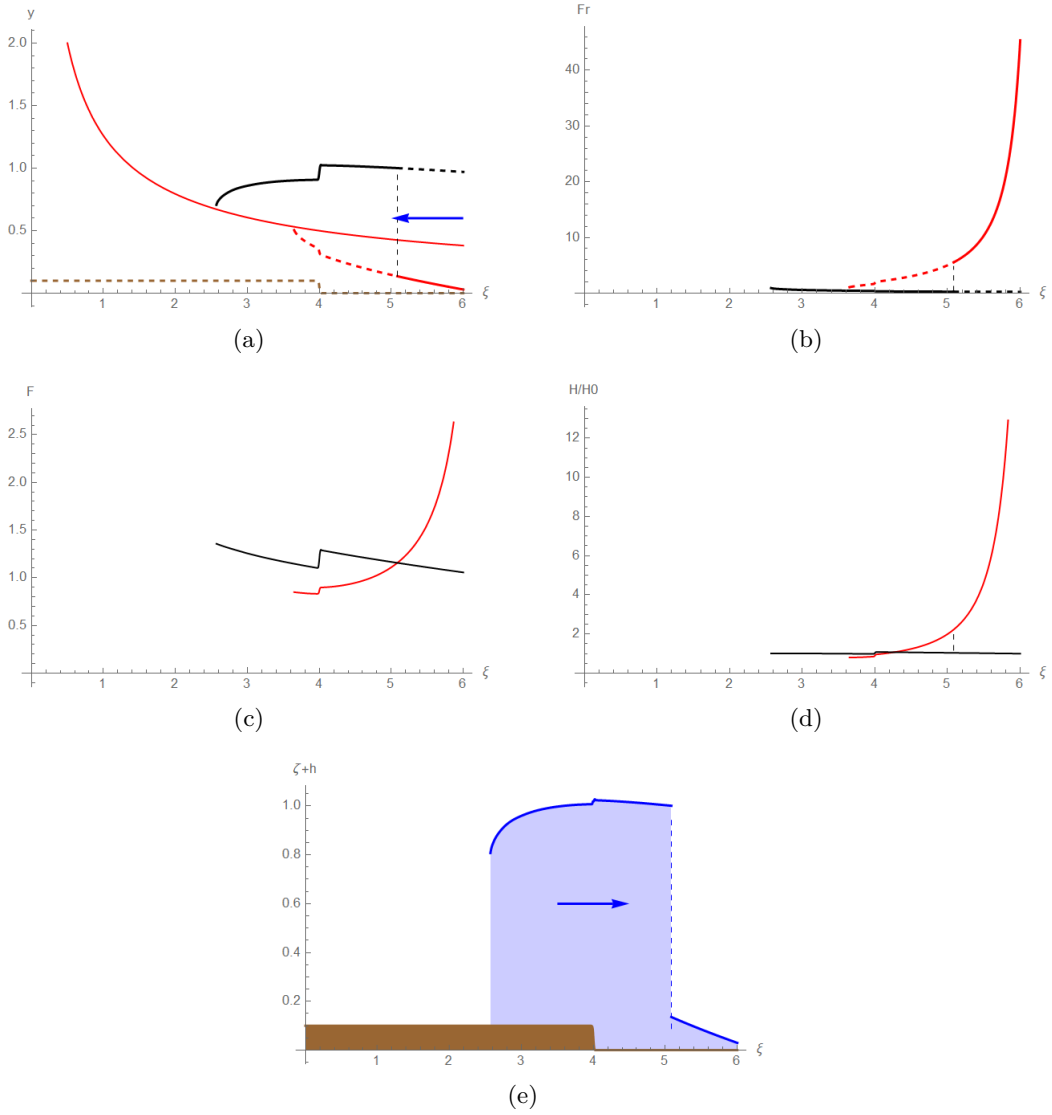

(a) (b) (c) (d) (e)

Figure 3.44: $\xi - y$ **Convergent Stream flowing down a Funnel-shaped Bed with Negative Step Bottom,** $\gamma_b = -0.05$**,** $\alpha = -0.2$. Solution is obtained for $h_s = 0.05$, $\sigma_s = 100$, $\xi_s = 4$. In all of the figures, supercritical and subcritical reaches are respectively represented by red and black line. Solid lines in Figures 3.44(a) (Height Profile) and 3.44(b) (Froude Number) represent the jump solution, black and red dashed lines the solutions without jump. In Fig. 3.44(a), brown dashed line represents bottom topography, while solid line separating supercritical and subcritical reaches is the Critical Line. The blue arrow indicates the flow direction. Fig. 3.44(c) reports the branches of the Specific Force. Fig. 3.44(d) reports the branches of the Stream Head, along with jump discontinuity. Fig. 3.44(e) depicts the free surface of the fluid, along with the step bottom.

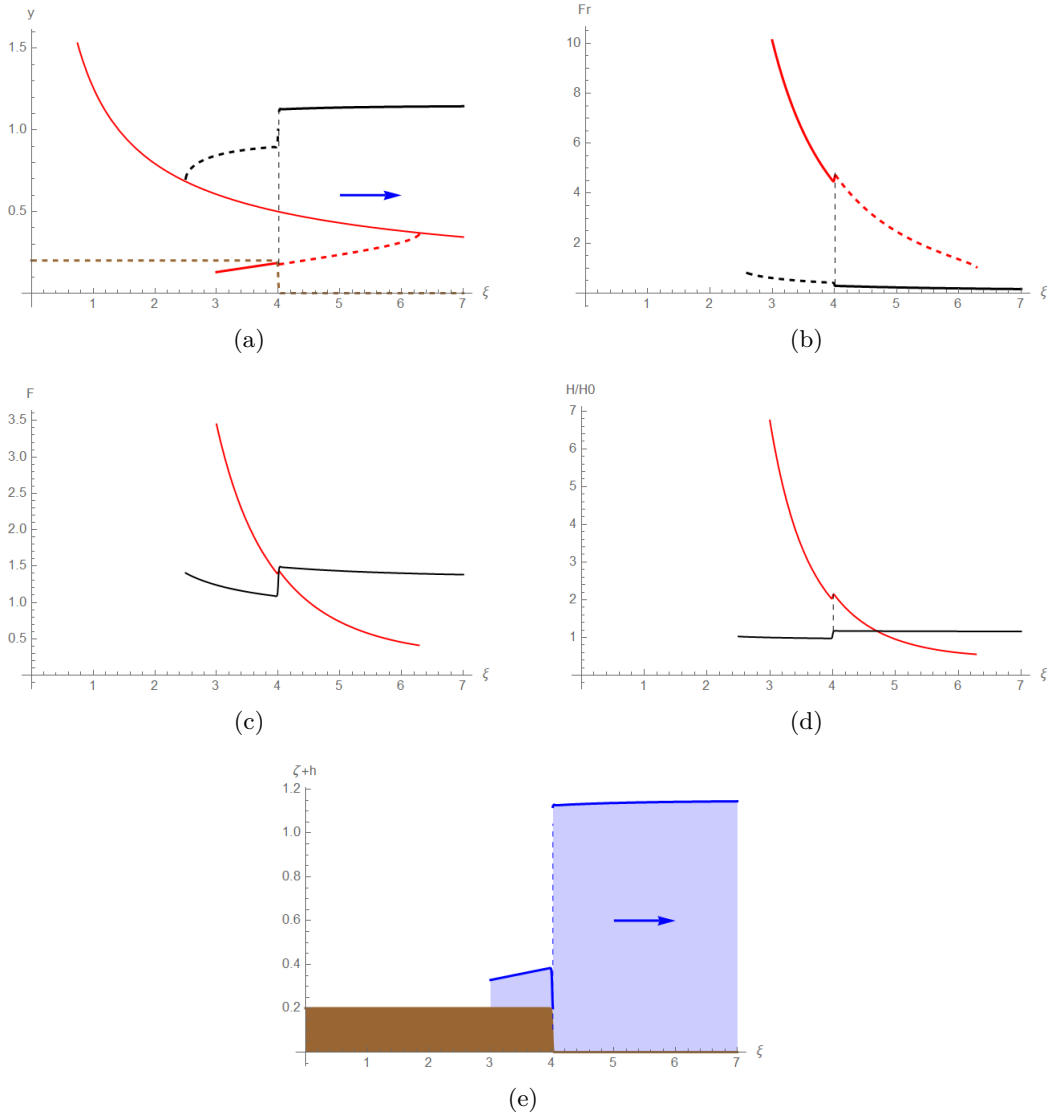

(a) (b) (c) (d) (e)

Figure 3.45: $\xi - y$ **Divergent Stream flowing along a Horizontal Bed with Negative Step Bottom,** $\gamma_b = 0$**,** $\alpha = 0.2$. Solution is obtained for $h_s = 0.1$, $\sigma_s = 100$, $\xi_s = 4$. In all of the figures, supercritical and subcritical reaches are respectively represented by red and black line. Solid lines in Figures 3.45(a) (Height Profile) and 3.45(b) (Froude Number) represent the jump solution, black and red dashed lines the solutions without jump. In Fig. 3.45(a), brown dashed line represents bottom topography, while solid line separating supercritical and subcritical reaches is the Critical Line. The blue arrow indicates the flow direction. Fig. 3.45(c) reports the branches of the Specific Force. Fig. 3.45(d) reports the branches of the Stream Head, along with jump discontinuity. Fig. 3.45(e) depicts the free surface of the fluid, along with the step bottom.

Chapter 4

Comparison between Inviscid and Viscous Profiles

Chapters 2 and 3 highlight that significant differences arise if turbulent friction, acting in the direction opposite to the stream, is included into the model. Indeed, it introduces a dissipative contribute which, interacting with gravity, alters the dynamics opening to the possibility of having discontinuous transitions from supercritical to subcritical flows, taking place through hydraulic jumps. Such differences are well evident, from a Dynamical System point of view, by the presence of critical points in the Phase Portrait, particularly focus and saddle points.
In this Chapter, two important features of the stream previously investigated are reported to make a comparison between the Inviscid model (in which turbulent friction is neglected) and the Viscous model (in which turbulent friction is included):

- the height profiles for the flat bottom, whose monotony reflects also on the overall trend of that obtained for the sinusoidal and the stepped bottom topographies;
- the stream response to the sinusoidal bottom topography.

This comparison will be done by recalling the basic explanations, collected in tables recalling also the related figures.

4.1 Behaviour of the Trajectories for Flat Bottom Topography

As explained in Sec. 3.3.1, the introduction of friction alter the behaviour of the trajectories, where, as expected:

- the subcritical trajectories appear governed by the basal slope γ_b;
- the supercritical trajectories appear instead governed by friction, by means of α.

This depends on the behaviour of the Radiant Specific Discharge, whose relation with the stream depth y is described by Eq. 3.32 and depicted in the $q-y$ phase portrait in Fig. 3.16, where it is evident that friction dissipation make a focus arise in the dynamical system, attracting or repulsing the $q(y)$ trajectories.
The difference in the behaviour of the height profiles is summarized in Table 4.1, where *one Froude Horizon* and *two Froude Horizons* behaviours describe the situations in which the trajectories collide with the Critical Line $y = \sqrt[3]{2/\xi^2}$ respectively at the sole minimum radius and at both minimum and maximum radii.
The same happens for the Sinusoidal Bottom Topography, which can be seen as a sinusoidal perturbation of the Flat Bottom Topography. This was already reported in Tab. 3.1.

Table 4.1: **Comparison between Geometric Structure of the Trajectories in the Phase Plane in the Inviscid ($\alpha = 0$) and Viscous ($\alpha \neq 0$) cases for Flat Bottom Topography.** . The table highlights the dependence of the geometric structure of trajectories described by Sys. 3.38 (equivalently, Eq. 3.37) on the main model parameters: basal slope γ_b and friction coefficient α. The abbreviations "SUB" and "SUP" respectively stand for "Subcritical branch" and "Supercritical branch", while "1 F.H." and "2 F.H." stand respectively for *one Froude Horizon* (i.e. only a minimum radius where the stream meets Critical conditions) and *two Froude Horizons* (i.e., both a minimum and a maximum radius where the stream meets Critical conditions).

Viscous (Sec. 3.3)					**Inviscid** (Sec. 2.1, 2.2)	
Fig. 2.3					Fig. 3.15	
	$\gamma_b \geq 0$		$\gamma_b < 0$		$\gamma_b \geq 0$	$\gamma_b < 0$
	$\alpha > 0$	$\alpha < 0$	$\alpha > 0$	$\alpha < 0$	$\alpha = 0$	
SUB	1 F.H.		2 F.H.		1 F.H.	2 F.H.
SUP	2 F.H.	1 F.H.	2 F.H.	1 F.H.	1 F.H.	2 F.H.

4.2 Stream Amplitude Response to the Sinusoidal Bottom Topography

Another significant difference between the Inviscid and the Viscous cases is the response of the Stream Height to the Bottom Topography. Indeed, in absence of friction and depending on the flow direction (convergent or divergent) and from its monotony , it can be felt as "ascending" or "descending" by the stream, thus respectively opposing or helping in terms of stream energy. Moreover, if the stream flows along favourable basal slope γ_b then it provides additional energy, while if the flow is on opposite slope the energy is subtracted. This explains the amplitude responses reported in Tab. 2.3 for the Inviscid Case. However, when friction is considered, the new *two Froude Horizons*

geometries in Tab. 3.1 give rise to non monotonic height profiles $y(\xi)$, which reflect on the amplitude response. The behaviour is summarized in Tab. 4.2. It is worth to notice that the transition from the Dampening to the Amplifying behaviour (and vice versa), when present, happens at the minimum or maximum point of the height profile: it appears instead governed by the Radiant Specific Kinetic Height $k_s(\xi)$, as earlier explained in Sec. 2.3.2.

Table 4.2: **Comparison of Flow Amplitude response to Sinusoidal Bottom Topography, for the Inviscid ($\alpha = 0$) and the Viscous ($\alpha \neq 0$) case**. Here, "A", "D" and "S" stand respectively for "AMPLIFYING", "DAMPING", "STABILIZING". For the Inviscid case $\alpha = 0$, the table must be read in the divergent flow direction (increasing ξ): for the convergent one, it suffices to invert the flow and, consequently, "DAMP" with "AMP". For the Viscous case, if $\alpha > 0$ the table must be read in divergent flow direction, while if $\alpha < 0$ it must be read in the convergent flow direction (they cannot be inverted without changing the sign of α as for the Inviscid case). The notation "D $\rightarrow$ A" and "A $\rightarrow$ D", present only in the *two Froude Horizons* height profiles, indicates that a change in the amplitude response occurs at a stationary point of the height profile. The notation "A $\rightarrow$ S" indicates that a stabilization occurs after an initial amplification.

	Viscous (Sec. 3.4)						**Inviscid** (Sec. 2.3.2)		
	$\alpha < 0$			$\alpha > 0$			$\alpha = 0$		
	$\gamma_b > 0$	$\gamma_b < 0$	$\gamma_b = 0$	$\gamma_b > 0$	$\gamma_b < 0$	$\gamma_b = 0$	$\gamma_b > 0$	$\gamma_b < 0$	$\gamma_b = 0$
SUB	D	A	D	A	A $\rightarrow$ D	A $\rightarrow$ S	D	D $\rightarrow$ A	D
SUP	A	A	A	D $\rightarrow$ A	D $\rightarrow$ A	D $\rightarrow$ A	A	A $\rightarrow$ D	A $\rightarrow$ S
Fig.	3.29	3.33	3.39	3.31	3.35	3.37	2.19		

Chapter 5

Linear Stability of de Saint-Venant Equation

In this chapter, an equation to perform the Linear Stability Analysis of the de Saint-Venant Equations 1.2 in radial simmetry is obtained, following a similar approach to that in [4]. However, as will be seen, an important obstacle to the procedure is represented by the singularities of the kind ξ^a, $a < 0$, that are exhibited by the equation. Although this problem will not be solved in this context, the study carried out in this Chapter provides an Equation and solution ideas that can be useful as a basis for future work.

5.1 Perturbations Equations

Let consider viscous, dimensional de Saint-Venant's Equations 1.2, here reported again already written in radial symmetry:

$$\begin{cases} \frac{\partial u}{\partial t} + u\frac{\partial u}{\partial r} = g\cos\phi\left(\tan\phi - \frac{\partial h}{\partial r} - \frac{\partial z_b}{\partial r}\right) - C_f f(u,h) \\ \frac{\partial h}{\partial t} + \frac{1}{r}\frac{\partial (rhu)}{\partial r} = 0 \end{cases} \tag{5.1}$$

where the generic closure term for friction is expressed as $C_f f(u,h)$ [1].
Let call $U_s = U(r)$ and $H_s = H_s(r)$ [2] a steady state solution of system 1.2 and consider a sufficiently small perturbation of such solution, expressed by means of functions $u'(r,t)$ and $h'(r,t)$ such that:

$$\begin{cases} |u'(r,t=0)| << |U_s(r)| \ \forall r > 0 \\ |h'(r,t=0)| << |H_s(r)| \ \forall r > 0 \end{cases}$$

[1] In case of Chèzy closure term, one has $C_f = 1/C^2$, where C is the Chèzy drag coefficient and $f(u,h) = u^2 \operatorname{sgn} u/h$.

[2] The subscript "S" stands for "Steady".

Then the perturbed solution can be expressed as:

$$\begin{cases} u(r,t) = U_s(r) + u'(r,t) \\ h(r,t) = H_s(r) + h'(r,t) \end{cases}$$

By plugging such expressions into Equations 5.1 and developing the radial derivative involved in the second equation, one obtains:

$$\begin{cases} \frac{\partial u'}{\partial t} + \frac{\partial U_s}{\partial t} + U_s\frac{\partial U_s}{\partial r} + U_s\frac{\partial u'}{\partial r} + u'\frac{\partial U_s}{\partial r} + u'\frac{\partial u'}{\partial r} = g\cos\phi\left[\tan\phi - \frac{\partial(H_s+h'+z_b)}{\partial r}\right] - C_f f(U_s+u', H_s+h') \\ \frac{\partial(H_s+h')}{\partial t} + \frac{1}{r}\Big[(H_s+h')(U_s+u') + r(U_s\frac{\partial H_s}{\partial r} + u'\frac{\partial H_s}{\partial r} + U_s\frac{\partial h'}{\partial r} + u'\frac{\partial h'}{\partial r} + h'\frac{\partial u'}{\partial r} + h'\frac{\partial U_s}{\partial r} + H_s\frac{\partial U_s}{\partial r} + H_s\frac{\partial u'}{\partial r}) \end{cases} \tag{5.2}$$

Because of the limit of small perturbations, assuming the function $f(\cdot,\cdot)$ to be differentiable with respect to its arguments, friction term can be approximated at first order as:

$$f(U_s+u', H_s+h') \approx f(U_s, H_S) + u'\frac{\partial f}{\partial u'}|_{u'=U_s} + h'\frac{\partial f}{\partial h'}|_{h'=Y_s} = f(U_s,H_s) + u'f_U + h'f_H$$

Moreover, in order to linearize the system, terms of order higher than the first can be identified by means of a simple dimensional analysis and neglected. Therefore, the system can be written as follows:

$$\begin{cases} \frac{\partial u'}{\partial t} + \frac{\partial U_s}{\partial t} + U_s\frac{\partial U_s}{\partial r} + U_s\frac{\partial u'}{\partial r} + u'\frac{\partial U_s}{\partial r} = g\cos\phi\left[\tan\phi - \frac{\partial(H_s+h'+z_b)}{\partial r}\right] - C_f(f(U_s,H_s) - u'f_U - h'f_H) \\ \frac{\partial H_s}{\partial t} + \frac{\partial h'}{\partial t} + \frac{1}{r}\Big[\frac{\partial r}{\partial r}(H_su' + H_sU_s + h'U_s) + rU_s\frac{\partial Y}{\partial r} + ru'\frac{\partial H_s}{\partial r} + rU_s\frac{\partial h'}{\partial r} + rh'\frac{\partial U_s}{\partial r} + rH_s\frac{\partial U_s}{\partial r} + rH_s\frac{\partial u'}{\partial r}\Big] = 0 \end{cases} \tag{5.3}$$

where the equality $1 = \frac{\partial r}{\partial r}$ is used in order to recognize notable derivatives.
Now, remembering that steady state solutions satisfy:

$$\begin{cases} \frac{\partial U_s}{\partial t} = 0 \\ \frac{\partial H_s}{\partial t} = 0 \end{cases}$$

together with the Continuity and steady Momentum Equations:

$$\begin{cases} \frac{1}{r}\frac{\partial(rH_sU_s)}{\partial r} = 0 \\ U_s\frac{\partial U_s}{\partial r} = g\cos\phi\Big(\tan\phi - \frac{\partial H_s}{\partial r} - \frac{\partial z_b}{\partial r}\Big) - C_f f(U_s,H_s) \end{cases}$$

one can simplify system 5.3 as follows:

$$\begin{cases} \frac{\partial u'}{\partial t} + U_s \frac{\partial u'}{\partial r} + u' \frac{\partial U_s}{\partial r} = -g \cos\phi \frac{\partial h'}{\partial r} - C_f(-u' \frac{\partial f}{\partial u'}|_{u'=U_s} - h' \frac{\partial f}{\partial h'}|_{h'=H_s}) \\ \frac{\partial h'}{\partial t} + \frac{1}{r}\left[\frac{\partial r}{\partial r}(H_s u' + h' U_s) + r u' \frac{\partial H_s}{\partial r} + r U_s \frac{\partial h'}{\partial r} + r h' \frac{\partial U_s}{\partial r} + r H_s \frac{\partial u'}{\partial r}\right] = 0 \end{cases} \tag{5.4}$$

Simple re-arrangement and usage of radial derivatives leads to the following dimensional system for height and velocity perturbations:

$$\begin{cases} \frac{\partial u'}{\partial t} + \frac{\partial (U_s u')}{\partial r} = -g \cos\phi \frac{\partial h'}{\partial r} - C_f(-u' \frac{\partial f}{\partial u'}|_{u'=U_s} - h' \frac{\partial f}{\partial h'}|_{h'=H_s}) \\ \frac{\partial h'}{\partial t} + \frac{1}{r}\frac{\partial}{\partial r}\left[r(H_s u' + U_s h')\right] = 0 \end{cases} \tag{5.5}$$

In order to write a non-dimensional form of System 5.5, proper reference scales for the variables must be taken into account. In particular, if Q is the constant discharge of the steady solution, such reference scales can be individuated by the radius $R = \frac{Q}{2\pi H_0 \sqrt{2gH_0 \cos\phi}}$, Stream Head H_0 of the steady solution at the boundary, $U_0 = \sqrt{2gH_0 \cos\phi}$ and $t_0 = \frac{R}{U_0}$ respectively for radial length, height and time.
The following non-dimensional variables can then be defined:

$$\xi = \frac{r}{R}\ , \quad \tau = \frac{t}{t_0}\ , \quad v' = \frac{u'}{U_0}\ , \quad V = \frac{U_s}{U_0}\ , \quad y' = \frac{h'}{H_0} \quad Y = \frac{H_s}{H_0}$$

where $t_0 = R/U_0$.
By plugging them into System 5.5, one obtains:

$$\begin{cases} \frac{U_0^2}{R}\frac{\partial v'}{\partial \tau} + \frac{U_0^2}{R}\frac{\partial (V v')}{\partial \xi} = -g\frac{H_0}{R}\cos\phi \frac{\partial y'}{\partial \xi} - C_f(-v' \frac{\partial f}{\partial v'}|_{v'=V} - y' \frac{\partial f}{\partial y'}|_{y'=Y}) \\ \frac{H_0 U_0}{R}\frac{\partial y'}{\partial \tau} + \frac{H_0 U_0}{R}\frac{1}{\xi}\frac{\partial}{\partial \xi}\left[\xi(Y v' + V y')\right] = 0 \end{cases} \tag{5.6}$$

Dividing both members of the first equation by $g\frac{H_0}{R}\cos\phi$ and both members of second equation by $\frac{H_0 U_0}{R}$, the final form of **Perturbation Equations** is:

$$\begin{cases} F^2\left[\frac{\partial v'}{\partial \tau} + \frac{\partial (V v')}{\partial \xi}\right] = \frac{\partial y'}{\partial \xi} - \frac{C_f R}{g H_0 \cos\phi}\left(- v' \frac{\partial f}{\partial v'}|_{v'=V} - y' \frac{\partial f}{\partial y'}|_{y'=Y}\right) \\ \frac{\partial y'}{\partial \tau} + \frac{1}{\xi}\frac{\partial}{\partial \xi}\left[\xi(Y v' + V y')\right] = 0 \end{cases} \tag{5.7}$$

where the Froude Number, denoted for all this chapter with F instead of Fr to simplify the notation, is again:

$$F = \frac{U_0}{\sqrt{gH_0 \cos\phi}}$$

These equations represent the analogous of those obtained by [4], taking into account

radial symmetry. As can be seen, the second equation exhibit a fuchsian singularity of order 1 in the variable ξ, which radically changes the dynamics of the perturbations with respect to the cartesian one-dimensional case. Notice that, also in this case, the Perturbation Equations do not depend on the bottom topography used.

5.2 Perturbation of Uniform Height Flow with flat bottom

5.2.1 Problem Formulation

Let consider the steady state solution corresponding to uniform height flow, described in Sec. 3.1.2 and which, in dimensional terms, correspond to:

$$h(r) = h_0 \tag{5.8}$$

Then, by remembering the continuity equation of system 1.2 and assuming steady state, one has:

$$ur = const = \frac{Q}{h_0} \tag{5.9}$$

where Q is the constant flow rate. By using the usual non-dimensional variables, the previous relations turn into the following form for the non-dimensional solutions $Y(\xi)$, $V(\xi)$:

$$\begin{cases} Y(\xi) = 1 \\ V(\xi) = \frac{1}{\xi} \end{cases} \tag{5.10}$$

Assuming again Chézy Parametrization for drag term, one obtains the following relations:

$$\begin{cases} \frac{\partial f}{\partial u}|_{(u,h)} = \frac{2u}{h} \\ \frac{\partial f}{\partial h}|_{(u,h)} = -\frac{u^2}{h^2} \end{cases} \tag{5.11}$$

which, evaluated at steady state solution 5.10 in non-dimensional form, become:

$$\begin{cases} f_U = \frac{2}{\xi} \\ f_H = -\frac{1}{\xi^2} \end{cases} \tag{5.12}$$

By plugging 5.10, 5.12 into Perturbations Equations 5.7, one has:

$$\begin{cases} \frac{\partial v'}{\partial \tau} + \frac{1}{\xi}\frac{\partial v'}{\partial \xi} - \frac{v'}{\xi^2} = \frac{1}{F^2}\frac{\partial y'}{\partial \xi} - \frac{C_f R}{F^2 g H_0 \cos\phi}\left(- \frac{2v'}{\xi} + \frac{y'}{\xi^2}\right) \\ \frac{\partial y'}{\partial \tau} + \frac{v'}{\xi} + \frac{\partial v'}{\partial \xi} + \frac{1}{\xi}\frac{\partial y'}{\partial \xi} = 0 \end{cases} \tag{5.13}$$

Both the equations of the previous linear system of ordinary differential equations exhibit fuchsian singularities at $\xi = 0$, derived from friction terms and the symmetry. In order to derive a solution to the previous linear system, let assume separation between time and space variables :

$$\begin{cases} v'(\xi) = \nu(k\xi)\exp(\sigma\tau) \\ y'(\xi) = \eta(k\xi)\exp(\sigma\tau) \end{cases} \tag{5.14}$$

Here,

$$k = k_r + ik_i \tag{5.15}$$

represents the wavenumber, while:

$$\sigma = \sigma_r + i\sigma_i \tag{5.16}$$

where σ_r and $k_r\sigma_i$ respectively denote the growth rate and the phase speed.
By plugging 5.14 into 5.17 and simplifying the exponential terms which arise at each addend involved the two equations, one has:

$$\begin{cases} \sigma\nu + \frac{k}{\xi}\frac{d\nu}{d\xi} - \frac{\nu}{\xi^2} = \frac{k}{F^2}\frac{d\eta}{d\xi} - \frac{C_f R}{F^2 g H_0 \cos\phi}\left(- \frac{2\nu}{\xi} + \frac{\eta}{\xi^2}\right) \\ \sigma\eta + \frac{\nu}{\xi} + k\frac{d\nu}{d\xi} + \frac{k}{\xi}\frac{d\eta}{d\xi} = 0 \end{cases} \tag{5.17}$$

where the partial derivatives descending from the original system can now be interpreted as total derivatives, since the dependence on the time variable τ has been removed by variable separation ansatz and the equation is extended to the Complex field $\mathbb{C}$.
Such equation is non-autonomous (with respect to the space variable ξ) and exhibits a Fuchsian singularity ([39]) at $\xi = 0$, thus requires a more accurate analysis to be solved numerically, which can be part of a future work. A drastic simplification could be that of solving for sufficiently large ξ by assuming that ν/ξ, ν/ξ^2, η/ξ, η/ξ^2, $1/\xi(d\nu/d\xi)$ and $1/\xi(d\eta/d\xi)$ are approximately 0, in order to obtain the following system:

$$\frac{d}{d\xi}\begin{bmatrix}\eta \\ \nu\end{bmatrix} = \begin{bmatrix} 0 & \frac{\sigma F^2}{k} \\ -\frac{\sigma}{k} & 0 \end{bmatrix}\begin{bmatrix}\eta \\ \nu\end{bmatrix} = \mathbf{A}\begin{bmatrix}\eta \\ \nu\end{bmatrix} \tag{5.18}$$

which is linear and homogeneous. The trace of the matrix $\mathbf{A}$ has null trace, while the determinant is:

$$\det A = \frac{\sigma^2 F^2}{k^2} \tag{5.19}$$

so that the nature of the eigenvalues depends on both σ and k. In particular, if they are

real, the determinant is positive, while the discriminant $\Delta = \operatorname{tr} \mathbb{A}^2 - 4 \det \mathbb{A} = -\det \mathbb{A}$ is negative, thus the system exhibits a stable center at the origin, giving rise to oscillating solutions for $\eta(\xi)$ and $\nu(\xi)$.

Conclusions

Circular Shallow water profiles, as well as Circular Hydraulic Jump, have been studied for at least two centuries, starting from the early work of Giorgio Bidone in 1820 (Ref. [7]). They can be observed in all day situations, including the case of a smooth jet impinging a plate. They are employed in a variety of applications, including stilling basins (Ref. [1, 28]) in River Engineering and in the context of Analogue Gravity (Ref. [18]), in order to investigate complex cosmological phenomena by studying other simpler, well known physical systems exhibiting the same properties (Ref. [40]).
Despite their usefulness, the related literature is currently partial and circumscribed to specific cases, often coming from the application. In particular, there not exists a systematic classification of models able to describe all of the basic physical and mathematical aspects of flows along radial, axially-symmetric channel, differently for the Open Channel Flows (Ref. [36, 25]). The only exceptions in this sense are the studies on the Circular Hydraulic Jump, including Ref. [8, 22, 23, 14, 11], while a first classification of Circular Shallow Water profiles can be found in Ref. [42] and, more systematic, in Ref. [29].
In this framework, this work proposes a two-dimensional Shallow water model, described by the set of de Saint-Venant equations with Chezy closure term for turbulent friction ([29]), with the aim of providing a systematic classification of the Circular Stream profiles for an inclined channel in radial, axially-symmetric geometry. Depending on the inclination, expressed by a so called "basal slope", the bed appears as Horizontal, Cone-shaped or Funnel-shaped. The bottom topography is then represented as a function describing the departures from the flat bottom, as done in [4]. In particular, the stream profiles are obtained for the flat, sinusoidal and stepped bottom topography.
A study of the dynamical system describing the height profiles for a generic bottom topography allows to recover general properties on the corresponding phase portrait, including the trajectories, which open to a variety of possible geometries. The presence of hydraulic jump is then deduced by the presence of eventual critical points in the physical region of the phase portrait, as described in [36] and is modeled as a shock discontinuity of zero length, ignoring lateral components of the hydrostatic force (Ref. [29, 42]).
When turbulent friction is not included into the model (*Inviscid* model), the general equation describing the height profile is symmetric under inversions of flow direction, provided that the sign of the basal slope changes coherently, generalizing what discussed in [29]. Therefore, the stream profiles obtained can be interpreted on both convergent (i.e., along decreasing radii) or divergent (i.e., along increasing radii) direction. In particular, those with negative basal slope start and end in critical conditions, showing a *two Froude*

Horizons behaviour already documented in Ref. [29] for the viscous case and finding an Analogue Gravity counterpart in Ref. [46] . When the sinusoidal bottom topography is introduced, the stream amplitude response varies and appears governed by the behaviour of the *Radiant Specific Kinetic Height*, which describes the distribution of the Kinetic Energy along each radial distance, by means of Ineq. 2.43.
When turbulent friction is included (*Viscous* Model), it is possible to obtain bottom topographies which, thanks to the balance with potential energy due to gravity and friction dissipation, guarantee Constant Stream Head Flow, Critical Flow and Uniform Flow: in this latter case, the transition from supercritical to subcritical regime is smooth and hydraulic jump does not form. When flat bottom topography is introduced, the monotony properties of the stream profiles change significantly: the subcritical profiles appear influenced mostly by basal slope, while the supercritical ones seem instead to be dominated by friction. The same happens for sinusoidal bottom topography, where due to this the amplitude response of the flow to the bottom topographies results different with respect to the Inviscid model. Due to friction, the behaviour of the trajectories in the Phase Portrait is more complex, being altered by critical points consisting of a single focus in case of Flat Bottom and multiple focus followed by saddles in case of sinusoidal bottom.
The stepped bottom topography, for both Inviscid and Viscous model, serves instead as a limit case to explore the validity of the hypothesis of gradually varied flow. For sufficiently small values of step height, the model is able to reproduce the main physical aspects, including the Hydraulic Jump and the energy jump (positive or negative) that arises nearby the step due to its presence , provided that a suitable numerical model is used to address the problem of stiffness. However, in the Viscous Model, the supercritical stream profiles exhibit quite rapid variations, also for small step heights and hydraulic jumps forms only for supercritical stream profiles starting with surprisingly high Froude Numbers. The model then performs badly when the step height becomes considerable, because of the violation of the hypothesis of gradually varied flow, so this cases has an academic validity more than for practical applications.
The physically meaningful steady Circular Stream Profiles obtained for an Inclined Bed with Flat Bottom topography are summarized in Tab. 5.1. In particular, while for the horizontal bed all of the cases are reported, for the Cone-shaped and the Funnel-shaped bed only profiles where water flows on favourable slope have been chosen. The results then can be extended also to the sinusoidal bottom topography and the stepped bottom topography, as they represent a fluctuation of the flat bottom which does not alter the overall trend of the stream profiles. In particular, for the sinusoidal case, the results in Tab. 5.1 can be integrated with the amplitude response of the flow in Tab. 4.2.
The model is able to capture the basic physics that governs the behaviour of the Circular stream profiles in radial, axially symmetric geometry, particularly for the energetic aspects, in the hypothesis of gradually varied flow. In particular, it explains the monotony properties without writing an explicit solution formula, by means of a detailed analysis

from a dynamical system point of view that can be used for a wide range of bottom topographies [3] and makes possible to obtain the radial position and the conjugate heights of the hydraulic jump. Moreover, it provides a class of novel steady solutions with respect to similar works including bottom topographies (Ref. [42, 4]) having a physical counterpart so that they can be reproduced in laboratory and can be used as a basis for a Linear Stability Analysis, particularly to investigate the stabiity of the Hydraulic Jump. In this sense, the height and velocity perturbations are described by the set of equations 5.7 in Chapter 5, which surprisingly result independent from the bottom topography chosen. The procedure followed to obtain 5.7 is similar to that for the perturbation equations of the Linear Stability Analysis performed in [4], which can be obtained by 5.7 by simply changing from polar to cartesian coordinates. The only steady profile perturbed, again similarly to [4], is that of uniform height. Despite the procedural simplicity to obtain the corresponding set of partial differential equations 5.17 describing the perturbations, its analytical or numerical solution is not discussed here, requiring more sophisticated mathematical techniques to manage the Fuchsian singularities (Ref. [39]) and making impossible to use the Floquet-Bloch Theory already seen in [4**?**].

[3] It suffices they are $C^2(\mathcal{D})$, where $\mathcal{D}$ is the physical domain of the problem and that they make the stream respect the hypothesis of gradually varied flows.

Table 5.1: **Physically significant Inviscid and Viscous Stream Profiles for an Inclined Bed with Flat Bottom ..** The table summarizes the physically meaningful stream profiles that can be obtained for a bed of general inclination and flat bottom topography, along with the respective figures and references (when present). The letters "H", "C", "F", respectively stand for "Horizontal", "Cone" and "Funnel". The abbreviations "SUB", "SUP", "FH", "HJ" stand respectively for "Subcritical", "Supercritical", "Froude Horizon" (i.e., a point where critical conditions are attained), "Hydraulic Jump", while "Conv." and "Div." again stand for "Convergent" and "Divergent" directions of the flow. Last, "Cons.", "Incr.", "Diss." stand for "Conservation", "Increase", "Dissipation". In the description, the symbol ">" means "followed by" and must be interpreted in the flow direction.

	Profile	**Bed**	**Flow Dir.**	**Flow Type**	**Energy**	**Figure**	**Ref.**
Inviscid	Inv. Drain	H	Conv.	SUB (SUP) > FH	Cons.	2.1	[29]
	Inv. Spring	H	Div.	FH > SUB (SUP)	Cons.	2.1	[29]
	Inv. Cone Spring	C	Div.	FH > SUB (SUP)	Incr.	2.8	
	Inv. 2 Horiz.	F	Conv.	FH > SUB (SUP) > FH	Incr.	2.7	
Viscous	Circular Jump	H	Conv.	SUP> HJ> SUB > FH	Diss.	3.17	[29]
	Circular Jump	H	Div.	SUP > HJ > SUB	Diss.	3.17	[29]
	Sub. (Sup.) Drain	H	Conv.	SUB (SUP.)	Diss.	3.17	[29]
	Sub. Spring	H	Div.	SUB	Diss.	3.17	[29]
	Cone Jump	C	Div.	FH > SUP > HJ > SUB	Diss.	3.19	
	Cone Spring	C	Div.	FH > SUB	Diss.	3.19	
	Sup. 2 Hor.	C	Div.	FH > SUP > FH	Diss.	3.19	
	Funnel Jump	F	Conv.	SUP > HJ > SUB > FH	Diss.	3.21	
	Sub. 2 Hor.	F	Conv.	FH > SUB > FH	Diss.	3.21	

Future Works

Future works possibly include a complete Linear Stability Analysis on the basis of the results in Chapter 5, in order to investigate the stability of the Circular Hydraulic Jump in presence of a bed slope and an uneven bottom, described by a given topography. Indeed, while several works including [18, 11, 16, 44] are devoted to the stability of the Circular Hydraulic Jump along a horizontal plate with flat bottom and the symmetry breaking, no studies including bottom topography and bed inclination are found in this sense. The results could be interesting, particularly for the sinusoidal bottom topography: indeed, it can be conjectured, on the basis of [4], that for certain amplitudes and flow conditions it is responsible, in combination with friction, for the onset of Roll Waves Instability. In this sense, an exhaustive study should include an Instability Criterion involving the local Froude Number, in order to be compared to the classical results for Open Channel Flows (Ref. [21, 4]). Useful in this sense can be to change turbulent friction closure term, as done in [37] and to study the response of the stream profiles with respect to several drag parametrizations. The study of the Circular Hydraulic Jump in the laminar case, which appears not to be significantly different for the flat bottom topography (Ref. [29]), brings instead more significant differences for the sinusoidal bottom topography (Ref. [4]), although more fascinating shapes due to instability (such as the polygonal ones) are obtained by considering the problem at smaller scales in which gravity is progressively less influencing and viscosity dominates (Ref. [16, 26]), thus it is not of interest in this context.

Appendix A

Intersection Points for the Step Bed Including Friction

Let consider Eq. 3.49 and define the functions describing left and right hand side members as:

$$L(\xi) = \operatorname{sech}^2[\sigma_s(\xi - \xi_s)] \tag{A.1}$$

and

$$R(\xi) = \frac{\gamma_b - \frac{\alpha}{2} + 2^{\frac{1}{3}}\xi^{-\frac{5}{3}}}{h_s\sigma_s} \tag{A.2}$$

Remembering that $\operatorname{sech}(\xi) = \frac{1}{\cosh(\xi)}$ and the Taylor Series of $\cosh(\xi)$, which converges for all ξ, one has that:

$$L(\xi) = \operatorname{sech}^2[\sigma_s(\xi - \xi_s)] = \left(\frac{1}{\sum_{n=0}^{+\infty} \frac{(\sigma_s(\xi-\xi_s))^{2n}}{2n\,!}}\right)^2 \tag{A.3}$$

Moreover, a re-arrangement allows to write:

$$R(\xi) = \frac{\gamma_b - \alpha/2}{h_s\sigma_s} + \frac{2^{\frac{1}{3}}}{h_s\sigma_s} \cdot \frac{1}{\xi^{\frac{5}{3}}} = A_s + \frac{2^{\frac{1}{3}}}{h_s\sigma_s} \cdot \frac{1}{\xi^{\frac{5}{3}}} \tag{A.4}$$

where A_s is defined in 3.50. By definition, one has:

$$L(\xi = \xi_s) = 1$$

while:

$$R(\xi = \xi_s) = \frac{\gamma_b - \frac{\alpha}{2} + 2^{\frac{1}{3}}\xi_s^{-\frac{5}{3}}}{h_s\sigma_s}$$

Let consider $\sigma_s > 0$. Then $R(\xi)$ defines a decreasing function with asymptotic lower bound A_s.
Immediately, if $A_s \geq 1$, Eq. 3.49 has no solutions because in this case $L(\xi) \leq R(\xi)\,\forall\xi > 0$. If instead $0 \leq A_s < 1$, three cases can be considered depending on $R(\xi = \xi_s)$:

- Assume $R(\xi = \xi_s) > 1$. Then one cannot have intersections points for $0 < \xi \leq \xi_s$ because $R(\xi)$ is strictly decreasing and $R(\xi_s) > 1$, hence suppose there exists an intersection point $\xi_* > \xi_s$. It means that, because of continuity, there exists a right neighbourhood of ξ_s where $R(\xi) \leq L(\xi)$. However, having a look at A.3 and A.4, it is easy to notice that if $0 \leq A_s < 1$, one has that $L(\xi$ decays to 0, while $R(\xi)$ decays to $A_s > 0$, hence there exists a point $\xi_0 > \xi_s$ such that $R(\xi) > L(\xi)$ definitely for all $\xi \geq \xi_0$. The same happens if $A_s = 0$, since $L(\xi)$ decays to 0 faster than $R(\xi)$. Therefore, in both cases there exists a point $\xi_0 > \xi_s$ such that $R(\xi) > L(\xi)$ definitely for all $\xi \geq \xi_0$. If $\xi_* \geq \xi_0$, it means that an intersection arises within an interval where $R(\xi) > L(\xi)$ definitely, falling into a contradiction. If $\xi_* < \xi_0$, a monotony variation of $R(\xi)$ is necessary within (ξ_*, ξ_0) in order to have $R(\xi) > L(\xi)$ for all $\xi > \xi_0$ as required, but $R(\xi)$ is strictly decreasing by definition. Therefore, if $0 \leq A_s < 1$ and $R(\xi = \xi_s) > 1$), Eq. 3.49 has no solution.

- Assume $R(\xi = \xi_s) = 1$. Again, one cannot have intersections points for $0 < \xi < \xi_s$, but $R(\xi = \xi_s) = L(\xi = \xi_s) = 1$, therefore $\xi = \xi_s$ is an intersection point. By applying a similar argument as before, one can conclude that the presence of another intersection point $\xi_* > \xi_s$ is subjected to a change of monotony of $R(\xi)$, thus falling into a contradiction. Therefore, if $0 \leq A_s < 1$, and $R(\xi = \xi_s) = 1$), Eq. 3.49 has the only solution $\xi = \xi_s$.

- Assume $R(\xi = \xi_s) < 1$. Since $R(\xi)$ and $L(\xi)$ are both continuous and $R(\xi)$ is strictly decreasing, there exists one intersection point $\xi_1 < \xi_s$. Since $L(\xi)$ is also symmetric with respect to $\xi = \xi_s$, there exists a second intersection point $\xi_2 > \xi_s$, which is non symmetric with respect to ξ_1 because of the decrease of $R(\xi)$. Similar argument to those adopted previously allow to conclude that ξ_1 and ξ_2 are the only two intersection points possible.

If instead $A_s < 0$, because of the monotony of $R(\xi)$ and the continuity of both functions within (0,1], there exists at least one intersection point ξ_1. Moreover, since the lower bound A_s of $R(\xi)$ is lower than 0, which is the one of $L(\xi)$, there exists a point ξ_0 such that $L(\xi) > R(\xi)$. Let call $\xi_{F,1}$ and $\xi_{F,2}$ the two symmetric inflection points of $L(\xi)$. If the lowest intersection ξ_1 is greater than $\xi_{F,2}$, than because of the strict decrease of $R(\xi)$ one can have only one intersection. In the other cases, one can have from one to three intersection points, this last case when the first two intersections are located between the two inflection points: the third arises because otherwise $R(\xi) > L(\xi)$ definitely, thus falling into a contradiction. For the same reason, one cannot have more than three intersections.

Let consider the case $\sigma_s < 0$. Then $R(\xi)$ defines an increasing function with asymptotic upper bound A_s. Immediately, if $A_s \leq 0$, Eq. 3.49 has no solution. If $A_s > 0$, because of the continuity of $R(\xi)$ and $L(\xi)$ one has at least one intersection point, until a maximum of three intersection points (it can be proved with similar arguments to those already adopted).

What discussed before is summarized in Table A.1. Notice that the results obtained are coherent with the sign of the generalized slope t_* defined in 1.44: solutions ξ_* of Eq. 3.49, which is a particular case of Eq. 1.36, must satisfy the inequality $t_* > 0$, which in this case turns into the following two inequalities (depending on the sign of σ_s):

$$A_s \gtrless \operatorname{sech}^2[\sigma_s(\xi_* - \xi_s)] \quad \text{if} \quad \sigma_s \lessgtr 0 \tag{A.5}$$

Indeed, if $\sigma_s > 0$ one has no solutions if $A_s \geq 1$, that is, when:

$$A_s \geq 1 = \max_{\xi_* > 0} \operatorname{sech}^2[\sigma_s(\xi_* - \xi_s)] \geq \operatorname{sech}^2[\sigma_s(\xi_* - \xi_s)] \Rightarrow t_* < 0$$

On the contrary, if $\sigma_s < 0$ one has no solutions if $A_s \leq 0$, that is, when:

$$A_s \leq 0 = \min_{\xi_* > 0} \operatorname{sech}^2[\sigma_s(\xi_* - \xi_s)] \leq \operatorname{sech}^2[\sigma_s(\xi_* - \xi_s)] \Rightarrow t_* < 0$$

Table A.1: Number of possible solutions of Eq. 3.49 depending on the parameters.

	$A_s \geq 1$	$0 \leq A_s < 1$	$A_s < 0$
$\sigma_s > 0$	None	From 0 to 3	From 1 to 3
$\sigma_s < 0$	From 1 to 3	From 1 to 3	None

List of Variables

The following is a list of the variables, both dimensional and non-dimensional. First, lower latin letters are reported in alphabetic order; they are followed by latin upper letters and greek letters, in alphabetic order. The abbreviation "Dim." and "Non Dim." stands for "Dimensional" and "Non Dimensional": if dimensions are not specified in the third column, the variables are to be considered as non-dimensional. The dimensions $[L]$, $[T]$, $[M]$ respectively stand for length, time and mass.

Symbol	**Description**	**Dimensions**
a	Amplitude of Sinusoidal Bottom Topography	
f	Function def. Chèzy Parametrization	$[L][T]^{-2}$
j	Turbulent Friction	$[L][T]^{-2}$
g	Gravity	$[L][T]^{-2}$
h	Dim. Fluid Depth	$[L]$
h'	Dim. Fluid Height Perturbation	$[L]$
h_G	Pressure at Baricentre of submerged Section	$[L]$
h_s	Non dim. Half-Height of Step Bottom Topography	
k_b	Wavenumber of Sinusoidal Bott. Top.	
k_s	Radiant Spec. Kinetic Height	
q	Non dim. Radiant Specific Discharge	
r	Radius	$[L]$
s	Non dim. Parameter for Curve Parametrization	
t	Dim. Time	[T]
t_*	Non dim. Generalized Slope	
u	Dim. Radial Velocity	$[L][T]^{-1}$
u'	Dim. Velocity Perturbation	$[L][T]^{-1}$

x	Dim. Cartesian longitudinal coordinate	$[L]$
y	Non dim. Fluid Depth	
y_{crit}	Non Dim. Critical Depth Line	
y_0	Non dim. Uniform Depth	
y'	Non dim. Height Perturbation	
z_b	Dim. Bottom Elevation	$[L]$
A	Slope ratio for Sinusoidal Bott. Top.	
A_s	Slope ratio for Step Bott. Top.	
C	Chèzy Coefficient	
C_f	Friction Coefficient	
$\mathcal{D}$	Physical Domain	
F	Non dim. Specific Force	
F_d	Dim. Dynamic Force	$[M][L][T]^{-2}$
F_h	Dim. Hydrostatic Force	$[M][L][T]^{-2}$
Fr	Froude Number	
H	Dim. Stream Head	$[L]$
H_s	Dim. Height Steady Solution	$[L]$
H_0	Stream Head at the Boundary	$[L]$
$\tilde{H}$	Non dim. Stream Head	
$\tilde{H}_-$	Inf. branch of Stream Head for Step Bott.	
$\tilde{H}_+$	Sup. branch of Stream Head for Step Bott.	
P	Fluid Weight per mass unit	$[L][T]^{-2}$
Q	Total Volumetric Flowrate	$[L]^3[T]^{-1}$
Q_r	Dim. Radiant Specific Discharge	$[L]^2[T]^{-1}$
R	Reference radius	$[L]$
U_s	Dim. Velocity of Steady Sol.	$[L][T]^{-1}$
U_0	Torricellian Velocity	$[L][T]^{-1}$
V	Non dim. Steady State Velocity	
Y	Non dim. Steady State Height	
α	Non dim. Friction Coefficient	

β	Momentum Coefficient	
γ_b	Basal Slope	
γ_s	Fluid Spec. Weight	$[M][L]^{-2}[T]^{-2}$
ζ	Non dim. Bed Elevation	
ζ_{CH}	Bottom Top. ensuring Const. Stream Head	
ζ_{CR}	Bottom Top. ensuring Critical Depth	
ζ_{UH}	Bottom Top. ensuring Uniform Depth	
θ	Central Angle of Circular Sector	rad
ν	Non dim. Velocity	
ν'	Non dim. Velocity Perturbation	
ξ	Non dim. radius	
ξ_{max}	Non dim. Maximum radius for Critical Cond.	
ξ_{min}	Non dim. Minimum radius for Critical Cond.	
ξ_s	Non dim. Step Position	
ξ_0	Non dim. Boundary Radius	
ρ	Fluid Density	$[M][L]^{-3}$
σ_s	Non dim. Steepness Param. of Step Bottom	
τ	Non dim. Time	
ϕ	Basal Angle of Bed	rad
Ω	Submerged Section	$[L]^2$

Bibliography

[1] GM Abdel-Aal, Abdelazim M Negm, TM Owais, and AA Habib. Theoretical modeling of hydraulic jumps at negative step in radial stilling basins with end sill.

[2] Hamidreza Safavi Abdorreza Kabiri-Samani, Mohammad Hossein Rabiei and Seyed Mahmood Borghei. Experimental–analytical investigation of super- to subcritical flow transition without a hydraulic jump. *Journal of Hydraulic Research*, 52 (1):129–136, 2014. doi: 10.1080/00221686.2013.822935.

[3] Milton Abramowitz and Irene A. Stegun. *Handbook of Mathematical Functions with Formulas, Graphs, and Mathematical Tables*. Dover Publications, New York, 1964. ISBN 0-486-61272-4.

[4] N. J. Balmforth and S. Mandre. Dynamics of roll waves. *Journal of Fluid Mechanics*, 514:1–33, 2004. doi: 10.1017/S0022112004009930.

[5] Carlos Barceló, Stefano Liberati, and Matt Visser. Analogue gravity. *Living Reviews in Relativity*, 8(1), dec 2005. doi: 10.12942/lrr-2005-12.

[6] Rajesh K. Bhagat, N. K. Jha, P. F. Linden, and D. Ian Wilson. On the origin of the circular hydraulic jump in a thin liquid film. *Journal of Fluid Mechanics*, 851:R5, 2018. doi: 10.1017/jfm.2018.558.

[7] G. Bidone. *Experiences sur le remou et sur la propagation des ondes par George Bidone. Lu dans la seance du 12 decembre 1819*. 1820.

[8] Tomas Bohr, Peter Dimon, and Vakhtang Putkaradze. Shallow-water approach to the circular hydraulic jump. *Journal of Fluid Mechanics*, 254:635–648, 1993. doi: 10.1017/S0022112093002289.

[9] T. A. A. Broadbent. The great art or the rules of algebra. by gerolamo cardano. translated and edited by t. r. witmer. pp. xxiv, 267. 93s. 1968. (massachusetts institute of technology press.). *The Mathematical Gazette*, 54(387):69–70, 1970. doi: 10.2307/3613177.

[10] Richard Runyon Brock. Development of roll waves in open channels. 1968.

[11] J Bush, A Hosoi, and J Aristoff. The stability of the circular hydraulic jump. *J. Fluid Mech.(submitted)*, 2003.

[12] Hubert Chanson. Convective transport of air bubbles in strong hydraulic jumps. *International Journal of Multiphase Flow*, 36(10):798–814, 2010. ISSN 0301-9322. doi: https://doi.org/10.1016/j.ijmultiphaseflow.2010.05.006.

[13] M. Codegone. *METODI MATEMATICI PER L'INGEGNERIA*. Zanichelli, 1995. ISBN 97788808098146.

[14] A. D. D. Craik, R. C. Latham, M. J. Fawkes, and P. W. F. Gribbon. The circular hydraulic jump. *Journal of Fluid Mechanics*, 112:347–362, 1981. doi: 10.1017/S002211208100044X.

[15] Robert F. Dressler. Mathematical solution of the problem of roll-waves in inclined opel channels. *Communications on Pure and Applied Mathematics*, 2(2-3):149–194, 1949. doi: https://doi.org/10.1002/cpa.3160020203.

[16] Clive Ellegaard, Adam Espe Hansen, Anders Haaning, and Tomas Bohr. Experimental results on flow separation and transitions in the circular hydraulic jump. *Physica Scripta Volume T*, 67:105–110, January 1996. doi: 10.1088/0031-8949/1996/T67/021.

[17] Zohre Fakhari and Abdorreza Kabiri-Samani. Scour in the transition from super- to subcritical flow without a hydraulic jump. *Journal of Hydraulic Research*, 55(4): 470–479, 2017. doi: 10.1080/00221686.2016.1275052.

[18] Thierry Foglizzo, Frédéric Masset, Jérôme Guilet, and Gilles Durand. Shallow water analogue of the standing accretion shock instability: Experimental demonstration and a two-dimensional model. *Phys. Rev. Lett.*, 108:051103, Jan 2012. doi: 10.1103/PhysRevLett.108.051103.

[19] K. A. Ivanova and S. L. Gavrilyuk. Structure of the hydraulic jump in convergent radial flows. *Journal of Fluid Mechanics*, 860:441–464, 2019. doi: 10.1017/jfm.2018.901.

[20] G. Jannes, R. Piquet, P. Maïssa, C. Mathis, and G. Rousseaux. Experimental demonstration of the supersonic-subsonic bifurcation in the circular jump: A hydrodynamic white hole. *Physical Review E*, 83(5), may 2011. doi: 10.1103/physreve.83.056312.

[21] H . Jeffreys. The flow of water in an inclined channel of rectangular section. *Philosophical Magazine*, 49 (293),:793–807, 1925. doi: 10.1080/14786442508634662.

[22] Abdelkawi M. Khalifa and John A. McCorquodale. Radial hydraulic jump. *Journal of the Hydraulics Division*, 105(9):1065–1078, 1979. doi: 10.1061/JYCEAJ.0005267.

[23] John D. Lawson and Brett C. Phillips. Circular hydraulic jump. *Journal of Hydraulic Engineering*, 109(4):505–518, 1983. doi: 10.1061/(ASCE)0733-9429(1983)109:4(505).

[24] Zhipeng Li, Longquan Sun, Xiongliang Yao, Duliang Wang, and Fochen Li. Experimental study on cavity dynamics in high froude number water entry for different nosed projectiles. *Applied Ocean Research*, 102:102305, 2020. ISSN 0141-1187. doi: https://doi.org/10.1016/j.apor.2020.102305.

[25] E. Marchi and A. Rubatta. *Meccanica dei fluidi. Principi e applicazioni.* Varia. Architettura. UTET, 1981. ISBN 9788802036595.

[26] Erik A. Martens, Shinya Watanabe, and Tomas Bohr. Model for polygonal hydraulic jumps. *Physical Review E*, 85(3), mar 2012. doi: 10.1103/physreve.85.036316.

[27] Jarosław Mikielewicz and Dariusz Mikielewicz. A simple dissipation model of circular hydraulic jump. *International Journal of Heat and Mass Transfer*, 52(1):17–21, 2009. ISSN 0017-9310. doi: https://doi.org/10.1016/j.ijheatmasstransfer.2008.06.007.

[28] Abdelazim M Negm, GM Abdel-Aal, TM Owais, and AA Habib. Theoretical modeling of free hydraulic jumps at negative step in radial stilling basins.

[29] Amilcare Porporato, Luca Ridolfi, and Lamberto Rondoni. Hydrodynamic holes and froude horizons: Circular shallow water profiles for astrophysical analogs. *Physical Review Research*, 3(2), may 2021. doi: 10.1103/physrevresearch.3.023119.

[30] A. Quarteroni, R. Sacco, F. Saleri, and P. Gervasio. *Matematica Numerica.* UNITEXT. Springer Milan, 2014. ISBN 9788847056442.

[31] N. RAJARATNAM. Hydraulic jumps. volume 4 of *Advances in Hydroscience*, pages 197–280. Elsevier, 1967. doi: https://doi.org/10.1016/B978-1-4831-9935-1.50011-2.

[32] G. L. Richard and S. L. Gavrilyuk. A new model of roll waves: comparison with brock's experiments. *Journal of Fluid Mechanics*, 698:374–405, 2012. doi: 10.1017/jfm.2012.96.

[33] Ralf Schützhold and William G. Unruh. Gravity wave analogues of black holes. *Phys. Rev. D*, 66:044019, Aug 2002. doi: 10.1103/PhysRevD.66.044019.

[34] Lawrence F. Shampine and Mark W. Reichelt. The matlab ode suite. *SIAM Journal on Scientific Computing*, 18(1):1–22, 1997. doi: 10.1137/S1064827594276424.

[35] John William Strutt. On the theory of long waves and bores. *Proc. R. Soc. Lond. A*, 90:324–328, 1914. doi: 10.1098/rspa.1914.0055.

[36] V. Te Chow. *Open-channel Hydraulics.* Civil engineering series. McGraw-Hill, 1959. ISBN 9780070859067.

[37] Olivier Thual, Louis-Romain Plumerault, and Dominique Astruc. Linear stability of the 1d saint-venant equations and drag parameterizations. *Journal of Hydraulic Research*, 48(3):348–353, 2010. doi: 10.1080/00221686.2010.481837.

[38] Wouter Tierens and Daniël De Zutter. A time-domain discretisation of maxwell's equations in nontrivial media using collocated fields. In *Proceedings of the 2012 IEEE International Symposium on Antennas and Propagation*, pages 1–2, 2012. doi: 10.1109/APS.2012.6348748.

[39] F. G. Tricomi. *Differential Equations.* Hafner Pub. Co, 1961. ISBN 9780486488196.

[40] W. G. Unruh. Experimental black-hole evaporation? *Phys. Rev. Lett.*, 46:1351–1353, May 1981. doi: 10.1103/PhysRevLett.46.1351.

[41] P. Toscano V. Armenio and V. Fiorotto. On the effects of a negative step in pressure fluctuations at the bottom of a hydraulic jump. *Journal of Hydraulic Research*, 38 (5):359–368, 2000. doi: 10.1080/00221680009498317.

[42] Alessandro Valiani and Valerio Caleffi. Free surface axially symmetric flows and radial hydraulic jumps. *Journal of Hydraulic Engineering*, 142:06015025, 2016.

[43] Hang () Wang, Chengyang () Ni, Wenlong () Lyu, and Lian () Tang. A-type hydraulic jumps over a negative step: Numerical investigation based on composite modeling and validation. *Physics of Fluids*, 35(10):105121, 10 2023. ISSN 1070-6631. doi: 10.1063/5.0168691.

[44] Shinya Watanabe, Vachtang Putkaradze, and Tomas Bohr. Integral methods for shallow free-surface flows with separation, 2000.

[45] Jong-Ju Yi, Min-Jae Kim, Seon-Hong Kim, Bu-Geun Paik, and Kyung Chun Kim. Prediction of supercavitation shapes for a wide range of froude numbers. *International Journal of Naval Architecture and Ocean Engineering*, 14:100426, 2022. ISSN 2092-6782. doi: https://doi.org/10.1016/j.ijnaoe.2021.11.009.

[46] Alexander F. Zakharov. Constraints on a charge in the reissner-nordström metric for the black hole at the galactic center. *Physical Review D*, 90(6), sep 2014. doi: 10.1103/physrevd.90.062007.